Novel Photomedicine

Guest Editors: Victor Loschenov, Rudolf Steiner, Alexander Potapov, and Alexander Douplik

Novel Photomedicine

Novel Photomedicine

Guest Editors: Victor Loschenov, Rudolf Steiner, Alexander Potapov, and Alexander Douplik

Editorial Board

Contents

Editorial
Novel Photomedicine

Victor Loschenov,[1,2] Rudolf Steiner,[3] Alexander Potapov,[4] and Alexander Douplik[5]

[1] *M. Prokhorov General Physics Institute of the Russian Academy of Sciences, Vavilov Street 38, Moscow 119991, Russia*
[2] *National Research Nuclear University MEPhI (Moscow Engineering Physics Institute), Kashirskoe Shosse 31, Moscow 115409, Russia*
[3] *Institut fuer Lasertechnologien in der Medizin und Messtechnik an der Universität Ulm, Helmholtz Street 12, 89081 Ulm, Germany*
[4] *Burdenko Neurosurgery Institute, 4th Tverskaya-Yamskaya Street 16, Moscow 125047, Russia*
[5] *Department of Physics, Ryerson University, 350 Victoria Street, Toronto, ON, Canada M5B 2K3*

Correspondence should be addressed to Victor Loschenov; loschenov@mail.ru

In the past years physicist, physicians, chemists, biologists, and other scientists are cooperating in developing new methods in treatment and diagnosis of a huge problem of nowadays—malignant lesions. The scientists are elaborating new methods, novel agents, improving existing methods of diagnosis and treatment of wide classes and types of cancers. Photomedicine—is a huge domain covering a wide area from diagnosis to treatment of a large spectrum of malignancies, from developing of new agents to improvement of already existing technologies. The special issue Novel Photomedicine highlights the recent advances and last approaches in optogenetics, fluorescence diagnosis, and photodynamic therapy and moreover suggests the post procedures to avoid side-effects of the photodynamic therapy. We give a short overview of the published articles below.

The review article "Optogenetics: Novel Tools for Controlling Mammalian Cell Functions with Light" is representing the recent approaches in optogenetics: techniques, methods, and so forth. The authors are primarily concentrating on the most commonly used photosensitive protein, channelrhodopsin protein. The most recently developed tools are also described. Undoubtedly, optogenetics is a fast developing tool with perspective future, although it appeared in recent decade.

An interesting approach of using microbubbles for enhancing optical properties was represented in paper entitled "Optical Scattering Properties of Intralipid Phantom in Presence of Encapsulated Microbubbles." The ability of the microbubbles as optical contrast agents is investigated in variety of intralipid phantoms. The results are showing the future potential of the encapsulated microbubbles in optical diagnosis, as they effectively change optical properties of the intralipid phantoms, which could help to improve the optical imaging of malignant tissues.

A promising mechanism for photodynamic therapy was described and investigated in "Autoregulatory Feedback Mechanism of P38MAPK/Caspase-8 in Photodynamic Therapy-hydrophilic/Lipophilic Tetra-α-(4-carboxyphenoxy) Phthalocyanine Zinc-Induced Apoptosis of Human Hepatocellular cCarcinoma Bel-7402 Cells." The authors firstly introduce the effect of T-alpha PCZn-PDT on apoptosis of human hepatocellular carcinoma cells with and without inhibitors, as well as on Caspase-3, Bid, Cytochrome c, and mitochondria membrane potential, respectively. Their investigation demonstrates that Caspase-3, Bcl-2, Bid, and mitochondria are involved in autoregulatory feedback of P38MAPK/Caspase-8 during photodynamic therapy of abovementioned cells.

The most recent problems and solutions for most common malignancy are reviewed in the paper "Overview on Topical 5-ALA Photodynamic Therapy use for Non-melanoma skin cancers." The review includes history of photodynamic therapy, procedure itself, and especially treatment of nonmelanoma skin cancer. Afterwards the postprocedure such as photorejuvenation is discussed, and new concepts for illumination and limits of application are widely highlighted.

A contribution to improve fluorescence diagnosis was represented in "Scattered and Fluorescent Photon Track Reconstruction in a Biological Tissue." The paper is considering the way laser-induced fluorescence spreads in tissue. The

authors firstly suggest and calculate an effective fluorescence anisotropy factor on example of brain tissue phantoms. The obtained result allows simplifying the process of fluorescence probing depth's determination in order to improve analysis of deep tissue regions during neurosurgical operations.

A variety of forward scattering quasi 1-D paths are discussed in the paper "Reflectance of Biological Turbid Tissues under Wide Area Illumination: Single Backward Scattering Approach." The contribution of single backward scattering to reflectance spectra is investigated and its potential effectiveness for the distances between transport and reduced scattering domain is argued. This remarkable achievement allows taking into account not only mismatched boundary conditions but also multilayer geometry and moreover can be used for real-time spectral processing.

A way to increase photodynamic efficiency is reflected in "Multiorganelle Localization of Metallated Phthalocyanine Photosensitizer in Colorectal Cancer Cells (DLD-1 and CaCo-2) Enhances Efficacy of Photodynamic Therapy." The authors' approach was in increasing the apoptotic cell death during PDT treatment of colorectal cancer on the example of two cancer cell lines (DLD-1 and CaCo-2). After 1 and 24 h there was a significant increase in both cathepsin D and cytochrome C. They state that the photosensitiser leads to different response from cells most probably according to the stage of the tumorogenesis. Although the way photosensitiser induces the cell death has to be studied further, it is hypothesized that sulfonated zinc phthalocyanine photosensitiser is capable of inducing apoptotic cell death that is promoted by lysosomal photooxidation.

A method of visualisation of the diffuse reflected light is described in research entitled "Two-Stage Analysis on Models for Quantitative Differentiation of Early-Pathological Bladder States." A simulation method is considering 5 states of epithelium tissue, from normal to precancerous. The authors found the influence of optical properties change on diffuse-reflectance signal distributions on the surface of the multilayered phantoms. The analysis is made on different threshold levels and could be used as a base for inverse problem solution to interpret diffuse-reflectance signals from epithelial tissues, although there were no additional markers used.

A residual effect of PDT treatment is investigated in a paper entitled "Photoprotective Effect of The Plant Collaea Argentina against Adverse Effects Induced by Photodynamic Therapy." The authors proposed to use a special agent— the methanolic extract of the Collaea argentina—to protect healthy cells from side-effects of PDT with different types of photosensitisers in different concentrations. However the additional research with *in vivo* experiments and isolation of the compound responsible for the photoprotection has to be conducted; it is already stated that the extract interferes with singlet oxygen production during photodynamic treatment, which is a promising result to protect skin from PDT-induced photodamage of healthy skin.

Another research is dealing with PDT safety to non-damaged tissue and entitled "Safety Study of Photodynamic Therapy Using Talaporfin Sodium in the Pancreas and Surrounding Tissues in the Syrian Golden Hamster." The authors investigated the ability of PDT with talaporfin sodium (TS) to treat pancreas without damaging surrounding tissues. Although minimisation of the exposure of the duodenum to light is required, the conducted research showed that PDT with TS in Phase 1 studies of PDT for pancreatic cancer in inoperable patients with localised disease is supported.

A new promising agent for PDT is announced in "Potential Use of C60/2-Hydroxypropyl-β-Cyclodextrin Nanoparticles as a New Photosensitizer in the Treatment of Cancer." The paper is studying photosensitizing abilities of the nanoparticles by means of electron spin resonance and phototoxicity on cancer cells, the photoinduced antitumor effect was evaluated as well. However accumulation of the nanoparticles and pharmacokinetics of the process after injection is still under investigation; the authors obtained the remarkable effect of tumor growth suppression and found the difference between light doses provided to tumor.

Another group presented an improvement of colon cancer diagnosis in the paper entitled "Fluorescence Diagnostics of Colon Malignant and Premalignant Lesions Using 5-Aminolevulinic Acid." The research was based on 5-ALA effectiveness for fluorescence diagnosis of colon polyps. Local fluorescent diagnosis as an additional step in combined approach during colonoscopy allowed for significantly increasing specificity from 62.5% to 93.7%. Moreover the method applied allowed targeting biopsy as well as identifying malignant transformations in colon.

Acknowledgment

Victor Loschenov
Rudolf Steiner
Alexander Potapov
Alexander Douplik

Review Article

Optogenetics: Novel Tools for Controlling Mammalian Cell Functions with Light

Toshihiro Kushibiki, Shinpei Okawa, Takeshi Hirasawa, and Miya Ishihara

Department of Medical Engineering, National Defense Medical College, 3-2 Namiki, Tokorozawa, Saitama 359-8513, Japan

Correspondence should be addressed to Toshihiro Kushibiki; toshi@ndmc.ac.jp

In optogenetics, targeted illumination is used to control the functions of cells expressing exogenous light-activated proteins. Adoption of the optogenetic methods has expanded rapidly in recent years. In this review, we describe the photosensitive channel proteins involved in these methods, describe techniques for their targeting to neurons and other cell types both within and outside the nervous system, and discuss their applications in the field of neuroscience and beyond. We focus especially on the channelrhodopsin protein ChR2, the photosensitive protein most commonly employed in optogenetics. ChR2 has been used by many groups to control neuronal activity, both *in vitro* and *in vivo*, on short time scales and with exquisite anatomical precision. In addition, we describe more recently developed tools such as opsin/G protein-coupled receptor chimeric molecules and a light-activated transgene system. In addition, we discuss the potential significance of optogenetics in the development of clinical therapeutics. Although less than a decade old, optogenetics is already responsible for enormous progress in disparate fields, and its future is unquestionably bright.

1. Introduction

Optogenetics comprises a growing family of related techniques in which genetically modified cells are stimulated by light in order to influence cellular behaviors. For target cells to be influenced by light, they must be engineered to express exogenous photosensitive proteins that alter membrane potential, or other cellular properties, in response to illumination [1–5]. The effects of membrane depolarization (or, less commonly, hyperpolarization) can then be monitored at the level of individual cells, groups of interacting cells (e.g., tissues or neural circuits), or the whole organism. Therefore, optogenetics encompasses several components: discovery and optimization of photosensitive proteins, techniques for targeting the genes encoding these proteins to specific cell types, and technologies for targeted illumination *in vivo*. In addition, optogenetics is a suitable method for observing the electrophysiological, functional, and behavioral changes resulting from photostimulation [6–10].

The field of optogenetics is quite young. Several of the light-sensitive proteins used in optogenetic experiments,

such as channelrhodopsin [11, 12] and halorhodopsin [13–15], were first identified decades ago. However, it was not until 2005 that they were first used to control neuronal activity [16]. The term "optogenetics" was itself coined around 2006 by Deisseroth, whose laboratory pioneered many of the genetic and optical techniques that facilitate the use of illumination to investigate neural dynamics [17]. The earliest studies were performed *in vitro* in cell culture, but by 2007, the advent of fiber-optic neural interfaces permitted the use of bacterial opsins to influence behavior in intact, freely behaving mammals [18, 19]. Since that time, the optogenetic applications have expanded rapidly to encompass studies of neural circuits, brain diseases, and nonneuronal systems such as stem cells, cardiac tissue, and skeletal muscle. Accordingly, based on its growing importance as a paradigm in many fields of biomedical research, optogenetics was selected as the "Method of the Year" in 2010 by *Nature Methods* [20].

In this review, we summarize the recent literatures describing the use of optogenetics to develop novel technologies for control of cellular functions. Because most of the literature published to date describes the use of photoactive
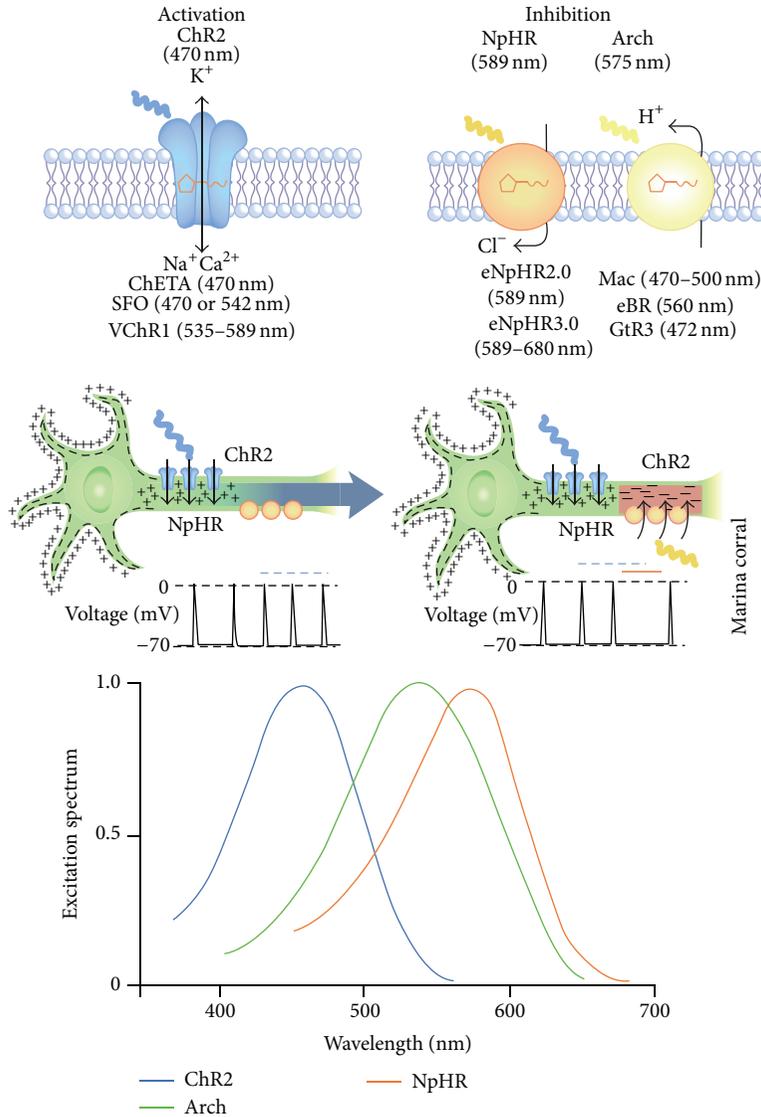
FIGURE 1: Optogenetic tools for modulating membrane voltage potential. Adapted with permission from Macmillan Publishers Ltd. (Nature Publishing Group): *Nature Methods* [7], copyright (2011).

proteins, such as microbial opsins and plant light sensors, we provide an overview of these representative photoactive proteins. In addition, we summarize the clinical significance of optogenetics.

2. Photoactive Proteins

2.1. Channelrhodopsin and Halorhodopsin. In general, the optogenetics manipulations involve altering the membrane potential of electrically excitable cells by illuminating them with controlled bursts of light. Membrane depolarization of neurons induces transient electrical signals (spikes or action potentials) that ultimately convey information between neurons within the same circuit. For neurons to be artificially depolarized by illumination, they are engineered to express proteins that alter the ion permeability of membranes in response to light. The first light-sensitive protein used as a

"switch" to control neuronal activity was the *Chlamydomonas* protein channelrhodopsin-2 (ChR2), a cation selective channel that permits entry of Na^+ and Ca^{2+} ions in response to blue light (470 nm wavelength) [21–31] (Figure 1). ChR2, an algal phototaxis receptor that uses light to depolarize the plasma membrane [32], acts as a light-gated cation channel when expressed in animal cells [12]. ChR2 is expressed mainly under low-light conditions, suggesting that the protein is involved in photoreception in dark-adapted *Chlamydomonas* cells. In contrast to the most cation-selective ion channels, ChR2 contains the seven transmembrane alpha helices characteristic of G protein-coupled receptors (GPCRs). Nagel et al. demonstrated that ChR2 could be used to depolarize the cells of various sizes simply by illuminating cells with the appropriate wavelength [12]. When ChR2 was expressed in a neuron and the cell was exposed to blue light, the channel immediately depolarized the neuron, triggering a spike.

Beginning with cultured neurons and proceeding to more elaborate *in vitro* systems, this property of ChR2 has been exploited to precisely control neuronal activity. In an initial study, the Deisseroth group [16] used ChR2 to reliably control neuronal spiking on millisecond timescales to control both excitatory and inhibitory synaptic transmissions. Because illumination can be controlled at very high spatial and temporal resolution, this approach permits experimental manipulation of neural processing with great precision, even at the level of single spikes and synaptic events. Millisecond- to second-scale control of neuronal function was also achieved by Li et al. [33], who developed systems for light activation of neurons using vertebrate rat rhodopsin 4 (RO4) and green algae ChR2. Their use of two light-activated proteins permitted precise and reversible antagonistic control of neuronal function, as demonstrated in both cultured neurons and intact spinal cords. Antagonistic control was also achieved by using alternative light-activated proteins with different wavelength sensitivities and ion permeabilities. For example, the chloride pump halorhodopsin (NpHR) hyperpolarizes neurons in response to yellow light (590 nm wavelength), in contrast to ChR, which depolarizes expressing cells under illumination with blue light (Figure 1).

In addition to cultured neurons, ChR2 has been exploited in the context of cultured brain slices also, allowing investigations in larger and more complex arrangements of cells. Zhang and Oertner [34] combined millisecond-scale activation of ChR2 with two-photon calcium imaging of slice cultures of rat hippocampus. In that study, the influx of calcium resulting from light-activated action potentials was greater than those resulting from somatic current injection; consequently, the authors were able to achieve highly reproducible synaptic transmission. Furthermore, correlation of light stimulation with postsynaptic depolarization in the slices induced long-term potentiation. Such *in vitro* systems will permit investigations of synaptic plasticity using the tools of both genetics and pharmacology.

Slice cultures had been used to address the challenges related to single-cell targeting of optogenetic activation with temporal precision comparable to spike timing. In hippocampal slices from mouse, Andrasfalvy et al. [35] used optogenetic methods to achieve submillisecond control of single neurons. The use of temporally focused laser illumination in that study allowed simultaneous excitation of large numbers of channels on individual neurons, resulting in depolarizations that were both large in magnitude (up to ~15 mV) and rapid (less than 1 ms). The high spatiotemporal resolution of their technique enabled selective illumination (and therefore selective activation) of subcellular features, including presynaptic terminals and dendrites, at considerable depth within the slice.

Although brain slices are more physiologically relevant than cultured individual neurons, they are still not intact brains. Illumination methods optimized for *in vivo* contexts (such as optical fibers), in combination with transgenic technologies, have enabled ChR2-mediated optogenetics to leap out of the culture dish into live organisms. For example, in the nematode *C. elegans*, ChR2 expressed in excitable cells has been used to activate specific neurons and muscles,

and thereby elicit specific behaviors in living and intact animals [36]. However, the greatest strengths of optogenetics have been revealed by extensive recent studies in rodents. Early studies employed transgenic animals expressing light-activated proteins throughout the brain, as in a study by Arenkiel et al. [37] using mice expressing a ChR2-YFP fusion protein in the CNS. Those authors were able to exploit *in vivo* activation of neurons to map neural circuits involved in olfaction; their data suggested that olfactory processing in mouse depends on mitral cell convergence onto olfactory cortex and subsequent integration by cortical cells. This work sets an early precedent for the value of optogenetics methods for influencing neuronal activity in the brains of intact animals and of using such experimental manipulations to probe the complex functional connections between neurons *in vivo*.

Even greater experimental power has been achieved by targeting the expression of ChR2 to specific subsets of neurons within the brain. Such targeting is often achieved by restricting channel expression both anatomically, by precise delivery of ChR2-encoding viral vectors to specific brain regions, or genetically, by placing ChR2 under the control of a promoter specifically activated in the cell type of interest. Genetic targeting can itself be achieved by multiple means, for example, by transgenesis or the use of viruses encoding channels driven by cell type-specific promoters. Furthermore, anatomical and genetic targeting methods are often used together. Examples of several targeting approaches and their applications are described below.

In an example of strictly anatomical targeting, Huber et al. [38] performed *in utero* electroporation of ChR2-GFP into neocortical pyramidal neurons of embryonic mice. As adults, the electroporated mice expressed the channel in a small fraction of layer 2/3 neurons, primarily in the barrel cortex. These animals could be conditioned to detect brief sequences of light pulses (resulting in corresponding brief trains of action potentials), demonstrating that very short periods of cortical activity in a sparse subset of cortical neurons can drive both decision making and learning. In a case of strictly genetic targeting, Wang et al. [39] generated transgenic mouse lines that express ChR2 in various subsets of neurons in different regions of the brain and used their system to map the synaptic circuits of cortical neurons in living animals.

Several studies have targeted delivery of ChR2 both genetically and anatomically in order to restrict expression of the channel to specific brain regions and/or cell types of interest. Tsai et al. [40] stereotactically injected a Cre (site-specific DNA recombinase)-inducible adeno-associated virus (AAV) encoding Chr2-EYFP into the ventral tegmental area (VTA) of tyrosine hydroxylase-internal ribosomal entry site (IRES)—Cre transgenic mice, resulting in expression of the light-activated protein specifically in the dopaminergic (DA) neurons of VTA. By selectively stimulating these cells in freely behaving animals, the authors were able to show that phasic activation of DA neurons in VTA resulted in behavioral conditioning that could not be achieved by longer, lower-frequency action potentials. Similarly, Kravitz et al. [41] injected AAV encoding Cre-activatable ChR2-EYFP

into dorsomedial striatum of transgenic mice expressing Cre in medium spiny neurons (MSNs), thereby restricting expression of the channel to direct- or indirect-pathway MSNs. Using this system, the authors showed that direct-pathway activation via fiber-optic illumination of ChR2 rescued disease-associated symptoms in a model of Parkinson's disease (PD). Their findings clearly demonstrated that the basal ganglia circuitry played a crucial role in regulation of parkinsonian motor behaviors and suggested that modulation of direct-pathway circuitry might be used therapeutically to treat the motor deficits associated with PD. In yet another example of combined anatomical and genetic targeting, Adamantidis et al. [18] introduced a lentivirus encoding ChR2-mCherry under the control of the hypocretin (Hcrt) promoter via stereotactic injection into the lateral hypothalamus of mice, resulting in channel expression in a subset of cells within this brain region. Specific patterns of stimulation of Hcrt neurons increased the likelihood of arousal from sleep, demonstrating that these cells played an active role in determining wakefulness. These results provided critical insights into the neural basis of sleep regulation.

It may be possible to achieve even higher spatial resolution, at the level of particular structures within specific cell types, using light-activated proteins that are targeted to subcellular compartments within neurons. (As noted above, this level of resolution can be achieved in brain slices using temporally focused lasers, but this mode of illumination is not optimal for use in the intact brain.) For example, Lewis et al. [42] showed that ChR2 fused to the myosin-binding domain of Melanophilin is localized to the somatodendritic compartment. In conjunction with the anatomical and genetic targeting methods described above, fusion proteins of this sort could be used to enable specific photostimulation of dendrites of particular cell types, dramatically increasing the potential power of circuit-level analyses.

The abovementioned reports suggest that ChR2 had widely been used to modulate the membrane potential in neurons, but recently, several groups also explored the possibility of ChR2 mediating optogenetic application in the brain cells other than the neurons. For example, in order to mimic the pH-induced calcium responses involved in regulation of breathing, Gourine et al. [43] used light to stimulate ChR2-expressing astrocytes. This stimulation resulted in activation of chemoreceptor neurons and influenced respiratory responses in live animals, indicating that glial cells are critically involved in the breathing reflex. Furthermore, ChR2 is increasingly being applied outside the central nervous system altogether. In particular, optogenetics methods have been used to control cardiomyocytes and other electrically active cells in the heart. Bruegmann et al. [44] expressed ChR2 in heart muscle, allowing them to stimulate cardiac tissue with spatial and temporal precision; their findings revealed the effects of prolonged depolarization on rhythm generation and calcium homeostasis in the heart. Skeletal muscle has also been investigated with the tools of optogenetics: Asano et al. [45] used light to induce action potentials in ChR2-expressing myotubes, ultimately resulting in controllable contractions of these cells. Because skeletal muscle transduces force effectively, such an approach could

be useful in biological microdevices in which contractile patterns are regulated by localized illumination. In addition, ChR2 has also been introduced into embryonic stem cells (ESCs), allowing reliable tracking of these cells and their progeny, as well as spatial and temporal control of the electrical activity of neurons (and other cell types) derived from ESCs [46, 47]. These approaches should allow precise optical regulation of the differentiation of ESCs both *in vivo* and *in vitro* and facilitate studies of the ways that transplanted ESCs contribute to the tissues and networks in which they ultimately reside.

2.2. Opsin/G Protein-Coupled Receptor (GPCR) Chimeras and Other Opsins.

As noted above, microbial opsins share structural similarities with GPCRs. Airan et al. exploited these similarities to construct opsin-GPCR chimeras, termed "optoXRs," whose signaling activities are responsive to light [48]. In conjunction with the light illumination technologies also used for ChR2-mediated optogenetics, optoXRs were used to precisely control intracellular signaling events in live cells and intact organisms. In their initial study, Airan et al. had developed two optoXRs that activate distinct signaling modules upon light illumination (Figure 2(a)). In the nucleus accumbens of living mice, these two optoXRs exhibited antagonistic effects on neuronal activity. Furthermore, when photostimulation was administered with specific timing, the influence of the optoXRs on intracellular signaling could modulate conditioning in freely moving animals. Thus, the use of optoXRs complements the use of ChR2 mediated for optogenetic control of behavior in mammals such as mice (Figure 2(b)).

In an analogous experiment, Gutierrez et al. [49] developed an optogenetic system in which vertebrate rhodopsin, a $G_{i/o}$ protein-coupled receptor, was expressed in cerebellar Purkinje cells (PCs) of mice. *In vivo* activation of rhodopsin by light illumination specifically expressed in PCs reduced simple spike firing that was comparable with the reduction in firing observed for the activation of cerebellar $G_{i/o}$-coupled $GABA_B$ receptors. In particular, the light illumination of the cerebellar vermis in freely moving mice changed the motor behavior. Thus, spike modulation via $G_{i/o}$-mediated signaling in cerebellar PCs affected motor coordination and showed a new promising approach for studying the physiological function of G protein-coupled receptor-mediated signaling in a cell type-specific manner. Karunarathne et al. [50] also exploited nonrhodopsin opsins in an optogenetic paradigm to target several classes of G protein-mediated intracellular signaling in precisely delineated areas of individual cells. Using this system, they were able to modulate behavior of polarized cells and early differentiation of neurons via controlled illumination. A similar strategy could be readily applied to investigate the roles of G proteins in other phenomena, such as the migration and homing of immune cells or the contractions of cardiac tissue.

2.3. Light-Switchable Transgene System.

The light sensors used in the systems described above are membrane proteins that localize to the cell surface. They either alter membrane potential or activate intracellular signaling cascades in

(a)

(b)
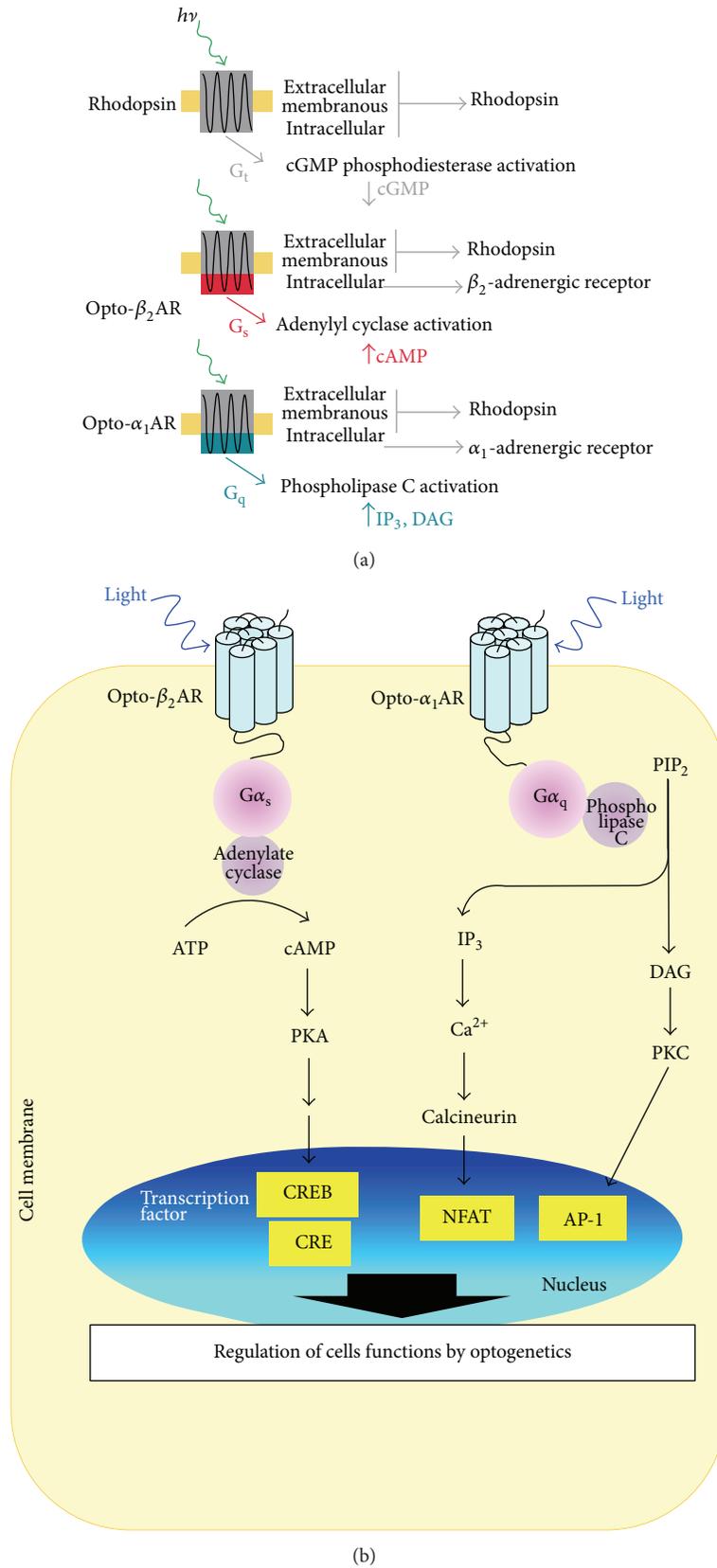
FIGURE 2: OptoXR: optogenetic control of intracellular signal transduction. (a) OptoXR design. Adapted with permission from Macmillan Publishers Ltd. (Nature Publishing Group): *Nature* [48], copyright (2009). (b) Possible intracellular signaling after the light illumination of OptoXR.

(a)

(b)
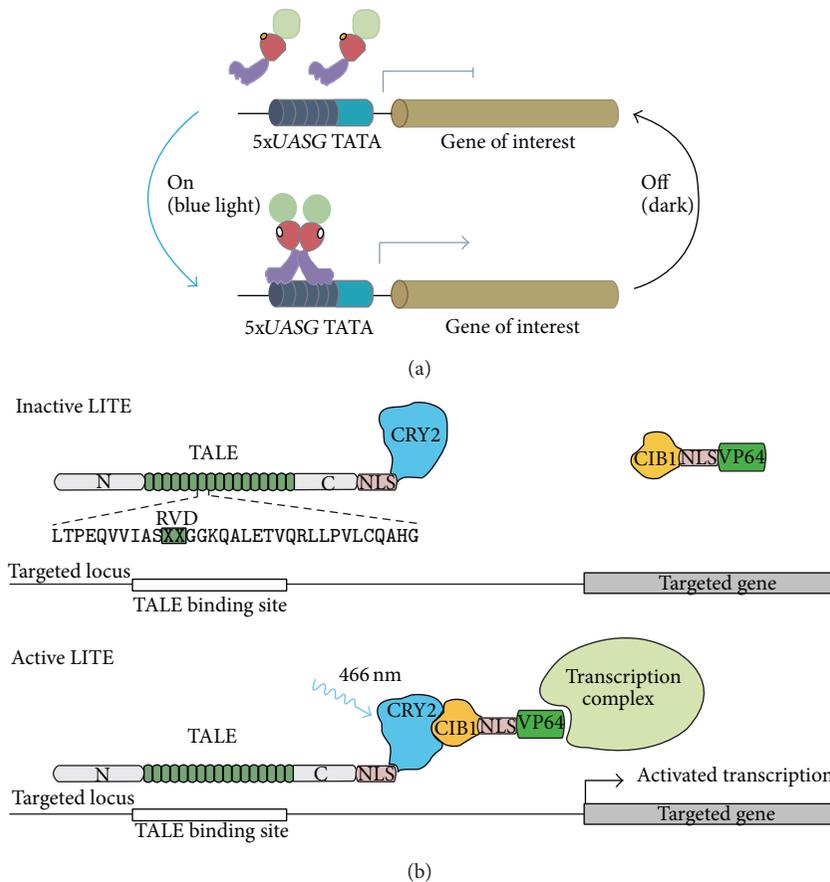
FIGURE 3: (a) Schematic representation of the LightOn system. After light activation, GAVP homodimerizes, interacts with *UASG* elements (5x*UASG*), and initiates expression of the gene of interest. Adapted with permission from Macmillan Publishers Ltd. (Nature Publishing Group): *Nature Methods* [51], copyright (2012). (b) Schematic of the LITE system. Light stimulation induces dimerization of CRY2 and CIB1, recruiting the effector to the target promoter. Adapted with permission from Macmillan Publishers Ltd. (Nature Publishing Group): *Nature* [63], copyright (2013).

response to light. Although light activation of these proteins certainly influences gene expression, the specificity of this regulation is quite low and moreover is limited to the downstream targets of the signaling pathways with which the light sensors communicate. In order to overcome these challenges and achieve highly specific gene activation by photostimulation, Wang et al. designed a synthetic light-switchable transactivator that binds to target promoters in response to blue light [51–53]. The core of the transactivator consists of the well-characterized Gal4 DNA-binding domain fused to VVD, which contains a light-oxygen-voltage (LOV) domain that dimerizes upon blue-light illumination. When this core was fused to be a suitable transactivation domain (e.g., from p65), the fusion protein homodimerized in response to light, bound to the *Gal* upstream activating sequence, and activated transcription of a target gene or genes (Figure 3(a)). This transgene system, "LightOn," allows spatially and temporally precise manipulation of gene expression levels with far greater specificity than could be achieved by stimulation of membrane proteins that act via intracellular signaling cascades.

The LOV domain was also exploited by Wu et al. [54] to generate photoactivatable derivatives of Rac1, a critical regulator of the actin cytoskeleton. In this system, in unilluminated cells, the LOV domain blocks Rac1's interactions with its partner proteins; irradiation causes a linker region connecting Rac1 and the LOV domain to unwind, liberating Rac1 to engage in downstream signaling. Using photoactivatable Rac1 (PA-Rac1), Wu et al. could use light to induce cell protrusions and ruffling with high spatial precision, stimulate cell motility, and influence the direction of movement.

The LOV domain is not the only protein module that might be exploited in strategies such as those described above. Known photoreceptors are distinguished into six classes according to their chromophores and photochemistry: LOV sensors, xanthopsins, phytochromes, blue-light sensors that use flavin adenine dinucleotide, cryptochromes, and rhodopsins [55–57]. Several reviews offer an in-depth discussion of natural LOV and phytochrome photoreceptors [58, 59].

Since we have reported that cryptochrome 2, one of the blue light photoreceptors and circadian clock proteins, is

the key factor controlling cell differentiation after blue light illumination [60–62], cryptochrome 2 is one of the applicable proteins for optogenetics of light-switchable transgene system. Konermann et al. reported the development of light-inducible transcriptional effectors (LITEs), an optogenetic two-hybrid system integrating the customizable TALE DNA-binding domain with the light-sensitive cryptochrome 2 protein and its interacting partner CIB1 (Figure 3(b)) [63]. LITEs do not require additional exogenous chemical cofactors, are easily customized to target many endogenous genomic loci, and can be activated within minutes with reversibility. They have applied that system in primary mouse neurons, as well as in the brain of freely behaving mice *in vivo* to mediate reversible modulation of mammalian endogenous gene expression as well as targeted epigenetic chromatin modifications. They conclude that the LITE system established a novel mode of optogenetic control of endogenous cellular processes and enables direct testing of the causal roles of genetic and epigenetic regulation in normal biological processes and disease states [63].

2.4. Photoactivated Adenylyl Cyclase (PAC). Intracellular cAMP has been known to play an important role. Iseki et al. firstly discovered that photoactivated adenylyl cyclase (PAC) is a unique protein that can act both as a photoreceptor and as an effector to catalyse cAMP synthesis, in contrast with G-protein-coupled receptor systems, in which three different proteins act sequentially to modulate the level of cyclic nucleotide [64, 65]. PAC was originally isolated from the flagellate *Euglena gracilis*. Following stimulation by blue light it causes a rapid increase in cAMP levels. Thus, using PAC allows manipulation of neurotransmitter release and behavior by directly affecting intracellular signaling [66, 67].

2.5. LiGluR. Volgraf et al. reported that an ionotropic glutamate receptor subtype 6 (iGluR6) was genetically and chemically engineered, rendering it light sensitive. Using structure-based design, they modified its ubiquitous clamshell-type ligand-binding domain to develop a light-activated channel, which was named LiGluR [68]. Their group also found that the LiGluR rapidly generated large currents (hundreds of pA), yielding substantial (tens of mV) depolarizations in hippocampal neurons. Millisecond flashes of light evoked action potentials or subthreshold voltage changes that mimic fast excitatory postsynaptic potentials. The ability to excite neurons with LiGluR compares favorably with the responses of ChR2 in that LiGluR currents were 5-fold larger, were stable during extended periods of illumination, and deactivated more quickly because deactivation was light-driven, thus enabling cells to be reliably fired at higher frequencies. In addition, LiGluR has the unique property that, once activated by a brief pulse of light, the channel will remain open for minutes in the dark, until a pulse of deactivating light closes it, thus enabling long depolarizations and trains of action potentials to be evoked with minimal light exposure [69].

2.6. HyLighter. Janovjak et al. also reported a potassium-selective ionotropic glutamate receptor that reversibly inhibits neuronal activity in response to light in dissociated neurons and brain slice and also reversibly suppresses behavior in zebrafish [70]. Chimeras were constructed in which the transmembrane helices and reentrant pore-loop of the K^+-selective sGluR0 were transplanted into iGluR6, and the best of these was modified for light-gating and termed HyLighter. This hyperpolarizing light-gated channel is turned on by a brief light pulse at one wavelength and turned off by a pulse at a second wavelength. After optical activation, the photocurrent and optical silencing of activity persist in the dark for extended periods. The low light requirement and bistability of HyLighter represent advantages for the dissection of neural circuitry [70].

3. Delivery of Light

Electronic systems that integrate with the body provide powerful diagnostic and therapeutic capabilities for basic research and clinical medicine. Recent research establishes materials and mechanical constructs for electronic circuits, light-emitting diodes (LEDs), sensors, and other components. In optogenetics, fiber optic devices restrict opportunities for *in vivo* use and widespread biological application. As a solution, Bruchas and Rogers group developed mechanically compliant, ultrathin multifunctional optoelectronic systems that mount on releasable injection needles for insertion into the depths of soft tissue [71, 72]. These devices incorporate cellular-scale components ranging from independently addressable multicolored microscale. In addition, Tamura et al. reported a tungsten microelectrode-based optical probe, optrode, that encloses optical fibers within its insulation glass [73]. This smooth glass-coated optrode is a promising tool for chronic *in vivo* experiments with various research targets including deep brain structures in behaving monkeys.

Those types of custom device represent a significant step forward for the optogenetics community for *in vivo* applications, allowing multiple bright excitation sites along the length of a minimally invasive probe.

4. Clinical Significance of Optogenetics

The utility of optogenetics is not limited to experimental manipulations but also encompasses potentially significant therapeutic applications. Some of the most promising opportunities for clinical use of optogenetic methods have arisen, perhaps unsurprisingly, in the visual system, where ChR2's original function as a photosensitive pigment is most pertinent. When ChR2 was introduced into second-order neurons (ON bipolar cells) in the *rd1* mouse model of retinal degeneration, the resultant photosensitive cells were able to stimulate light-evoked responses in both retinal ganglion and visual cortex [74]. Likewise, introduction of ChR2 into retinal ganglion cells restored vision in genetically blind rats [75]. The results of these studies raise the possibility that this ChR2 could be used in gene therapy of certain forms of congenital or acquired blindness in humans [75].

In another field of medicine, ChR2 has been used to probe the roles of specific brain regions and activity patterns in governing seizures [76], revealing the potential significance

of bidirectional networks in the hippocampus in determining the beginning and end of epileptic seizures. By facilitating development of methods to selectively block or activate relevant circuits, these findings may someday contribute to improved treatments for epilepsy.

Trauner and Isacoff group reported an approach whereby a genetically and chemically engineered LiGluR was expressed selectively in retinal ganglion cells (RGCs), the longest-surviving cells in retinal blinding diseases. When expressed in the RGCs of a well-established rat model of retinal degeneration, LiGluR restored light sensitivity to the RGCs, reinstated light responsiveness to the primary visual cortex, and restored both the pupillary reflex and a natural light-avoidance behavior [77].

5. Conclusion

Given the rate of progress over the last few years, it is reasonable to predict that the molecular techniques for optogenetics will continue to evolve rapidly and that the applications of these methods will continue to expand. Just as anatomical and genetic targeting of light-sensitive proteins had contributed tremendously to our knowledge of neural circuits, the growing tool set for subcellular targeting of optogenetic components should facilitate advances in our understanding of the importance of subcellular domains and intracellular compartments in the physiology and function of neurons and other cell types. Likewise, the control of protein-protein interactions via light-activated dimerization domains will further enable controlled localization of proteins and production of signaling intermediates in specific subcellular regions.

From its origins in neuroscience, optogenetic technology had spread rapidly across disciplinary lines, and its vast range of potential applications has only begun to be sampled. As the technology grows and matures, optogenetics should continue to transform biology in the years to come.

Conflict of Interests

The authors declare that there is no conflict of interests regarding the publication of this paper.

Acknowledgment

References

[1] V. Plaiasu, "Update in genetics," *Maedica (Buchar)*, vol. 6, no. 1, p. 70, 2011.

[2] G. Miesenböck, "The optogenetic catechism," *Science*, vol. 326, no. 5951, pp. 395–399, 2009.

[3] G. Miesenböck, "Optogenetic control of cells and circuits," *Annual Review of Cell and Developmental Biology*, vol. 27, pp. 731–758, 2011.

[4] T. Fehrentz, M. Schönberger, and D. Trauner, "Optochemical genetics," *Angewandte Chemie*, vol. 50, no. 51, pp. 12156–12182, 2011.

[5] M. Izquierdo-Serra, D. Trauner, A. Llobet, and P. Gorostiza, "Optical modulation of neurotransmission using calcium photocurrents through the ion channel LiGluR," *Frontiers in Molecular Neuroscience*, vol. 6, p. 3, 2013.

[6] K. Deisseroth, "Optogenetics," *Nature Methods*, vol. 8, no. 1, pp. 26–29, 2011.

[7] E. Pastrana, "Optogenetics: Controlling cell function with light," *Nature Methods*, vol. 8, no. 1, pp. 24–25, 2011.

[8] G. Kauwe and E. Y. Isacoff, "Rapid feedback regulation of synaptic efficacy during high-frequency activity at the Drosophila larval neuromuscular junction," *Proceedings of the National Academy of Sciences of the United States of America*, vol. 110, no. 22, pp. 9142–9147, 2013.

[9] C. Wyart, F. D. Bene, E. Warp et al., "Optogenetic dissection of a behavioural module in the vertebrate spinal cord," *Nature*, vol. 461, no. 7262, pp. 407–410, 2009.

[10] R. H. Kramer, A. Mourot, and H. Adesnik, "Optogenetic pharmacology for control of native neuronal signaling proteins," *Nature Neuroscience*, vol. 16, no. 7, pp. 816–823, 2013.

[11] G. Nagel, D. Ollig, M. Fuhrmann et al., "Channelrhodopsin-1: a light-gated proton channel in green algae," *Science*, vol. 296, no. 5577, pp. 2395–2398, 2002.

[12] G. Nagel, T. Szellas, W. Huhn et al., "Channelrhodopsin-2, a directly light-gated cation-selective membrane channel," *Proceedings of the National Academy of Sciences of the United States of America*, vol. 100, no. 2, pp. 13940–13945, 2003.

[13] A. Matsuno-Yagi and Y. Mukohata, "ATP synthesis linked to light-dependent proton uptake in a red mutant strain of Halobacterium lacking bacteriorhodopsin," *Archives of Biochemistry and Biophysics*, vol. 199, no. 1, pp. 297–303, 1980.

[14] B. Schobert and J. K. Lanyi, "Halorhodopsin is a light-driven chloride pump," *Journal of Biological Chemistry*, vol. 257, no. 17, pp. 10306–10313, 1982.

[15] E. N. Spudich and J. L. Spudich, "Control of transmembrane ion flux to select halorhodopsin-deficient and other energy-transduction mutants of Halobacterium halobium," *Proceedings of the National Academy of Sciences of the United States of America*, vol. 79, no. 14 I, pp. 4308–4312, 1982.

[16] E. S. Boyden, F. Zhang, E. Bamberg, G. Nagel, and K. Deisseroth, "Millisecond-timescale, genetically targeted optical control of neural activity," *Nature Neuroscience*, vol. 8, no. 9, pp. 1263–1268, 2005.

[17] K. Deisseroth, G. Feng, A. K. Majewska, G. Miesenböck, A. Ting, and M. J. Schnitzer, "Next-generation optical technologies for illuminating genetically targeted brain circuits," *Journal of Neuroscience*, vol. 26, no. 41, pp. 10380–10386, 2006.

[18] A. R. Adamantidis, F. Zhang, A. M. Aravanis, K. Deisseroth, and L. De Lecea, "Neural substrates of awakening probed with optogenetic control of hypocretin neurons," *Nature*, vol. 450, no. 7168, pp. 420–424, 2007.

[19] A. M. Aravanis, L. P. Wang, F. Zhang et al., "An optical neural interface: in vivo control of rodent motor cortex with integrated fiberoptic and optogenetic technology," *Journal of neural engineering*, vol. 4, no. 3, pp. S143–156, 2007.

[20] "Method of the Year 2010," *Nature Methods*, vol. 8, no. 1, 2010.

[21] A. M. Aravanis, L.-P. Wang, F. Zhang et al., "An optical neural interface: in vivo control of rodent motor cortex with integrated fiberoptic and optogenetic technology," *Journal of neural engineering*, vol. 4, pp. S143–S156, 2007.

[22] B. R. Arenkiel, J. Peca, I. G. Davison et al., "In vivo light-induced activation of neural circuitry in transgenic mice expressing channelrhodopsin-2," *Neuron*, vol. 54, no. 2, pp. 205–218, 2007.

[23] E. S. Boyden, F. Zhang, E. Bamberg, G. Nagel, and K. Deisseroth, "Millisecond-timescale, genetically targeted optical control of neural activity," *Nature Neuroscience*, vol. 8, no. 9, pp. 1263–1268, 2005.

[24] X. Han and E. S. Boyden, "Multilpe-color optical activation, silencing, and desynchronization of neural activity, with single-spike temporal resolution," *PLoS ONE*, vol. 2, no. 3, article e299, 2007.

[25] T. Ishizuka, M. Kakuda, R. Araki, and H. Yawo, "Kinetic evaluation of photosensitivity in genetically engineered neurons expressing green algae light-gated channels," *Neuroscience Research*, vol. 54, no. 2, pp. 85–94, 2006.

[26] G. Nagel, M. Brauner, J. F. Liewald, N. Adeishvili, E. Bamberg, and A. Gottschalk, "Light activation of Channelrhodopsin-2 in excitable cells of caenorhabditis elegans triggers rapid behavioral responses," *Current Biology*, vol. 15, no. 24, pp. 2279–2284, 2005.

[27] L. Petreanu, D. Huber, A. Sobczyk, and K. Svoboda, "Channelrhodopsin-2-assisted circuit mapping of long-range callosal projections," *Nature Neuroscience*, vol. 10, no. 5, pp. 663–668, 2007.

[28] C. Schroll, T. Riemensperger, D. Bucher et al., "Light-induced activation of distinct modulatory neurons triggers appetitive or aversive learning in Drosophila larvae," *Current Biology*, vol. 16, no. 17, pp. 1741–1747, 2006.

[29] J. B. Bryson, C. B. Machado, M. Crossley et al., "Optical control of muscle function by transplantation of stem cell-derived motor neurons in mice," *Science*, vol. 344, no. 6179, pp. 94–97, 2014.

[30] F. Zhang, L. P. Wang, M. Brauner et al., "Multimodal fast optical interrogation of neural circuitry," *Nature*, vol. 446, no. 7136, pp. 633–639, 2007.

[31] F. Zhang, L. P. Wang, E. S. Boyden, and K. Deisseroth, "Channelrhodopsin-2 and optical control of excitable cells," *Nature Methods*, vol. 3, no. 10, pp. 785–792, 2006.

[32] O. A. Sineshchekov, K. H. Jung, and J. L. Spudich, "Two rhodopsins mediate phototaxis to low- and high-intensity light in Chlamydomonas reinhardtii," *Proceedings of the National Academy of Sciences of the United States of America*, vol. 99, no. 13, pp. 8689–8694, 2002.

[33] X. Li, D. V. Gutierrez, M. G. Hanson et al., "Fast noninvasive activation and inhibition of neural and network activity by vertebrate rhodopsin and green algae channelrhodopsin," *Proceedings of the National Academy of Sciences of the United States of America*, vol. 102, no. 49, pp. 17816–17821, 2005.

[34] Y. P. Zhang and T. G. Oertner, "Optical induction of synaptic plasticity using a light-sensitive channel," *Nature Methods*, vol. 4, no. 2, pp. 139–141, 2007.

[35] B. K. Andrasfalvy, B. V. Zemelman, J. Tang, and A. Vaziri, "Two-photon single-cell optogenetic control of neuronal activity by sculpted light," *Proceedings of the National Academy of Sciences of the United States of America*, vol. 107, no. 26, pp. 11981–11986, 2010.

[36] G. Nagel, M. Brauner, J. F. Liewald, N. Adeishvili, E. Bamberg, and A. Gottschalk, "Light activation of Channelrhodopsin-2 in excitable cells of caenorhabditis elegans triggers rapid behavioral responses," *Current Biology*, vol. 15, no. 24, pp. 2279–2284, 2005.

[37] B. R. Arenkiel, J. Peca, I. G. Davison et al., "In vivo light-induced activation of neural circuitry in transgenic mice expressing channelrhodopsin-2," *Neuron*, vol. 54, no. 2, pp. 205–218, 2007.

[38] D. Huber, L. Petreanu, N. Ghitani et al., "Sparse optical microstimulation in barrel cortex drives learned behaviour in freely moving mice," *Nature*, vol. 451, no. 7174, pp. 61–64, 2008.

[39] H. Wang, J. Peca, M. Matsuzaki et al., "High-speed mapping of synaptic connectivity using photostimulation in Channelrhodopsin-2 transgenic mice," *Proceedings of the National Academy of Sciences of the United States of America*, vol. 104, no. 19, pp. 8143–8148, 2007.

[40] H.-C. Tsai, F. Zhang, A. Adamantidis et al., "Phasic firing in dopaminergic neurons is sufficient for behavioral conditioning," *Science*, vol. 324, no. 5930, pp. 1080–1084, 2009.

[41] A. V. Kravitz, B. S. Freeze, P. R. L. Parker et al., "Regulation of parkinsonian motor behaviours by optogenetic control of basal ganglia circuitry," *Nature*, vol. 466, no. 7306, pp. 622–626, 2010.

[42] T. L. Lewis, T. Mao, K. Svoboda, and D. B. Arnold, "Myosin-dependent targeting of transmembrane proteins to neuronal dendrites," *Nature Neuroscience*, vol. 12, no. 5, pp. 568–576, 2009.

[43] A. V. Gourine, V. Kasymov, N. Marina et al., "Astrocytes control breathing through pH-dependent release of ATP," *Science*, vol. 329, no. 5991, pp. 571–575, 2010.

[44] T. Bruegmann, D. Malan, M. Hesse et al., "Optogenetic control of heart muscle in vitro and in vivo," *Nature Methods*, vol. 7, no. 11, pp. 897–900, 2010.

[45] T. Asano, T. Ishizua, and H. Yawo, "Optically controlled contraction of photosensitive skeletal muscle cells," *Biotechnology and Bioengineering*, vol. 109, no. 1, pp. 199–204, 2012.

[46] J. P. Weick, M. A. Johnson, S. P. Skroch, J. C. Williams, K. Deisseroth, and S.-C. Zhang, "Functional control of transplantable human ESC-derived neurons via optogenetic targeting," *Stem Cells*, vol. 28, no. 11, pp. 2008–2016, 2010.

[47] A. Stroh, H. C. Tsai, L. P. Wang et al., "Tracking stem cell differentiation in the setting of automated optogenetic stimulation," *Stem Cells*, vol. 29, no. 1, pp. 78–88, 2011.

[48] R. D. Airan, K. R. Thompson, L. E. Fenno, H. Bernstein, and K. Deisseroth, "Temporally precise in vivo control of intracellular signalling," *Nature*, vol. 458, no. 7241, pp. 1025–1029, 2009.

[49] D. V. Gutierrez, M. D. Mark, O. Masseck et al., "Optogenetic control of motor coordination by Gi/o protein-coupled vertebrate rhodopsin in cerebellar purkinje cells," *Journal of Biological Chemistry*, vol. 286, no. 29, pp. 25848–25858, 2011.

[50] W. K. Karunarathne, L. Giri, V. Kalyanaraman, and N. Gautam, "Optically triggering spatiotemporally confined GPCR activity in a cell and programming neurite initiation and extension," *Proceedings of the National Academy of Sciences of the United States of America*, vol. 110, no. 17, pp. E1565–E1574, 2013.

[51] X. Wang, X. Chen, and Y. Yang, "Spatiotemporal control of gene expression by a light-switchable transgene system," *Nature Methods*, vol. 9, no. 3, pp. 266–269, 2012.

[52] X. Chen, X. Wang, Z. Du, Z. Ma, and Y. Yang, "Spatiotemporal control of gene expression in mammalian cells and in mice using the LightOn system," *Current Protocols in Chemical Biology*, vol. 5, no. 2, pp. 111–129, 2013.

[53] Z. Ma, Z. Du, X. Chen, X. Wang, and Y. Yang, "Fine tuning the LightOn light-switchable transgene expression system," *Biochemical and Biophysical Research Communications*, vol. 440, no. 3, pp. 419–423, 2013.

[54] Y. I. Wu, D. Frey, O. I. Lungu et al., "A genetically encoded photoactivatable Rac controls the motility of living cells," *Nature*, vol. 461, no. 7260, pp. 104–108, 2009.

[55] M. A. Van Der Horst and K. J. Hellingwerf, "Photoreceptor proteins, "star actors of modern times": a review of the functional dynamics in the structure of representative members of six different photoreceptor families," *Accounts of Chemical Research*, vol. 37, no. 1, pp. 13–20, 2004.

[56] S. Masuda, "Light detection and signal transduction in the BLUF photoreceptors," *Plant and Cell Physiology*, vol. 54, no. 2, pp. 171–179, 2013.

[57] A. Möglich and K. Moffat, "Engineered photoreceptors as novel optogenetic tools," *Photochemical and Photobiological Sciences*, vol. 9, no. 10, pp. 1286–1300, 2010.

[58] S. Crosson, S. Rajagopal, and K. Moffat, "The LOV domain family: photoresponsive signaling modules coupled to diverse output domains," *Biochemistry*, vol. 42, no. 1, pp. 2–10, 2003.

[59] N. C. Rockwell, Y.-S. Su, and J. C. Lagarias, "Phytochrome structure and signaling mechanisms," *Annual Review of Plant Biology*, vol. 57, pp. 837–858, 2006.

[60] T. Kushibiki and K. Awazu, "Controlling osteogenesis and adipogenesis of mesenchymal stromal cells by regulating a circadian clock protein with laser irradiation," *International Journal of Medical Sciences*, vol. 5, no. 6, pp. 319–326, 2008.

[61] T. Kushibiki and K. Awazu, "Blue laser irradiation enhances extracellular calcification of primary mesenchymal stem cells," *Photomedicine and Laser Surgery*, vol. 27, no. 3, pp. 493–498, 2009.

[62] T. Kushibiki, T. Tajiri, Y. Ninomiya, and K. Awazu, "Chondrogenic mRNA expression in prechondrogenic cells after blue laser irradiation," *Journal of Photochemistry and Photobiology B: Biology*, vol. 98, no. 3, pp. 211–215, 2010.

[63] S. Konermann, M. D. Brigham, A. Trevino et al., "Optical control of mammalian endogenous transcription and epigenetic states," *Nature*, vol. 500, no. 7463, pp. 472–476, 2013.

[64] M. Iseki, S. Matsunaga, A. Murakami et al., "A blue-light-activated adenylyl cyclase mediates photoavoidance in Euglena gracilis," *Nature*, vol. 415, no. 6875, pp. 1047–1051, 2002.

[65] S. Yoshikawa, T. Suzuki, M. Watanabe, and M. Iseki, "Kinetic analysis of the activation of photoactivated adenylyl cyclase (PAC), a blue-light receptor for photomovements of Euglena," *Photochemical and Photobiological Sciences*, vol. 4, no. 9, pp. 727–731, 2005.

[66] J. Looser, S. Schröder-Lang, P. Hegemann, and G. Nagel, "Mechanistic insights in light-induced cAMP production by photoactivated adenylyl cyclase alpha (PACα)," *Biological Chemistry*, vol. 390, no. 11, pp. 1105–1111, 2009.

[67] S. Schröder-Lang, M. Schwärzel, R. Seifert et al., "Fast manipulation of cellular cAMP level by light in vivo," *Nature Methods*, vol. 4, no. 1, pp. 39–42, 2007.

[68] M. Volgraf, P. Gorostiza, R. Numano, R. H. Kramer, E. Y. Isacoff, and D. Trauner, "Allosteric control of an ionotropic glutamate receptor with an optical switch," *Nature Chemical Biology*, vol. 2, no. 1, pp. 47–52, 2006.

[69] S. Szobota, P. Gorostiza, F. del Bene et al., "control of neuronal activity with a light-gated glutamate receptor," *Neuron*, vol. 54, no. 4, pp. 535–545, 2007.

[70] H. Janovjak, S. Szobota, C. Wyart, D. Trauner, and E. Y. Isacoff, "A light-gated, potassium-selective glutamate receptor for the optical inhibition of neuronal firing," *Nature Neuroscience*, vol. 13, no. 8, pp. 1027–1032, 2010.

[71] T. i. Kim, J. G. McCall, Y. H. Jung et al., "Injectable, cellular-scale optoelectronics with applications for wireless optogenetics," *Science*, vol. 340, no. 6129, pp. 211–216, 2013.

[72] J. G. McCall, T. I. Kim, G. Shin et al., "Fabrication and application of flexible, multimodal light-emitting devices for wireless optogenetics," *Nature Protocols*, vol. 8, no. 12, pp. 2413–2428, 2013.

[73] K. Tamura, Y. Ohashi, T. Tsubota et al., "A glass-coated tungsten microelectrode enclosing optical fibers for optogenetic exploration in primate deep brain structures," *Journal of Neuroscience Methods*, vol. 211, no. 1, pp. 49–57, 2012.

[74] P. S. Lagali, D. Balya, G. B. Awatramani et al., "Light-activated channels targeted to ON bipolar cells restore visual function in retinal degeneration," *Nature Neuroscience*, vol. 11, no. 6, pp. 667–675, 2008.

[75] H. Tomita, E. Sugano, H. Isago, and M. Tamai, "Channelrhodopsins provide a breakthrough insight into strategies for curing blindness," *Journal of Genetics*, vol. 88, no. 4, pp. 409–415, 2009.

[76] S. Osawa, M. Iwasaki, R. Hosaka et al., "Optogenetically induced seizure and the longitudinal hippocampal network dynamics," *PLoS ONE*, vol. 8, no. 4, Article ID e60928, 2013.

[77] N. Caporale, K. D. Kolstad, T. Lee et al., "LiGluR restores visual responses in rodent models of inherited blindness," *Molecular Therapy*, vol. 19, no. 7, pp. 1212–1219, 2011.

Research Article

Optical Scattering Properties of Intralipid Phantom in Presence of Encapsulated Microbubbles

Homa Assadi,[1] Raffi Karshafian,[1] and Alexandre Douplik[1,2]

[1] Department of Physics, Ryerson University, 350 Victoria Street, Toronto, ON, Canada M5B 2K3
[2] Erlangen Graduate School in Advanced Optical Technologies (SAOT), Friedrich-Alexander-Universität Erlangen-Nürnberg, Paul Gordan Strasse 6, D-91052 Erlangen, Germany

Correspondence should be addressed to Homa Assadi; homa.assadi@ryerson.ca

In imaging, contrast agents are utilized to enhance sensitivity and specificity of diagnostic modalities. In ultrasound imaging, microbubbles (MBs)—a gas-core shell-encapsulated agent—are used clinically as contrast agents. The working hypothesis of this study is that microbubbles can be employed as an intravascular contrast agent in optical imaging systems. In this work, the interaction of light and microbubbles in a turbid medium (intralipid) was investigated, particularly, the effect of MBs on the reduced scattering and absorption coefficients. Diffuse reflectance (DR) and total transmittance (TT) measurements of highly scattering intralipid suspension (0.5–5%) were measured using spectroscopic integrating sphere system in the absence and presence of Definity microbubbles. The optical properties were computed using the inverse adding doubling (IAD) software. The presence of microbubbles increased DR and decreased TT of intralipid phantoms. In the presence of MBs (0.5% volume concentration), the reflectance of the intralipid phantom increased from 35% to 100%. The reduced scattering coefficient increased significantly (30%) indicating potential use of MBs as optical contrast agents in light based modalities.

1. Introduction

Microbubbles (MBs), a gas-core shell-encapsulated bubble of 1–5 micrometers in diameter, are utilized clinically in diagnostic ultrasound imaging as a contrast agent [1]. The gas of microbubbles is usually comprised of perfluorocarbon, nitrogen, or sulfur hexafluoride gas. The shell of microbubbles normally comprises of lipids, proteins, and polymers [1] and its thickness is in nanometer range (60–200 nm) [2]. Microbubbles behave as an intravascular contrast agent; they remain within the circulation. They generally have a short lifetime; generally MBs disappear within a few minutes following an intravenous injection [3]. Encapsulated microbubbles potentially can be used as optical contrast agents since MBs contribute to the media refraction index mismatch. The presence of MBs in tissue can cause refractive index mismatches and potentially allow the MBs to be distinguished from its surrounding media. The gas and shell of microbubbles will only affect the real part of refractive index. There is no considerable optical absorption and only refraction occurs as a result of light-microbubble interactions which may increase light scattering and subsequently increase optical contrast. The size of microbubbles is on the order of a wavelength, and therefore the main optical effect of light-MB interaction is Mie scattering [4].

Light based modalities are nonionizing methods with significant potential for noninvasive, portable, and cost-effective medical diagnostics [5]. However, at visible and near IR wavelengths (400–1200 nm) light scattering contrast is limited between adjacent tissues [6]. Although, for example, morphological differences between normal and malignant tissues can be obvious at later stages of tumor development, it is challenging to detect early-stage tumors or tumors that are optically similar to surrounding normal tissue [7]. This can be potentially improved by contrast agents to differentiate normal tissue from the pathological lesions exploiting MBs as contrast agents in similar manner as for US imaging contrast enhancement [8].

The goal of this work is to study the effect of MBs on light propagation in a turbid media. Intralipid was used to mimic biological tissue scattering properties. In biomedical photonics, light propagation is an important process in both diagnostic and therapeutic applications [9]. Light propagation through any media is determined by its optical properties, which are wavelength dependent [10]. The intrinsic optical properties of tissues are absorption coefficient, μ_a, scattering coefficient, μ_s, scattering anisotropy, g, reduced scattering coefficient, μ_s', and refraction index n [11]. Typically, tissue is a turbid media and the optical reduced scattering coefficient for soft tissues is in the range 10–100 [1/cm]. Intralipid is turbid and has no strong absorption in the visible region and is often used as a tissue mimicking phantom medium [12].

In this work, various concentrations of intralipid were used to demonstrate a diffuse reflectance similar to soft tissues with known scattering coefficients. The absorption and scattering coefficients are obtained from measured transmittance and reflectance using an inverse adding doubling method (IAD) based on radiative transfer theory. IAD is an accurate solution of the radiative transport equation for all albedos, all optical depths, and all phase functions and can be applied to any medium for which the radiative transport equation is valid [13]. In this study, the effect of microbubbles mixed with intralipid upon the optical properties of the intralipid solutions at various concentrations is studied using the integrating sphere spectroscopy measurements and inverse adding doubling algorithm.

2. Materials and Method

2.1. Materials

2.1.1. Intralipid Phantom. Intralipid (IL) phantoms with varying concentrations of IL 0.5%, 1%, 1.5%, 2%, 3%, and 5% (v/v: volume concentration) of the original 20% stock solution (Sigma-Aldrich, Canada) were used to mimic the scattering properties of biological tissue. The intralipid 20%, according to the manufacturer, is made of 20% soybean oil, 1.2% egg yolk phospholipids, 2.25% glycerin, and water. The glycerin is dissolved into individual molecules in the water and does not scatter light. The difference in the refractive index of water-glycerin solution from that of pure water has no measurable influence on the scattering parameters [4]. The dilutions of IL can yield wavelength-dependent reduced scattering coefficients (μ_s') in the range from 5.7 to 26.7 [1/cm] that are similar to values reported for tissues [14].

2.1.2. Microbubbles. Definity (perflutren lipid microspheres, Lantheus Medical Imaging, Billerica, MA), an FDA approved commercially available ultrasound microbubble contrast agent, was used in this study. Definity microbubbles with the mean size of $1.2 \pm 0.5\,\mu m$, measured using a Coulter Counter Multisizer (Beckman Coulter, USA) (Figure 3), were added to the intralipid phantom at 2.5% v/v (volume concentration). The microbubble concentration is comparable to values used in ex vivo ultrasound experiments [15]. Definity has a concentration of $1.2 * 10^{10}$ bubbles/mL.

2.2. Methods

2.2.1. Spectroscopy. Double beam integrating sphere technique (UV-VIS-NIR Spectrophotometer Shimadzu UV-3600, Japan) was used to determine the total transmittance (TT) and diffuse reflectance (DR) of intralipid phantoms with and without microbubbles. Visible and near infrared wavelengths (300–850 nm) and 8 nm slit width measurements were performed [16]. The wavelength accuracy in UV/VIS region: ±0.2 nm and NIR region: ±0.8 nm.

The intralipid phantom was placed in 2 mm light path quartz cuvettes (Starna Cells Inc., USA). Cuvette dimensions were 45 mm × 4.5 mm × 12.5 mm (considered as an infinite in the direction perpendicular to the incident beam) and held at the integrating sphere sample port. The experimental conditions satisfy the requirement of optically thick ($\tau \sim 1$) tissue sample which ensures the validity of the multiple scattering [10]. In diffusive regime, μ_s' completely describes the light scattering profile.

2.2.2. Analysis. Inverse adding doubling (IAD) software (developed by Prahl, 2011) program was used to compute the optical properties of the samples [17]. The settings of the IAD program were sample index of refraction (1.47: phantom (the scattering particles of intralipid are soybean oil. The refractive index of soybean oil is $n = 1.47$ and was considered as the refractive index of the sample [18])), index of refraction of the top and bottom slides (1.5138: BK-7), sample thickness (2 mm), illumination beam diameter (7.1365 mm), reflectivity of the reflectance calibration standard (0.98), and number of spheres used during each measurement (1). The properties of reflectance measurement sphere were sphere diameter (60 mm), sample port diameter (18.74 mm), entrance port diameter (16.73 mm), detector port diameter (13.12 mm), and reflectivity of the sphere wall (0.98). The properties of transmittance measurement sphere were sphere diameter (60 mm), sample port diameter (16.73 mm), entrance port diameter (0.00), detector port diameter (13.12), and reflectivity of the sphere wall (0.98).

Measured DR and TT were used as input for the IAD software to extract μ_a and μ_s' as a function of wavelength [11]. The inverse adding doubling algorithm initially guesses the intrinsic optical properties set, comparing the expected observables with those measured by the integrating sphere system and then iteratively approaching the final set of intrinsic parameters minimizing the deviation from the measured values of TT and DR [17]. The IAD technique is shown to calculate optical properties within ten percent of the true optical properties for all sample thicknesses greater than one optical depth τ [10].

2.3. Experiments. The diffuse reflectance (DR) and total transmittance (TT) were measured at visible and near infrared wavelengths (from 300 to 850 nm) for intralipid phantoms (0.5%, 1%, 1.5%, 2%, 3%, and 5%) before and after adding microbubbles. 2 mm light path quartz cuvettes (Starna Cells Inc., USA) were used to hold the samples at the integrating sphere sample ports. This ensured the validity
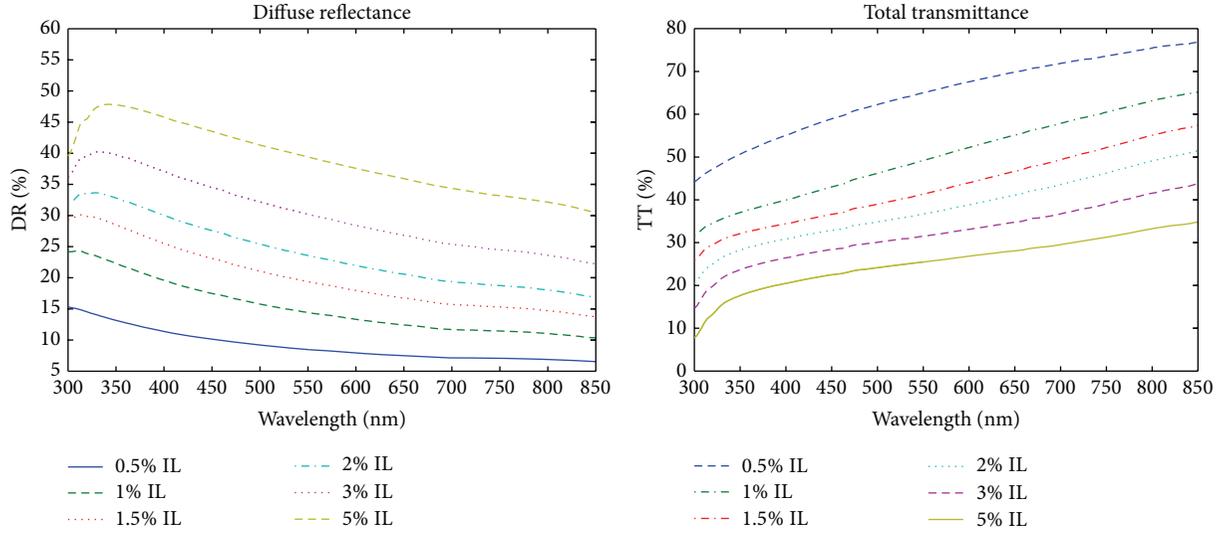
FIGURE 1: Diffuse reflectance and total transmittance for all concentrations of intralipid.
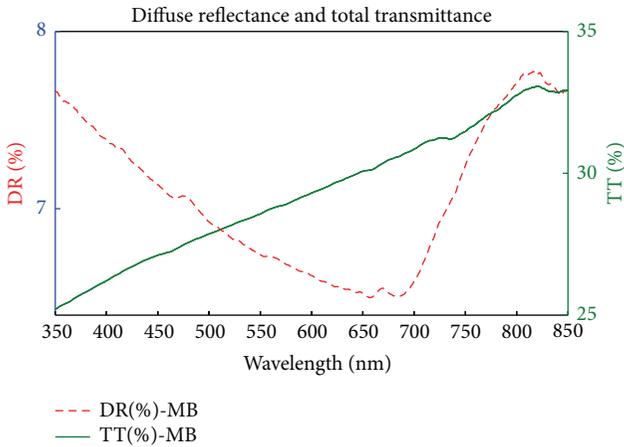
FIGURE 2: Diffuse reflectance and total transmittance for microbubbles diluted in deionized water (without intralipid).
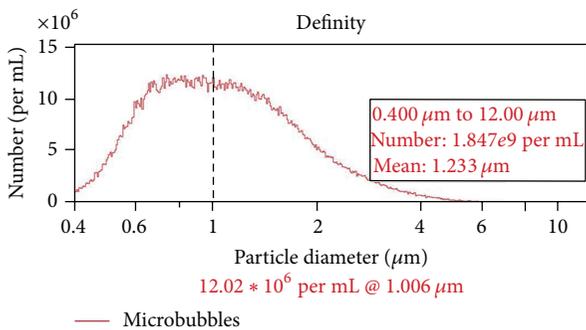
FIGURE 3: Coulter Counter Multisizer 4 measurements of the size of Definity microbubbles.

of the multiple scattering for optically thick ($\tau \sim 1$) tissue samples [10]. Thus, the μ_s' describes the light scattering profile completely. Spectra in the range from 300 to 850 nm at a spectral resolution of 0.1 nm were obtained for (1) intralipid solutions only (no MBs) and (2) intralipid solutions with MBs. The MB volume ratio was 1 : 40 for all measurements which is in the range of ex vivo ultrasound studies [15].

3. Results and Discussion

3.1. Reflectance and Transmittance Spectra. The diffuse reflectance (DR) and total transmittance (TT) of intralipid phantoms at varying concentrations in the absence of MBs are shown in Figure 1. DR increases and TT decreases with increasing intralipid concentration, as expected. The DR and TT for microbubbles alone diluted in deionized water are shown in Figure 2. The size distribution of Definity microbubbles is shown in Figure 3.

The DR and TT of phantoms in the absence and presence of microbubbles at varying concentrations of intralipids are shown in Figures 4, 5, 6, and 7; the spectra with the addition of microbubbles are shown in solid line. The DR increases and TT decreases in the presence of microbubbles for all intralipid concentrations. For example, in the 0.5% intralipid concentration phantom, DR increased by 35–100% and TT decreased by 25–40% in the presence of MBs (Figure 4). In addition, the effect of microbubbles depended on the wavelength. At longer wavelengths, the effect of microbubbles on reflectance signal is decreased, whereas the effect is increased for total transmittance. Furthermore, the reflectance and transmittance spectra depended on intralipid concentration. With increasing intralipid concentration, the effect of MB on DR and TT was significantly reduced. At intralipid concentrations higher than 1.5%, DR and TT with and without microbubbles appear to be similar (Figure 7).

Diffuse reflectance

Total transmittance
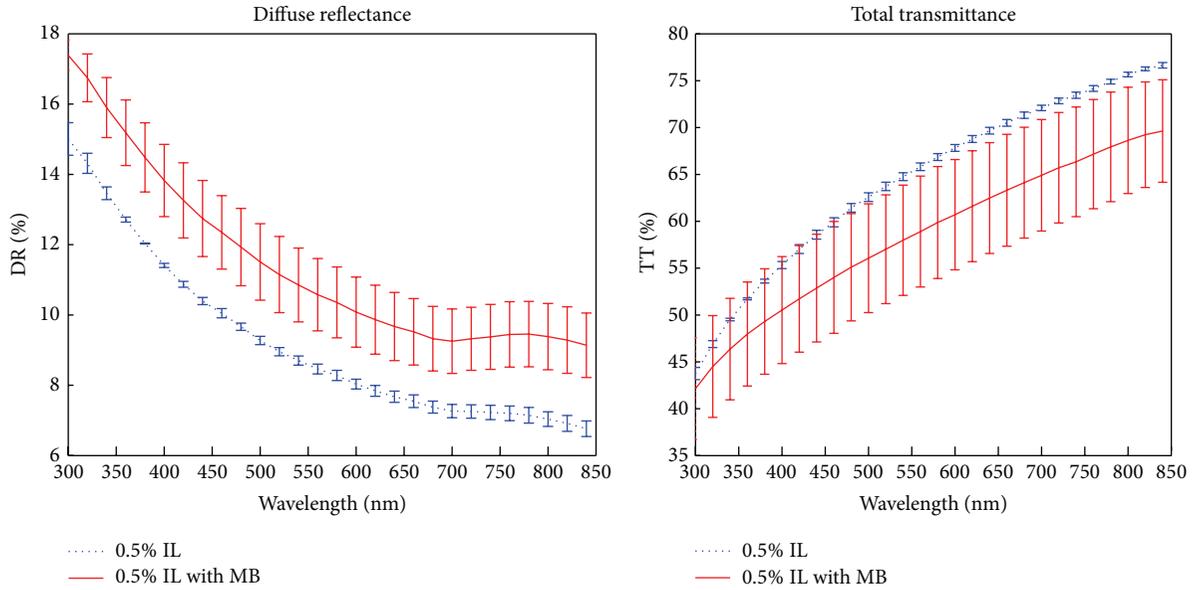
FIGURE 4: Diffuse reflectance (DR) and total transmittance (TT) of diluted intralipid (IL), 0.5% concentration, before and after adding Definity microbubbles.

Diffuse reflectance

Total transmittance
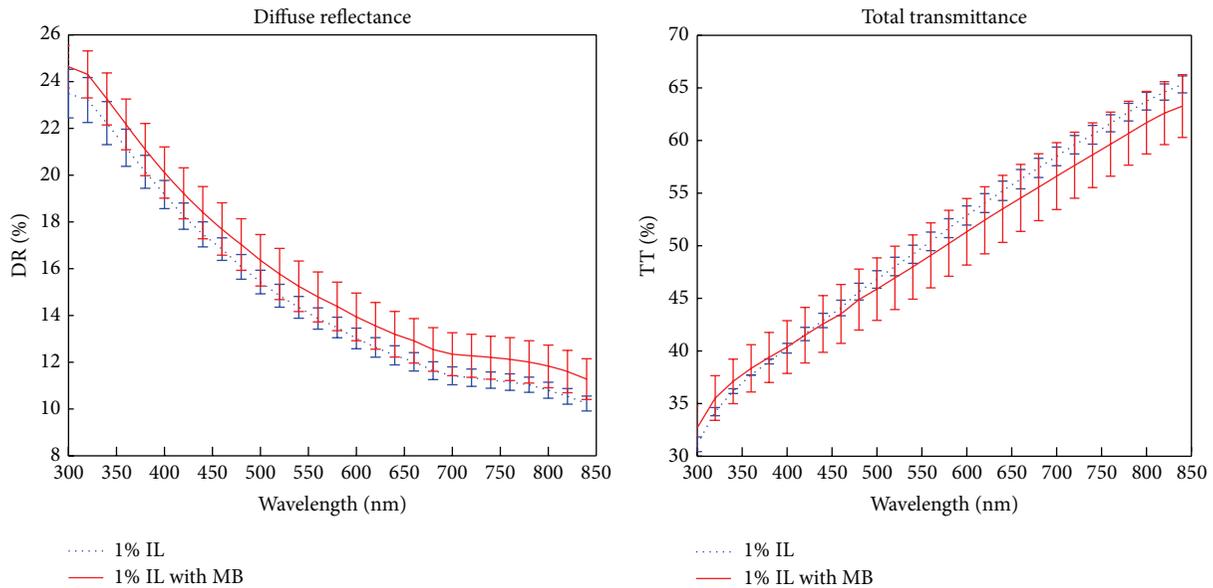
FIGURE 5: Diffuse reflectance (DR) and total transmittance (TT) of diluted intralipid (IL), 1% concentration, before and after adding Definity microbubbles.

3.2. Spectra of Intrinsic Optical Properties in Presence of Microbubbles.

The optical properties (reduced scattering and absorption coefficients) for intralipid phantoms (0.5% to 5.0%) and microbubbles only in deionized water are shown in Figures 8 and 9, respectively. The reduced scattering and the absorption coefficients increase with increasing intralipid concentration (**Figure 8**). The characteristics of the spectra

were similar; the amplitude in the reduced scattering spectrum decreased with intralipid concentration. Microbubbles act as optical scatterers in deionized water (**Figure 9**).

The computed reduced scattering and absorption coefficients as a function of wavelength for various concentrations of IL in the absence and presence of microbubbles are shown in Figures 10, 11, 12, and 13. The altered μ_a and μ_s'
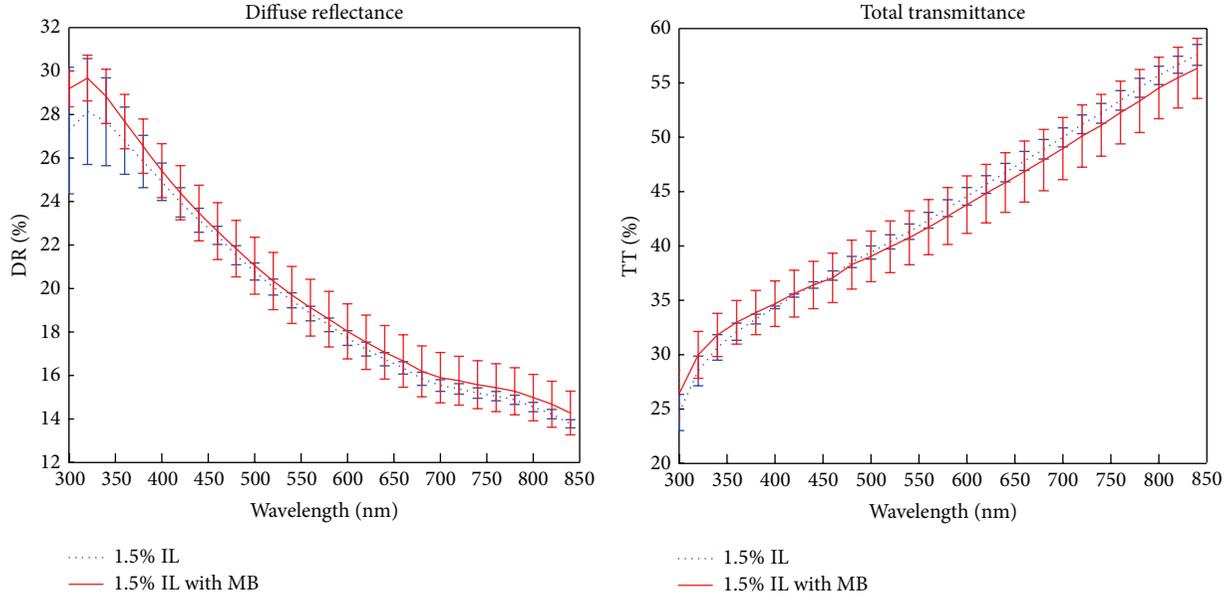
FIGURE 6: Diffuse reflectance (DR) and total transmittance (TT) of diluted intralipid (IL), 1.5% concentration, before and after adding Definity microbubbles.
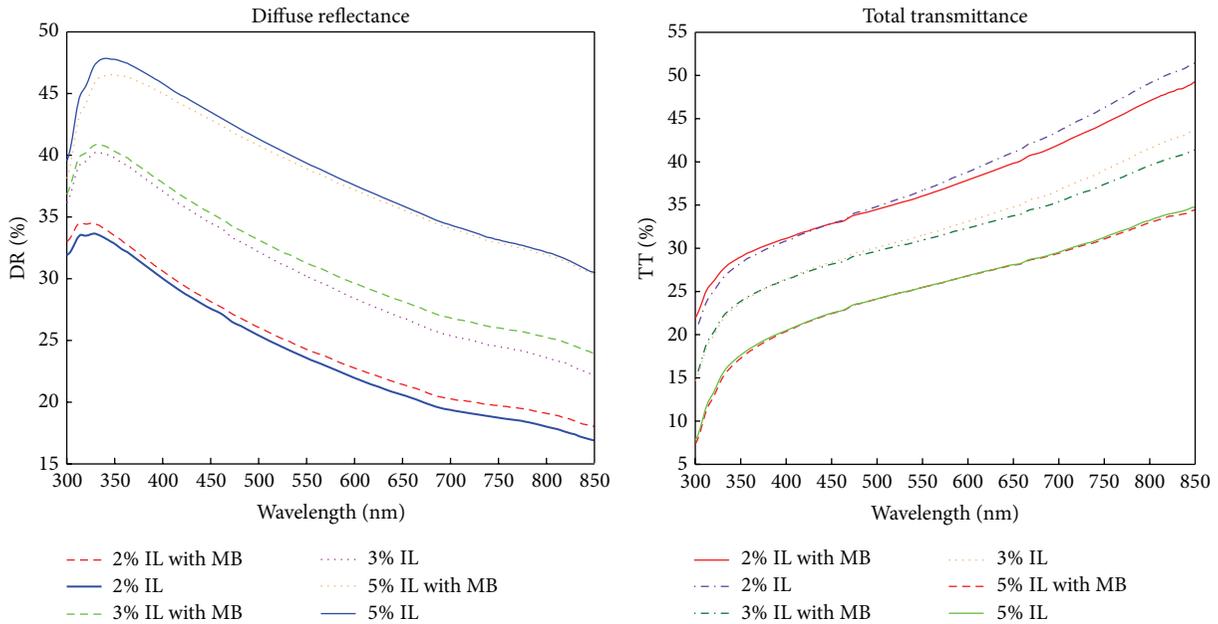
FIGURE 7: Diffuse reflectance (DR) and total transmittance (TT) of diluted intralipid (IL), 2%, 3%, and 5% concentrations, before and after adding Definity microbubbles.

caused by microbubbles are depicted in a solid line. The absorption coefficient of intralipid phantom measured in the study (Figure 8) was higher compared to those reported in the literature: 0.01 (1/cm) at 500 nm [19]. This may be due to integrating sphere corrections and lost light during the measurements [13]. The lost light is considered part of absorption and consequently overestimating μ_a. The results indicate that both μ_a and μ'_s increase significantly after adding microbubbles to the phantom intralipid solution at 0.5%, 1%, and 1.5% (Figures 10–12). The reduced scattering coefficient decreased with the wavelength; at wavelengths of 700 nm and longer, the absorption coefficient is lower
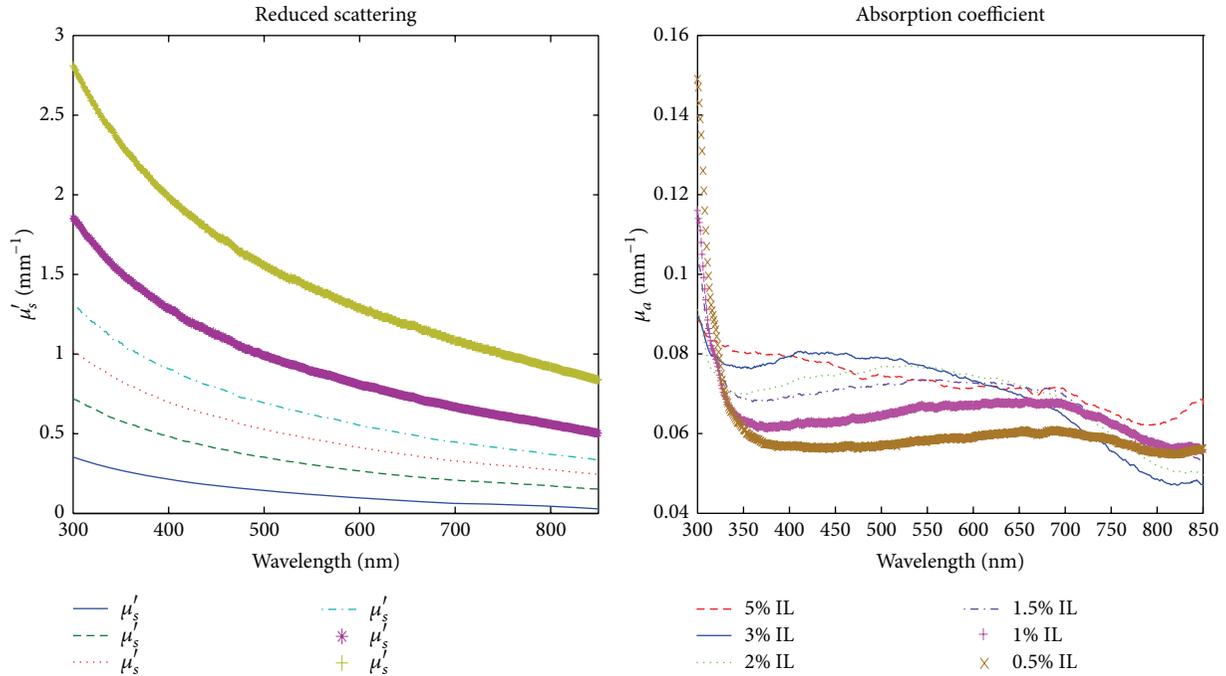
FIGURE 8: Reduced scattering and absorption coefficient of all concentrations of intralipid.

than 0.1. However, at higher intralipid concentrations, the intrinsic optical properties were not significantly different in the presence and absence of microbubbles (Figure 13). The absorption coefficient μ_a and the reduced scattering coefficient μ_s' increased in the presence of microbubbles. The growth of the scattering coefficient was more significant (1.35 fold at 300 nm and 6-fold at 850 nm) compared to the absorption coefficient (1.12 fold maximum across the spectrum) for the 0.5% intralipid phantom.

The scattering and absorbing particles of intralipid are soybean oil and water. It has been stated that water is the significant light absorber of intralipid in near infrared light for the wavelength range over 950 nm which is beyond the range we explored for the study [4]. It is found that in the red and far-red regions of the spectrum, both water and soybean oil contribute to the absorption while in the blue region, the absorption is primarily due to soybean oil [14].

4. Discussion and Conclusions

The presence of microbubbles in a scattering-mimicking tissue phantom significantly changed its optical properties in the 300–850 nm wavelength range. The scattering coefficient increased in the presence of microbubbles within the biological tissue transparency window where tissue absorption is minimal [20]. Microbubbles affected the intrinsic optical properties of the tissue phantom—both scattering and absorption. The microbubbles introduced an extrarefractive index mismatch that increased the probability of scattering
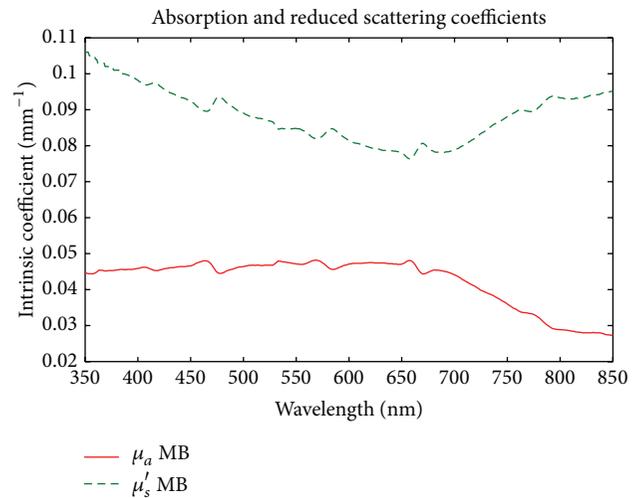
FIGURE 9: Reduced scattering and absorption coefficient for microbubbles diluted in deionized water (without intralipid).

events. The increase in light attenuation events is associated with the presence of microbubbles. Adding microbubbles changes the intrinsic optical properties of the tissue phantom not only for scattering but also for the absorption. The effect of microbubbles on reduced scattering and absorption
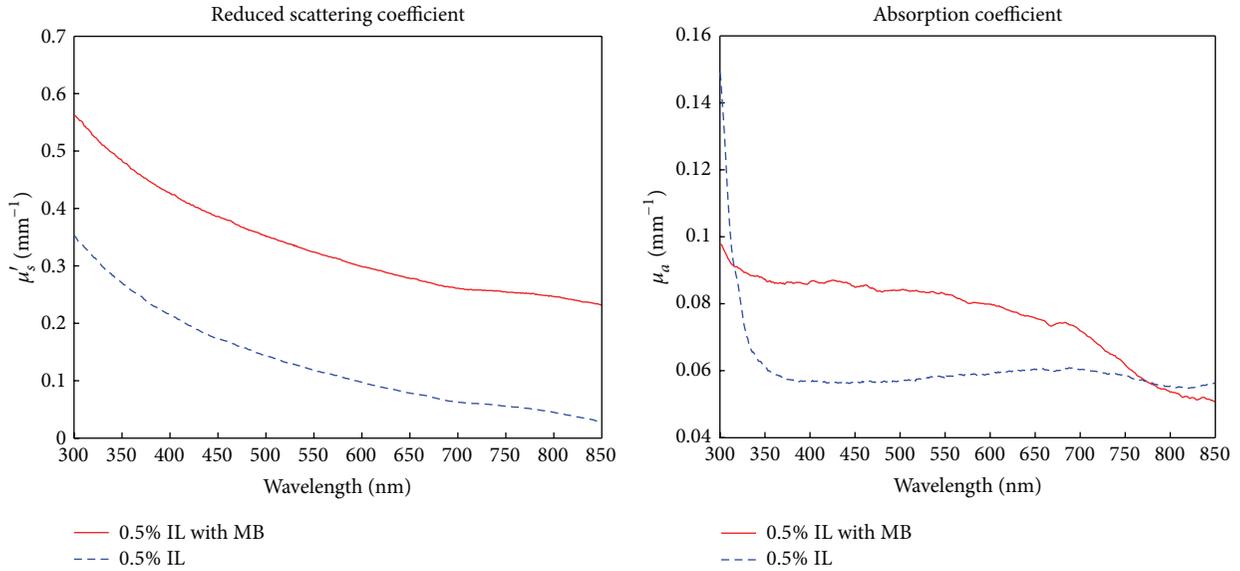
FIGURE 10: Absorption coefficient (μ_a) and reduced scattering coefficient (μ_s') of diluted intralipid (IL), 0.5% concentration, before and after adding Definity microbubbles.
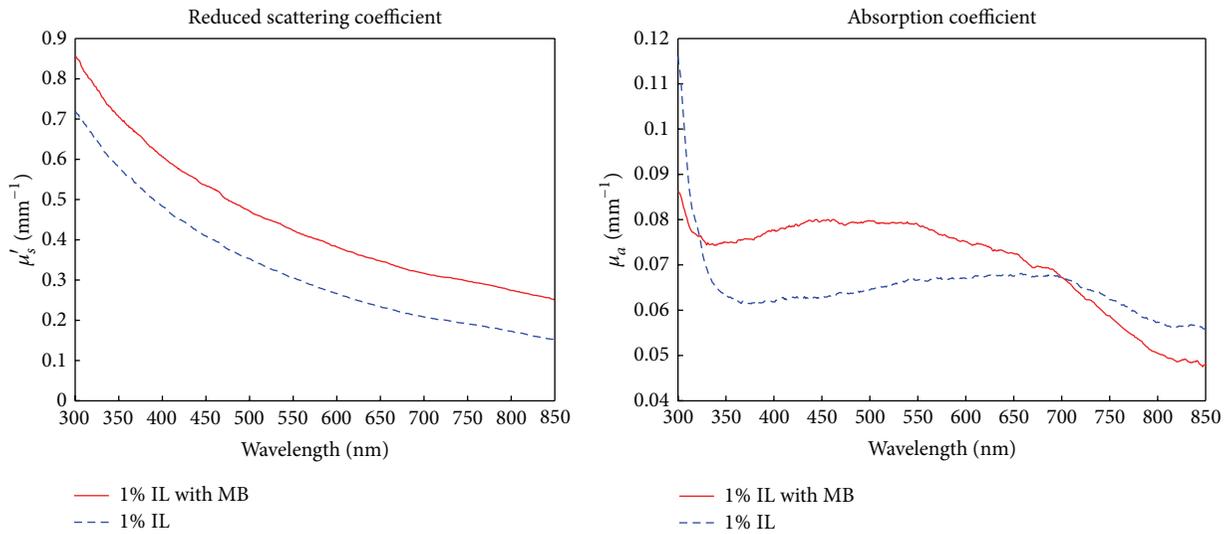
FIGURE 11: Absorption coefficient (μ_a) and reduced scattering coefficient (μ_s') of diluted intralipid (IL), 1% concentration, before and after adding Definity microbubbles.

coefficients decreased at longer wavelengths. In addition, at higher concentrations of intralipid (>1.5%), the effect of adding microbubbles is significantly reduced. The scattering properties of most biological tissues can be approximated at intralipid concentrations from 0.5% to 5.0% [12], indicating that the enhancement of the backscattering and reflectance due to the presence of microbubbles (2.5% v/v) can be potentially employed for improving optical imaging diagnostics. In contrast-enhanced ultrasound imaging, the dose of

microbubbles depends on the contrast agent characteristics and mode of administration. The microbubbles can be administered through infusion or bolus injection. Bolus injection is a delivery of an agent in a single bolus usually over a few seconds as opposed to infusion where the agent is delivered over a longer period and lower flow rate (e.g., saline bag infusion). A dose of 2.5% can be potentially achieved when microbubbles are administered through a bolus injection [21].
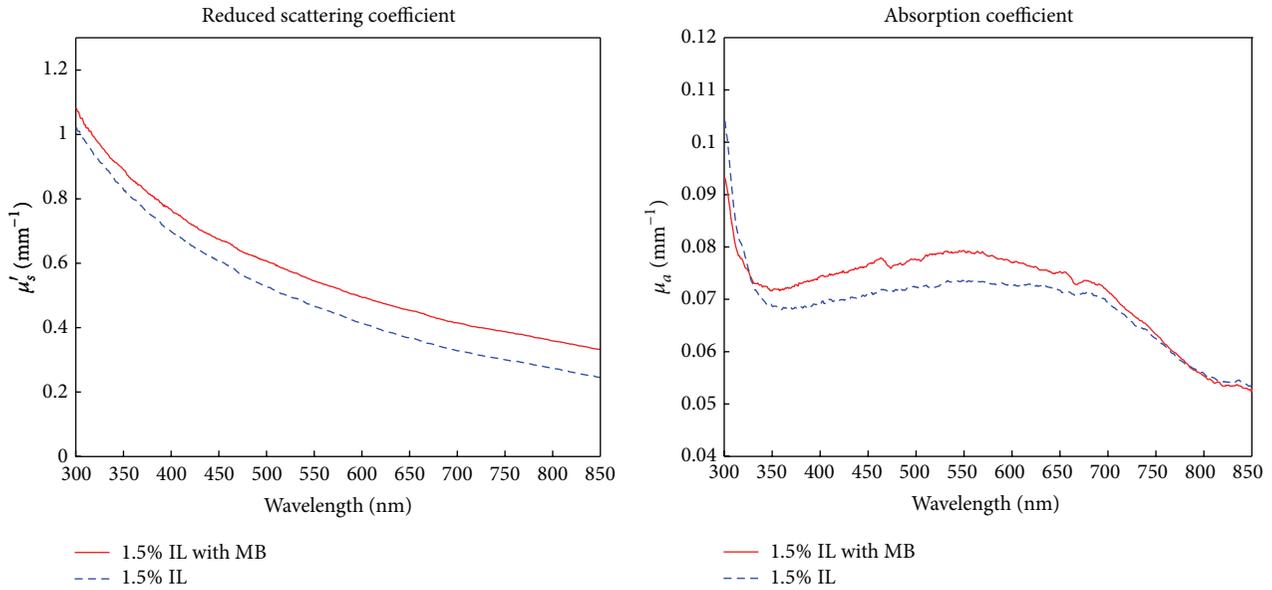
FIGURE 12: Absorption coefficient (μ_a) and reduced scattering coefficient (μ_s') of diluted intralipid (IL), 1.5% concentration, before and after adding Definity microbubbles.
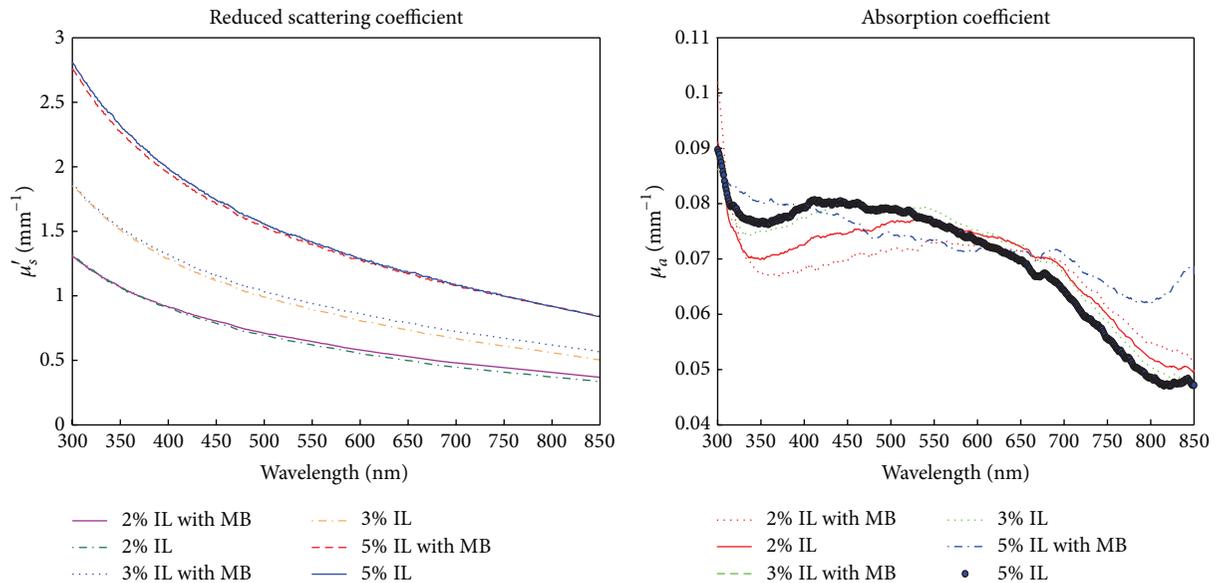
FIGURE 13: Absorption coefficient (μ_a) and reduced scattering coefficient (μ_s') of diluted intralipid (IL), 2%, 3%, and 5% concentrations, before and after adding Definity microbubbles.

Conflict of Interests

The authors declare that there is no conflict of interests regarding the publication of this paper.

Acknowledgments

School in Advanced Optical Technologies (SAOT), University Erlangen-Nuremberg, Germany.

References

[1] S. R. Sirsi and M. A. Borden, "Microbubble compositions, properties and biomedical applications," *Bubble Science, Engineering and Technology*, vol. 1, no. 1-2, pp. 3–17, 2009.

[2] F. Saglimbeni, S. Bianchi, G. Bolognesi, G. Paradossi, and R. di Leonardo, "Optical characterization of an individual polymer-shelled microbubble structure via digital holography," *Soft Matter*, vol. 8, no. 34, pp. 8822–8825, 2012.

[3] J. J. Kwan and M. A. Borden, "Lipid monolayer collapse and microbubble stability," *Advances in Colloid and Interface Science*, vol. 183-184, pp. 82–99, 2012.

[4] H. J. van Staveren, C. J. Moes, J. van Marie, S. A. Prahl, and M. J. van Gemert, "Light scattering in intralipid-10% in the wavelength range of 400–1100 nm," *Applied Optics*, vol. 30, no. 31, pp. 4507–4514, 1991.

[5] A. P. Dhawan, B. d'Alessandro, and X. Fu, "Optical imaging modalities for biomedical applications," *IEEE Reviews in Biomedical Engineering*, vol. 3, pp. 69–92, 2010.

[6] T. M. Lee, A. L. Oldenburg, S. Sitafalwalla et al., "Engineered microsphere contrast agents for optical coherence tomography," *Optics Letters*, vol. 28, no. 17, pp. 1546–1548, 2003.

[7] M. Douas, M. I. Marqués, and P. A. Serena, "Optical image contrast enhancement in near-field optics induced by water condensation," *Ultramicroscopy*, vol. 135, pp. 50–55, 2013.

[8] P. A. Dijkmans, L. J. M. Juffermans, R. J. P. Musters et al., "Microbubbles and ultrasound: from diagnosis to therapy," *European Journal of Echocardiography*, vol. 5, no. 4, pp. 245–256, 2004.

[9] CRCnetBASE, *Biomedical Photonics Handbook*, CRC Press, 2003.

[10] A. E. Profio, "Light transport in tissue," *Applied Optics*, vol. 28, no. 12, pp. 2216–2222, 1989.

[11] A. J. Welch and M. J. C. Gemert, Eds., *Optical-Thermal Response of Laser-Irradiated Tissue*, chapter 8, Springer, Dordrecht, The Netherlands, 2011.

[12] S. T. Flock, S. L. Jacques, B. C. Wilson, W. M. Star, and M. J. C. van Gemert, "Optical properties of intralipid: a phantom medium for light propagation studies," *Lasers in Surgery and Medicine*, vol. 12, no. 5, pp. 510–519, 1992.

[13] S. Prahl, "Optical Property Measurements Using the Inverse Adding-Doubling Program".

[14] P. D. Ninni, F. Martelli, and G. Zaccanti, "Intralipid: towards a diffusive reference standard for optical," *Physics in Medicine and Biology*, vol. 56, no. 2, pp. N21–N28, 2011.

[15] S. K. Cool, B. Geers, S. Roels et al., "Coupling of drug containing liposomes to microbubbles improves ultrasound triggered drug delivery in mice," *Journal of Controlled Release*, vol. 172, no. 3, pp. 885–893, 2013.

[16] "UV-2600, UV-2700 UV-VIS Spectrophotometer: SHIMADZU (Shimadzu Corporation)," http://www.shimadzu.com/an/uv/uv2600_2700.html.

[17] S. Prahl, "Everything i think you should know about inverse adding-doubling," vol. 2197, 2011.

[18] M. L. Dong, K. G. Goyal, B. W. Worth et al., "Accurate in situ measurement of complex refractive index and particle size in intralipid emulsions," *Journal of Biomedical Optics*, vol. 18, no. 8, Article ID 87003, 2013.

[19] "Optical Properties of Intralipid," http://omlc.ogi.edu/spectra/intralipid/index.html.

[20] R. R. Anderson and J. A. Parrish, "The optics of human skin," *Journal of Investigative Dermatology*, vol. 77, no. 1, pp. 13–19, 1981.

[21] T. A. Fritz, E. C. Unger, G. Sutherland, and D. Sahn, "Phase I clinical trials of MRX-115: a new ultrasound contrast agent," *Investigative Radiology*, vol. 32, no. 12, pp. 735–740, 1997.

Research Article

Autoregulatory Feedback Mechanism of P38MAPK/Caspase-8 in Photodynamic Therapy-Hydrophilic/Lipophilic Tetra-α-(4-carboxyphenoxy) Phthalocyanine Zinc-Induced Apoptosis of Human Hepatocellular Carcinoma Bel-7402 Cells

Yu Wang,[1] Chunhui Xia,[1] Wei Chen,[2] Yuhang Chen,[1] Yiyi Wang,[1] and Tao Li[1]

[1] *Basic Medicine Department, Qiqihar Medical College, Qiqihar 161006, China*
[2] *College of Chemistry and Chemical Engineering, Qiqihar University, Qiqihar 161006, China*

Correspondence should be addressed to Tao Li; litao888@sohu.com

Photodynamic therapy (PDT) is a novel and promising antitumor treatment. Our previous study showed that hydrophilic/lipophilic tetra-α-(4-carboxyphenoxy) phthalocyanine zinc- (TαPcZn-) mediated PDT (TαPcZn-PDT) inhibits the proliferation of human hepatocellular carcinoma Bel-7402 cells by triggering apoptosis and arresting cell cycle. However, mechanisms of TαPcZn-PDT-induced apoptosis of Bel-7402 cells have not been fully clarified. In the present study, therefore, effect of TαPcZn-PDT on apoptosis, P38MAPK, p-P38MAPK, Caspase-8, Caspase-3, Bcl-2, Bid, Cytochrome c, and mitochondria membrane potential in Bel-7402 cells without or with P38MAPK inhibitor SB203580 or Caspase-8 inhibitor Ac-IEFD-CHO was investigated by haematoxylin and eosin (HE) staining assay, flow cytometry analysis of annexin V-FITC/propidium iodide (PI) double staining cells and 5,5′,6,6′-tetrachloro-1,1′,3,3′-tetraethylbenzimidazolylcarbocyanine iodide (JC-1), and immunoblot assay. We found that TαPcZn-PDT resulted in apoptosis induction, activation of P38MAPK, Caspase-8, Caspase-3, and Bid, downregulation of Bcl-2, release of Cytochrome c from mitochondria, and disruption of mitochondrial membrane potential in TαPcZn-PDT-treated Bel-7402 cells. In contrast, SB203580 or Ac-IEFD-CHO attenuated induction of apoptosis, activation of P38MAPK, Caspase-8, Caspase-3, and Bid, downregulation of Bcl-2, release of Cytochrome c from mitochondria, and disruption of mitochondrial membrane potential in TαPcZn-PDT-treated Bel-7402 cells. Taken together, we conclude that Caspase-3, Bcl-2, Bid, and mitochondria are involved in autoregulatory feedback of P38MAPK/Caspase-8 during TαPcZn-PDT-induced apoptosis of Bel-7402 cells.

1. Introduction

Photodynamic therapy (PDT), also known as photochemotherapy, is a developing strategy and has shown promising antitumor efficacy. It is based on the concept that photosensitizing drugs, when exposed to appropriate wavelength of light, are capable of resulting in photochemical destruction of tumors by yielding reactive oxygen species (ROS), such as singlet oxygen and free radicals [1–4]. Compared with traditional therapies, such as surgery and chemotherapy, the outstanding advantage of PDT is that it destroys tumor cells selectively because it is possible to expose the photosensitizer to light and to activate it specifically in the target tumor tissue.

Photosensitizers play a crucial role in PDT. Currently, although only a few photosensitizers (temoporfin, talaporfin, verteporfin, and 5-aminolevulinic acid), which are approved for antitumor treatment, have been proved to be effective in a wider spectrum of antitumor, they present various defects that stimulate the development of better photosensitizer candidates [5–7]. Phthalocyanines, consisting of a planar macrocycle with an 18 π-electron system, are one of the most potential photosensitizer candidates because of the desirable electronic absorption and photophysical properties [8–10]. In addition, phthalocyanines with hydrophilic/lipophilic structure may become promising candidates for selectivephotosensitizers inasmuch as hydrophilic group contributes to the

transport of drug in the body and lipophilic group redounds to the uptake of drug in cancer cells. Accumulating evidences have shown highly selective growth inhibitory effects of hydrophilic/lipophilic phthalocyanines-mediated PDT on a variety of cancer cells [11–13].

Apoptosis that plays a crucial role during development and maintenance of tissue homeostasis by eliminating old cells, unnecessary cells, and unhealthy cell is the process of programmed cell death that may occur in multicellular organisms. Apoptosis is characterized by morphologic and biochemical changes including chromatin condensation, cell shrinkage, nucleus and cytoplasm fragment, DNA fragmentation, and formation of membrane blebs and apoptotic bodies. Accumulating evidences clearly indicate that apoptosis is one key pathway in phthalocyanines-PDT process [11–13].

P38 mitogen-activated protein kinase (MAPK) is a member of the MAPK family of kinases that is responsive to stress stimuli (ionizing radiation, ultraviolet irradiation, oxidative stress, FAS ligand, and cytokines) and is involved in cell proliferation, differentiation, apoptosis, and autophagy. Nowadays, P38MAPK has been documented to play a crucial regulatory role in phthalocyanines-PDT-induced apoptosis of cancer cells [14, 15].

Caspases, a family of cysteine proteases, are central regulators of apoptosis signaling [16]. Initiator Caspase-8 is closely coupled to proapoptotic signals. Once activated, Caspase-8 cleaves and activates downstream effector Caspase-3, whose cleavage leads to the morphological and functional changes associated with apoptosis [17]. Nowadays, Caspase-8 and Caspase-3 have been documented to play a crucial regulatory role in phthalocyanines-PDT-induced apoptosis of cancer cells [18–21].

Apoptosis regulator Bcl-2 is a family of evolutionarily related proteins. These proteins govern mitochondrial outer membrane permeabilization and comprise proapoptotic (Bax, Bid, Bak, etc.) and antiapoptotic (Bcl-2, Bcl-XL, Bcl-w, etc.) molecules. Recent studies have demonstrated that induction of proapoptotic proteins and inhibition of antiapoptotic proteins can be caused by phthalocyanines-PDT in apoptosis of cancer cells [11, 21, 22].

Mitochondrion is a membrane-enclosed organelle found in most eukaryotic cells. Cytochrome c is a small heme protein found loosely associated with the inner membrane of the mitochondrion. Membrane potential (also transmembrane potential or membrane voltage) is the difference in electrical potential between the interior and the exterior of a biological cell. Accumulated evidences have demonstrated that release of Cytochrome c from mitochondria and reduction of mitochondrial membrane potential appear to be key events in phthalocyanines-PDT-induced apoptosis of cancer cells [19, 20].

We found previously that tetra-α-(4-carboxyphenoxy) phthalocyanine- (TαPcZn-) mediated PDT (TαPcZn-PDT) (Figure 1) resulted in the inhibition of proliferation and induction of apoptosis in Bel-7402 cells [11], which is one of the most widely used experiment models for hepatocellular carcinoma. However, mechanisms of TαPcZn-PDT-induced apoptosis of Bel-7402 cells have not been fully clarified. In the present study, the objective of our study is to investigate the

autoregulatory feedback mechanism of P38MAPK/Caspase-8 in TαPcZn-PDT-induced apoptosis of Bel-7402 cells. Based on in vitro model, we found that Caspase-3, Bcl-2, Bid, and mitochondria were involved in autoregulatory feedback of P38MAPK/Caspase-8 during TαPcZn-PDT-induced apoptosis of Bel-7402 cells.

2. Materials and Methods

2.1. Materials. Anti-P38MAPK, anti-phos-P38MAPK, anti-Caspase-8, anti-Caspase-3, anti-Bcl-2, anti-Bid, and anti-Cytochrome c antibodies were purchased from Cell Signals (OH, USA). P38MAPK inhibitor SB203580 and Caspase-8 inhibitor Ac-IEFD-CHO were obtained from Merck Calbiochem (Darmstadt, Germany). JC-I (5,5$'$,6,6$'$-tetrachloro-1,1$'$,3,3$'$-tetraethylbenzimidazolylcarbocyanine iodide) Staining Kit was purchased from Genmed Scientifics (MA, U.S.A). Annexin-V-FLUOS Staining Kit was purchased from Roche (Basel, Switzerland). DMSO was purchased from Sigma (MO, USA). DMEM medium was purchased from Gibco (CA, USA). Fetal bovine serum was purchased from PAA (Coelbe, Germany). Penicillin was purchased from Harbin Pharmaceutical Group (Heilongjiang, China). Streptomycin was purchased from Dalian Merro Pharmaceutical (Liaoning, China). Polyvinylidene difluoride membrane (PVDF) membrane was purchased from Amersham Pharmacia Biotech (NJ, USA). TαPcZn was synthesized as described in our previous report [23]. The TαPcZn stock solution was prepared in DMSO and stored at $4°C$ in the dark. When used, the stock solution was appropriately diluted to obtain the desired concentration with a final DMSO concentration of 0.1%. All other chemicals and reagents were of analytic grade.

2.2. Cell Culture and Treatment. Hepatocellular carcinoma Bel-7402 cells were obtained from Harbin Medical University, China, and cultured in DMEM medium supplemented with 10% fetal bovine serum, 100 U/mL penicillin, and 100 mg/L streptomycin in a humidified atmosphere of 5% CO_2 at $37°C$. Bel-7402 cells in logarithmic growth phase were seeded in culture plates and incubated for 24 h in a humidified atmosphere of 5% CO_2 at $37°C$. After being rinsed with phosphate-buffered saline, the cells were treated with TαPcZn stock solution diluted in medium for 2.5 h at $37°C$ in the presence or absence of SB203580 or Ac-IEFD-CHO. Then the cells were irradiated with a SS-B instrument (Wuxi Holyglow Physiotherapy Instrument Co., Ltd., Jiangsu, China) emitting red light within the wavelength range of 600 to 700 nm. The light dose was about 53.7 J/cm^2. Thereafter, cells were harvested at 3 h. Control cells were treated with 0.1% DMSO under the same conditions.

2.3. Cell Morphology Assay. At 3 h posttreatment, Bel-7402 cells on a glass slide within 6-well culture plates were fixed with 10% formaldehyde for 15 min, washed with phosphate-buffered saline, and stained with haematoxylin and eosin (HE). Cells morphology was then observed under IX70 inverted microscope (Olympus, Tokyo, Japan).
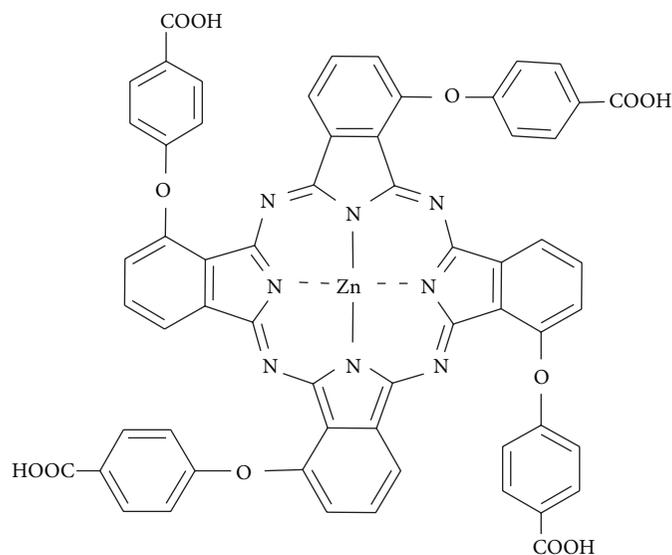
FIGURE 1: Chemical structure of TαPcZn [11].
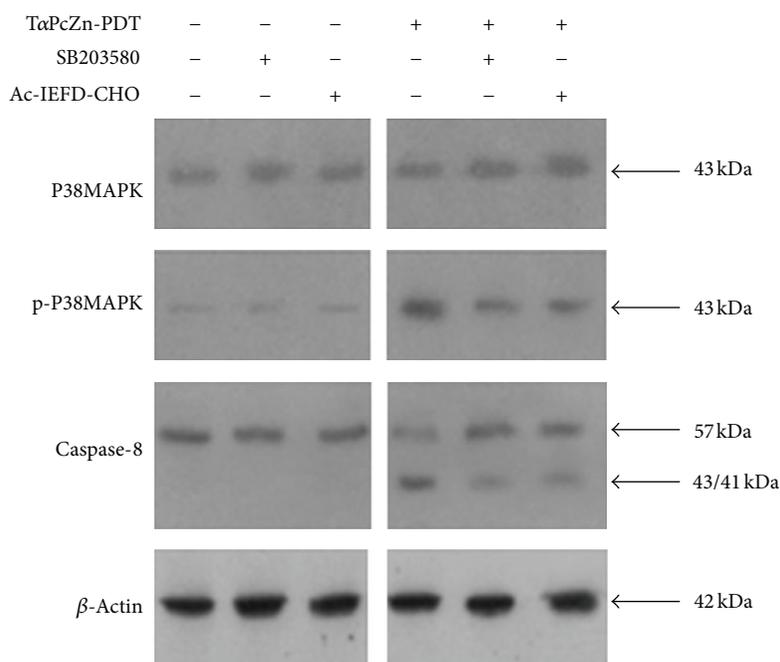
FIGURE 2: Effect of TαPcZn-PDT on P38MAPK, p-P38MAPK, and Caspase-8, respectively, without or with SB203580 or Ac-IEFD-CHO in TαPcZn-PDT-induced apoptosis of Bel-7402 cells analyzed by immunoblot assay. Bel-7402 cells were pretreated with TαPcZn ($54\,\mu$M) in the absence or presence of SB203580 ($10\,\mu$M) or Ac-IEFD-CHO ($10\,\mu$M) for 2.5 h, exposed to red-light irradiation ($53.7\,$J/cm^2), and then incubated for 3 h. Expression of P38MAPK, p-P38MAPK, and Caspase-8 was analyzed by immunoblot assay.

2.4. Flow Cytometry Analysis Of Annexin V-FITC/PI Double Stained Cells for Apoptosis.

Confirmation of apoptosis was determined by measurement of externalized phosphatidylserine residues as detected using annexin V-FITC. The harvested Bel-7402 cells were collected and washed with ice-cold phosphate-buffered saline and then suspended in $500\,\mu$L of annexin V binding buffer A. $100\,\mu$L aliquot was taken, $2\,\mu$L of annexin V-FITC and $2\,\mu$L of propidium iodide (PI) were added, and the mixture was incubated for 5 min at room temperature in the dark. After the addition of $400\,\mu$L of binding buffer, 1×10^4 cells were analyzed on a FACSCAN flow cytometer (Becton Dickinson, CA, USA) by using CellQuest software. The results are shown as a dot plot graph. In each graph, the percentages of viable cells, early apoptotic cells, and late apoptotic cells are, respectively, indicated in lower-left, lower-right, and upper-right quadrant; the y-axis corresponds to relative PI staining; the x-axis corresponds to the log of the FITC signal.

(a)

(b)

(c)
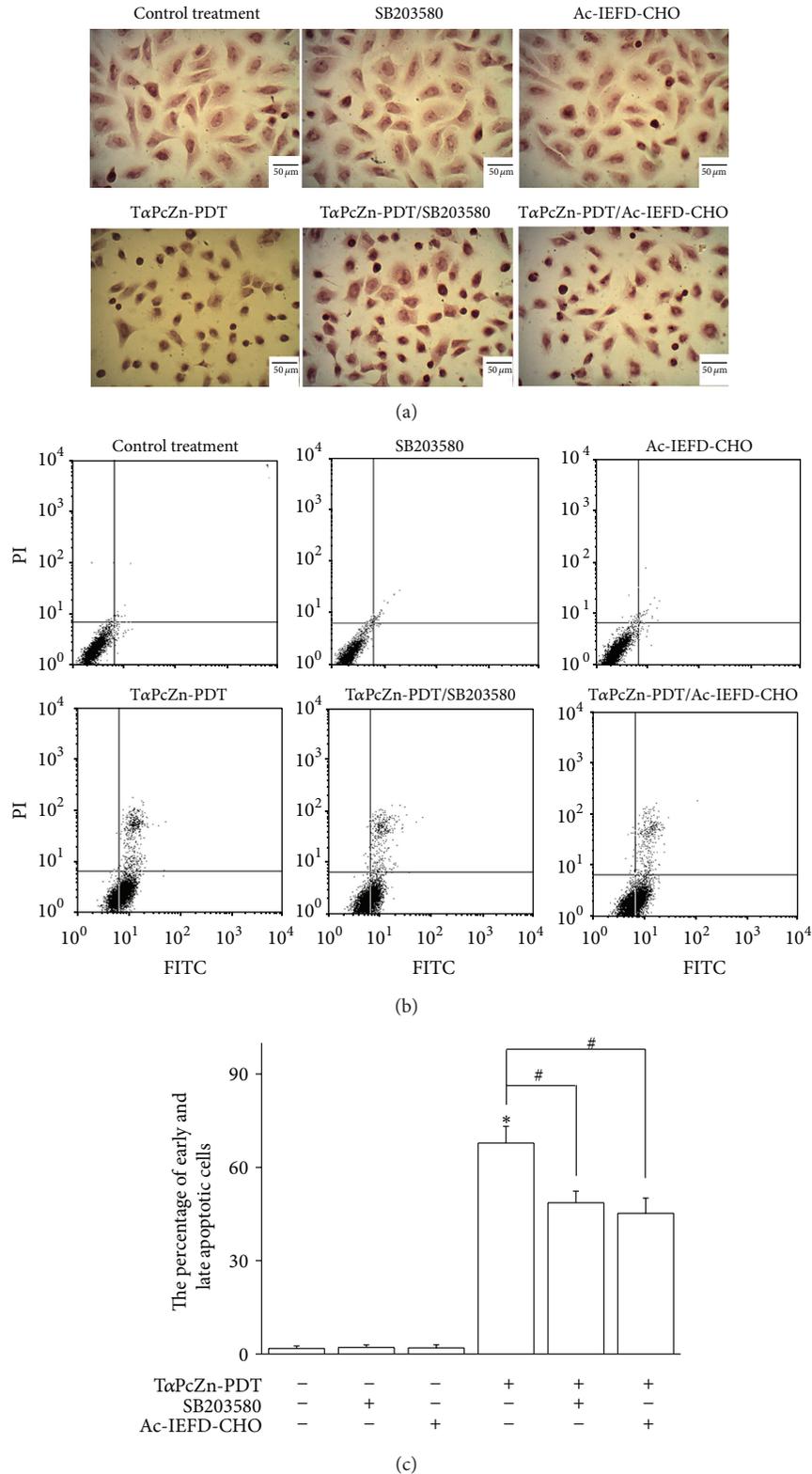
FIGURE 3: Effect of TαPcZn-PDT on apoptosis of Bel-7402 cells in the absence or presence of SB203580 or Ac-IEFD-CHO. Bel-7402 cells were pretreated with TαPcZn (54 μM) in the absence or presence of SB203580 (10 μM) or Ac-IEFD-CHO (10 μM) for 2.5 h, exposed to red-light irradiation (53.7 J/cm^2), and then incubated for 3 h. The morphology of apoptotic cells was analyzed by HE staining assay (a), and the percentage of apoptotic cells was assayed by flow cytometry analysis of annexin V-FITC/PI double stained cells (b and c). Bars under each panel represent 50 μm. Values presented are representative of three independent experiments (means ± S.D.; $^*P < 0.05$, compared with control treatment; $^\#P < 0.05$, compared with TαPcZn-PDT treatment).
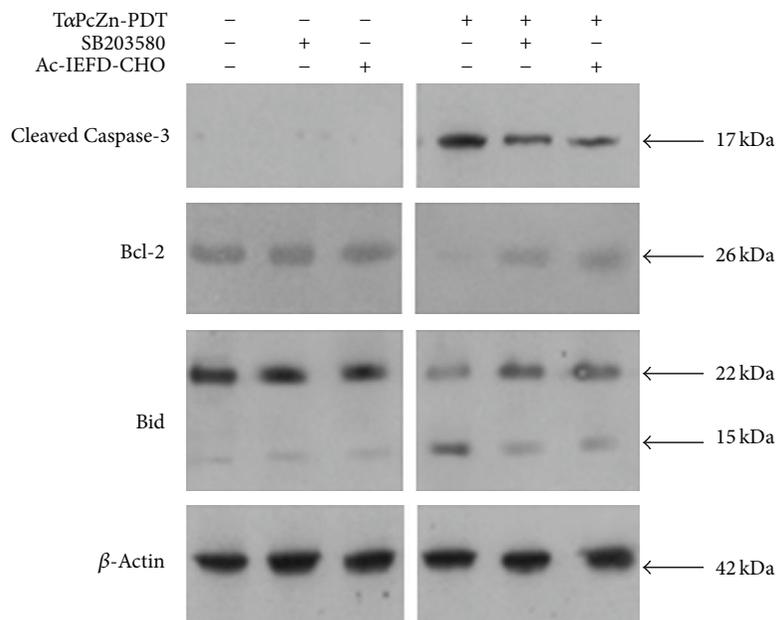
FIGURE 4: Effect of TαPcZn-PDT on Caspase-3, Bcl-2, and Bid, respectively, without or with SB203580 or Ac-IEFD-CHO in TαPcZn-PDT-induced apoptosis of Bel-7402 cells analyzed by immunoblot assay. Bel-7402 cells were pretreated with TαPcZn (54 μM) in the absence or presence of SB203580 (10 μM) or Ac-IEFD-CHO (10 μM) for 2.5 h, exposed to red-light irradiation (53.7 J/cm^2), and then incubated for 3 h. Expression of cleaved Caspase-3, Bcl-2, and Bid was analyzed by immunoblot assay.

2.5. JC-1 Assay for Mitochondrial Membrane Potential. Mitochondrial membrane potential was detected using JC-1 fluorescent dye by flow cytometry. The harvested cells were incubated with fresh culture medium containing JC-1 dye (2.5 ug/mL) for 20 min at 37°C in the dark, and then about 1×10^4 cells were analyzed on a flow cytometer by using CellQuest software. The results are shown as a dot plot graph. In each graph, the y-axis corresponds to JC-1 oligomer-associated red fluorescence, the x-axis corresponds to JC-1 monomer-associated green fluorescence, and the shift down of fluorescence from red to green indicates the collapse of mitochondrial membrane potential.

2.6. Immunoblot Assay. All immunoblots were performed using sodium dodecyl sulfate-polyacrylamide gel electrophoresis (SDS-PAGE) Bis-Tris gel electrophoresis as outlined by the supplier. For total cellular protein, Bel-7402 cells were lysed in buffer containing 25 mM HEPES, pH 7.5, 0.3 M NaCl, 1.5 mM MgCl$_2$, 0.2 mM EDTA, 0.1% Triton X-100, 20 mM β-glycerophosphate, 0.5 mM DTT, 1 mM sodium orthovanadate, 0.1 μM okadaic acid, and 1 mM phenyl-methylsulfonyl fluoride. Equal amounts of lysate protein ran on 12% SDS-PAGE and electrophoretically transferred to PVDF membrane. After blocking, the blots were incubated with specific primary antibodies (anti-P38MAPK, anti-phos-P38MAPK, anti-Caspase-3, anti-Caspase-8, anti-Bcl-2, and anti-Bid antibodies) overnight at 4°C and further incubated for 1 h with horseradish peroxidase-conjugated respective secondary antibody. Bound antibodies were detected by enhanced chemiluminescence kit with Lumino Image Analyzer (Founder, Beijing, China). The mitochondria and

cytosolic fractions isolated from the cells were collected for immunoblot assay of Cytochrome c as previously described [24]. The Cytochrome c protein was assayed using an anti-Cytochrome c antibody.

2.7. Statistical Analysis. Values are means ± S.D. of three independent experiments. Statistical significance was determined using Student's unpaired two-tailed t-test. P value less than 0.05 was considered significant in all cases.

3. Results

3.1. Autoregulatory Feedback of P38MAPK/Caspase-8 Is Essential for TαPcZn-PDT-Induced Apoptosis of Bel-7402 Cells. Our previous study showed that TαPcZn-PDT apparently induced apoptosis of Bel-7402 cells [11]. To evaluate whether P38MAPK and Caspase-8 are involved in TαPcZn-PDT-induced apoptosis of Bel-7402 cells, effect of TαPcZn-PDT on P38MAPK, p-P38MAPK, and Caspase-8, respectively, was investigated by immunoblot assay in the present study. Compared with the control treatment, TαPcZn-PDT resulted in little effect on P38MAPK, upregulation of p-P38MAPK, and activation of active Caspase-8 (Figure 2), suggesting that active P38MAPK and Caspase-8 might modulate TαPcZn-PDT-induced apoptosis of Bel-7402 cells.

To determine whether attenuation of P38MAPK, p-P38MAPK, and Caspase-8 influences Bel-7402 cells in TαPcZn-PDT-induced apoptosis, we used the P38MAPK inhibitor SB203580 or Caspase-8 inhibitor Ac-IEFD-CHO. Compared with TαPcZn-PDT treatment, SB203580 resulted

TαPcZn-PDT	−	−	−	+	+	+
SB203580	−	+	−	−	+	−
Ac-IEFD-CHO	−	−	+	−	−	+

Cytochrome c ← 12.4 kDa

β-Actin ← 42 kDa

(a)

Control treatment   SB203580   Ac-IEFD-CHO

TαPcZn-PDT   TαPcZn-PDT/SB203580   TαPcZn-PDT/Ac-IEFD-CHO

JC-1 monomer-associated green fluorescence

(b)

TαPcZn-PDT	−	−	−	+	+	+
SB203580	−	+	−	−	+	−
Ac-IEFD-CHO	−	−	+	−	−	+

(c)
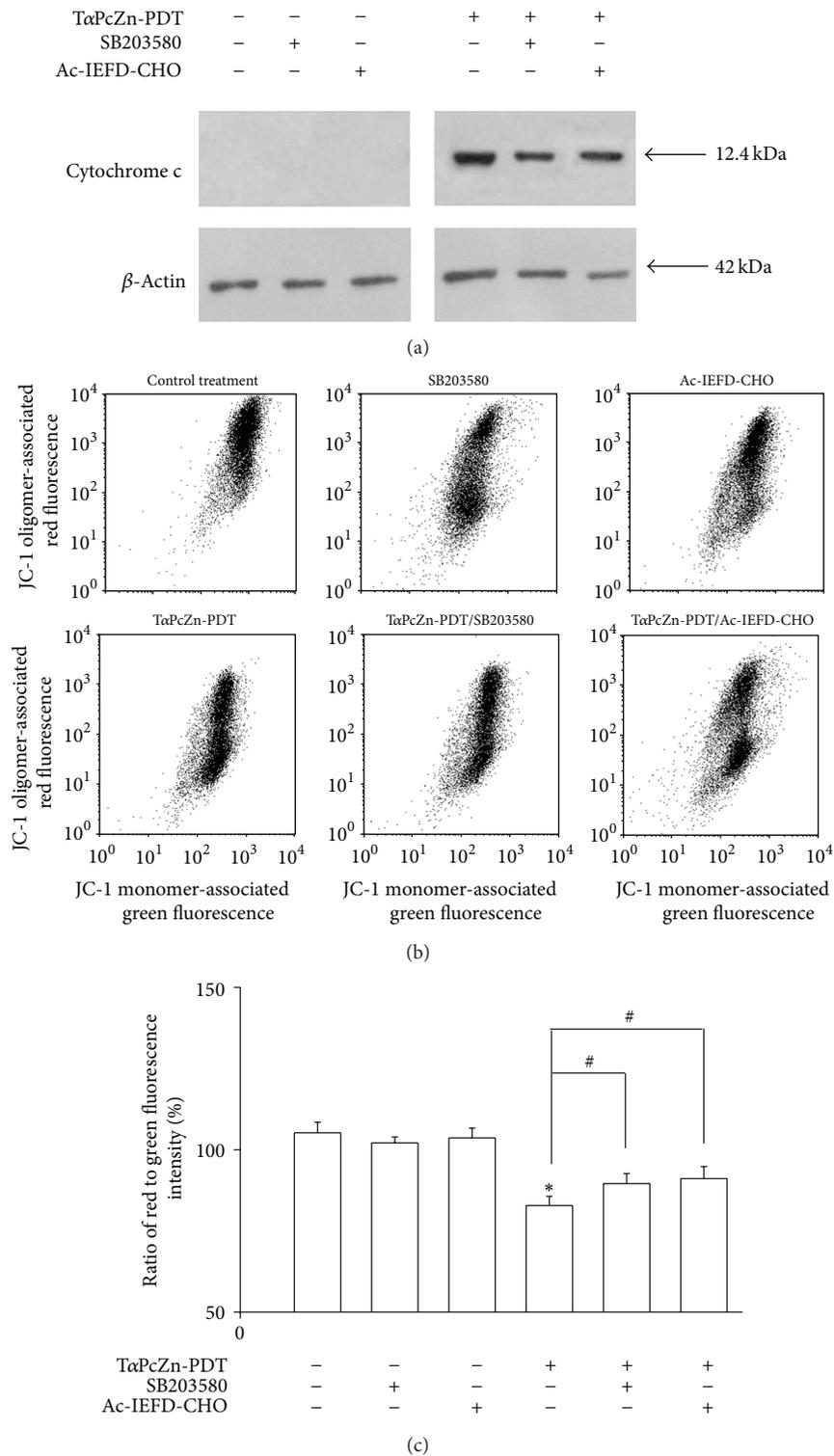
FIGURE 5: Effect of TαPcZn-PDT on mitochondria of Bel-7402 cells in the absence or presence of SB203580 or Ac-IEFD-CHO. Bel-7402 cells were pretreated with TαPcZn (54 μM) in the absence or presence of SB203580 (10 μM) or Ac-IEFD-CHO (10 μM) for 2.5 h, exposed to red-light irradiation (53.7 J/cm^2), and then incubated for 3 h. Expression of Cytochrome c was analyzed by immunoblot assay (a), and mitochondria membrane potential (b) and ratio of red to green fluorescence intensity (c) in Bel-7402 cells were determined by JC-1 assay of flow cytometry, respectively. Values presented are representative of three independent experiments (means ± S.D.; $^*P < 0.05$, compared with control treatment; $^\#P < 0.05$, compared with TαPcZn-PDT treatment).

in little effect on P38MAPK and downregulation of p-P38MAPK, and Ac-IEFD-CHO led to downregulation of 43/41-kDa subunit of active Caspase-8 in TαPcZn-PDT-treated Bel-7402 cells (Figure 2), suggesting that attenuation of active P38MAPK and Caspase-8 might be involved in TαPcZn-PDT-induced apoptosis of Bel-7402 cells.

To confirm whether Caspase-8 or P38MAPK regulates apoptosis in TαPcZn-PDT-treated Bel-7402 cells, effect of SB203580 or Ac-IEFD-CHO on apoptosis, respectively, was investigated by several ways in the present study. Firstly, the morphological characteristics of apoptotic cells were assessed by HE staining assay. Compared with control cells, cells treated with TαPcZn-PDT apparently exhibited morphological characteristics of apoptotic cells, such as cell shrinkage, chromatin condensation, nucleus and cytoplasm fragment, and membrane blebs formation (Figure 3(a)). However, compared with TαPcZn-PDT treatment, SB203580 or Ac-IEFD-CHO resulted in less morphological characteristics of apoptosis in TαPcZn-PDT-treated cells (Figure 3(a)). Furthermore, apoptosis of cells was quantitatively evaluated by flow cytometry analysis of annexin V-FITC/PI double staining cells. Compared with control treatment, TαPcZn-PDT apparently induced cells apoptosis (Figures 3(b) and 3(c)). However, compared with TαPcZn-PDT treatment, SB203580 or Ac-IEFD-CHO resulted in less effect of apoptosis on TαPcZn-PDT-treated cells (Figures 3(b) and 3(c)). These results indicate that active P38MAPK and Caspase-8 are essential for TαPcZn-PDT-induced apoptosis of Bel-7402 cells.

To determine whether P38MAPK regulates Caspase-8 and whether Caspase-8 regulates P38MAPK, effect of SB203580 on Caspase-8 and effect of Ac-IEFD-CHO on P38MAPK in TαPcZn-PDT-treated Bel-7402 cells were, respectively, investigated by immunoblot assay in the present study. Compared with TαPcZn-PDT treatment, SB203580 downregulated 43/41-kDa subunit of active Caspase-8 and Ac-IEFD-CHO downregulated p-P38MAPK in TαPcZn-PDT-treated Bel-7402 cells (Figure 2), suggesting that autoregulatory feedback of P38MAPK/Caspase-8 is involved in TαPcZn-PDT-induced apoptosis of Bel-7402 cells. All of the above results suggest that autoregulatory feedback of P38MAPK/Caspase-8 is essential for TαPcZn-PDT-induced apoptosis of Bel-7402 cells.

3.2. Caspase-3 and Bcl-2 Family Proteins Are Involved in Autoregulatory Feedback of P38MAPK/Caspase-8 in TαPcZn-PDT-Induced Apoptosis of Bel-7402 Cells.

To determine whether Caspase-3 and Bcl-2 family are involved in autoregulatory feedback of P38MAPK/Caspase-8 during TαPcZn-PDT-induced apoptosis of Bel-7402 cells, effect of TαPcZn-PDT on Caspase-3, Bcl-2, and Bid, respectively, in the absence or presence of SB203580 or Ac-IEFD-CHO was investigated by immunoblot assay in the present study. Compared with the control treatment, TαPcZn-PDT resulted in upregulation of 17-kDa subunit of active Caspase-3, downregulation of Bcl-2, and upregulation of 15-kDa subunit of active Bid (Figure 4), suggesting that Caspase-3, Bcl-2, and Bid are involved in

TαPcZn-PDT-induced apoptosis of Bel-7402 cells. Furthermore, compared with the TαPcZn-PDT treatment, SB203580 or Ac-IEFD-CHO resulted in downregulation of 17-kDa subunit of active Caspase-3, upregulation of Bcl-2, and downregulation of 15-kDa subunit of active Bid (Figure 4), suggesting that autoregulatory feedback of P38MAPK/Caspase-8 might regulate Caspase-3, Bcl-2, and Bid in TαPcZn-PDT-induced apoptosis of Bel-7402 cells.

3.3. Mitochondrion Is Involved in Autoregulatory Feedback of P38MAPK/Caspase-8 in TαPcZn-PDT-Induced Apoptosis of Bel-7402 Cells.

To determine whether mitochondrion is involved in autoregulatory feedback of P38MAPK/Caspase-8 during TαPcZn-PDT-induced apoptosis of Bel-7402 cells, effect of TαPcZn-PDT on Cytochrome c and mitochondria membrane potential, respectively, in the absence or presence of SB203580 or Ac-IEFD-CHO was investigated by immunoblot assay and JC-1 assay of flow cytometry in the present study. Compared with the control treatment, TαPcZn-PDT resulted in upregulation of Cytochrome c and a decrease in ratio of red to green fluorescence intensity, suggesting that release of Cytochrome c from mitochondria and disruption of mitochondrial membrane potential are involved in TαPcZn-PDT-induced apoptosis of Bel-7402 cells (Figure 5). Furthermore, compared with the TαPcZn-PDT treatment, SB203580 or Ac-IEFD-CHO resulted in downregulation of Cytochrome c and an increase in ratio of red to green fluorescence intensity (Figure 5), suggesting that autoregulatory feedback of P38MAPK/Caspase-8 might regulate mitochondria in TαPcZn-PDT-induced apoptosis of Bel-7402 cells.

4. Discussion

Accumulated evidences have suggested that P38MAPK and Caspase-8 are involved in phthalocyanines-PDT-induced apoptosis of cancer cells [14, 15, 18]. Our previous study has showed that TαPcZn-PDT can apparently induce apoptosis of Bel-7402 cells [11]. However, it is unclear whether autoregulatory feedback of P38MAPK/Caspase-8 is essential for TαPcZn-PDT-induced apoptosis of Bel-7402 cells. Therefore, effect of TαPcZn-PDT on P38MAPK, p-P38MAPK, and Caspase-8, respectively, in TαPcZn-PDT-induced apoptosis of Bel-7402 cells without or with SB203580 or Ac-IEFD-CHO was firstly investigated in the present study. The result showed that TαPcZn-PDT caused activation of P38MAPK and Caspase-8, but SB203580 or Ac-IEFD-CHO, respectively, resulted in downregulation of active P38MAPK and Caspase-8, suggesting that activation of P38MAPK and Caspase-8 might be involved in TαPcZn-PDT-induced apoptosis of Bel-7402 cells. Furthermore, to confirm whether Caspase-8 and P38MAPK regulate apoptosis in TαPcZn-PDT-treated Bel-7402 cells, effect of SB203580 or Ac-IEFD-CHO on apoptosis, respectively, was investigated in the present study. The results showed that TαPcZn-PDT apparently induced apoptosis, but SB203580 or Ac-IEFD-CHO attenuated apoptosis of Bel-7402 cells in TαPcZn-PDT-treated cells, suggesting that activated P38MAPK and

Caspase-8 are essential for TαPcZn-PDT-induced apoptosis of Bel-7402 cells. Accumulated evidences have suggested that Caspase-8 regulates P38MAPK or P38MAPK regulates Caspase-8 in drugs-induced apoptosis of cancer cells [25–27]. However, it is unclear whether autoregulatory feedback of P38MAPK/Caspase-8 is involved in TαPcZn-PDT-induced apoptosis of Bel-7402 cells. Therefore, effect of SB203580 on Caspase-8 and effect of Ac-IEFD-CHO on P38MAPK were further investigated in the present study. The results showed that SB203580 attenuated activation of Caspase-8 and that Ac-IEFD-CHO attenuated activation of P38MAPK in TαPcZn-PDT-induced apoptosis of Bel-7402 cells, suggesting that autoregulatory feedback of P38MAPK/Caspase-8 might modulate TαPcZn-PDT-induced apoptosis of Bel-7402 cells. All of the above results suggest that autoregulatory feedback of P38MAPK/Caspase-8 is essential for TαPcZn-PDT-induced apoptosis of Bel-7402 cells.

Several studies have demonstrated that Caspase-3, Bcl-2 family proteins, and mitochondria are involved in phthalocyanines-PDT-induced apoptosis of cancer cells [18–22]. Our previous study has showed that Bcl-2 is involved in TαPcZn-PDT-induced apoptosis of Bel-7402 cells [11]. However, it is not clear whether Caspase-3, Bid, and mitochondria were involved in TαPcZn-PDT-induced apoptosis of Bel-7402 cells. Therefore, effect of TαPcZn-PDT on Caspase-3, Bid, Cytochrome c, and mitochondria membrane potential, respectively, in TαPcZn-PDT-induced apoptosis of Bel-7402 cells was firstly investigated in the present study. The result showed that TαPcZn-PDT apparently resulted in activation of Caspase-3 and Bid, release of Cytochrome c from mitochondria, and disruption of mitochondrial membrane potential, suggesting that Caspase-3, Bid, and mitochondria might modulate TαPcZn-PDT-induced apoptosis of Bel-7402 cells. Accumulated evidences have suggested that Caspase-3, Bcl-2 family proteins, and mitochondria are downstream of P38MAPK [27–30] or Caspase-8 [31–33]. However, it is unclear whether autoregulatory feedback of P38MAPK/Caspase-8 can regulate Caspase-3, Bcl-2, Bid, and mitochondria in TαPcZn-PDT-induced apoptosis of Bel-7402 cells. Therefore, effect of TαPcZn-PDT on Caspase-3, Bcl-2, Cytochrome c, and mitochondrial membrane potential, respectively, in the presence of SB203580 or Ac-IEFD-CHO was investigated in the present study. The results showed that SB203580 or Ac-IEFD-CHO attenuated activation of Caspase-3 and Bid, downregulation of Bcl-2, release of Cytochrome c from mitochondria, and disruption of mitochondrial membrane potential, suggesting that Caspase-3, Bcl-2 family proteins, and mitochondria are involved in autoregulatory feedback of P38MAPK/Caspase-8 during TαPcZn-PDT-induced apoptosis of Bel-7402 cells.

Taken together, our findings demonstrate that Caspase-3, Bcl-2, Bid, and mitochondria are involved in autoregulatory feedback of P38MAPK/Caspase-8 during TαPcZn-PDT-induced apoptosis of Bel-7402 cells.

Conflict of Interests

The authors do not have any conflict of interests with the content of the paper.

References

[1] A. Kamkaew, S. H. Lim, H. B. Lee, L. V. Kiew, L. Y. Chung, and K. Burgess, "BODIPY dyes in photodynamic therapy," *Chemical Society Reviews*, vol. 42, pp. 77–88, 2013.

[2] R. Vallinayagam, J. Weber, and R. Neier, "Novel bioconjugates of aminolevulinic acid with vitamins," *Organic Letters*, vol. 10, no. 20, pp. 4453–4455, 2008.

[3] H. Xu, C. Liu, J. Mei et al., "Effects of light irradiation upon photodynamic therapy based on 5-aminolevulinic acid-gold nanoparticle conjugates in K562 cells via singlet oxygen generation," *International Journal of Nanomedicine*, vol. 7, pp. 5029–5038, 2012.

[4] L. Lilge, M. Portnoy, and B. C. Wilson, "Apoptosis induced in vivo by photodynamic therapy in normal brain and intracranial tumour tissue," *British Journal of Cancer*, vol. 83, no. 8, pp. 1110–1117, 2000.

[5] H. Lu, W. Syu, N. Nishiyama, K. Kataoka, and P. Lai, "Dendrimer phthalocyanine-encapsulated polymeric micelle-mediated photochemical internalization extends the efficacy of photodynamic therapy and overcomes drug-resistance in vivo," *Journal of Controlled Release*, vol. 155, no. 3, pp. 458–464, 2011.

[6] S. Cui, D. Yin, Y. Chen et al., "In vivo targeted deep-tissue photodynamic therapy based on near-infrared light triggered upconversion nanoconstruct," *ACS Nano*, vol. 7, pp. 676–688, 2013.

[7] M. Laranjo, A. C. Serra, M. Abrantes et al., "2-bromo-5-hydroxyphenylporphyrins for photodynamic therapy: photosensitization efficiency, subcellular localization and in vivo studies," *Photodiagnosis and Photodynamic Therapy*, vol. 10, pp. 51–61, 2013.

[8] Z. A. Carneiro, J. C. B. de Moraes, F. P. Rodrigues et al., "Photocytotoxic activity of a nitrosyl phthalocyanine ruthenium complex—a system capable of producing nitric oxide and singlet oxygen," *Journal of Inorganic Biochemistry*, vol. 105, no. 8, pp. 1035–1043, 2011.

[9] K. Sutoris, J. Rakusan, M. Karaskova et al., "Novel topical photodynamic therapy of prostate carcinoma using hydroxy-aluminum phthalocyanine entrapped in liposomes," *Anticancer Research*, vol. 33, pp. 1563–1568, 2013.

[10] S. G. Kimani, T. A. Shmigol, S. Hammond et al., "Fully protected glycosylated zinc (II) phthalocyanine shows high uptake and photodynamic cytotoxicity in MCF-7 cancer cells," *Photochemistry and Photobiology*, vol. 89, pp. 139–149, 2013.

[11] C. Xia, Y. Wang, W. Chen, W. Yu, B. Wang, and T. Li, "New hydrophilic/lipophilic tetra-α-(4-carboxyphenoxy) phthalocyanine zinc-mediated photodynamic therapy inhibits the proliferation of human hepatocellular carcinoma Bel-7402 cells by triggering apoptosis and arresting cell cycle," *Molecules*, vol. 16, no. 2, pp. 1389–1401, 2011.

[12] Z. Zhao, P. Chan, H. Li et al., "Highly selective mitochondria-targeting amphiphilic silicon(IV) phthalocyanines with axially ligated rhodamine B for photodynamic therapy," *Inorganic Chemistry*, vol. 51, no. 2, pp. 812–821, 2012.

[13] R. M. Amin, C. Hauser, I. Kinzler, A. Rueck, and C. Scalfi-Happ, "Evaluation of photodynamic treatment using aluminum

phthalocyanine tetrasulfonate chloride as a photosensitizer: new approach," *Photochemical and Photobiological Sciences*, vol. 11, pp. 1156–1163, 2012.

[14] L. Xue, J. He, and N. L. Oleinick, "Promotion of photodynamic therapy-induced apoptosis by stress kinases," *Cell Death and Differentiation*, vol. 6, no. 9, pp. 855–864, 1999.

[15] C. M. Whitacre, D. K. Feyes, T. Satoh et al., "Photodynamic therapy with the phthalocyanine photosensitizer Pc 4 of SW480 human colon cancer xenografts in athymic mice," *Clinical Cancer Research*, vol. 6, no. 5, pp. 2021–2027, 2000.

[16] N. A. Thornberry and Y. Lazebnik, "Caspases: enemies within," *Science*, vol. 281, no. 5381, pp. 1312–1316, 1998.

[17] L. E. Broker, F. A. E. Kruyt, and G. Giaccone, "Cell death independent of caspases: a review," *Clinical Cancer Research*, vol. 11, no. 9, pp. 3155–3162, 2005.

[18] L. Xue, S. Chiu, and N. L. Oleinick, "Differential responses of Mcl-1 in photosensitized epithelial vs lymphoid-derived human cancer cells," *Oncogene*, vol. 24, no. 46, pp. 6987–6992, 2005.

[19] J. Shao, J. Xue, Y. Dai et al., "Inhibition of human hepatocellular carcinoma HepG2 by phthalocyanine photosensitiser ZnPcS2P2: ROS production, apoptosis, cell cycle arrest," *European Journal of Cancer*, vol. 48, pp. 2086–2096, 2012.

[20] C. M. H. Chan, P. Lo, S. Yeung, D. K. P. Ng, and W. Fong, "Photodynamic activity of a glucoconjugated silicon(IV) phthalocyanine on human colon adenocarcinoma," *Cancer Biology and Therapy*, vol. 10, no. 2, pp. 126–134, 2010.

[21] M. E. Rodriguez, P. Zhang, K. Azizuddin et al., "Structural factors and mechanisms underlying the improved photodynamic cell killing with silicon phthalocyanine photosensitizers directed to lysosomes versus mitochondria," *Photochemistry and Photobiology*, vol. 85, no. 5, pp. 1189–1200, 2009.

[22] H. Huang, X. Zhao, Y. Chen, R. Lu, and Y. Wu, "Apoptosis induced by ZnPcH1-based photodynamic therapy in Jurkat cells and HEL cells," *International Journal of Hematology*, vol. 94, no. 6, pp. 539–544, 2011.

[23] H. Y. Wu, W. Chen, T. Li, Y. Wang, C. H. Xia, and X. L. Li, "Study on synthesis and antineoplastic activity of α-tetra-(4-carboxyphenoxy)phthalocyanine zinc," *Journal of Liaoning Normal University. Natural Science Edition*, vol. 32, pp. 94–97, 2009.

[24] M. C. Bi, R. Rosen, R. Y. Zha, S. A. McCormick, E. Song, and D. N. Hu, "Zeaxanthin induces apoptosis in human uveal melanoma cells through Bcl-2 family proteins and intrinsic apoptosis pathway," *Evidence-Based Complementary and Alternative Medicine*, vol. 2013, Article ID 205082, 12 pages, 2013.

[25] A. M. M. Kober, S. Legewie, C. Pforr et al., "Caspase-8 activity has an essential role in CD95/Fas-mediated MAPK activation," *Cell Death and Disease*, vol. 2, no. 10, article e212, 2011.

[26] S. J. Kang, B. M. Kim, Y. J. Lee, S. H. Hong, and H. W. Chung, "Titanium dioxide nanoparticles induce apoptosis through the JNK/p38-caspase-8-Bid pathway in phytohemagglutinin-stimulated human lymphocytes," *Biochemical and Biophysical Research Communications*, vol. 386, no. 4, pp. 682–687, 2009.

[27] L. D. Huong, J.-A. Shin, E.-S. Choi et al., "β-phenethyl isothiocyanate induces death receptor 5 to induce apoptosis in human oral cancer cells via p38," *Oral Diseases*, vol. 18, no. 5, pp. 513–519, 2012.

[28] L. Yuan, J. Wang, H. Xiao, W. Wu, Y. Wang, and X. Liu, "MAPK signaling pathways regulate mitochondrial-mediated apoptosis induced by isoorientin in human hepatoblastoma cancer cells," *Food and Chemical Toxicology*, vol. 53, pp. 62–68, 2013.

[29] J. Yu, Z. Zheng, Y. Son, X. Shi, Y. Jang, and J. Lee, "Mycotoxin zearalenone induces AIF- and ROS-mediated cell death through p53- and MAPK-dependent signaling pathways in RAW264.7 macrophages," *Toxicology in Vitro*, vol. 25, no. 8, pp. 1654–1663, 2011.

[30] L. Cipak, "Novel nonclassical antifolate, 2-[N-(2′-Hydroxyethyl)amino]methyl-3H-quinazolin-4-one, with a potent antineoplastic activity toward leukemia cells," *Neoplasma*, vol. 59, pp. 641–649, 2012.

[31] H. J. Cho, S. Y. Park, E. J. Kim, J. Kim, and J. H. Y. Park, "3,3′-diindolylmethane inhibits prostate cancer development in the transgenic adenocarcinoma mouse prostate model," *Molecular Carcinogenesis*, vol. 50, no. 2, pp. 100–112, 2011.

[32] M. Lin, Y. Lu, H. Su et al., "Destabilization of CARP mRNAs by aloe-emodin contributes to caspase-8-mediated p53-independent apoptosis of human carcinoma cells," *Journal of Cellular Biochemistry*, vol. 112, no. 4, pp. 1176–1191, 2011.

[33] J. J. Choi, O. Kwon, S. Oh, H. Lee, and K. Ahn, "The effect of isolancifolide on the apoptosis in HL-60 cells through caspase-8-dependent and -independent pathways," *Archives of Pharmacal Research*, vol. 35, no. 1, pp. 137–143, 2012.

Review Article

Overview on Topical 5-ALA Photodynamic Therapy Use for Non Melanoma Skin Cancers

Carmen Cantisani, Giovanni Paolino, Valentina Faina, Federica Frascani, Franca Cantoresi, Daniela Bianchini, Gilda Fazia, and Stefano Calvieri

Department of Dermatology, "Sapienza" University of Rome, Policlinico Umberto I, Viale del Policlinico 15, 00186 Rome, Italy

Correspondence should be addressed to Carmen Cantisani; carmencantisanister@gmail.com

Ultraviolet radiation (UV) contributes to a variety of skin diseases including inflammation, degenerative aging, and cancer. Historically, humans have been exposed to UV radiation mainly through occupational exposure; recreational UV exposure, however, has increased dramatically in recent years, because of outdoor leisure activities and to purposely tan for cosmetic purposes. Both UVB and UVA radiation have been shown to cause DNA damage and immunosuppression, the important forms of biological damage that lead to NMSC. Nonmelanoma skin cancer (NMSC) is the most common malignancy, whose public health significance is often unrecognized which continues to grow at an alarming rate, becoming an occupational disease. Available treatments alternative to surgery include photodynamic therapy, electrochemotherapy, cryotherapy, ablative lasers, 5-fluorouracil, imiquimod, ingenol mebutate, and diclofenac. Among these, photodynamic therapy is a noninvasive technique with excellent cosmetic outcome and good curative results, when used in initial stages of skin cancers for superficial lesions. It is administered under numerous and significantly varied regimens and there are a wide range of cure rates reported, permitting treatment of large and multiple lesions with excellent cosmetic results. This is an overview of photodynamic applications especially for the treatment of NMSC, with a short focus on daylight modality.

1. Introduction

UV energy can be subdivided into UV-A, UV-B, and UV-C components based on electrophysical properties, with UV-C photons having the shortest wavelengths (100–280 nm) and highest energy, UV-A having the longest (315–400 nm), but least energetic photons, and UV-B falling in between. Each component of UV can exert a variety of effects on cells, tissues, and molecules. Not surprisingly, skin cancer risk generally mirrors this geographic pattern, particularly among fair-skinned sun-sensitive persons. One of the greatest risk factors for the development of cutaneous melanoma is having a fair skin complexion, which is characterized by low levels of a UV-blocking dark pigment called eumelanin in the epidermis. Individuals with light skin pigmentation suffer comparatively more skin damage from UV, because it is relatively easy for UV rays to penetrate the epidermis to damage both keratinocytes and melanocytes in the deeper layers of the epidermis. Fair-skinned individuals are exposed

to higher-realized doses of UV radiation in the skin and UV-induced mutations, which directly contribute to melanoma and other forms of skin cancer, accumulating over time. Much UV-induced pathology, including skin cancer, can be avoided by minimizing UV exposure [1].

Nonmelanoma skin cancer (NMSC) is the most common malignancy, whose public health significance is often unrecognized. They comprise more than one-third of all cancers and are increasing worldwide, causing a significant economic burden at the individual and community levels. The most common NMSCs are basal cell carcinoma (BCC) and squamous cell carcinoma (SCC), occurring at a ratio of about 4 : 1 and accounting for about 90% of all skin cancers diagnosed globally. As these cancers are not reported to cancer registries in most countries, precise statistics are generally not available. However, it is estimated that between two and three million people are diagnosed worldwide each year, with an average annual increase of 3% to 8% in white

populations in Australia, Europe, United States, and Canada over the last 30 years. The global incidence rates vary by skin complexion and geographical region and are expected to continue to rise in the coming years, due to growing exposure to ultraviolet (UV) sunlight associated with increased sun-seeking behaviors and depletion of stratospheric ozone. Phenotype characteristics, environmental exposures, and genetic predisposition appear to be risk factors for their development and progression. Early detection through established methods or newer technologies is critical for reducing both skin cancer mortality and the overall skin cancer burden [1, 2].

2. Photodynamic Therapy

Topical photodynamic therapy (PDT) broadband red light source 570–670 nm is acknowledged to be an effective and safe treatment for NMSCs with favorable cosmetic outcomes. PDT involves the topical application of a photosensitizer, 5-aminolevulinic acid (ALA), or its methyl ester-methyl aminolevulinate (MAL) which are precursor of the endogenous photosensitizer Protoporphyrin IX and subsequent illumination of the skin lesion with light of the appropriate wavelength. In Europe, currently, only MAL is approved for the treatment of AKs, but it is significantly more expensive than ALA and therefore ALA is being used widely off label. It is a useful nonsurgical treatment option for actinic keratosis (AK), basal cell carcinoma (BCC), and in situ squamous cell carcinoma (Bowen disease), especially at sites that are cosmetically sensitive or prone to impaired wound healing [3]. It is a rapidly evolving form of phototherapy using nontoxic light-sensitive compounds that are exposed selectively to light, whereupon they become toxic to targeted malignant and other diseased cells, and it has proven ability to kill microbial cells, including bacteria, fungi and viruses (warts and molluscum contagiosum). It is used clinically to treat a wide range of medical conditions, including acne, skin aging, psoriasis, granuloma annulare, age-related macular degeneration and malignant cancers, CTCL, and extramammary Paget disease and is recognized as a treatment strategy which is both minimally invasive and minimally toxic [4–7]. The combination of photosensitizer, a light source and tissue oxygen, leads to the chemical destruction of any tissues which have either selectively taken up the photosensitizer or have been locally exposed to light, with recruitment of inflammatory cells, increased immune response, and vascular compromise. Single oxygen can also destroy photosensitizing agent itself preventing further action, a process referred to as photobleaching. The wavelength of the light source needs to be appropriate for exciting the photosensitizer to produce reactive oxygen species. These reactive oxygen species generated through PDT are free radicals (Type I PDT) generated through electron abstraction or transferred from a substrate molecule and highly reactive state of oxygen known as singlet oxygen (Type II PDT). In understanding the mechanism of PDT it is important to distinguish it from other light-based and laser therapies such as laser wound healing and rejuvenation, or intense pulsed light hair removal, which do not require a photosensitizer [3, 8].

3. History

While the applicability and potential of PDT have been known for over a hundred years, the development of modern PDT has been a gradual one, involving scientific progress in the fields of photobiology and cancer biology, as well as the development of modern photonic devices, such as lasers and LEDs. John Toth, in 1981, acknowledged the "photodynamic chemical effect" of the therapy and wrote the first "white paper" branding the therapy as "Photodynamic Therapy" (PDT). PDT received even greater interest as result of Thomas Dougherty helping expand clinical trials and forming the International Photodynamic Association, in 1986 [3, 9].

4. PDT in Ancient Medicine

The earliest recorded treatments that exploited a photosensitizer and a light source, in this case sunlight, for medical effect can be found in ancient Egyptian and Indian sources. Annals over 3000 years report the use of topically applied vegetable and plant substances to produce photoreactions in skin and cause a repigmentation of depigmented skin lesions, as seen with vitiligo and leukoderma. The photosensitizing agents used in these ancient therapies have been characterised with modern science as belonging to the psoralen family of chemicals. Psoralens are still in use today in PDT regimes to treat a variety of skin conditions, including vitiligo, psoriasis, neurodermitis, eczema, cutaneous T-cell lymphoma, and lichen ruber planus now called "PUVA-therapy" [10].

5. 20th Century Development of PDT

The first detailed scientific evidence that agents, photosensitive synthetic dyes, in combination with a light source and oxygen could have potential therapeutic effect was made at the turn of the 20th century in the laboratory of von Tappeiner in Munich, Germany. Historically this was a time when Germany was leading the world in the industrial synthesis of dyes.

While studying the effects of acridine on paramecia cultures, Oscar Raab, a student of von Tappeiner observed a toxic effect. Fortuitously Raab also observed that light was responsible for the killing of paramecia cultures to take place. Subsequent work in the laboratory of von Tappeiner showed that oxygen was essential for the "photodynamic action"—a term coined by von Tappeiner.

With the discovery of photodynamic effects, von Tappeiner and colleagues went on to perform the first PDT trial on patients with skin carcinoma using the photosensitizer, eosin. Out of 6 patients with a facial basal cell carcinoma, treated with a 1% eosin solution and a long-term exposure either to sunlight or to arc-lamp light, 4 patients showed total tumour resolution and a relapse-free period of 12 months.

It was only much later when Thomas Dougherty and coworkers at Roswell Park Cancer Institute, Buffalo NY, clinically tested PDT again. In 1978, they published striking results in which they treated 113 cutaneous or subcutaneous malignant tumors and observed a total or partial resolution

of 111 tumors. The active photosensitizer used in the clinical PDT trial by Dougherty was an agent called hematoporphyrin Derivative (HpD), which was first characterized in 1960 by Lipson. In his research, Lipson wanted to find a diagnostic agent suitable for the detection of tumours in patients. With the discovery of HpD, Lipson went onto pioneering the use of endoscopes and HpD fluorescence to detect tumours. As its name suggests, HpD is a porphyrin species derived from hematoporphyrin. Porphyrins have long been considered as suitable agents for tumour photodiagnosis and tumour PDT because cancerous cells exhibit a significantly greater uptake and affinity for porphyrins compared to normal quiescent tissues. This important observation, which underlies the success of PDT to treat cancers, had been established by a number of scientific researchers prior to the discoveries made by Lipson. In 1924, Policard first revealed the diagnostic capabilities of hematoporphyrin fluorescence when he observed that ultraviolet radiation excited red fluorescence in the sarcomas of laboratory rats. Policard hypothesized at that time that the fluorescence was associated with endogenous hematoporphyrin accumulation. In 1948, Figge with coworkers showed on laboratory animals that porphyrins exhibit a preferential affinity to rapidly dividing cells, including malignant, embryonic, and regenerative cells, and because of this, they proposed that porphyrins should be used in the treatment of cancer. Subsequently many scientific authors have repeated the observation that cancerous cells naturally accumulate porphyrins and have characterised a number of mechanisms to explain it.

HpD, under the pharmaceutical name Photofrin, was the first PDT agent approved for clinical use in 1993 to treat a form of bladder cancer in Canada. Over the next decade, both PDT and the use of HpD received wider international attention and grew in their clinical use, and lead to the first PDT treatments to receive U.S. Food and Drug Administration approval. Of all the nations beginning to use PDT in the late 20th century, the Russians were the quickest to advance its use clinically and to make many developments. Around this time, Russian scientists also collaborated with NASA medical scientists who were looking at the use of LEDs as more suitable light sources, compared to lasers, for PDT applications. PDT has also seen considerable development in Asia. Since 1990, the Chinese have been developing specialist clinical expertise with PDT using their own domestically produced photosensitizers, derived from hematoporphyrin, and light sources. PDT in China is especially notable for the technical skill of specialists in effecting resolution of difficult to reach tumours [11].

6. Procedure

In order to achieve the selective destruction of the target area using PDT while leaving normal tissues untouched, either the photosensitizer can be applied locally to the target area or photosensitive targets can be locally excited with light. For instance, in the treatment of skin conditions, including acne, psoriasis, and also skin cancers, the photosensitizer can be applied topically and locally excited by a light source. In the local treatment of internal tissues and cancers, after

photosensitizers have been administered intravenously, light can be delivered to the target area using endoscopes and fiber optic catheters. Photosensitizers can also target many viral and microbial species, including HIV and MRSA. Using PDT, pathogens present in samples of blood and bone marrow can be decontaminated before the samples are used further for transfusions or transplants. PDT can also eradicate a wide variety of pathogens of the skin and of the oral cavities. Given the seriousness that drug resistant pathogens have now become, there is increasing research into PDT as a new antimicrobial therapy. Compared to normal tissues, most types of cancers are especially active in both the uptake and accumulation of photosensitizer agents, which makes cancers especially vulnerable to PDT. Since photosensitizers can also have a high affinity for vascular endothelial cells the net result is both the direct tumor cell death and a shutdown of the tumor vasculature. Therefore hypoxic regions of tumors are insensitive to PDT. O_2 is the predominant actor of the photokilling. PDT is intended to kill malignant cells, with apoptotic or necrotic death and autophagy. It is not entirely clear which pathways to cell death are more effective. As new photosensitizer agents are developed an examination of their localization patterns and photochemistry may aid in the selection of optimal agents for tumor eradication [3, 4, 8].

Methyl aminolevulinate (MAL) is a porphyrin precursor approved for the treatment of actinic keratoses (AKs) of the face and scalp [12–14]. The approved protocol combines topical application of MAL to individual lesions under occlusion for 3 hours followed by 37 J/cm^2 of red light. PpIX is then activated by red light, resulting in damage and killing of the diseased cells. In order to simplify the treatment procedure and improve tolerability, effect of daylight exposure was observed [3, 15, 16]. Instead of fast activation of large amounts of PpIX accumulated after occlusive treatment with MAL, it was thought that continuous activation of PpIX during its development might be just as efficient. The red and blue light required to activate porphyrins are part of the daylight spectrum. PDT treatment with daylight would make the treatment much easier, as the patient would not have to come back to the clinic after 3 h to be illuminated but we would like to add that after almost 30 minutes under artificial light patients can go under visible light and go back home. The continuous activation of small amounts of PpIX could possibly reduce treatment-related pain, which is the only acute severe adverse effect of PDT [4, 5]. The aim of this study was to compare conventional MAL-PDT using red light-emitting diode (LED) lamps with MAL-PDT without occlusive treatment and illumination with daylight, with the primary endpoint being complete response rates of AK. The adverse effects of the treatments were assessed as secondary endpoints.

7. Treatment of NMSC

Internationally licensed for the treatment of NMSC, PDT is indicated for superficial and multiple lesions, especially in the case of multifocal lesions, unclear lesion edges, risk of keloids or surgical risk factors. Red light in BCC has a superior

penetration compared to blue and green, although experience is limited. Bowen disease has an effective result with good cosmetic results as effective as 5-FU, imiquimod 5%, with fewer side effects, as BCCs; nodular BCC < 2 mm can be effective, while insufficient evidence after SCC, which can have Greater results with imiquimod 5%, excision and Mohs surgery. For nBCCs 3 to 6 h of incubation are needed; better results are seen combining different treatments, as topical treatments, CO_2 laser, fractional laser, curettage, and debulking 1 week before treatment and iron chelation (CP94) to increase chelation of PpIX reducing its bioconversion to heme, which is able to reduce tumor penetration. Pigmented lesions respond poorly because of interference of melanin. Many reports showed efficacy in the treatment of erythroplasia of Queyrat [17, 18].

8. Photorejuvenation

The visible signs of photodamage are characterized by wrinkling, coarse skin texture, pigmentation alterations, telangiectases, and case actinic keratosis (AKs). Intense pulsed light (IPL) photorejuvenation has been shown to improve each of the different components of photodamaged skin. Photodynamic therapy with topical 5-aminolevulinic acid (ALA-PDT) may be made also using IPL as a light source for treatment of AK. They can therefore now be treated as part of the photorejuvenation process rather than necessitating separate topical therapy with 5-fluorouracil (5-FU) or cryotherapy [19, 20].

9. Photosensitizer Licensed for Mild to Moderate AKs on Face and Scalp

The effectiveness of PDT depends on the photosensitizer used. New photosensitizer formulations have been developed

(i) Methyl aminolevulinate licensed in combination with red light 570–670 nm for a total dose of 75 J/cm² (metvix/Metvixia 16%) are not currently available in USA.

(ii) ALA licensed in combination with blue light (levulan kerastick 20%) approved for AK is the only agent approved in USA. It is a hydrophilic, low molecular weight molecule that is absorbed readily through abnormal but not from normal keratin.

(iii) ALA Patch (Alacare, 4 cm² containing 8 mg ALA) is recently licensed Europe.

Once ALA is absorbed by epidermal or appendage cells, it is converted to PpIX, a potent photosensitizer. Due to of limited supplies of iron, a necessary catalyst for ferrochelatase, recipient cells are unable to complete the final stage of conversion of PpIX to heme, leading to PpIX accumulation. With short application time (<4 hours) PpIX is largely limited to the target site. Photosensitizer typically resolves within 24 hours after application is completed. Maximal light absorption is seen at 409 nm, and smaller peaks occur at 509 nm, 584 nm, and 625 nm. FDA approved 14- to 18-hour application time; however studies have demonstrated efficacy with shorter incubation period (1 h), more convenient for patients and doctors. MAL is more lipophillic than ALA and improved tumor tissue specificity while it was almost similar for penetration. Except for Methyl aminolevulinate the others are new formulations for AK treatment, with different light sources. New indications (not yet approved) are for actinic cheilitis, acral AK and AK in immunosupred patients, combination therapy for AK treatment [12, 18, 21].

10. New Concepts for Illumination Are Being Investigated

Both ALA and MAL lead to the production of PpIX, which displays a large peak in absorption spectra at 409 nm, with much smaller peak at 509 nm, 584 nm, and 625 nm. While blue light BluU (DUSA Pharmaceuticals, Wilmington, MA) or Omnilux Blue (Photo Therapeutics Inc., Carlsbad, CA) takes advantage of the largest absorption spike at 417 nm, it is limited by depth of penetration to about 1.5 to 2 mm. Red light >600 nm requires higher energy levels to achieve the same effect, but it is able to penetrate deeper (8–10 mm). Filtered red or green noncoherent light sources are commonly used in Europe, whereas in USA longer wavelength light sources include diode and pulsed dye lasers as well as intense pulsed light (IPL) [16, 18].

5-ALA-patch for PDT of AK self-adhesive, skin coloured ALA-Patch (2 mg/cm² ALA) easy handling application in one step, and built-in occlusion. There was no lesion preparation on treatment session. Efficacy and side effects were comparable with other photosensitizers. Nano-emulsion-based ALA formulation (BF-200) for AK phase III study using BF-200 ALA (10% ALA in gel matrix to stabilize ALA and to improve penetration); 3 h of incubation, illumination with Aktilite (37 J/cm² 50–70 mW/cm²), or Photodyn 750 (broad band lamps 170 J/cm²), 1-2tx better efficacy. New concepts for illumination are being investigated such as PDT of AK using different incoherent light sources which were evaluated, ALA, or MAL PDT with LED (633 ± 3 nm, 40 J/cm²) versus incoherent lamp (580–700 nm, 100 J/cm², 160 mW/cm²); no difference regarding efficacy, pain, patient satisfaction, and cosmetic results was seen. MAL-PDT with red light (633 ± 3 nm, 37 J/cm², 50 mW/cm²) versus IPL (610–950 nm filtered band piece 80 J/cm²), have no difference in term of efficacy but significantly less pain with IPL. Gold standards are incoherent broadband lamps or LEDs; more studies are needed to prove efficacy of IPL. MAL-PDT is not as effective for AK on extremities, probably due to the absence of pilosebaceous glands. PDT can be used as chemoprevention in transplanted patients [22].

11. Limits of the Procedure

Tumour resistance and recurrence rates after PDT are however reported to range from 10 to 45%. Treatment failure in PDT is thought to be multifactorial, with insufficient tumour uptake of photosensitizer and PDT-induced suppression of cutaneous antitumour responses, potentially

important contributors for incomplete tumour killing [23]. Antitumour immunity plays a key role in reducing skin cancer development and also in skin cancer treatment responses. Immune-suppressed organ transplant recipients have significantly higher PDT failure rates compared with immunocompetent controls. The immune suppressive effects of PDT have been reported in mice and recently in humans. At the light doses and irradiance rates in current clinical use, topical PDT causes significant suppression of delayed-type hypersensitivity responses to recall antigens and depletes Langerhans cells in both normal human skin and within BCCs. The immune effects of PDT are sensitive to changes in irradiance rate; while light delivered at a high irradiance rate (approximately 75 mW cm) as in clinical practice is highly immune suppressive, delivery of the same total light dose at a lower irradiance rate (15 mW cm) does not cause significant immune suppression in healthy volunteers. Oxidative DNA photolesions, observed in ex vivo human skin after high, but not low irradiance rate PDT, may be a key trigger of PDT-induced immunosuppression. The main disadvantage of PDT is that it can be painful, limiting its applicability [18, 24], which can be due to PpIX concentration, fluence rate, wavelength, treatment area size, location, sex, photosensitizer used, skin type, age, and lesion type. Pain is the major drawback of photodynamic therapy (PDT), an otherwise effective treatment for actinic keratoses (AKs). Pain is a frequent side effect of PDT. It is largely unpredictable and a major drawback of the treatment. It varies from patient to patient and the experience of burning, stinging, and prickling sensation ranges from mild to severe. In order to find the best pain prevention, investigators have tried to identify susceptible patients. In the last decade especially, there has been a spate of articles concerned with pain and PDT. Various factors have been identified to have influence on pain, but none of them has been consistently reported in all publications. Pain during PDT is associated with AK location and size. Treatment of bigger lesions (>130 mm^2) results in more pain than smaller ones and treatment of the face is more painful than the scalp area. It is explained by tissue hypoxia and/or singlet oxygen generation, increasing the amount of pain experienced during PDT. However, other studies support our findings that the beginning of the procedure is most painful and pain is more intensive during the first procedure than during the second [24]. Pain diminution might be explained by desensitization of nociceptors, acclimatization to the treatment situation, or decreasing levels of photosensitizer during the treatment. This would indicate that pain is related to the photodynamic process itself in a time and dose dependent fashion [25]. Usually no association between the pain and the treatment dose are observed. Though Radakovic-Fijan observed a trend toward higher doses causing more pain, the finding was not statistically significant. Photodynamic therapy (PDT) is an effective but time-consuming and often painful treatment for NMSC. Daylight is the combination of direct and diffuse sunlight outdoors during daytime [15, 25]. The spectrum of electromagnetic radiation striking the earth's atmosphere is the ultraviolet light ranging from 1000 to 380 nm, visible light from 380 to 780 nm, and infrared

light ranging from 780 nm to 10^6 nm. Home-based daylight-PDT has the potential to facilitate treatment procedure and to reduce associated pain due to continuous activation of small amounts of porphyrins. Moreover, a reduced methyl aminolevulinate (MAL) concentration may reduce associated inflammation, making the treatment more tolerable for the patients. The procedure is characterized by curettage of lesions, application of medium (20–30 SPF) sun block, or photolyase inhibitors on the whole exposed area both treated and untreated; ask the patient to wait in an artificial light place for 20–30 minutes and then go under daylight from 1.5 to 2.5 hours, or the whole day under sunlight, then wash off the cream with thermal spring water, from the treated area, apply a pain relief cream exactly after PDT, and go on twice daily for 10 to 20 days, to reduce itching and burning sensation. Home-based daylight-mediated MAL-PDT was an effective and well-tolerated treatment in sun exposed areas. Pain is the major drawback of photodynamic therapy (PDT), an otherwise effective treatment for actinic keratoses (AKs). Pain during PDT is associated with AK location and size. PDT performed following MAL application to the entire face is not only more convenient but offers the potential of preventing new AKs. In order to simplify the treatment procedure and improve tolerability, effect of daylight exposure was observed [15]. Instead of fast activation of large amounts of PpIX accumulated after occlusive treatment with MAL, it was thought that continuous activation of PpIX during its development might be just as efficient. The red and blue light required to activate porphyrins are part of the daylight spectrum. PDT treatment with daylight would make the treatment much easier, as the patient would not have to come back to the clinic after 3 h to be illuminated but they can just go under visible light after almost 30 minutes. The continuous activation of small amounts of PpIX could possibly reduce treatment-related pain, which is the only acute severe adverse effect of PDT. Daylight-PDT would make the treatment independent of the clinic and less painful due to the continuous activation of small amounts of porphyrins during its formation. Due to the high incidence and the potential of the AK to become invasive SCC it is important to treat all of them and that their treatment be not only effective but also uncomplicated, without side effects and with good cosmetic results [21, 26]. With these results, clinicians can identify patients most likely to experience pain to provide them with timely and adequate pain-control approaches during PDT or personalize treatments according to age, gender, Fitzpatrick skin type, size, clinical grade and location of the AK, pretreatment fluorescence intensity, and the red light dose during the ALA-PDT for AKs treated on the face and scalp. The immune suppressive effects of topical photodynamic therapy (PDT) are potential contributors to treatment failure after PDT for nonmelanoma skin cancer. Nicotinamide (vitamin B3) prevents immune suppression by ultraviolet radiation, but its effects on PDT-induced immunosuppression are unknown. While the clinical relevance of these findings is currently unknown, nicotinamide may provide an inexpensive means of preventing PDT-induced immune suppression and enhancing PDT cure rates. Oral nicotinamide is well tolerated even at high doses

(up to approximately 3/5 g per day) with a lack of reported side effects. It can be considered as an inexpensive, convenient, and nontoxic agent for skin cancer chemoprevention [27].

New chemopreventive agents that can be used to complement sunscreens may result in decreased incidence, morbidity, and mortality of skin cancer. Therefore, further research is urgently required to find an ideal chemopreventive agent that is effective, safe, accessible, and convenient either topical or systemical.

12. Conclusion

NMSC, with their rapidly growing incidence, negatively influence quality of life; some of them can develop in more aggressive tumor, and therefore all of them need to be treated. Their treatment needs to be efficacious and easy to be performed. PDT is a safe and effective noninvasive treatment; MAL or ALA is an attractive, well established and approved, single day therapy for mild to moderate AK, actinic cheilitis, and superficial BCC (especially of the eyelid) on face, scalp, and some SCC [15, 24]. PDT may be the first treatment choice for multiple AK or field cancerisation on face and scalp with additional photorejuvenation effects. ALA-PDT using IPL as a light source is an effective treatment for both photorejuvenation and AKs [12]. For hypertrophic lesions a keratolityc agent applied before treatment and the curettage of lesions may help in improving absorption. However the conventional type is associated with inconveniently long clinic visits and discomfort during therapy; this may ride out with daylight mediated PDT, which is a simpler and more tolerable treatment procedure; it is nearly pain-free and more pleasant for both patients and physicians, especially for sun-exposed areas where there are multiple lesions, independent of the weather conditions [15, 16]. As BCC and nodular BCC are thicker lesions than AKs, the effective daylight dose, which effectively treats AK, might not provide enough red light to ensure effective activation of PpIX in the deeper part of the lesion, probably leaving MAL-PDT under occlusion for more than 5 hours especially on special anatomical area as periocular one and may lead to a higher local skin reaction, with consequent better results. As daylight PDT is nearly pain-free it is possible to treat larger areas than with conventional type; the clinical attendance is much shorter making the clinicians able to visit and treat more patients [21, 26]. Further studies will be needed to understand ideal condition of daylight PDT, for instance season, time, outdoor temperature, duration, geographical condition, and kind of lesions.

Conflict of Interests

The authors declare that there is no conflict of interests regarding the publication of this paper.

Acknowledgments

References

[1] M. A. Weinstock, "Epidemiology and UV exposure," *Journal of Investigative Dermatology*, vol. 133, no. E1, pp. E11–E12, 2013.

[2] T. L. Diepgen and V. Mahler, "The epidemiology of skin cancer," *British Journal of Dermatology*, vol. 146, supplement 61, pp. 1–6, 2002.

[3] C. A. Morton, K. E. McKenna, and L. E. Rhodes, "Guidelines for topical photodynamic therapy: update," *British Journal of Dermatology*, vol. 159, no. 6, pp. 1245–1266, 2008.

[4] M. R. Hamblin and T. Hasan, "Photodynamic therapy: a new antimicrobial approach to infectious disease?" *Photochemical and Photobiological Sciences*, vol. 3, no. 5, pp. 436–450, 2004.

[5] R. Sidi Boumédine and D. C. Roy, "Elimination of alloreactive T cells using photodynamic therapy," *Cytotherapy*, vol. 7, no. 2, pp. 134–143, 2005.

[6] I.-M. Stender, R. Na, H. Fogh, C. Gluud, and H. C. Wulf, "Photodynamic therapy with 5-aminolaevulinic acid or placebo for recalcitrant foot and hand warts: randomised double-blind trial," *The Lancet*, vol. 355, no. 9208, pp. 963–966, 2000.

[7] K. Kostović, Z. Pastar, R. Ceović, Z. B. Mokos, D. S. Buzina, and A. Stanimirović, "Photodynamic therapy in dermatology: current treatments and implications," *Collegium Antropologicum*, vol. 36, no. 4, pp. 1477–1481, 2012.

[8] E. Skovsen, J. W. Snyder, J. D. C. Lambert, and P. R. Ogilby, "Lifetime and diffusion of singlet oxygen in a cell," *Journal of Physical Chemistry B*, vol. 109, no. 18, pp. 8570–8573, 2005.

[9] Z. Huang, "A review of progress in clinical photodynamic therapy," *Technology in Cancer Research and Treatment*, vol. 4, no. 3, pp. 283–293, 2005.

[10] M. D. Daniell and J. S. Hill, "A history of photodynamic therapy," *Australian and New Zealand Journal of Surgery*, vol. 61, no. 5, pp. 340–348, 1991.

[11] R. Ackroyd, C. Kelty, N. Brown, and M. Reed, "The history of photodetection and photodynamic therapy," *Photochemistry and Photobiology*, vol. 74, no. 5, pp. 656–669, 2001.

[12] S. R. Wiegell, S. Fabricius, I. M. Stender et al., "A randomized, multicentre study of directed daylight exposure times of 11/2 vs. 21/2 h in daylight-mediated photodynamic therapy with methyl aminolaevulinate in patients with multiple thin actinic keratoses of the face and scalp," *British Journal of Dermatology*, vol. 164, no. 5, pp. 1083–1090, 2011.

[13] R. L. Lipson, E. J. Baldes, and M. J. Gray, "Hematoporphyrin derivative for detection and management of cancer," *Cancer*, vol. 20, no. 12, pp. 2255–2257, 1967.

[14] R. L. Lipson, E. J. Baldes, and A. M. Olsen, "The use of a derivative of hematoporhyrin in tumor detection," *Journal of the National Cancer Institute*, vol. 26, pp. 1–11, 1961.

[15] S. R. Wiegell, M. Hædersdal, P. Eriksen, and H. C. Wulf, "Photodynamic therapy of actinic keratoses with 8% and 16% methyl aminolaevulinate and home-based daylight exposure: a double-blinded randomized clinical trial," *British Journal of Dermatology*, vol. 160, no. 6, pp. 1308–1314, 2009.

[16] S. R. Wiegell, H. C. Wulf, R.-M. Szeimies et al., "Daylight photodynamic therapy for actinic keratosis: an international

consensus: International Society for Photodynamic Therapy in Dermatology Wiegell et al. Daylight-mediated PDT," *Journal of the European Academy of Dermatology and Venereology*, vol. 26, no. 6, pp. 673–679, 2012.

[17] J. Chen, L. Keltner, J. Christophersen et al., "New technology for deep light distribution in tissue for phototherapy," *Cancer Journal*, vol. 8, no. 2, pp. 154–163, 2002.

[18] P. K. Lee and A. Kloser, "Current methods for photodynamic therapy in the US: comparison of MAL/PDT and ALA/PDT," *Journal of Drugs in Dermatology*, vol. 12, no. 8, pp. 925–930, 2013.

[19] K. Negishi, Y. Tezuka, N. Kushikata, and S. Wakamatsu, "Photorejuvenation for Asian skin by intense pulsed light," *Dermatologic Surgery*, vol. 27, no. 7, pp. 627–632, 2001.

[20] P. H. Bitter Jr., "Noninvasive rejuvenation of photodamaged skin using serial, full-face intense pulsed light treatments," *Dermatologic Surgery*, vol. 26, no. 9, pp. 835–843, 2000.

[21] S. R. Wiegell, S. Fabricius, J. Heydenreich et al., "Weather conditions and daylight-mediated photodynamic therapy: protoporphyrin IX-weighted daylight doses measured in six geographical locations," *British Journal of Dermatology*, vol. 168, no. 1, pp. 186–191, 2013.

[22] T. Dirschka, P. Radny, R. Dominicus et al., "Long term (6 and 12 months) followup of two prospective, randomized, controlled phase IIItrials of photodynamic therapy with BF-200 ALA and methyl aminolaevulinate for the treatmentof actinic keratosis," *British Journal of Dermatology*, vol. 168, no. 4, pp. 825–836, 2013.

[23] Y. J. Matthews and D. L. Damian, "Topical photodynamic therapy is immunosuppressive in humans," *British Journal of Dermatology*, vol. 162, no. 3, pp. 637–641, 2010.

[24] I. M. Miller, J. S. Nielsen, S. Lophaven, and G. B. E. Jemec, "Factors related to pain during routine photodynamic therapy: a descriptive study of 301 patients," *Journal of the European Academy of Dermatology and Venereology*, vol. 25, no. 11, pp. 1275–1281, 2011.

[25] S. R. Wiegell, M. Hædersdal, and H. C. Wulf, "Cold water and pauses in illumination reduces pain during photodynamic therapy: a randomized clinical study," *Acta Dermato-Venereologica*, vol. 89, no. 2, pp. 145–149, 2009.

[26] S. R. Wiegell, M. Hædersdal, P. A. Philipsen, P. Eriksen, C. D. Enk, and H. C. Wulf, "Continuous activation of PpIX by daylight is as effective as and less painful than conventional photodynamic therapy for actinic keratoses; a randomized, controlled, single-blinded study," *British Journal of Dermatology*, vol. 158, no. 4, pp. 740–746, 2008.

[27] D. Surjana, G. M. Halliday, and D. L. Damian, "Nicotinamide enhances repair of ultraviolet radiation-induced DNA damage in human keratinocytes and ex vivo skin," *Carcinogenesis*, vol. 34, no. 5, pp. 1144–1149, 2013.

Research Article

Scattered and Fluorescent Photon Track Reconstruction in a Biological Tissue

Maria N. Kholodtsova,[1,2,3] **Pavel V. Grachev,**[1] **Tatiana A. Savelieva,**[1] **Nina A. Kalyagina,**[1,2,3]
Walter Blondel,[2,3] **and Viktor B. Loschenov**[1]

[1] *A. M. Prokhorov General Physics Institute of the Russian Academy of Sciences, Vavilov Street 38, Moscow 119991, Russia*
[2] *Université de Lorraine, CRAN, UMR 7039, 2 avenue de la Forêt de Haye, 54516 Vandoeuvre-Lès-Nancy Cedex, France*
[3] *CNRS, CRAN, UMR 7039, 2 avenue de la Forêt de Haye, 54516 Vandoeuvre-Lès-Nancy Cedex, France*

Correspondence should be addressed to Maria N. Kholodtsova; m.kholodtsova@gmail.com

Appropriate analysis of biological tissue deep regions is important for tumor targeting. This paper is concentrated on photons' paths analysis in such biotissue as brain, because optical probing depth of fluorescent and excitation radiation differs. A method for photon track reconstruction was developed. Images were captured focusing on the transparent wall close and parallel to the source fibres, placed in brain tissue phantoms. The images were processed to reconstruct the photons most probable paths between two fibres. Results were compared with Monte Carlo simulations and diffusion approximation of the radiative transfer equation. It was shown that the excitation radiation optical probing depth is twice more than for the fluorescent photons. The way of fluorescent radiation spreading was discussed. Because of fluorescent and excitation radiation spreads in different ways, and the effective anisotropy factor, g_{eff}, was proposed for fluorescent radiation. For the brain tissue phantoms it were found to be 0.62 ± 0.05 and 0.66 ± 0.05 for the irradiation wavelengths 532 nm and 632.8 nm, respectively. These calculations give more accurate information about the tumor location in biotissue. Reconstruction of photon paths allows fluorescent and excitation probing depths determination. The g_{eff} can be used as simplified parameter for calculations of fluorescence probing depth.

1. Introduction

Methods of fluorescence diagnosis (FD) and photodynamic therapy (PDT) are widely used in almost all medical fields, that is, dermatology, ophthalmology, gynecology, and urology, as well as in neurology [1–4]. Intraoperative FD in neurology is a rapidly developing area. It allows differentiation of altered brain tissue from normal brain tissue with high specificity and sensitivity and as consequence helps to prevent resection of healthy tissue [5, 6]. However, there are limits to the applicability of the method to the spinal cord and brain surgical interventions, which needs to be further addressed.

One of the most widely used photosensitisers for the FD for brain tissue is 5-aminolevulinic acid (5-ALA) which induces elevated protoporphyrin IX (PpIX) production in malignant cells. The PpIX fluoresces in the 630–700 nm wavelength range and is excited throughout the entire optical region. However, the wavelengths of 405, 532, and 632.8 nm are usually used as excitation wavelengths during laser-induced FD [6, 7]. The long wavelength irradiation is of special interest due to its deep penetration into biological tissue, whereas the short-wavelength irradiation can provide higher resolution. In this work the investigation was conducted in two regions, the red ($\lambda = 632.8$ nm) and green ($\lambda = 532$ nm) regions of the spectrum.

By means of fluorescent diagnosis surgeon decides to reject or to leave tissue, so it is necessary to know from which area or depth all the data were collected to leave the healthy tissue and to remove tumor which accumulate photosensitiser.

The aim of the work was the estimation of the optical probing depth dependence on the distance between source and detector, allowing for an interpretation of FD results. We describe an experiment carried out on brain tissue phantoms,

(a)

(b)
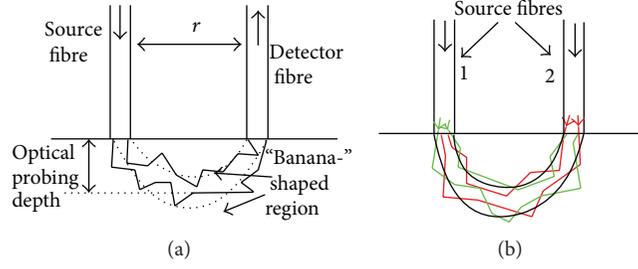
FIGURE 1: The most probable photon path distribution for (a) photons migrating from the source fibre to detector fibre, where the most probable area is limited by a "banana-" shaped region (dotted line) and (b) for photons migrating from two source fibres.

then compare it with numerical calculations using Monte Carlo (MC) modeling, and describe the use of self-developed software and theoretical results, based on the diffusion theory (DT) for analysis of photon migration in biological and other turbid media. It should be taken into account that the results of the experiment on the phantoms highly depend on the configuration of the fibres such as numerical aperture and diameter.

During surgery, it is important to remove a tumor without damaging healthy tissue. It is also essential to develop diagnostic methods, allowing for precise determination of the depth about which information can be collected during FD. We propose the effective fluorescence g-factor to be a parameter as it can show the depth of fluorescent photons

propagation after their emission due to excitation of a photosensitiser contained in the tissue.

2. Material and Methods

2.1. Diffusion Theory of the Radiative Transfer Equation. According to the DT the incident photons in a semi-infinite medium will migrate to the fibre detector through the "banana-" shaped area. The ends of such a region originate from the fibres, and the middle reaches the deepest part [8]. Such a form is derived from the analytical DT solution of the radiative transfer equation (RTE) [9, 10]. The radiation distribution equation at point $\vec{r_1} = (x, y, z)$ is as follows [10]:

$$P\left(x, y, z\right) = \frac{z^2 e^{-k\left(\sqrt{(r-x)^2+y^2+z^2}+\sqrt{x^2+y^2+z^2}\right)}\left(k\sqrt{(r-x)^2+y^2+z^2}+1\right)\left(k\sqrt{x^2+y^2+z^2}+1\right)}{\left((r-x)^2+y^2+z^2\right)^{3/2}(x^2+y^2+z^2)^{3/2}}, \tag{1}$$

with r—distance between two fibres, L_a—absorbance length (in cm) where $L_a = \sqrt{D/\mu_a}$ and $k = 1/L_a$, D—diffusion coefficient where $D = 1/(3[\mu_a + (1-g)\mu_s])$, μ_a—absorbance coefficient (in cm^{-1}), μ_s—scattering coefficient (in cm^{-1}), and g—mean scattering cosine.

Given that $y = 0$ (because of symmetry) and due to weak absorption ($kr \ll 1$) it can be pointed out that the minima of the photon distribution function $P(x, y, z)$ in YZ-plane is as follows [10]:

$z(r)$

$$= \sqrt{\frac{1}{8}\left[\sqrt{\left(x^2 + (r-x)^2\right)^2 + 32x^2(r-x)^2} - x^2 - (r-x)^2\right]}. \tag{2}$$

Hence the optical probing depth is defined as the maximum distance from an irradiated object surface between source and detector to the most probable photon migration area (Figure 1) whereby (2) defines the optical probing depth for a fixed distance between source and detector.

In this contribution, the equations above were used because we are not considering the signal on the surface

which is detected by fibres, but we are investigating the path of photons propagating in the medium.

2.2. Monte Carlo Simulations. MC modeling is well known and widely used for biological tissue optical properties derivation [10, 11]. This method is based on numerical modeling of photon propagation in turbid media. During migration, photons undergo multiple scattering processes and, finally, absorption.

We developed the MClight program which models three-dimensional (3D) light distribution in turbid media. One feature of this program is the ability to set different geometries for the experiment such as fibre position, numerical aperture (NA), and diameter of fibres, as well as the multilayered model where one can set optical properties (μ_a, μ_s, g) and the thickness of each layer. The results of calculations are presented as a black and white intensity distribution image. Such a representation is clear and allows comparison with the experimental data. Each pixel of this b/w image corresponds to a point in the medium: if a photon is scattered at this point, the brightness at this point will be increased by one. As more photons are scattered at this point, the brighter the pixel will be. Resolution was $5\,\mu m$ per pixel as it was sufficient to

be compared with the experimental data, also the resolution could be changed from 2 μm/p to 20 μm/p.

It should also be taken into account that the image of 32 bit color depth allows small brightness changes in a light field to be detected, so the derived distributions are saved with *.tif extension. Another self-developed program (TiffReader) allows processing files with *.tif extension (if the color depth is more than 32 bytes, then the image is processed without image quality loss). This program has the ability to measure the distance between two chosen points, thereby obtaining brightness profiles as well as 3D brightness distribution. It is also possible to reduce noise by means of Sobel and Prewitt masks [12].

Moreover, the program includes maximum brightness and optical probing depth search algorithms. The algorithm is as follows: the area of the medium which photons cross the most is the brightest. According to this, the program searches for the brightest points and derives the area, where the photon flow is at its highest level. This area is colored red and the results can be saved in a graphics file. The distance between the surface plane and the lowest point of the obtained region are the optical probing depth, which can be measured 4 directly in the program developed.

2.3. Determination of Anisotropy Factor.

Firstly, brain tissue phantoms were made for comparative pictures of photon distribution. These were made up of "Intralipid 10%" and sulfonated aluminum phthalocyanine (Photosens, Science Center "NIOPIK", Moscow, Russia) at a concentration of 2 mg/kg (recommended dosage for FD) and had similar scattering and absorbing properties to real brain tissue. As "Intralipid 10%" is not an optical standard, it has a bottle-to-bottle variation in the optical properties, which had to be verified experimentally for each bottle at the time of use [13, 14]. As the main parameter affecting the photon distribution in a single scattering medium is the anisotropy factor (g-factor), the scattering (μ_s) and absorption (μ_a) coefficients are scaling and have an influence on photon free path length. Consequently, in order to obtain the g-factor, goniophotometry was used in a spectrometer of dynamic light scattering (Photocor Complex optical unit; Photocor Instruments, Inc., College Park, MD, USA) (Figure 2).

To perform this method, the layer of Intralipid (1.6% in water solution, 70 μm thick) was placed in a special cuvette with 150 μm thick walls and the indicatrix was obtained by means of photon counter (Photocor-PC2; Photocor Instruments, Inc., College Park, MD, USA). The results were approximated with the Henyey-Greenstein (HG) phase function, using the least square method. Also the free path length of photon in medium was determined, which is defined as a reversed sum of scattering and absorption coefficients.

2.4. Experimental Setup.

A special methodology of the experiment was developed to determine the optical probing depth taking the following into account. As induced photons from one fibre migrate to another through the "banana-" shaped region (by virtue of the symmetry and isotropy of the turbid medium), changing the detector fibre to the source fibre
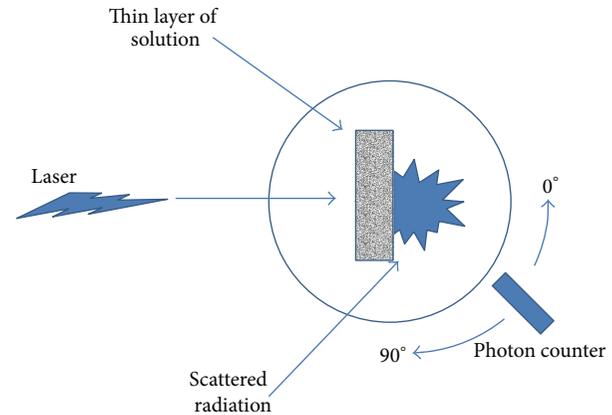
Figure 2: Scattering indicatrix measurement setup. Laser wavelength is 632.8 nm.

will not affect the photon distribution because a correlation between the two fibres is absent. Also the areas of the most probable photon migration paths, from one fibre to another, add up (Figure 1(b)). Thus, using the TiffReader program, it is possible to obtain both regions where photons migrate through the paths distributed in a "banana-" shaped region and the optical probing depth.

The experiments were performed in four steps.

Firstly, in order to obtain the light field of diffusely scattered photon distribution between two fibres a setup was designed, which can be described as follows. It consists of a special cuvette (50 mm × 60 mm × 30 mm) with a thin transparent wall (80 μm), optical fibres (material: quartz-polymer; NA = 0.48; diameter = 600 μm), a b/w 32 bit color depth camera (VideoScan-415; VideoScan, Moscow, Russia), and two lasers, that is, a helium neon (HeNe) laser (λ = 632.8 nm, P = 150 mW; Biospec, Moscow, Russia) and a continuous diode (λ = 532 nm, P = 150 mW; Biospec, Moscow, Russia). The fibres were placed in the cuvette at a depth of 10 mm and close to the transparent wall. Then the images of photon path distribution were recorded with the camera which was placed parallel to the transparent wall. As the distortions obtained are minimal (due to thin wall presence), the effects of multipath are also minimal. This is because the photon path length is compared with the wall thickness and the refractive index of the wall differs from that of the solution by no more than 10%. Furthermore, the photon path distribution is parallel to the wall and symmetrical to the plane which goes through the middle of the fibres.

Secondly, to obtain the fluorescent light field distribution, optical filters were used (for 532 nm light excitation: Orange Glass-14 ($T_{50} \approx$ 580 nm, $T_{100} \approx$ 620 nm), for 632.8 nm: Red Glass-17 ($T_{50} \approx$ 670 nm, $T_{100} \approx$ 700 nm)). These filters were placed between VideoScan camera and the transparent wall of the cuvette. In order to reduce the signal-to-noise ratio, 10 images of each field distribution were averaged. During the experiment, the distance between the sources was varied in the range 0.5–7.5 mm (Figure 3).
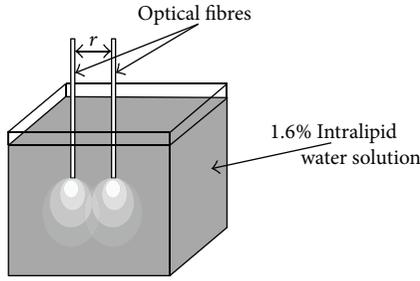
FIGURE 3: Scheme of the experimental setup.

TABLE 1: Optical properties of the brain tissue model for Photosens emission wavelength (668 nm) [15, 16].

Material	μ_s (cm^{-1})	μ_a (cm^{-1})	g^*
1.6% Intralipid/water solution	~274	~0.001	~0.71

*Not used in the calculations.

Thirdly, the 3D light distributions were obtained by means of MClight program for the two excitation wavelengths (532 nm and 632.8 nm). The geometry of the simulations replicates that of the real experiment and the optical properties of the simulated turbid medium were chosen according to the optical properties of Intralipid at the already mentioned wavelengths.

Finally, fluorescence and excitation field distributions obtained experimentally were processed in TiffReader using MClight after which the optical probing depths and regions of the most probable photon path were obtained. The optical probing depth was the distance from the end of fibre till the middle of the fluorescent or excitation field.

2.5. Effective Anisotropy Factor of Fluorescence. It was assumed that the effective fluorescent g-factor depends on several events such as scattering emitted from the source photons in tissue, fluorescent photon emission in any direction with equal probability, scattering of photon with the wavelength corresponding to the fluorescent wavelength of photosensitiser in tissue, and, finally, absorption of this photon or its escape from the area under consideration. So for the brain tissue phantoms containing the photosensitiser Photosens, the fluorescent effective g-factors were derived using four parameters. These were the experimentally derived optical probing depth, the preset distance between fibres (not shown in Table 1), and the known optical properties (scattering and absorption coefficient) of the model at the photosensitiser emission wavelength $\lambda = 668$ nm (Table 1). These parameters were substituted in (1) and then the effective anisotropy factor of fluorescence was derived using the mean root square method.

3. Results and Discussion

3.1. Determination of Anisotropy Factor. The anisotropy factor for $\lambda = 632.8$ nm was found to be 0.83 ± 0.03, the free path length 27 ± 2 μm, and for $\lambda = 532$ nm 0.85 ± 0.03 and 20 ± 3 μm,
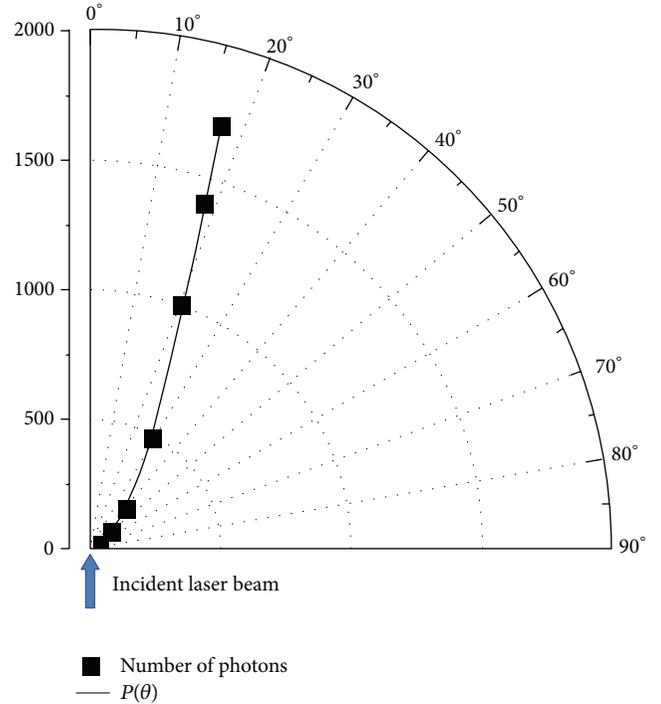
FIGURE 4: Dependence of the photon number counter on angle θ. Experimental results are marked with squares; line is HG function for $g = 0.83$.
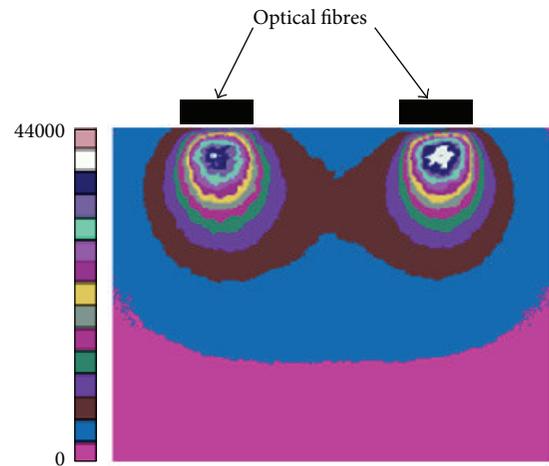
FIGURE 5: The image of light field distribution obtained by MClight and processed by means of the TiffReader program. Each tone corresponds to its own brightness range which is shown on the left side.

respectively, (Figure 4). These results are acceptable and can be used to model brain tissue and as input parameters for MC simulations.

3.2. Monte Carlo Simulations and the Diffusion Theory of the Radiative Transfer Equation. Firstly, the light field distribution was obtained by MClight and processed in TiffReader program (Figure 5). In this distribution, each color corresponds to its own brightness range. One can see that the
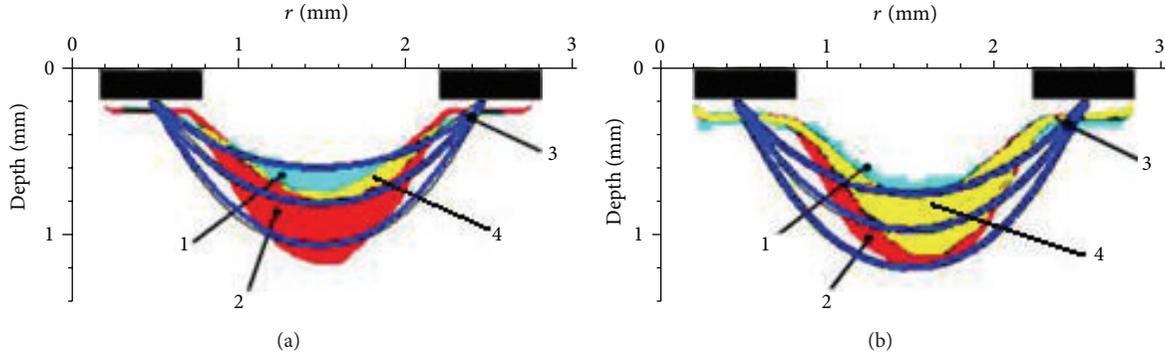
Figure 6: The most probable photon paths distribution between two sources for (a) 532 nm and (b) 632.8 nm (distance between the fibres, 1.7 mm). 1—Experiment, 2—MC simulations, 3—diffuse approximation, and 4—intersection of 1 and 2.
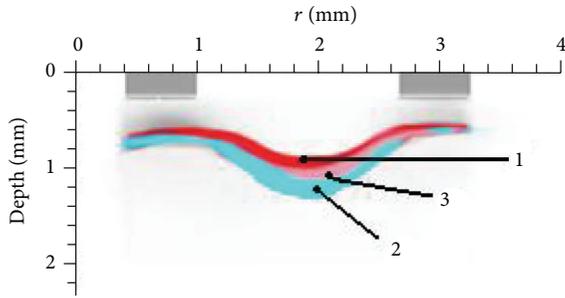
Figure 7: The most probable path distribution between two sources for fluorescent and diffusely scattered photons (excitation wavelength, 532 nm; distance between fibres, 1.7 mm). 1—fluorescent photons, 2—diffusely scattered photons, and 3—intersection of 1 and 2.

Figure 8: Dependence of optical probing depth on the distance between the fibres. Green: excitation wavelength λ = 532 nm (circles—diffusely scattered radiation, full line—solution of (2), triangles—fluorescent radiation, and dashed line—approximation with logarithmic function). Red: excitation wavelength λ = 632.8 nm (circles—diffusely scattered radiation, full line—solution of (2), triangles—fluorescent radiation, and dashed line—approximation with logarithmic function).

Table 2: Optical properties of the brain tissue model [15, 16].

Material	Wavelength (nm)	μ_s (cm^{-1})	μ_a (cm^{-1})	g
1.6% Intralipid/	532.0	514	0.008	0.85
water solution	632.8	341	0.003	0.83
Brain tissue	532.0	410	0.01	0.87
(white matter)	632.8	409	0.08	0.84

maximum brightness is 300 μm deeper than the ends of the fibre tips because in these areas brightness is the sum of the diffusely scattered light and the light emitted from fibres, without interaction with medium.

Secondly, the theoretical MC simulations were compared with the experimental results for the most probable photon propagation paths. These distributions were derived for two wavelengths of excitation radiation. Theoretical borders for the "banana-" shaped region were derived from (2). These areas are shown in Figure 6.

It is apparent that nearby the fibres' tips, the obtained theoretical results do not fit the experimental one. This fact is explained by the point-source assumption of the DT.

Thirdly, the experimentally obtained distributions of the most probable paths of fluorescent and excitation photons paths distributions are compared in Figure 7.

After that, the dependencies of the optical probing depth on the distance between the fibres for fluorescent and diffusely scattered light were determined. These results are presented in Figure 8. From the data in Figure 8 it can be seen that the optical probing depth dependencies on the distance between the fibres match the theoretical models as well as the experimental data (coefficients of determination R^2 are shown near corresponding lines). It was also found that the optical probing depth for an excitation wavelength of 532 nm

is less than for 632.8 nm on 20–30%. This fact is explained by the difference in scattering coefficients, which are being lower for the shorter wavelength (Table 2).

Moreover, it was noticed that the optical probing depth dependence on the distance between the fibres for fluorescent light is approximated with the logarithmic function $a \ln(r) + b$, where r is the distance between the fibres and a, b are the proportionality factors. R^2 is 0.95 and 0.98 for 632.8 nm and for 532 nm, respectively (shown in Figure 8).

(a)

(b)
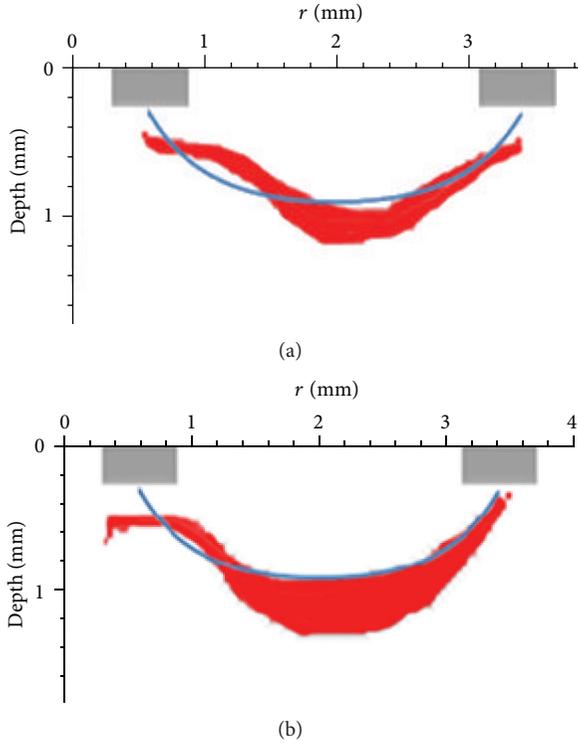
FIGURE 9: Calculated effective anisotropy factor substituted in (1) and experimental most probable photon path for (a) 532 nm excitation and (b) 632.8 nm excitation. Distance between fibres is 2.2 mm.

TABLE 3: Effective fluorescent g-factor for the two-excitation wavelengths.

Excitation wavelength (nm)	532.0	632.8
Effective g-factor	0.62 ± 0.05	0.66 ± 0.06

It is also important that the fluorescent probing depth is less than the excitation depth by 60–70% (it is followed from calculations and can be seen from Figure 8).

3.3. Effective Fluorescent g-Factor. After derivation of the probing depth for fluorescence, it was then possible to determine the effective fluorescent g-factor; the results are presented in Table 3 and Figure 9.

The error which can occur if one uses an ordinary g-factor for fluorescence radiation while determining the optical probing depth was calculated. In the case of 532 nm excitation, the error can be estimated to be 14%, and in the case of 632.8 nm, the error is 7%. So it can be concluded that use of the effective fluorescent g-factor gives more accurate results and that the error will be higher for the shorter irradiation wavelength.

3.4. Discussion. The theoretical study of photon migration in a tissue has been performed by several research groups [8, 9, 11]. They considered the DT of the RTE and used MC simulations for light propagation in a turbid medium,

including experiments on biological tissue phantoms. Equations for photon path distribution in presence and absence of absorbing element between emitter and detector were also derived. The authors showed that the photon flow through medium is in a confined region and suggested that distribution of photon paths may affect the spatial resolution.

We performed the calculations of photon migration process in a brain tissue phantom comparable with white matter from the brainas this is where malignant tumors mostly occur, using the excitation wavelengths most commonly used for FD during surgical interventions. It should be mentioned that if measurements are made on real brain tissue, the error will be greater for green light than for the red (absorbance of hemoglobin is 50x more for 532 nm than for 632.8 nm). This is because the given results were obtained without taking the hemoglobin absorbance into consideration as soon as hemoglobin content highly depends on physiological state of tissue and requires deeper investigation.

The optical probing depth for shorter wavelength excitation is less than that for the longer ones. This can be explained by the difference in mean free path length; for shorter wavelengths it is lower so light is scattered earlier, and because of the lower g-factor, light is scattered less in a forward direction. Thus, the optical probing depth of 632.8 nm excitation is higher for 20–30% than for 532 nm.

Considering the fluorescent optical probing depth, it is lower for shorter excitation wavelengths. This difference can be explained by several factors. First of all, it is partly due to the NA of the fibre which affects the initial angle of the photons emitted from the fibre. Secondly, the following motion of photons is defined by a g-factor, the closer it is to 1, and the less the photons are deviated from the initial direction. Thus, the "banana-" shaped region is the result of step-by-step deviation of the photons from the initial direction. The absence of a propagation direction is the distinctive feature of fluorescent photons relative to diffusely scattered ones. A fluorescent photon is emitted by an excited atom in a 4π angle equiprobable and then it interacts with tissue according to the tissue's optical properties at the photon's wavelength. Consequently, the deviation from the initial direction for fluorescent photons is less than for diffusely scattered, so the optical probing depth is also smaller.

As was expected, the fluorescent g-factor for 532 nm excitation is smaller than that for 632.8 nm excitation. It was mentioned before that effective fluorescent g-factor depends on the excitation wavelength and further propagation of fluorescent photons. After a fluorescent photon emission, process of diffusion is the same, and obtained distribution depends only on the path which excitation photon travelled. Emitted photons of a longer wavelength propagate further into biotissue than photons at a shorter wavelength, so excitation of a fluorophore and the following emission of photons occur deeper than at a longer wavelength excitation. As a result, the effective fluorescent g-factor is closer to 1 at a longer excitation wavelength.

4. Conclusion

The results obtained are applicable for the FD of brain tissue where precise knowledge about spectral data obtained by means of FD is required. The use of longer wavelengths, as well as the use of a wider distance between source and detector, could possibly enable deeper tissue regions to be reached. This can be seen in the experiment, where the optical probing depth of the emission irradiation with the 532 nm wavelength was found to be 20–30% less than for the 632.8 nm wavelength. The most probable path of photons can be determined from the DT and MC simulations. Our calculations showed that both of these two methods correspond well with the experiment described in this paper. The middle region or the optical probing depth matches each of the methods, unless there is a difference near the fibre ends. Furthermore, the optical probing depth is proportional to the logarithmic function which depends on the distance between source and detector with the R^2 equal to 0.95 for the 632.8 nm and to 0.98 for the 532 nm wavelengths. Even though the choice of the excitation wavelength depends on the type of photosensitiser, it is also recommended to take the difference in the probing depth between excitation and fluorescent photons into account. This is due to the 60–70% difference in the probing depth (in the investigated wavelengths region), causing collection of the fluorescent photons from the regions lying above the area of the excitation photons path.

Conflict of Interests

The authors declare that there is no conflict of interests regarding the publication of this paper.

References

[1] J. de Leeuw, H. C. de Vijlder, P. Bjerring, and H. A. M. Neumann, "Liposomes in dermatology today," *Journal of the European Academy of Dermatology and Venereology*, vol. 23, no. 5, pp. 505–516, 2009.

[2] N. Fotinos, M. A. Campo, F. Popowycz, R. Gurny, and N. Lange, "5-Aminolevulinic acid derivatives in photomedicine: characteristics, application and perspectives," *Photochemistry and Photobiology*, vol. 82, no. 4, pp. 994–1015, 2006.

[3] Q. Peng, T. Warloe, K. Berg et al., "5-Aminolevulinic acid-based photodynamic therapy. Clinical research and future challenges," *Cancer*, vol. 79, no. 12, pp. 2282–2308, 1997.

[4] R. Richards-Kortum and E. Sevick-Muraca, "Quantitative optical spectroscopy for tissue diagnosis," *Annual Review of Physical Chemistry*, vol. 47, pp. 555–606, 1996.

[5] V. Tuchin, *Tissue Optics: Light Scattering Methods and Instruments for Medical Diagnosis*, SPIE Press, Bellingham, Wash, USA, 2000.

[6] V. B. Loschenov, V. I. Konov, and A. M. Prokhorov, "Photodynamic therapy and fluorescence diagnostics," *Laser Physics*, vol. 10, no. 6, pp. 1188–1207, 2000.

[7] A. A. Stratonnikov and V. B. Loschenov, "Evaluation of blood oxygen saturation in vivo from diffuse reflectance spectra," *Journal of Biomedical Optics*, vol. 6, no. 4, pp. 457–467, 2001.

[8] M. S. Patterson, B. Chance, and B. C. Wilson, "Time resolved reflectance and transmittance for the non-invasive measurement of tissue optical properties," *Applied Optics*, vol. 28, no. 12, pp. 2331–2336, 1989.

[9] S. Feng, F. A. Zeng, and B. Chance, "Photon migration in the presence of a single defect: a perturbation analysis," *Applied Optics*, vol. 34, no. 19, pp. 3826–3837, 1995.

[10] W. Cui, C. Kumar, and B. Chance, "Experimental study of migration depth for the photons measured at sample surface," in *Time-Resolved Spectroscopy and Imaging of Tissues*, vol. 1431 of *Proceedings of SPIE*, pp. 180–191, Los Angeles, Calif, USA, January 1991.

[11] S. A. Prahl, M. Keijzer, S. L. Jacques, and A. J. Welch, "A Monte Carlo model of light propagation in tissue," in *Dosimetry of Laser Radiation in Medicine and Biology*, vol. 5 of *Proceedings of SPIE*, pp. 102–111, 1989, http://omlc.ogi.edu/~prahl/pubs/abs/prahl89.html.

[12] R. C. Gonzalez and R. E. Woods, *Digital Image Processing*, Person Prentice Hall, Upper Saddle River, NJ, USA, 3rd edition, 2007.

[13] R. Michels, F. Foschum, and A. Kienle, "Optical properties of fat emulsions," *Optics Express*, vol. 16, no. 8, pp. 5907–5925, 2008.

[14] S. T. Flock, S. L. Jacques, B. C. Wilson, W. M. Star, and M. J. C. van Gemert, "Optical properties of intralipid: a phantom medium for light propagation studies," *Lasers in Surgery and Medicine*, vol. 12, no. 5, pp. 510–519, 1992.

[15] A. N. Yaroslavsky, P. C. Schulze, I. V. Yaroslavsky, R. Schober, F. Ulrich, and H.-J. Schwarzmaier, "Optical properties of selected native and coagulated human brain tissues in vitro in the visible and near infrared spectral range," *Physics in Medicine and Biology*, vol. 47, no. 12, pp. 2059–2073, 2002.

[16] W.-F. Cheong, S. A. Prahl, and A. J. Welch, "A review of the optical properties of biological tissues," *IEEE Journal of Quantum Electronics*, vol. 26, no. 12, pp. 2166–2185, 1990.

Research Article

Reflectance of Biological Turbid Tissues under Wide Area Illumination: Single Backward Scattering Approach

Guennadi Saiko and Alexandre Douplik

Department of Physics, Ryerson University, Toronto, ON, Canada M5B 2K3

Correspondence should be addressed to Alexandre Douplik; douplik@ryerson.ca

Various scenarios of light propagation paths in turbid media (single backward scattering, multiple backward scattering, banana shape) are discussed and their contributions to reflectance spectra are estimated. It has been found that a single backward or multiple forward scattering quasi-1D paths can be the major contributors to reflected spectra in wide area illumination scenario. Such a single backward scattering (SBS) approximation allows developing of an analytical approach which can take into account refractive index mismatched boundary conditions and multilayer geometry and can be used for real-time spectral processing. The SBS approach can be potentially applied for the distances between the transport and reduced scattering domains. Its validation versus the Kubelka-Munk model, path integrals, and diffusion approximation of the radiation transport theory is discussed.

1. Introduction

Propagation of light in biological turbid tissues is a complex interplay between scattering and absorption. Light propagation in biological tissues is important for calculation of the exact amount of light in tissue, that is, the light dose for estimating thermal damage of biological tissues. The propagation of light in biotissue is also important for diagnostics technologies. The diffuse approximation and Monte Carlo simulations are widely used for these purposes [1, 2].

If we know optical properties of the media, then the light distribution within the media or the tissue reflectance or transmittance can be calculated by various methods [1]. With the advancements of computational power, Monte Carlo (MC) simulations [2] become the most common approach. It is also the most versatile and accurate approach, which can give an answer with required accuracy. The most common task in optical diagnostics however is to solve an inverse problem and reconstruct optical properties of the tissue from a certain reflectance (and less typically transmittance) spectrum. To solve it, various methods have been developed including inverse MC [1], inverse adding-doubling [3], and spatially[4] and spectrally resolved [5] diffuse reflectance methods. Some of them are applicable to

very particular measurements (e.g., inverse adding-doubling method for single and double integrating sphere geometry); others (lookup MC tables, diffuse approximation) can be applied to certain simplified geometries (finite slab or semi-infinite slab). In real life, however, most of surface tissues are characterized by multilayered geometries and internal reflection due to the refraction index mismatched boundary conditions, which significantly complicate solving the inverse problem by existing techniques. Thus, a simplified analytical approach, which can facilitate processing of experimental data of light scattering processes into biotissues in realistic geometries, is of great importance.

The related question is to understand clear physical picture of light propagation within the media. In particular, we are interested in estimation of the sampling depth and the closely related question which we can actually see in the reflectance spectra (photons which entered the biotissue nearby (short pass) or diffuse photons, which entered far from the detector (long pass)). The most clear physical picture can be obtained using the path integrals approach to photon migration [6]. This analytical method is based on finding a classical path [7] for a nondissipating system and then calculating the path integral for all possible trajectories using Feynman formalism. The method can be used to find

approximate solutions for forward and inverse problems in semi-infinite slab geometries. However, due to computational difficulties it is problematic to apply this approach in realistic geometries with refraction index mismatched boundary conditions, multilayered structures, and so forth.

Reflection spectra depend on particular illumination scenario. There are four major illumination scenarios: wide beam diffuse, wide beam collimated, point collimated (e.g., laser beam) and point diffuse (e.g., light through optical fiber) illumination. In medical biooptics, wide beam collimated and point diffuse (e.g., fiber source) illuminations are the most common illumination modalities used in therapeutic applications. The wide and point collimated beam illuminations are used or shortly will be used in quickly emerging diagnostic modality of photoacoustics [8]. In daily life we typically see the reflectance from the tissues under wide beam diffuse illumination (e.g., overcast conditions).

Thus, the question can be transformed into the following one: which volume exactly can we interrogate at different illumination scenarios?

Obviously, the diffusion is an important mechanism of light propagation in turbid media [1]. However, the light propagation in the vicinity of the light source (within the transport length) does not follow the diffuse approximation [9]. Moreover, some skin marks, such as birthmarks, scars or other skin inhomogeneity are seen with sharp borders, which indicates that the optical paths contribute in reflectance not only diffusively.

Existing models (diffuse approximation, Kubelka-Munk, and Monte Carlo simulations) do not address this question directly. The interrogation depth can be approximated from the light distribution; it is still unclear what is the typical optical path for photons measured by a detector. Monte Carlo code can be amended [10] to address this question, although it is difficult to process numerical simulations for multilayered geometries close to real time. Thus, a simple analytical model, which can address this question, will be very useful for interpretation of results.

By the way, this question is important not only for biological tissue optics but also for other turbid media applications. In particular, in paper and paint industry applications their typical geometry (dull colour layer parallel to an opaque plane substrate) is pretty similar to the typical geometry in tissue optics (e.g., papillary dermis over subcutaneous fat). Moreover, similar to surface tissues, paper is also a complex structure consisting of cellulose fibers, fillers, and additives (including chromophores).

The purpose of this paper is to develop a simplified analytical approach elucidating the physical picture of scattering processes in turbid tissues and providing interpretation of experimental results, particularly in tissues with high absorption and within a small distance (comparable to the transport length, $I_t = 1/(\mu_a + \mu_s')$) from the source. We show how this method can be used for estimating reflectance of tissue and sampling depth.

The paper is composed as follows: first, we develop an analytical approach to the light propagation in the turbid tissues; then, we compare predictions with diffuse approximation, Kubelka-Munk theory and path integrals approaches; finally, we discuss the physical picture of scattering in the tissue based on comparison of these models.

2. Theory

2.1. Individual Scattering Event. Individual scattering events in body tissues are primarily attributed to intracellular organelles (mitochondria, nuclei, etc.) with the size comparable to the photon wavelength (Mie regime [1]). These scattering events are highly anisotropic and primarily directed forward. We will be interested in probability of backward (with scattering angle $\theta > \pi/2$) scattering p. This probability can be calculated directly from the Mie theory; however, for illustration purposes as one of the probability density functions characterizing the angular distribution of scattering we will use the Heiney-Greenstein scattering phase function [11], which is routinely used for light propagation in biotissues:

$$p(g, \theta) = \frac{1}{2} \frac{1 - g^2}{\left(1 + g^2 - 2g\cos\theta\right)^{3/2}}. \tag{1}$$

Here g is "the mean cosine" of scattering, $\langle\cos\theta\rangle$. If $g = 0$, we have isotropic scattering; $g = 1$ or -1 corresponds to fully forward or fully backward scattering, respectively. The light scattering in tissues is strongly anisotropic with g ranging from 0.785 (dermis) to 0.995 (blood).

From (1) we can estimate the probability of backward scattering p—the probability that photon will be scattered with $\theta > \pi/2$: $p(g) = \int_{\pi/2}^{\pi} p(g, \theta)\sin\theta\,d\theta$:

$$p(g) = \frac{1}{2}\frac{1 - g^2}{g}\left[\frac{1}{\sqrt{1 + g^2}} - \frac{1}{1 + g}\right]. \tag{2}$$

On Figure 1 the probability of backward scattering $p(g)$ is plotted as function of "average cosine" g together with the probability of backward scattering in 1D model ($g = \langle\cos\theta\rangle = \cos 0 * (1 - p) + \cos\pi * p = 1 - 2p$-dotted line).

It can be seen that the probability of backward scattering for body tissues p is not bigger than 0.05 (dermis) and typical value of p in tissues with blood is even smaller.

2.2. Multiple Scattering in Turbid Tissues. Let us consider the path of a photon that started and finished on the surface of tissue (reflection spectrum). We can classify the optical paths based on the number of backscattering events (as defined in the previous section) along this path. Optical paths obtained by Monte Carlo simulations can be visually grouped into 3 major classes: (1) quasi-1D paths with one or more backward scatterings, (2) a "sausage" or "banana shape" paths with multiple tilted forward scatterings, and (3) pure diffuse paths with multiple forward and backward scattering events. Backward scattering and "banana shape" paths are depicted in Figure 2. We can distinguish between paths with one backward scattering and multiple (more than 1) backward scatterings, but we also can consider paths with tilted forward scattering as a subset of the diffuse paths. Thus, the amended classification can be presented as follows.
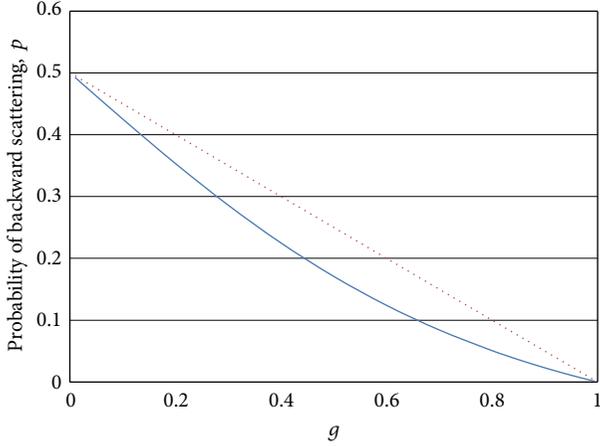
FIGURE 1: Probability of backward scattering $p(g)$ in the Heiney-Greenstein model (solid line) and 1D model (dotted line) as a function of g.

(1) Path with one backward scattering (see Figure 2(a)).

(2) Path with multiple backward scatterings (see Figure 3).

(3) Diffuse path, including path with tilted forward scatterings (see Figure 2(b)).

Let us consider contributions of each of these scenarios in the total reflected flux. To calculate this contribution we consider homogeneous medium with coefficients of absorption μ_a and scattering μ_s, respectively. To simplify our calculations we also consider normal (or almost normal) incidence of the external light flux.

2.2.1. Path with One Backward Scattering. Let us consider that each scattering event occurs on the distance $l_s = 1/\mu_s$ (this assumption can be relaxed; however, it will complicate the calculations). Such as forward and almost forward scattering events dominate substantially, so we can consider the following quasi-1D model (the path is almost ballistic; however, it can slightly deviate in transverse directions): if the photon was scattered n times forwardly (with probability $1 − p$) and then was scattered backwardly (with probability p), then to reach the surface again it must undergo additionally n forward scattering events (see Figure 2(a)). The probability of this $n − 1 − n$ path is $p(1 − p)^{2n}$. However, here we did not take into account yet that during this path the photon flux undergoes also absorption.

To take into account absorption let us consider the photon flux propagation between two scattering events. The intensity of out coming flux $I_{\text{out}} = I_{\text{in}} \exp(−\mu_a l_s) = I_{\text{in}} \exp(−\mu_a/\mu_s)$. So, we can attribute an absorption multiplier $a = \exp(−\mu_a/\mu_s)$ to each pathway between two closest scattering events.

Thus in previously considered case of $n − 1 − n$ scatterings we have to multiply scattering probability $p(1 − p)^{2n}$ on probability to survive in absorption between $2n + 1$ scattering events: a^{2n+2}. So, the total contribution of this path to the total backward flux will be $p(1 − p)^{2n}a^{2n+2}$.

It is easy to calculate the total contribution of all paths with single backward scattering (coefficient of reflectance based on superposition of the paths with single backward scattering events):

$$R_1 = pa^2 + \ p(1 − p)^2 a^4 \cdots + p(1 − p)^{2n}a^{2n+2} \cdots$$

$$= \frac{pa^2}{1 − (1 − p)^2 a^2}. \tag{3}$$

We can also develop continuous version of our approach. For this reason we in (3) switch from summation to integration: $\sum_{n=0}^{\infty} \Rightarrow \int dn$. Thus, if we consider a semifinite tissue, then we can integrate from 0 to infinity, and our integral is equal to

$$R_1 = \frac{pa^2}{2\left((\mu_a/\mu_s) − \ln(1 − p)\right)}. \tag{4}$$

2.2.2. Path with Multiple Backward Scattering. It is easy to see that if we exclude purely diffuse paths and limit ourselves to quasi-1D quasiballistic model, then the total number of backward scattering events must be odd. So, a diagram with three backward scattering events will be the next order one (see Figure 3).

These lowest order diagrams will be proportional to p^3a^6. To each diagram with the total path length $2N$ we can assign a weight $W(2N, 3)$ the number of different diagrams with the same length $2N$ and 3 backward scatterings. This weight can be estimated from the geometry of this path. For our $n_1 − 1 − n_2 − 1 − n_3 − 1 − n_4$ scattering path (here n_i is the i-th path length between two backward scattering events) we can write $n_1 + n_3 = n_2 + n_4 = N$. Thus, we have $(N − 2)^2$ nonequivalent diagrams (such as $1 < n_1, n_4 < N$). And the contribution of these diagrams can be approximated as $(N − 2)^2 p^3(1 − p)^{2N−4}a^{2N}$. It is easy to see that for strongly anisotropic body tissues with blood we can neglect them in the future. A more accurate estimation of multiscattering contribution is provided in the Appendix. However, given that $p \ll 1$, we can expect that for $\mu_a/\mu_s > 0.01$, the impact of all p^{2l+1}, where $l \geq 1$ is rather small. For small g (less than 0.5 which does not represent significant interest for biological tissues), multiple backward scattering can have measurable impact; however, the validity of quasi-1D model for $g < 0.5$ is very questionable and this impact will likely be masked by the contribution of diffuse paths. We will discuss applicability of this quasi-1D model later.

2.2.3. Diffuse Path. Contribution of diffuse paths is well known in diffusion theory and can be calculated using various approaches. We can make some estimations of reflectance near the light entry point by visualizing light propagation as a random walk on cubic lattice with the unit size $l'_s = 1/\mu'_s$ [12]. Thus, if the light entered the tissue at point $(x, y, 0)$, then it travels to $(x, y, 1)$ and from that point it occurs random walk through the media. However, to exit tissue in the close vicinity of the entry point it should travel again through $(x, y, 1)$ to $(x, y, 0)$. To take into account absorption and scattering for
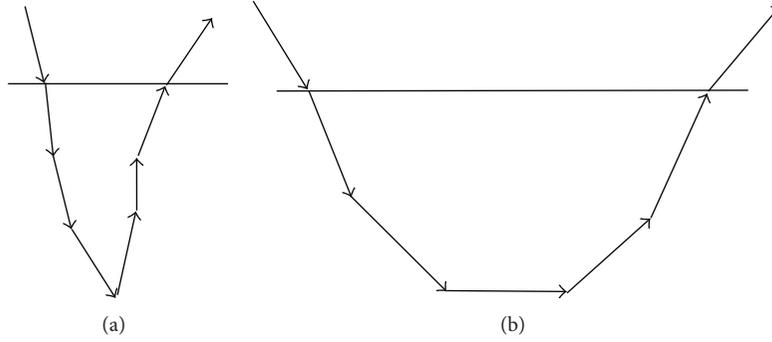
FIGURE 2: Paths with backward scattering (a) and "tilted" forward scatterings (b).
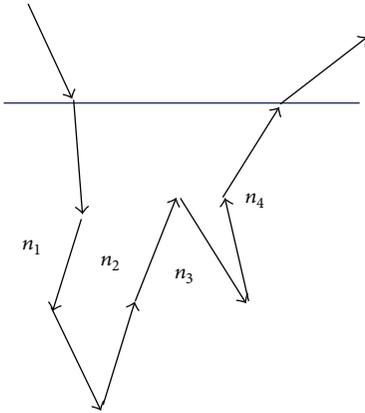
FIGURE 3: 3-fold backward scattering.

each edge of the lattice we can assign attenuation multiplier $\exp(-(\mu_a + \mu_s')l_s') = \exp(-1/a')$, where $a' = \mu_s'/(\mu_s' + \mu_a)$ is the reduced albedo. So, the reflectance at the light entry point $(x, y, 0)$ in the lattice model will be $R_d = \exp(-2/a')(1/6+C)$, where 1/6 is attributed to the shortest path $((x, y, 0) \rightarrow (x, y, 1) \rightarrow (x, y, 0))$ and C is the contribution of all paths with nonzero length which started and finished at $(x, y, 1)$. It is easy to see that to reach the surface the photon has to undergo $2/(1 - g)$ scattering events. Thus, in the case of small reduced albedo (e.g., $a' < 0.67$ if the absorption is high or g is close to 1 in case of moderate absorption) the impact of diffuse paths can be quite low.

Thus, we have found that the single backward scattering can dominate among scattering mechanisms in turbid tissues under certain conditions, such as high absorption. A more accurate comparison of areas of applicability of diffuse approximation and SBS will be presented later, when we estimate the penetration depth.

3. Results

Now, we can apply the developed single backward scattering model (SBS) to calculate tissue reflectance and sampling depth.

3.1. Diffuse Reflectance. We will calculate tissue reflectance in SBS model and compare it with the K-M, diffuse approximation, and path integrals models. To compare models we will consider a semi-infinite media with matched boundary conditions.

3.1.1. Kubelka-Munk Model. One of the standard approaches to calculate reflectance in the geometry with homogeneous and totally diffuse illumination is the Kubelka-Munk model (K-M model) [13]. The K-M model has been widely used for multiple-scattering calculations in paper, paint, plastic, and textile industries for many years mostly due to its simple use and its acceptable prediction accuracy [14]. The K-M model works best for optically thick materials where more than 50% of light is reflected and less than 20% is transmitted.

Using the standard notation: s-scattering per unit length, k-absorption per unit length the reflection coefficient R for the semi-infinite media is equal to

$$R_{\mathrm{KM}} = 1 + \frac{k}{s} - \sqrt{\left(1 + \frac{k}{s}\right)^2 - 1}. \tag{5}$$

It is easy to see that in terms of our model k is the coefficient of absorption μ_a, while s is the coefficient of backward scattering per unit length. Thus, s is equal to the scattering coefficient μ_s times the probability of backward scattering p: $s = p\mu_s$

3.1.2. Path Integrals. It was found by Perelman et al. [6] that the steady-state diffuse reflectance for semi-infinite media using path integrals formalism is given by a formula

$$R_{\mathrm{PI}} = \exp\left[-2\left(\beta_{\mathrm{eff}}\frac{-\ln a}{1 - g}\right)^{1/2}\right], \tag{6}$$

where a is the albedo ($a = \mu_s/(\mu_s + \mu_a)$) and β_{eff} is the numeric coefficient ($\beta_{\mathrm{eff}} = 2.17$ and 2.47 for $g = 0.757$ and 0.908, resp.).

3.1.3. Diffuse Approximation. For collimated light beam illumination developed by Reynolds et al. [15] and Groenhuis et al. [16] in diffusion dipole model [17] the reflectance is given by

$$R_d = \frac{\mu_s'}{2\mu_t'} \exp\left(-\mu_{\text{eff}}\left(z_0 + 2h\right)\right), \tag{7}$$

where $z_0 \approx 1/\mu_t'$ and $h \approx 2/3\mu_t'$ for refractive index matching (here $\mu_t' = \mu_a + \mu_s'$).

The tissue reflectance predicted by this model is significantly smaller (see Figure 4) than those of provided by K-M, path integrals, and SBS, which means that this approach can be likely used just for spatially resolved geometries. The simplified expression 8.7 from [9] (index matching at the surface)

$$R_d = \frac{a'}{1 + 2\left(1 - a'\right) + (5/3)\sqrt{3\left(1 - a'\right)}}, \tag{8}$$

where $a' = \mu_s'/(\mu_s' + \mu_s)$ is the reduced albedo, provides much more reasonable approximation.

On Figure 4 one can see the total diffuse reflectance as a function of μ_a/μ_s ratio for different models: diffuse approximation model (8) (squares), SBS (rhomboids), path integrals (triangles), Kubelka-Munk (crosses), and diffusion dipole model (stars).

3.2. Sampling Depth. By definition the expression for the reflectance of tissue in single backward scattering approximation (3) is the sum of infinite number of terms. We can compare this expression with the contribution into reflectance of the first m-terms (scattering layers):

$$R_{1,m} = \frac{pa^2}{1 - \left(1 - p\right)^2 a^2}\left(1 - \left(1 - p\right)^{2m} a^{2m}\right). \tag{9}$$

So, if we limit ourselves by some threshold criteria (say we are interested in $1 - \alpha = 95\%$ of total contribution) we can easily calculate the number of the most contributing m-term:

$$\left(1 - p\right)^{2m} a^{2m} = \alpha. \tag{10}$$

Thus,

$$
\begin{aligned}
m &= \frac{\ln\left(\alpha\right)}{2\ln\left(a\left(1 - p\right)\right)} \\
&= \frac{\ln\left(\alpha\right)}{2\left(-\mu_a/\mu_s + \ln\left(1 - p\right)\right)} \approx \frac{-\ln\left(\alpha\right)}{2\left(\mu_a/\mu_s + p\right)}.
\end{aligned} \tag{11}
$$

On Figure 5 we can see the dependence of light penetration depth as a function of μ_a/μ_s for different α and g.

So, it is easy to see that information is being gathered from relatively thin surface scattering layer which is not deeper than 0.5–1 mm, while the major part of information propagates from the top 2-3 transport depths (0.1 mm). Therefore, 2–5 upper scattering layers (m-terms) contribute

more than 50% in the total reflected flux. Also, the higher absorption is (or the lower g), the higher contributors the upper layers are.

Based on the previous discussion we can estimate the area of applicability of the single backward scattering approach. In order to do it, we take into account that for the quasi-1D model the transversal component of scattering expected to be much smaller than the scattering along the initial path. If we take into account that g-factor can be used as a proxy of the transverse component, then the longitudinal component after m scatterings will be g^m and thus applicability of the theory can be formulated as $1 - g^m$.

4. Discussion

Let us discuss how these results can be applied to various illumination geometries. Comparison between different models gives us important insights about scattering scenarios in the media. For instance, the difference between Kubelka-Munk (single + multiple backward scatterings) and single backward scattering (SBS) approaches gives an estimation of impact of multiple backward scatterings.

4.1. Point Illumination with a Collimated Light. This geometry is directly addressed by all 4 models. This configuration is a typical measurement setup for numerous optical spectroscopy studies in clinics [1]. From Figure 5 it can be seen that the Kubelka-Munk model approximates well the diffuse reflectance calculated using path integrals and diffuse model in a wide range of parameters. SBS gives results close to Kubelka-Munk and path integrals within $\mu_a/\mu_s = 0.01$–0.1 range, particularly for high anisotropy. It means that the single back scattering dominates in this range, while within the ultralow absorption range ($\mu_a/\mu_s = 0.001$–0.01) the other mechanisms dominate, namely, multiple backward scattering and diffusion.

As the diffuse approximation model predicts lower reflectance, one can expect that in the close vicinity of the light source (within the transport length, $l < 1/(\mu_a + \mu_s')$), the backward scattering scenarios will dominate and the primary part of the reflectance spectra will be contributed by the backward scattering. For the sites located further away from the light source, the diffuse approximation scenario will dominate.

4.2. Broad Illumination with a Collimated Light. This geometry (with a beam diameter wider than the transport length, $d > 1/(\mu_a + \mu_s')$ and collection from the illuminated area) can be considered as a superposition of multiple collimated point sources; thus, most results from the previous discussion are directly transferable. In particular, we can expect that the backward scattering will contribute more than the diffuse paths approaching from the remote part of the photon paths. Thus, in this scenario in case of high absorption ($a' < 0.67$) primarily we collect backward scattered photons.

As it has been just shown the sampling depth is rather small, and the major impact is attributed to only a couple of surface layers (m-terms).

(a)

(b)
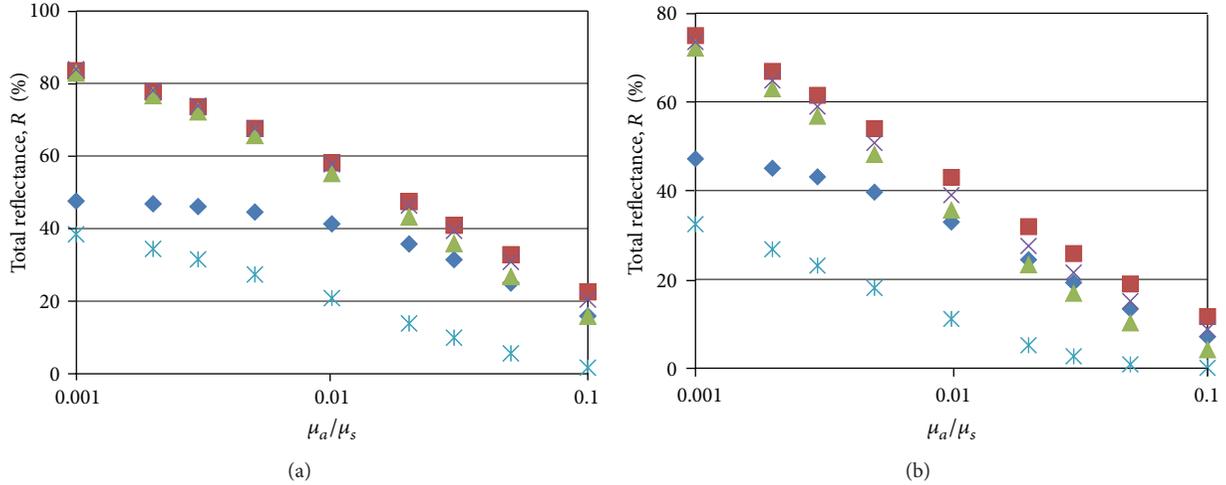
FIGURE 4: Total diffuse reflectance as a function of μ_a/μ_s ratio for different models ($g = 0.757$ (a), $g = 0.908$ (b)): diffuse approximation (8) (squares), single back scattering model (SBS) (rhomboids), path integrals (triangles), Kubelka-Munk (crosses), and diffusion dipole model (7) (stars).
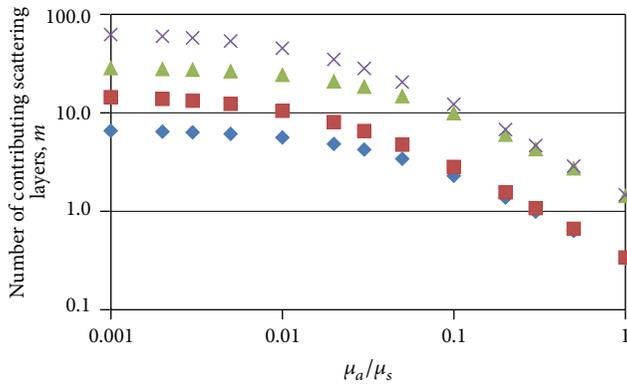
FIGURE 5: Number of contributing m-terms (scattering layers or transport depths) as a function of μ_a/μ_s ratio for different α and g. $\alpha = 0.5$, $g = 0.8$ (rhomboids), $\alpha = 0.5$, $g = 0.9$ (squares), $\alpha = 0.05$, $g = 0.8$ (triangles), $\alpha = 0.05$, and $g = 0.9$ (crosses).

Thus, based on this discussion we can expect that SBS can be applicable for interpretation of spectra obtained by endoscopic measurements with wide area illumination. In this case, blood, which is highly absorbing in visual spectra, is much closer to the surface than in skin, and backward scattering paths may dominate over longer diffuse paths.

4.3. Single Backward Scattering Approach versus Kubelka-Munk Model. These models are relatively close to each other (e.g., they both consider scattering as primarily forward and backward, they both can consider layered geometries, and they both can take into account realistic phase function or probabilities can be calculated directly from the Mie theory). The major difference consists in that the Kubelka-Munk model does not take into account the refractive index mismatched boundary conditions, although Saunderson took the internal reflection on the border with the opaque substrate into account [18]. However, the mismatched boundary

conditions can be naturally integrated into SBS approach through additional reflection coefficients on the media layer interfaces.

The advantage of Kubelka-Munk model is that it incorporates multiple backward scattering. Consequently, in some specific geometries and conditions this model can be used to gauge the applicability of the single backward scattering (SBS) model.

It is easy to see (Figure 4) that the single backward scattering model matches Kubelka-Munk predictions perfectly for $\mu_a/\mu_s = 0.02$–0.3. Thus, we can conclude that we can neglect the multiple backward scattering events for this range of parameters and the single backward scattering approach is applicable for biological tissues with $\mu_a/\mu_s > 0.02$.

4.4. The Single Backward Scattering Model and Diffuse Approximation. SBS and the scattering-dominant limit of Radiation Transport Model are complimentary to each other, such as they have different areas of applicability (see Figure 6).

The diffusion scattering approach is not applicable on the distances shorter than inversed reduced scattering coefficient $1/\mu_s'$. It is related to the fact that light propagation on the short distances (due to highly anisotropic nature of scattering) cannot be considered as truly random walk processes, and consequently the law of large numbers is not applicable here. The diffusion approximation is more applicable for the photon paths with more than $1/(1 - g)$ scattering events, after which the photon does not "remember" its original direction and scattering can be considered isotropic. However, this number in case of tissues with high blood content can be quite big (compare 200 for pure blood with 5 for dermis). For shorter distances, the photon propagation more resembles ballistic transfer than random walk process. The presented single backward scattering model can incorporate also features typical for short distances, and consequently is applicable for such shorter distances as well.
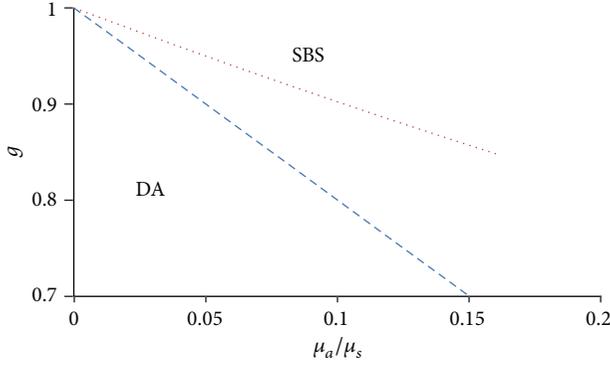
FIGURE 6: Areas of applicability of diffuse approximation (DA) and single backward scattering (SBS) models for biological tissues. Dashed line is $a' = 0.67$ and dotted line is $g^m = 0.7$ (see (11) for definitions).

Also, it is known that diffuse approximation gives good agreement with Monte Carlo when $g < 0.99$ and reduced albedo $a' > 0.67$ With higher absorption, the diffuse approximation predicts much higher reflectance than MC. Longer optical paths, typical for diffusion, have smaller impact than the backscattering paths. This is the area where SBS is particularly applicable to fill out the shortage in analytical approach tool spectrum.

5. Conclusions and Future Work

Single backward scattering approximation allows developing an analytical approach which can take into account mismatched boundary conditions and multilayer geometry and can be used for real-time spectral processing.

The single backward scattering model is probably applicable on distances shorter than $1/\mu'_s$ from the source in point illumination by collimated light and at certain scenarios in broad illumination by collimated light. The SBS approach can be potentially applied for the distances between the transport and reduced scattering domains—the remaining "grey" area where an analytical approach is in great demand.

Monte Carlo and experimental verification will be in focus of our future work.

Appendix

Exact Calculations for 3-, and 5-Fold Backward Scattering

Now we consider case $l = 1$ (3-fold backward scattering; see Figure 3). For this geometry we have $n_1 + n_3 = N, n_2 + n_4 = N$, where $n_1, n_2, \ldots, n_4 > 0$. For each $n_1 > 1, n_2$ can vary from 1 to $n_1 - 1$. Thus, we have $W(2N, 3) = \sum_{n=1}^{N-1}(n-1)$ nonequivalent paths, which is equal to $(1/2)(N-1)(N-2)$.

If we define new variables $x = a(1 - p), k = N - 2$, we have an exact expression for the impact of 3-fold backward scattering:

$$R_3 = p^3 a^4 \sum_{k=0}^{\infty} \frac{1}{2} k(k+1) x^{2k}. \tag{A.1}$$

This expression can be rewritten as

$$R_3 = \frac{p^3 a^3 x}{4} \sum_{k=1}^{\infty} 2k(k+1) x^{2k-1}. \tag{A.2}$$

It is easy to see that this expression can be transformed into

$$R_3 = \frac{p^3 a^3 x}{4} \frac{d}{dx} \sum_{k=1}^{\infty} (k+1) x^{2k}. \tag{A.3}$$

Taking into account that the sum in above expression is the expansion of $(1/(1 - x^2)^2) - 1$, we have a transformed expression for (A.1):

$$R_3 = \frac{p^3 a^4 x}{4} \frac{d}{dx} \left(\frac{1}{(1 - x^2)^2} - 1 \right). \tag{A.4}$$

Differentiating over x and substituting x, we finally have an expression for 3-fold backward scattering:

$$R_3(p, a) = p^3 a^4 \frac{a^2(1 - p)^2}{\left(1 - (a(1 - p))^2\right)^3}. \tag{A.5}$$

We can also determine the combinatory term for $l = 2$ (5-fold backward scattering). First, we estimate range for n_1: $0 < n_1 < N - 1$. Then, for chosen n_1, n_2 can vary in the range $0 < n_2 < n_1$. For chosen n_1 and n_2, n_3 can vary in the range $0 < n_3 < N - n_1$. For chosen n_1, n_2, and n_3 we have a range for n_4 $0 < n_4 < n_1 + n_3 - n_2$. Finally, for chosen n_1, n_2, n_3, and n_4, we have one trajectory with $n_5 = N - n_1 - n_3$ and $n_6 = N - n_2 - n_4$. Thus, to calculate all combinations for given N we have an expression

$$W(2N, 5) = \sum_{n_1=1}^{N-2} \sum_{n_2=1}^{n_1-1} \sum_{n_3=1}^{N-1-n_1} \sum_{n_4=1}^{n_1+n_3-1-n_2} 1. \tag{A.6}$$

After some easy transformations finally we have

$$W(2N, 5) = \frac{1}{12}(N - 2)^2 (N - 1)(N - 3). \tag{A.7}$$

Making the same substitutions and applying the same approach with differentiating of the series (see (A.2)-(A.3)) 4 times we can get the following expression for R_5:

$$R_5 = \frac{p^5 a^6}{12} \frac{x}{2} \frac{d}{dx}$$
$$\times \left\{ \frac{1}{2x^3} \frac{d}{dx} \left\{ \frac{x^3}{2} \frac{d}{dx} \left\{ \frac{x}{2} \frac{d}{dx} \left\{ \frac{1}{1 - x^2} - 1 - x^2 \right\} \right\} \right\} \right\}. \tag{A.8}$$

After differentiating and substituting x we finally get

$$R_5 = p^5 a^6 \frac{1 + a^2(1 - p)^2}{\left(1 - (a(1 - p))^2\right)^5}. \tag{A.9}$$

Single, 3-fold and 5-fold backward scatterings are compared on Figure 7. It is easy to see that multiple backward scattering is negligible in the whole range of g even in case of low absorption ($a = 0.95$).
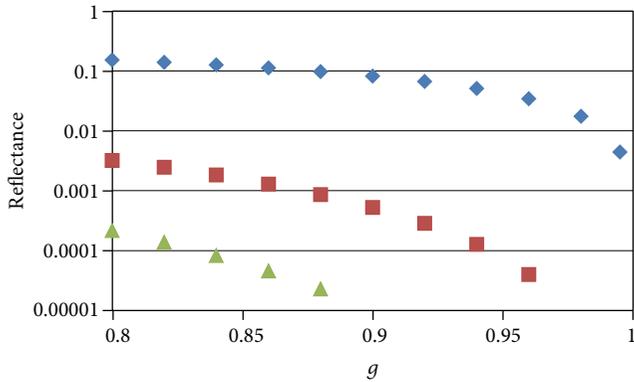
FIGURE 7: Dependence of single backward scattering (rhomboids), 3-fold (squares) and 5-fold (triangles) backward scattering as a function of $g (a = 0.95)$.

Conflict of Interests

The authors declare that there is no conflict of interests regarding the publication of this paper.

References

[1] V. V. Tuchin, *Tissue Optics: Light Scattering Methods and Instruments for Medical Diagnosis*, vol. 166, SPIE Press, Bellingham, Wash, USA, 2nd edition, 2007.

[2] S. A. Prahl, M. Keijzer, S. L. Jacques, and A. J. Welch, "A Monte Carlo model for light propagation in tissue," in *Dosimetry of Laser Radiation in Medicine and Biology*, G. Muller and D. Sliney, Eds., vol. 5 of *SPIE Series*, pp. 102–111, 1989.

[3] S. A. Prahl, M. J. C. van Gemert, and A. J. Welch, "Determining the optical properties of turbid media by suing the adding-doubling method," *Applied Optics*, vol. 32, no. 4, pp. 559–568, 1993.

[4] A. Kienle, L. Lilge, M. S. Patterson, R. Hibst, R. Steiner, and B. C. Wilson, "Spatially resolved absolute diffuse reflectance measurements for noninvasive determination of the optical scattering and absorption coefficients of biological tissue," *Applied Optics*, vol. 35, no. 13, pp. 2304–2314, 1996.

[5] R. Reif, O. A'Amar, and I. J. Bigio, "Analytical model of light reflectance for extraction of the optical properties in small volumes of turbid media," *Applied Optics*, vol. 46, no. 29, pp. 7317–7328, 2007.

[6] L. T. Perelman, J. Wu, I. Itzkan, and M. S. Feld, "Photon migration in turbid media using path integrals," *Physical Review Letters*, vol. 72, no. 9, pp. 1341–1344, 1994.

[7] R. P. Feynman and A. R. Hibbs, *Quantum Mechanics and Path Integrals*, McGraw-Hill, New York, NY, USA, 1965.

[8] T. Harrison, J. C. Ranasinghesagara, H. Lu, K. Mathewson, A. Walsh, and R. J. Zemp, "Combined photoacoustic and ultrasound biomicroscopy," *Optics Express*, vol. 17, no. 24, pp. 22041–22046, 2009.

[9] A. Kim and B. C. Wilson, "Measurement of *ex vivo* and *in vivo* tissue optical properties: methods and theories," in *Optical-Thermal Response of Laser-Irradiated Tissue*, A. J. Welch, Ed., pp. 267–319, Springer, Dordrecht, The Netherlands, 2nd edition, 2011.

[10] S. C. Kanick, D. J. Robinson, H. J. Sterenborg, and A. Amelink, "Monte Carlo analysis of single fiber reflectance spectroscopy: photon path length and sampling depth," *Physics in Medicine and Biology*, vol. 54, no. 22, pp. 6991–7008, 2009.

[11] L. G. Henyey and J. L. Greenstein, "Diffuse radiation in the galaxy," *Nature*, vol. 147, no. 3733, pp. 613–626, 1941.

[12] G. Saiko and A. Douplik, "Real-time optical monitoring of capillary grid spatial pattern in epithelium by spatially resolved diffuse reflectance probe," *Journal of Innovative Optical Health Sciences*, vol. 5, no. 2, Article ID 1250005, 9 pages, 2012.

[13] P. Kubelka and F. Munk, "Ein beitragzur optik der far-banstriche," *Zeitschrift für Technische Physik*, vol. 12, pp. 593–601, 1931.

[14] V. Džimbeg-Malčić, Ž. Barbarić-Mikočević, and K. Itrić, "Kubelka-Munk theory in describing optical properties of paper (I)," *Technical Gazette*, vol. 18, no. 1, pp. 117–124, 2011.

[15] L. Reynolds, C. Johnson, and A. Ishimaru, "Diffuse reflectance from a finite blood medium: applications to the modeling of fiber optic catheters," *Applied Optics*, vol. 15, no. 9, pp. 2059–2067, 1976.

[16] R. A. J. Groenhuis, H. A. Ferwerda, and J. J. T. Bosch, "Scattering and absorption of turbid materials determined from reflection measurements," *Applied Optics*, vol. 22, no. 16, pp. 2456–2462, 1983.

[17] T. J. Farrell, M. S. Patterson, and B. C. Wilson, "A diffusion theory model of spatially resolved, steady-state diffuse reflectance for the noninvasive determination of tissue optical properties *in vivo*," *Medical Physics*, vol. 19, no. 4, pp. 879–888, 1992.

[18] J. L. Saunderson, "Calculation of the color pigmented plastics," *Journal of the Optical Society of America*, vol. 32, no. 12, pp. 727–729, 1942.

Research Article

Multiorganelle Localization of Metallated Phthalocyanine Photosensitizer in Colorectal Cancer Cells (DLD-1 and CaCo-2) Enhances Efficacy of Photodynamic Therapy

Palesa Rose Sekhejane, Nicolette Nadene Houreld, and Heidi Abrahamse

Laser Research Centre, Faculty of Health Sciences, University of Johannesburg, P.O. Box 17011, Doornfontein 2028, South Africa

Correspondence should be addressed to Heidi Abrahamse; habrahamse@uj.ac.za

Colorectal cancer is the third most commonly diagnosed cancer. Amongst treatments that have been explored, photodynamic therapy (PDT) is a treatment that is of interest as it poses ideal advantages such as affinity for cancer cells. This study aimed to determine the correlation between the localization site of a sulfonated zinc phthalocyanine ($ZnPcS_{mix}$) photosensitizer (PS) and its associated cell death pathway *in vitro* in colorectal cancer cell lines (DLD-1 and CaCo-2). Visible morphological changes were observed in PDT treated cells after 24 h. Reactive oxygen species (ROS) were detected and visualized 1 h after PDT. $ZnPcS_{mix}$ was predominantly localized in lysosomes and partially in the mitochondria. FITC Annexin V staining showed a significant decrease in the percentage of viable DLD-1 and CaCo-2 cells 24 h after PDT, with an increase in apoptotic cell population. Moreover, there was a significant increase in both cathepsin D and cytochrome C at 1 and 24 h. In conclusion, $ZnPcS_{mix}$ showed the ability of inducing apoptotic cell death features in PDT treated cells.

1. Introduction

Cancer is defined as a group of diseases that have an unbalanced rate between apoptosis and proliferation. Rapid multiplication of abnormal cells may be caused by various factors ranging from genetic to external factors such as chemicals or diet [1]. Colorectal cancer is amongst the top ranking cancers that have a high mortality rate worldwide [1]. It occurs as a result of genetic and epigenetic changes of normal glandular epithelial cells into invasive adenocarcinoma [2]. The treatment for colorectal cancer remains a challenge due to the high metastatic incidence and recurrence of the disease [3], as well as toxicity caused by chemotherapeutic drugs to noncancerous cells. Colectomy, chemotherapy and radiation are regarded as primary treatment methods. However, there are concerns that these treatments commonly result in poor quality of life, lower overall survival rate, and resistance to treatment [4, 5]. Thus, it is essential to develop other therapeutic strategies that may potentially enhance the quality of life and eventually improve survival rate.

Photodynamic therapy (PDT) has been under investigation as an alternative treatment modality to adjuvant chemotherapy or chemoradiotherapy. PDT utilizes three components, namely, light with wavelengths ranging between 650 and 750 nm, a photosensitive drug (referred to as a photosensitizer, PS) capable of intracellular localization, and molecular oxygen, which renders the modality effective [6]. It is a comparatively better modality than surgery, radiotherapy, and chemotherapy as it is a minimally invasive therapy. In addition to being a minimally invasive treatment, a good PS should possess a low dark (inactive) and administrative toxicity [7]. Additionally, a well-formulated PS has a high affinity for cancer cells due to the high content of low density lipoprotein (LDL) receptors in cancer cells which enhances uptake of the PS [8–10]. PDT is an ablative energy requiring process that utilizes natural or synthetic structures that are photosensitive and capable of absorbing energy in the form of light. Castano et al. [7] suggested that an ideal PS should absorb light in the red to near infrared spectra,

as shorter wavelengths have lower tissue penetration capacity [11, 12].

Although PDT was discovered over a century ago, it is has become a field of interest with progressive developments and advances, especially with regard to the development of PSs. The photodynamic reaction occurs when the PS is activated by absorption of energy from light (at a specific wavelength) in the form of photons, thereby producing reactive oxygen species (ROS) which then result in the photodynamic reaction [13]. Light interaction with the PS is one of the most crucial factors that determine the efficacy of treatment [14]. The photodynamic reaction can occur via two known photochemistry pathways. The first pathway, usually termed Type I, produces free radicals and ROS through electron transfer between the PS triplet state and surrounding molecules. The Type II reaction produces singlet oxygen ($^1O_2$) through energy transfer from the PS ground state to surrounding oxygen molecules [7, 15]. Both pathways can occur concurrently, although the ratio may depend on the type of PS, binding affinity of the substrate, and oxygen and substrate concentration. However, the Type II reaction is considered the most frequent pathway responsible for cell death [14, 16–18].

Oxidative stress caused by PDT is known to cause membrane lipid peroxidation or rupture and DNA damage that may lead to apoptosis or necrosis [19]. Apoptosis occurs through a series of intracellular and extracellular biochemical milieu. Lysosomes and mitochondria are vital membranous organelles that also play a role in cell death dynamics. PSs that target mitochondria have been thought to be more effective as opposed to those that localize in other organelles [20, 21] as it is believed that they can induce apoptosis directly. However, lysosomal targeting PSs have also been emerging as good candidates [22, 23]. Lysosomes have an acidic environment and host hydrolases that have the potential to degrade proteins and the entire cell upon leakage [24]. Amongst well-studied lysosomal hydrolases is cathepsin D which belongs to the aspartyl proteases [25]. Besides its catalytic role, cathepsin D also participates in apoptosis. When triggered by cytotoxic factors, depending on the environment, it can induce apoptosis or inhibit it [26, 27]. Permeabilization of the lysosomal membrane can be activated by oxidative stress which usually leads to mitochondrial outer membrane destabilization and caspase activation through spillage of its acidic contents or catalytic enzymes [28, 29]. Subsequently, this may lead to leakage of cytochrome C from mitochondria into the cytosol and thus activate caspases.

Cellular uptake of the PS is a fundamental factor in order for the drug to be effective and its intracellular localization site may help understand the mode of cell death as molecular singlet oxygen may be primarily formed by PDT in that preferred organelle. Zinc phthalocyanines (ZnPcs) have desirable PDT application qualities as they are said to have an intensive absorption of light in the visible red region and high singlet and triplet production [30]. Barr et al. used an aluminium sulphonated phthalocyanine (AlSPc) for the treatment of dimethylhydrazine-induced colon cancer in Wistar rats. They reported a significant eradication of the colonic mucosa tumour with necrosis and further suggested that it may be useful as an adjunctive treatment as they doubt that PDT alone will have magnanimous effects for deep seated tumours such as colon cancer *in vivo* [31]. Woodhams et al. conducted a study using bacteriopherophorbide (Tookad) based photodynamic therapy (PDT) in the colonic mucosa of the Hooded Lister rats [32]. They reported short drug light interval as an advantage; however, the treatment induced necrosis accompanied by inflammatory response three days after PDT [32].

In this study, we sought to determine the correlation between the localization site of sulfonated zinc phthalocyanine (ZnPcS$_{mix}$) in colorectal cancer cells (DLD-1 and CaCo-2) and mode of cell death induced after PDT.

2. Materials and Methods

2.1. Cell Culture. This research was approved by the Academic Ethics Committee of the Faculty of Health Sciences, University of Johannesburg, under ethics clearance number AEC81/2009. Commercially obtained colorectal cancer cells were used (CaCo-2 ATCC HTB-37 and DLD-1 ATCC CCL-221). CaCo-2 cells were cultured in Dulbecco's modified Eagle's media (DMEM, Sigma-Aldrich, D6429) with 1.2 g/L sodium carbonate, supplemented with 10% foetal bovine serum (FBS, Gibco, 306.00301), nonessential amino acids (NEAA, Gibco, 11140), 0.5 mM sodium pyruvate (Gibco, 11360), 2.5 mM L-glutamine (Gibco, 25030), 1% antibiotic (penicillin-streptomycin, Gibco, 15140), and 1% antifungal (amphotericin-B, Gibco, 104813). DLD-1 cells were cultured in Dulbecco's modified Eagle's media and Ham's nutrient mixture F-12 (DMEM/F12, Sigma-Aldrich, D6421), supplemented as for CaCo-2 cells. Cultures were maintained in 5% CO_2 and 85% humidity at 37°C. Once cells reached 80–90% confluence, they were harvested and seeded at a density of 5×10^4 in 3 mL media into sterile culture dishes, with a diameter of 3.4 cm. Cells were allowed to attach overnight.

2.2. PDT Experiments. The ZnPcS$_{mix}$ used in this study contained various sulfo groups that have been reported to enhance the solubility [33]. The photochemical and photophysical properties of the ZnPcS$_{mix}$ in phosphate buffered saline (PBS) were determined at the Department of Chemistry, Rhodes University, South Africa. ZnPcS$_{mix}$ had a fluorescence quantum yield (Φ_F) of 0.16; triplet quantum yield (Φ_T) of 0.53; singlet oxygen quantum yield ($\Phi\Delta$) of 0.45, and triplet lifetime (τ_T) of 2.95 μs [33]. Cells were divided into three control groups: untreated cells, that is, cells that neither received irradiation nor PS, cells receiving laser irradiation alone (5 J/cm^2), and cells receiving PS alone (ZnPcS$_{mix}$) at a concentration of 20 μM. The test group received both PS and irradiation (PDT). Cells that did not receive laser irradiation were sham irradiated. After cells had attached, they were rinsed in Hank's Balanced Salt Solution (HBSS, Invitrogen, 10-543F) and fresh media were added to a volume of 1 mL before the addition of ZnPcS$_{mix}$ or irradiation. Cells were irradiated in the dark from above in an open culture dish, using a continuous diode laser emitting light at a wavelength

Wavelength	680 nm
Average power output	42 mW
Light source	Diode
Illuminated area	9.1 cm^2
Irradiance	4.6 mW/cm^2
Irradiation time	18 min 6 s
Fluence	5 J/cm^2
Power meter	Coherent, fieldmate

of 680 nm; cells were irradiated with a fluence of 5 J/cm^2, as it was determined optimum from dose response studies [34]. A combination of 20 μM ZnPcS$_{mix}$ and a fluence of 5 J/cm^2 was used based on the morphological changes that resembled apoptosis as well as loss of cell viability beyond 40% as discussed in Manoto et al. [34]. Laser irradiation parameters are tabulated in Table 1. Biological responses were evaluated after further incubation for 1 or 24 h.

2.3. Cellular Morphology.

The effect of the PS or PDT on cell morphology was determined using an inverted light microscope (Wirsam, Olympus CKX41). Once digital images were recorded, cells were trypsinized using 1 mL/25 cm^2 of TrypLE Express (Invitrogen, 12605-028) and resuspended in HBSS (unless otherwise specified) to perform further assays.

2.4. Reactive Oxygen Species (ROS) Detection.

Oxidative stress caused by ZnPcS$_{mix}$ when activated by laser light was shown qualitatively by fluorescent staining of the cells with carboxy-H$_2$DCFDA Reactive Oxygen Species detection kit (Invitrogen, Image-iT, I36007). Cells cultured on cover slips were washed with warm HBSS and covered with 25 μM carboxy-H$_2$DCFDA working solution and incubated for 30 min at 37°C in the dark. Thereafter, cells were washed three times with HBSS and nuclei were counterstained with 0.1 mg/mL of DAPI (4$'$-6-diamidino-2-phenylindole, Sigma-Aldrich, D9564) for 1 min and washed. The ROS positive control was prepared according to the protocol prescribed by the manufacturer. Briefly, ROS was induced in CaCo-2 cells by adding 100 μM of *tert*-butyl hydroperoxide (TBHP) for duration of 1 h at 37°C. Cells that received neither PDT treatment, nor TBHP, nor laser irradiation were used as negative controls. Cells were stained for ROS detection 1 h after PDT by following the same procedure as mentioned above. Fluorescence was visualized using a Carl Zeiss Axio observer Z1 fluorescent microscope. Production of oxidation by carboxy-H$_2$DCFDA was viewed using $459_{Ex}/529_{Em}$ and DAPI $350_{Ex}/461_{Em}$ filters.

2.5. Intracellular Localization of ZnPcS$_{mix}$.

Fluorescence imaging was used to determine intracellular localization of ZnPcS$_{mix}$. Briefly, cells were cultured overnight on sterile cover slips placed in 3.4 cm diameter culture dishes. Cells were rinsed with warm HBSS before incubating with 1 μM ZnPcS$_{mix}$ in supplemented media for 1 h. Localization sites of ZnPcS$_{mix}$ were determined using fluorescent markers for intracellular organelles. For mitochondria, cells were stained with 50 nM MitoTracker Green FM (Invitrogen, M7514) and 75 nM LysoTracker Green DND-26 (Invitrogen, L7526) was used for lysosomes. Cells were then incubated for 15 min in the dark. Nuclei were counterstained with DAPI. Fluorescence was visualized using a Carl Zeiss Axio observer Z1 fluorescent microscope [34].

2.6. Lysosomal Cathepsin D.

Lysosomal protease cathepsin D was measured using an enzyme-linked immunosorbent assay (ELISA) kit (Biocombiotech, Cusabio Biotech, CSB-E09221h). Standard, blank (media only), or supernatants from experimental cells were added to their respective wells to a final volume of 100 μL. The plate was then incubated for 2 h at 37°C. Wells were aspirated and 100 μL of biotin-antibodyworking solution was added to each well and incubated for 1 h at 37°C. Each well was aspirated and washed with washing buffer three times. Horseradish peroxide- (HRP-) avidin working solution was then added to each well, and the plate was incubated for 1 h at 37°C. The plate was aspirated and washed three times and then tetramethylbenzidine (TMB) substrate was added and incubated for 30 min at 37°C. Stop solution was added and the plate was read at 450 nm absorbance using the Victor 3 multilabel microplate reader (Perkin-Elmer).

2.7. Cytosolic Cytochrome C.

Cytosolic human cytochrome C was measured by ELISA (Biocombiotech, eBioscience, BMS263/BMS263TEN). Cell lysates were prepared according to the manufacturer's protocol. Briefly, cells were centrifuged at 137 $\times$g for 15 min and washed with cold PBS. Cells were then resuspended in lysis buffer at a concentration of 1.5 $\times$ 10^6 per 1 mL and incubated at room temperature for 1 h with gentle shaking (10 rpm) using an orbital shaker (Labotech, Heidolph, Polymax 1040). Cells were then centrifuged at 200 $\times$g for 15 min. The supernatant was diluted 50-fold in assay buffer. Wells were washed with 400 μL of washing buffer prior to commencing. Samples and standards were added to their respective wells and biotin-conjugate was added. The plate was incubated at room temperature for 2 h and then washed as before. Streptavidin-HRP was added and incubated for 1 h at room temperature. Thereafter, the plate was washed and TMB substrate was added for approximately 10 min and the reaction was stopped. Absorbance was read at 450 nm using the Victor [3] multilabel microplate reader (Perkin-Elmer).

2.8. FITC Annexin V.

To determine the mode of cell death (necrosis or apoptosis), FITC Annexin V stain was used and the fluorescence was read using a flow cytometer (FACSAria). FITC Annexin V was used in conjunction with propidium iodide (PI) vital stain for necrotic cells. Cells were stained by washing detached cells twice with cold PBS and resuspended in 500 μL of 1x assay binding buffer. A volume of 100 μL was transferred into a 5 mL culture tube and incubated with 5 μL of FITC Annexin V and another 5 μL of PI. Cells were mixed by vortexing and incubated for 5 min on ice away from direct light. Then 400 μL of 1x binding buffer was added to all the

samples and were analyzed on the FACSAria flow cytometer by reading 10 000 events.

2.9. Statistical Analysis.

Each experiment was repeated four times ($n = 4$). Biochemical assays were done in duplicate and an average of the results was used. Statistics were analyzed using the SigmaPlot software version 8.0 (Systat Software) and the mean, standard deviation, standard error, and significant changes were calculated. Student t-test and one-way ANOVA were performed to determine the statistical difference between the controls and the experimental group. Statistical differences are shown in graphs as (*) $P < 0.05$, (**) $P < 0.01$, and (***) $P < 0.001$ and dispersion bars represent standard error.

3. Results and Discussion

3.1. Cellular Morphology.

Control cells did not show any morphological changes at both 1 and 24 h incubation periods (Figure 1). After 1 h incubation, morphology of PDT treated CaCo-2 cells appeared altered as compared to control cells. PDT treated cells appeared less uniform with loss of membrane integrity, although still intact; this was not observed in the DLD-1 cell line. Furthermore, after 24 h significant changes were noticed whereby cells appeared pyknotic, intact membrane, and condensed nuclei. Some cells had detached from the culture plate and lost their original morphological features compared to those incubated for 1 h and the control cells.

We have previously shown that DLD-1 colorectal cancer cells are sensitive to ZnPcS$_{mix}$ alone and PDT using the same PS [34]. The morphological features of DLD-1 and CaCo-2 control cells (untreated; 5 J/cm^2 or ZnPcS$_{mix}$) remained unchanged. However, morphological changes in the cells that received PDT treatment resembled that of apoptotic features as seen by the cells detaching from the culture dish surface, cellular shrinking, and an intact membrane [34]. Nonetheless, based on these morphological findings, it is not conclusive that the cells were definitely undergoing apoptosis.

3.2. Reactive Oxygen Species (ROS) Detection.

ROS such as hydroxyl radicals ($^{\bullet}$OH) and hydrogen peroxide (H_2O_2) are normally generated in small amounts in cellular organisms due to aerobic metabolism [34]. However, oxidative stress caused by increased ROS concentration is known to cause cellular damage, and ROS induction has also been implicated in apoptosis [35, 36]. ROS were detected in both cell lines that were treated with PDT as shown by distinct green fluorescence in the cytoplasm (Figure 2). PDT treated cells showed ROS fluorescence intensity similar to that of the positive control, thus proving that there was photooxidation after PDT. Based on this observation, we could anticipate that cell damage will follow eventually as ROS are known to kill cells by oxidizing lipid membranes and biomolecules [37, 38]. This was shown by the time dependent loss of cellular viability seen in PDT treated cells resulting in more than 40% cell death [34].

3.3. Intracellular Localization of ZnPcS$_{mix}$.

It is known that the localization site of a PS is of importance as it is indicative of where the initial damage will occur [20, 39]. When cells were visualized using fluorescent microscopy, ZnPcS$_{mix}$ predominantly localized in the lysosomes and to a lesser extent in the mitochondria (Figure 3).

Kessel and Luo deduced from their research that subcellular localization of the PS is a primary determinant of the cell death mechanism in PDT. Since the PS used in this study localizes predominantly in lysosomes and minimally in mitochondria, it is suggestive that ZnPcS$_{mix}$ has chemical properties or charge that target both lysosomes and mitochondria [40]. A study conducted by Kessel and Luo used two Zn based phthalocyanine PSs in human cervical squamous carcinoma (HeLa) and murine colon adenocarcinoma (CT26) cells; one was cationic and the other was anionic [41]. The cationic porphyrin PS was more effective than the anionic PS as the former localized in both lysosomes and mitochondria. They further reported enhanced efficacy at concentrations between 2 and 10 μM for the cationic PS and 10 and 50 μM for the anionic PS, both activated at a fluence of 10 J/cm^2. However, CT26 cells were not sensitive enough to the initial concentration of 5 μM cationic PS that was activated with 20 J/cm^2, although HeLa cells were sensitive [41]. Since our results coincide with Mroz et al.'s results, it may be suggested that the PDT of colon adenocarcinoma using phthalocyanines may require high dosage in order to render the therapy beneficial, provided that the PS has significantly low dark toxicity.

3.4. Lysosomal Cathepsin D.

At both time points, cathepsin D in DLD-1 and CaCo-2 cells that received irradiation alone (5 J/cm^2) did not result in significant changes when compared to untreated control cells, Table 2. After 1 h incubation, cathepsin D release was significantly increased in DLD-1 cells incubated with ZnPcS$_{mix}$ alone ($P < 0.05$) or those that received PDT ($P < 0.01$) in comparison to untreated control cells. A significant change was also noted in CaCo-2 cells that received PDT compared to controls that were untreated or irradiated (5 J/cm^2) ($P < 0.01$) and those that received ZnPcS$_{mix}$ alone ($P < 0.05$) after 1 h incubation. Comparing cathepsin D in PDT treated DLD-1 and CaCo-2 cells after 1 h incubation revealed a significant increase in CaCo-2 cells ($P < 0.05$).

After 24 h, both DLD-1 and CaCo-2 PDT treated cells had a significant increase in cathepsin D release ($P < 0.001$) when compared to all control cells (untreated, 5 J/cm^2 and ZnPcS$_{mix}$). Additionally, after 24 h, ZnPcS$_{mix}$ alone induced a significant increase in cathepsin D release in CaCo-2 cells when compared to cells that received irradiation alone ($P < 0.05$). Cathepsin D release in PDT treated DLD-1 cells had significantly increased after 24 h incubation in comparison to 1 h incubation ($P < 0.01$). Moreover, there was a significant difference between DLD-1 and CaCo-2 PDT treated cells after 24 h incubation ($P < 0.05$).

Assuming that a high concentration of ROS is formed around the lysosomes, increased amounts of H_2O_2 can
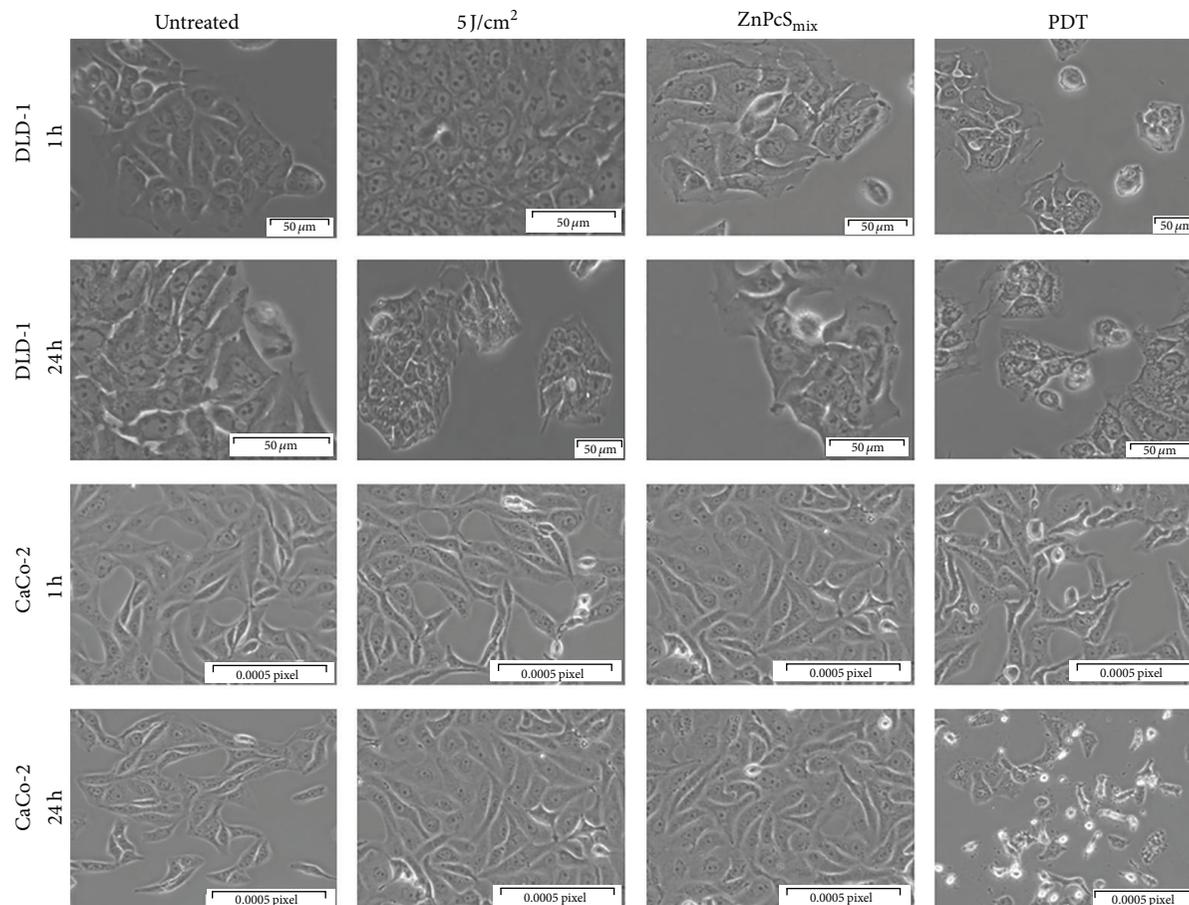
FIGURE 1: Morphology of DLD-1 and CaCo-2 cells after 1 or 24 h after PDT. After 1 h incubation after PDT, there were no significant visible differences in both DLD-1 and CaCo-2 cells, but, to some extent, cells showed membranal irregularity. After 24 h incubation, PDT cells appeared shrunken and rounded and had detached.

diffuse into lysosomes and react with intralysosomal metalloproteins (iron containing proteins) that have degraded as a result of acidic pH. Iron is then reduced and hydroxyl radicals are formed which promote lipid peroxidation, causing leakage of lysosomal contents [42]. Therefore, perhaps the cell death mechanism induced in the DLD-1 and CaCo-2 cells after PDT could primarily be initiated from lysosomes. Mroz et al. reported that lysosomal membrane destabilization is an early event in apoptosis as compared to mitochondrial membrane destabilization [43]. However, even if photodamage is initiated in the lysosomes, the mitochondrial pathway is responsible for cell death as the activation of Bid is as a result of lysosomal protease release as hypothesized by Kurz and colleagues, in their study that also used a phthalocyanine PS that localized in lysosomes [44]. Our findings are in accordance with Kurz and colleagues' findings [44].

Based on the localization pattern of the $ZnPcS_{mix}$, we determined that there was a proteolytic release of lysosomal aspartate cathepsin D, which is associated with cell death [45]. Oxidative stress can directly disrupt the lysosomal membrane. It has been hypothesized that limited release of lysosomal contents can trigger apoptosis or apoptosis-like cell death as opposed to generalized membrane rupture which

may cause necrosis [46, 47]. In our study we found that there was a significant release of cathepsin D in both PDT treated cell lines especially after 24 h incubation. However, $ZnPcS_{mix}$ alone also induced a significant leakage of the aspartic enzyme after 1 h incubation in DLD-1 cells and 24 h in CaCo-2 cells in comparison to sham irradiated control cells, although it was to a lesser extent. This could be due to the prolonged incubation with the PS which may eventually lead to osmotic stress and can trigger membrane permeabilization [37].

3.5. Cytosolic Cytochrome C. Relocation of mitochondrial cytochrome C to the cytosol was quantitatively determined by ELISA in order to investigate mitochondrial membrane destabilization, as it is a hallmark of apoptosis. DLD-1 cells exposed to $ZnPcS_{mix}$ alone proved to be susceptible to the photosensitizer at a concentration of 20 μM, and there was a significant increase in cytochrome C when compared to untreated control cells after 1 h incubation ($P < 0.001$), Table 2. There was a significant relocation of cytochrome C to the cytosol in PDT treated DLD-1 and CaCo-2 cells at both 1 and 24 h incubation ($P < 0.001$) when compared to all the control groups. Comparison of the incubation times
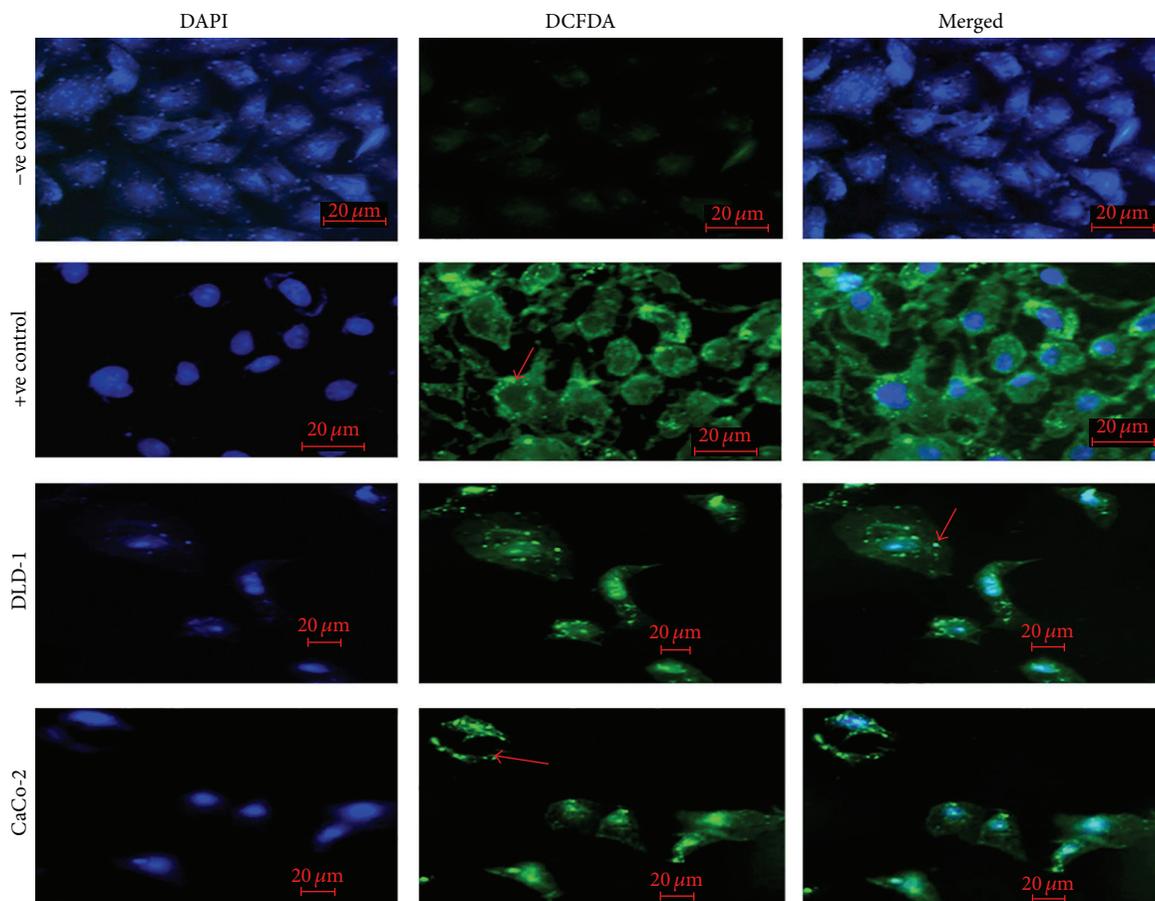
FIGURE 2: ROS production was qualitatively detected by staining cells with carboxy-H_2DCFDA which appears as green fluorescence if present as pointed out by the arrows. Nuclei were counterstained with DAPI (blue).

showed that there was a significant increase ($P < 0.01$) in cytochrome C in PDT treated cells (DLD-1 and CaCo-2) at 24 h compared to 1 h. When DLD-1 and CaCo-2 cells that were incubated with ZnPcS$_{mix}$ alone were compared after 1 h incubation, there was a significant difference ($P < 0.05$) in cytochrome C release. However, the difference was not seen after 24 h incubation.

These results are in agreement with the cathepsin D results, denoting that the mitochondrial membrane is destabilized by lysosomal enzymes. This is supported by the idea proposed by Brunk and Svensson that lysosomal proteases can cause direct detrimental damage to the mitochondrial membrane [48]. The release of cytochrome C is believed to be an important event in PDT induced apoptosis as a result of ROS damage produced at the localization site [49, 50].

3.6. FITC Annexin V. There was a significant increase in the number of apoptotic DLD-1 cells as compared to the viable population 1 h after PDT ($P < 0.001$), Figure 4(a). Incubation of DLD-1 cells 24 h after PDT also showed a significant increase in apoptotic cells as compared to the viable and necrotic population ($P < 0.001$). Similarly, a significant increase was also seen compared to the apoptotic population in control cells ($P < 0.001$). There was a significant decrease in the percentage of viable PDT treated CaCo-2 cells after 1 h incubation as compared to the same cell population in control cells ($P < 0.001$), Figure 4(b). When the apoptotic population in PDT treated CaCo-2 cells was compared to the viable and necrotic population within the same group, there was a significant increase in apoptosis at 1 and 24 h after PDT incubation ($P < 0.001$).

Incubation with PS alone appeared to be a crucial factor for cell toxicity, as longer incubation periods may have resulted in unnecessary toxicity, rendering dosimetry a fundamental component of the treatment of colorectal cancer. This was proven otherwise by the FITC Annexin V results which showed that ZnPcS$_{mix}$ in its inactive form was ineffective in inducing necrotic or apoptotic cell death as there was a fair amount of dead cells similar to untreated control cells. Activation of ZnPcS$_{mix}$ potentially resulted in cell death and confirmed that the prevailing mode of cell death after PDT was apoptosis. Our results suggest that the apoptotic cell death pathway is initiated by lysosomes which prompts delayed mitochondrial cytochrome C leakage as induced by the proteolytic enzyme cathepsin D as well as the low pH from lysosomes in response to PDT. Moreover, it is possible that the mitochondrial membrane could be directly destabilized

(a)

(b)
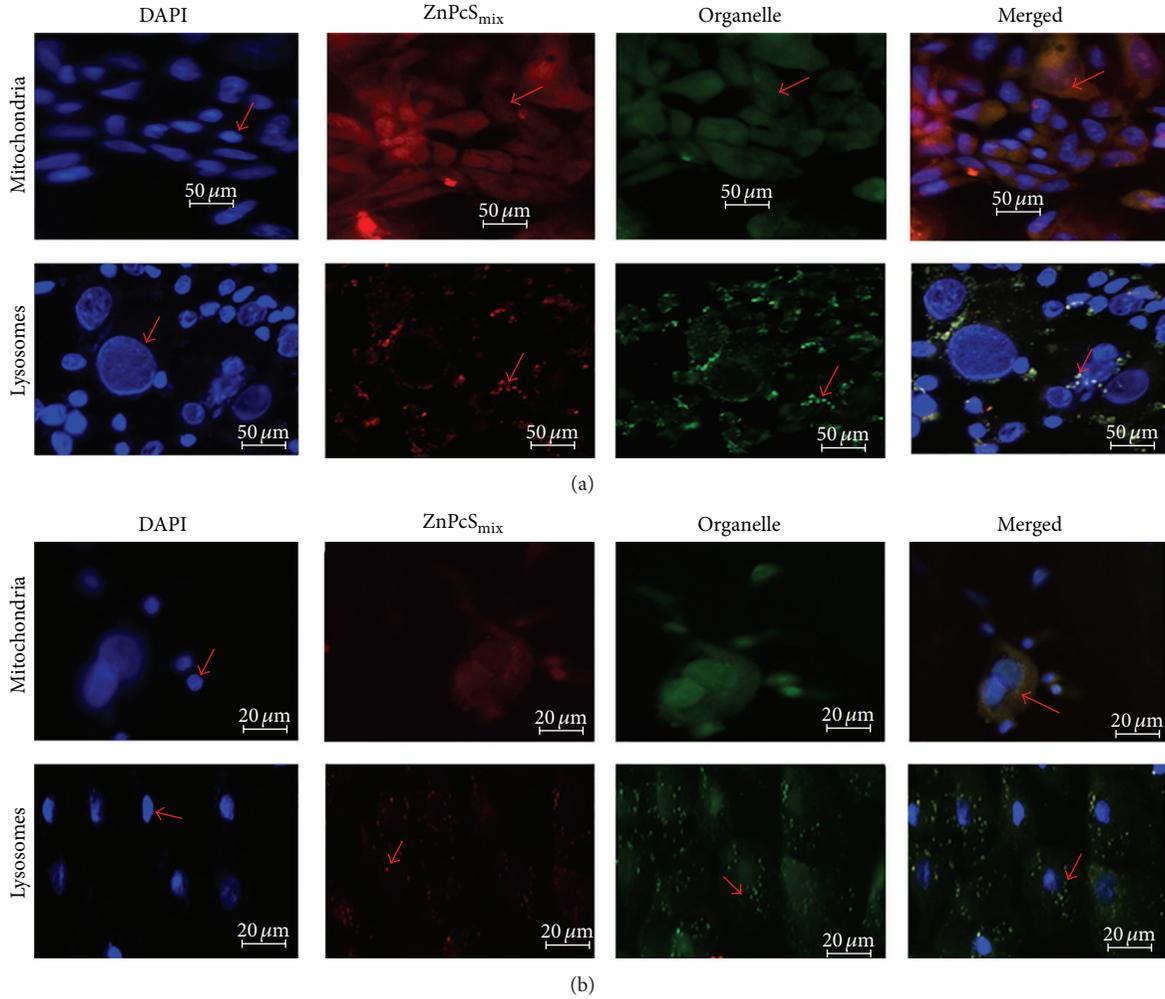
FIGURE 3: Intracellular localization of ZnPcS$_{mix}$ PS in DLD-1 and CaCo-2 cells. PS localized in lysosomes in both cell lines as seen by the merging red and green colours as pointed out by the arrows. In mitochondria, there was an indefinite localization pattern. However, the orange colour meant that there was PS in mitochondria, as pointed out by the arrows. Nuclei were stained with DAPI (blue).

TABLE 2: Cathepsin D and cytosolic cytochrome C were measured after 1 and 24 h incubation after PDT. Significant differences shown in the table represent comparison between PDT treated cells and their respective untreated control cells after 1 or 24 h incubation ($^*P < 0.05$; $^{**}P < 0.01$, and $^{***}P < 0.001$). Cathepsin D was significantly increased in DLD-1 ($P < 0.01$) and CaCo-2 ($P < 0.05$) after 24 h incubation in comparison to after 1 h incubation. In both cell lines, cytochrome C was significantly increased after 24 h incubation as compared to 1 h incubation ($P < 0.01$).

Assay	Time	Untreated		5 J/cm^2		ZnPcS$_{mix}$		PDT	
		DLD-1	CaCo-2	DLD-1	CaCo-2	DLD-1	CaCo-2	DLD-1	CaCo-2
Cath-D	1 h	$0.05^a \pm 1.16^b$	0.06 ± 2.84	0.06 ± 2.52	0.06 ± 1.78	$0.06^* \pm 9.76$	$0.07^* \pm 2.28$	$0.07^* \pm 3.82$	$0.08^{**} \pm 4.31$
	24 h	0.06 ± 2.39	0.07 ± 1.31	0.06 ± 3.03	0.06 ± 9.38	0.07 ± 5.12	0.07 ± 2.02	$0.10^{***} \pm 2.78$	$0.09^{***} \pm 3.89$
Cyto-C	1 h	0.10 ± 2.194	0.24 ± 0.15	0.12 ± 0.02	0.11 ± 0.01	$0.20^{***} \pm 0.03$	0.11 ± 0.02	$2.41^{***} \pm 0.12$	$2.22^{***} \pm 0.18$
	24 h	0.09 ± 4.33	0.09 ± 4.57	0.12 ± 0.01	0.09 ± 5.47	0.27 ± 0.09	0.14 ± 0.02	$3.14^{***} \pm 0.22$	$3.05^{***} \pm 0.22$

^{a}Mean; ^{b}standard error of mean (SEM).

by ROS that are formed immediately at the localization site and the acidic milieu from the lysosomal compartments. Furthermore, the fact that ZnPcS$_{mix}$ activation can induce lysosomal rupture, thereby releasing cathepsin D, renders ZnPcS$_{mix}$ an interesting and effective PS since it can localize in two vital organelles. Work conducted by Oleinick's group also affirmed that the lysosomal targeted phthalocyanine PSs (Pc181) was surprisingly effective as opposed to the mitochondrial targeted PSs [39].

It is not clear from these results which subcellular organelle can be held responsible for cell death initiation, so further work needs to be conducted to determine which

(a)

Necrotic
Apoptotic
Viable

(b)
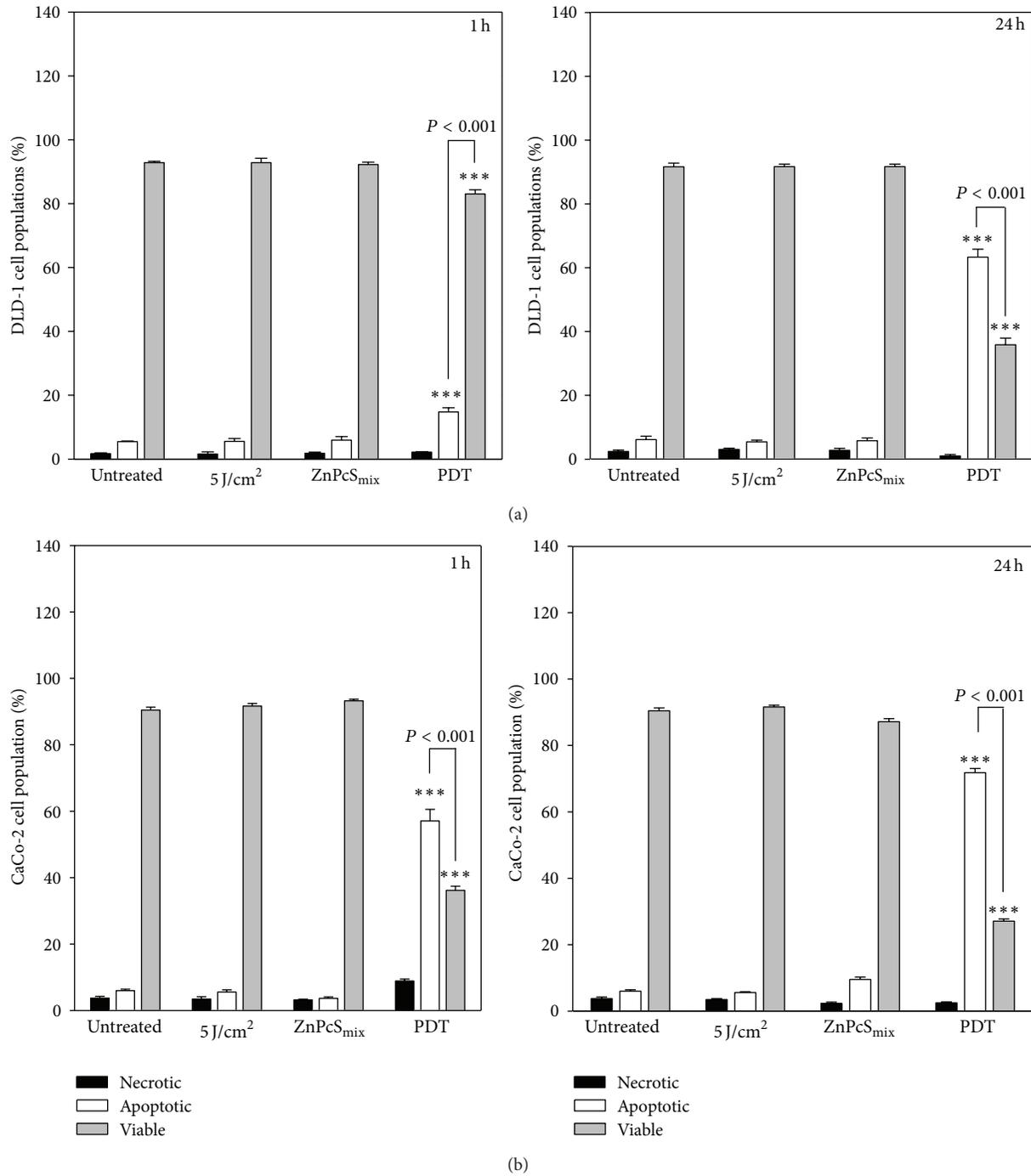
FIGURE 4: FITC Annexin V staining was used for the assessment of cell death mode in DLD-1 (a) and CaCo-2 (b) cells. Significant differences as compared to untreated cells are shown as *** $P < 0.001$. After 24 h, there was a significant increase in the percentage of apoptotic cell population compared to 1 h incubation in PDT treated DLD-1 cells (a). PDT treated CaCo-2 cells (b) had a significantly increased apoptotic population percentage after both 1 and 24 h incubation compared to their respective viable or necrotic cell population percentage ($P < 0.001$).

subcellular organelle is responsible for dissemination of cell death signals.

4. Conclusion

Despite the fact that the same PS was used on two different colorectal cancer cells, these cell lines responded differently.

It is evident that the CaCo-2 cells are more susceptible to PDT than the DLD-1 cells. This could be explained by the different cancer stages that these cells are in CaCo-2 cells are at Duke's B stage (well differentiated, less tumourigenic, and invasive), while DLD-1 cells are at Duke's C stage (metastatic and involves one or three regional lymph nodes). Thus the stage of cancer should be taken into consideration when

conducting such experiments. We hypothesize that $ZnPcS_{mix}$ is capable of inducing apoptotic cell death that is promoted by lysosomal photooxidation. The mechanism in which this PS induces cell death needs to be further studied in order to understand how it triggers cell death, from which initiation point cell death is triggered and how the various cancer stages respond to the treatment.

Disclosure

The material in this paper submitted to *International Journal of Photoenergy* neither has been published nor is being considered elsewhere for publication.

Conflict of Interests

The authors indicate that there is no conflict of interests regarding the publication of this paper.

Acknowledgments

References

[1] http://www.cancer.org/Research/CancerFactsFigures/Global-CancerFactsFigures/global-facts-figures-2nd-ed.

[2] C. C. Pritchard and W. M. Grady, "Colorectal cancer molecular biology moves into clinical practice," *Gut*, vol. 60, no. 1, pp. 116–129, 2011.

[3] A. Millan and S. Huerta, "Apoptosis-Inducing Factor and Colon Cancer," *Journal of Surgical Research*, vol. 151, no. 1, pp. 163–170, 2009.

[4] G. Wilkes and K. Hartshorn, "Colon, Rectal, and Anal Cancers," *Seminars in Oncology Nursing*, vol. 25, no. 1, pp. 32–47, 2009.

[5] A. G. Pallis, D. Papamichael, R. Audisio et al., "EORTC Elderly Task Force experts' opinion for the treatment of colon cancer in older patients," *Cancer Treatment Reviews*, vol. 36, no. 1, pp. 83–90, 2010.

[6] S. Banfi, E. Caruso, L. Buccafurni, R. Ravizza, M. Gariboldi, and E. Monti, "Zinc phthalocyanines-mediated photodynamic therapy induces cell death in adenocarcinoma cells," *Journal of Organometallic Chemistry*, vol. 692, no. 6, pp. 1269–1276, 2007.

[7] A. P. Castano, T. N. Demidova, and M. R. Hamblin, "Mechanisms in photodynamictherapy: part one—photosensitizers, photochemistry and cellular localization," *Photodiagnosis and Photodynamic Therapy*, vol. 1, no. 4, pp. 279–293, 2004.

[8] P. Agostinis, K. Berg, K. A. Cengel et al., "Photodynamic therapy of cancer: an update," *CA: Cancer Journal for Clinicians*, vol. 61, no. 4, pp. 250–281, 2011.

[9] S. B. Brown, E. A. Brown, and I. Walker, "The present and future role of photodynamic therapy in cancer treatment," *The Lancet Oncology*, vol. 5, no. 8, pp. 497–508, 2004.

[10] R. R. Allison, G. H. Downie, R. Cuenca, X.-H. Hu, C. J. H. Childs, and C. H. Sibata, "Photosensitizers in clinical PDT," *Photodiagnosis and Photodynamic Therapy*, vol. 1, no. 1, pp. 27–42, 2004.

[11] A. P. Castano, T. N. Demidova, and M. R. Hamblin, "Mechanisms in photodynamic therapy: part three—photosensitizer pharmacokinetics, biodistribution, tumor localization and modes of tumor destruction," *Photodiagnosis and Photodynamic Therapy*, vol. 2, no. 2, pp. 91–106, 2005.

[12] L. B. Josefsen and R. W. Boyle, "Photodynamic therapy and the development of metal-based photosensitisers," *Metal-Based Drugs*, vol. 2008, Article ID 276109, 23 pages, 2008.

[13] R. R. Allison and C. H. Sibata, "Oncologic photodynamic therapy photosensitizers: a clinical review," *Photodiagnosis and Photodynamic Therapy*, vol. 7, no. 2, pp. 61–75, 2010.

[14] D. E. J. G. J. Dolmans, D. Fukumura, and R. K. Jain, "Photodynamic therapy for cancer," *Nature Reviews Cancer*, vol. 3, no. 5, pp. 380–387, 2003.

[15] N. L. Oleinick and H. H. Evans, "The photobiology of photodynamic therapy: cellular targets and mechanisms," *Radiation Research*, vol. 150, no. 5, pp. S146–S156, 1998.

[16] S. W. Ryter, P. K. Hong, A. Hoetzel et al., "Mechanisms of cell death in oxidative stress," *Antioxidants and Redox Signaling*, vol. 9, no. 1, pp. 49–89, 2007.

[17] J. Zawacka-Pankau, J. Krachulec, I. Grulkowski, K. P. Bielawski, and G. Selivanova, "The p53-mediated cytotoxicity of photodynamic therapy of cancer: recent advances," *Toxicology and Applied Pharmacology*, vol. 232, no. 3, pp. 487–497, 2008.

[18] R. Bhowmick and A. W. Girotti, "Signaling events in apoptotic photokilling of 5-aminolevulinic acid-treated tumor cells: inhibitory effects of nitric oxide," *Free Radical Biology and Medicine*, vol. 47, no. 6, pp. 731–740, 2009.

[19] M. Zhao, F. Antunes, J. W. Eaton, and U. T. Brunk, "Lysosomal enzymes promote mitochondrial oxidant production, cytochrome c release and apoptosis," *European Journal of Biochemistry*, vol. 270, no. 18, pp. 3778–3786, 2003.

[20] N. L. Oleinick, R. L. Morris, and I. Belichenko, "The role of apoptosis in response to photodynamic therapy: what, where, why, and how," *Photochemical and Photobiological Sciences*, vol. 1, no. 1, pp. 1–21, 2002.

[21] A. P. Castano, T. N. Demidova, and M. R. Hamblin, "Mechanisms in photodynamic therapy: part one—photosensitizers, photochemistry and cellular localization," *Photodiagnosis and Photodynamic Therapy*, vol. 1, no. 4, pp. 279–293, 2004.

[22] J. A. Caruso, P. A. Mathieu, and J. J. Reiners Jr., "Sphingomyelins suppress the targeted disruption of lysosomes/endosomes by the photosensitizer NPe6 during photodynamic therapy," *Biochemical Journal*, vol. 392, no. 2, pp. 325–334, 2005.

[23] D. Kessel, Y. Luo, P. Mathieu, and J. J. Reiners Jr., "Determinants of the apoptotic response to lysosomal photodamage," *Photochemistry and Photobiology*, vol. 71, no. 2, pp. 196–200, 2000.

[24] C. De Duve, "Lysosomes revisited," *European Journal of Biochemistry*, vol. 137, no. 3, pp. 391–397, 1983.

[25] L. Emert-Sedlak, S. Shangary, A. Rabinovitz, M. B. Miranda, S. M. Delach, and D. E. Johnson, "Involvement of cathepsin D in chemotherapy-induced cytochrome c release, caspase activation, and cell death," *Molecular Cancer Therapeutics*, vol. 4, no. 5, pp. 733–742, 2005.

[26] A. Minarowska, Ł. Minarowski, A. Karwowska, and M. Gacko, "Regulatory role of cathepsin D in apoptosis," *Folia Histochemica et Cytobiologica*, vol. 45, no. 3, pp. 159–163, 2007.

[27] L. P. Deiss, H. Galinka, H. Berissi, O. Cohen, and A. Kimchi, "Cathepsin D protease mediates programmed cell death induced by interferon-γ, Fas/APO-1 and TNF-α," *The EMBO Journal*, vol. 15, no. 15, pp. 3861–3870, 1996.

[28] G. Kroemer and M. Jaatella, "Lysosomes and autophagy in cell death control," *Nature Reviews Cancer*, vol. 5, pp. 886–897, 2005.

[29] A.-C. Johansson, H. Steen, K. Öllinger, and K. Roberg, "Cathepsin D mediates cytochrome c release and caspase activation in human fibroblast apoptosis induced by staurosporine," *Cell Death and Differentiation*, vol. 10, no. 11, pp. 1253–1259, 2003.

[30] T. G. Gantchev, J. E. Van Lier, and D. J. Hunting, "Molecular models of zinc phthalocyanines: semi-empirical molecular orbital computations and physicochemical properties studied by molecular mechanics simulations," *Radiation Physics and Chemistry*, vol. 72, no. 2-3, pp. 367–379, 2005.

[31] H. Barr, P. Chatlani, C. J. Tralau, A. J. MacRobert, P. B. Boulos, and S. G. Bown, "Local eradication of rat colon cancer with photodynamic therapy: correlation of distribution of photosensitiser with biological effects in normal and tumour tissue," *Gut*, vol. 32, no. 5, pp. 517–523, 1991.

[32] J. H. Woodhams, A. J. MacRobert, M. Novelli, and S. G. Bown, "Photodynamic therapy with WST09 (Tookad): quantitative studies in normal colon and transplanted tumours," *International Journal of Cancer*, vol. 118, no. 2, pp. 477–482, 2006.

[33] A. Ogunsipe and T. Nyokong, "Photophysical and photochemical studies of sulphonated non-transition metal phthalocyanines in aqueous and non-aqueous media," *Journal of Photochemistry and Photobiology A*, vol. 173, no. 2, pp. 211–220, 2005.

[34] S. L. Manoto, P. R. Sekhejane, N. N. Houreld, and H. Abrahamse, "Localization and phototoxic effect of zinc sulfophthalocyanine photosensitizer in human colon (DLD-1) and lung (A549) carcinoma cells (*in vitro*)," *Photodiagnosis and Photodynamic Therapy*, vol. 9, no. 1, pp. 52–59, 2012.

[35] A. Saratse and K. Pulkki, "Morphologic and biochemical hallmarks of apoptosis," *Cardiovascular Research*, vol. 45, pp. 528–537, 2000.

[36] H. Wiseman and B. Halliwell, "Damage to DNA by reactive oxygen and nitrogen species: role in inflammatory disease and progression to cancer," *Biochemical Journal*, vol. 313, no. 1, pp. 17–29, 1996.

[37] J. M. Matés and F. M. Sanchez-Jimenez, "Role of reactive oxygen species in apoptosis: implications for cancer therapy," *The International Journal of Biochemistry & Cell Biology*, vol. 32, no. 2, pp. 157–170, 2000.

[38] G. Quiogue, S. Saggu, H.-I. Hung et al., "Signaling from lysosomes enhances mitochondria-mediated photodynamic therapy in cancer cells," in *Photodynamic Therapy: Back to the Future*, vol. 7380 of *Proceedings of SPIE*, pp. 1–8, Seattle, Wash, USA, June 2009.

[39] A.-C. Johansson, H. Appelqvist, C. Nilsson, K. Kågedal, K. Roberg, and K. Öllinger, "Regulation of apoptosis-associated lysosomal membrane permeabilization," *Apoptosis*, vol. 15, no. 5, pp. 527–540, 2010.

[40] M. E. Rodriguez, P. Zhang, K. Azizuddin et al., "Structural factors and mechanisms underlying the improved photodynamic cell killing with silicon phthalocyanine photosensitizers directed to lysosomes versus mitochondria," *Photochemistry and Photobiology*, vol. 85, no. 5, pp. 1189–1200, 2009.

[41] D. Kessel and Y. Luo, "Intracellular sites of photodamage as a factor in apoptotic cell death," *Journal of Porphyrins and Phthalocyanines*, vol. 5, no. 2, pp. 181–184, 2001.

[42] H. L. Persson, "Iron-dependent lysosomal destabilization initiates silica-induced apoptosis in murine macrophages," *Toxicology Letters*, vol. 159, pp. 124–133, 2005.

[43] P. Mroz, J. Bhaumik, D. K. Dogutan et al., "Imidazole metalloporphyrins as photosensitizers for photodynamic therapy: role of molecular charge, central metal and hydroxyl radical production," *Cancer Letters*, vol. 282, no. 1, pp. 63–76, 2009.

[44] T. Kurz, A. Terman, B. Gustafsson, and U. T. Brunk, "Lysosomes in iron metabolism, ageing and apoptosis," *Histochemistry and Cell Biology*, vol. 129, no. 4, pp. 389–406, 2008.

[45] S.-M. Chiu, L.-Y. Xue, M. Lam et al., "A requirement for bid for induction of apoptosis by photodynamic therapy with a lysosome- but not a mitochondrion-targeted photosensitizer," *Photochemistry and Photobiology*, vol. 86, no. 5, pp. 1161–1173, 2010.

[46] U. Repnik and B. Turk, "Lysosomal-mitochondrial cross-talk during cell death," *Mitochondrion*, vol. 10, no. 6, pp. 662–669, 2010.

[47] U. T. Brunk, H. Dalen, K. Roberg, and H. B. Hellquist, "Photo-oxidative disruption of lysosomal membranes causes apoptosis of cultured human fibroblasts," *Free Radical Biology and Medicine*, vol. 23, no. 4, pp. 616–626, 1997.

[48] U. T. Brunk and I. Svensson, "Oxidative stress, growth factor starvation and Fas activation may all cause apoptosis through lysosomal leak," *Redox Report*, vol. 4, no. 1-2, pp. 3–11, 1999.

[49] J. J. Reiners Jr., J. A. Caruso, P. Mathieu, B. Chelladurai, X.-M. Yin, and D. Kessel, "Release of cytochrome c and activation of pro-caspase-9 following lysosomal photodamage involves bid cleavage," *Cell Death and Differentiation*, vol. 9, no. 9, pp. 934–944, 2002.

[50] J. Kim, H. Fujioka, N. L. Oleinick, and V. E. Anderson, "Photosensitization of intact heart mitochondria by the phthalocyanine Pc 4: correlation of structural and functional deficits with cytochrome c release," *Free Radical Biology and Medicine*, vol. 49, no. 5, pp. 726–732, 2010.

Research Article

Two-Stage Analysis on Models for Quantitative Differentiation of Early-Pathological Bladder States

Nina Kalyagina,[1,2,3] **Tatiana Savelieva,**[1] **Walter Blondel,**[2,3] **Christian Daul,**[2,3] **Didier Wolf,**[2,3] **and Victor Loschenov**[1]

[1] *Prokhorov General Physics Institute, Russian Academy of Sciences, Vavilov Street 38, Moscow 119991, Russia*
[2] *Université de Lorraine, CRAN, UMR 7039, 2 avenue de la forêt de Haye, 54516 Vandoeuvre-lès-Nancy Cedex, France*
[3] *CNRS, CRAN, UMR 7039, 54516 Vandoeuvre-lès-Nancy, France*

Correspondence should be addressed to Nina Kalyagina; nina.kalyagina@gmail.com

A mathematical simulation method was developed for visualization of the diffuse reflected light on a surface of 3-layered models of urinary bladder wall. Five states, from normal to precancerous, of the urinary bladder epithelium were simulated. With the use of solutions of classical electrodynamics equations, scattering coefficients μ_s and asymmetry parameters g of the bladder epithelium were found in order to perform Monte Carlo calculations. The results, compared with the experimental studies, has revealed the influence of the changes in absorption and scattering properties on diffuse-reflectance signal distributions on the surfaces of the modelled media.

1. Introduction

Laser light wave, penetrated into a biological tissue, changes its direction and intensity in a unique way due to the medium specific optical properties: density and structure, absorption, and concentration of the scattering elements inside the tissue. Thereafter, optical (spectroscopy and imaging) techniques exploiting the interactions of laser light with the tissue are of considerable interest for *in vivo* noninvasive (minimally invasive) diagnosis [1]. The main advantage of optical diagnostic techniques is to be sensitive to pathological lesions at the early stages, that is, when the microscopic changes begin to occur. Such precise information about tissue state at a microscopic level can be revealed by the tissue biopsy, which is, however, an invasive method and sometimes is taken randomly [2, 3].

The present study aimed to analyse the variations in the surface diffuse-reflected (DR) light signals measured at the surface of biological and mathematical bladder wall models with the reference to different pathology-based structural changes. Such information is useful for noninvasive detection and interpretation of the light signals, obtained on the tissue surface. Previously described techniques [4, 5] for analysis

of the DR light distributions, based on the irradiation of a tissue by a narrow collimated coherent laser beam and collection of a surface backscattered nonpolarized light signal by a photodetector, showed that such an approach allows for detecting differences in light signals according to the optical properties tissues and tissue phantoms and can be applied *in vivo* for internal organs, such as urinary bladder (UB). This principle will be used in our study.

Due to its multilayered and multiconstituent structure the UB wall is a turbid, inhomogeneous medium and can be divided by its properties into three main layers: (1) mucosal (transitional epithelium), (2) submucosal, and (3) muscle. Precancerous lesions of the UB mostly arise in the first, epithelial layer of 4–7 rows of densely-packed orbicular-shaped cells [6] and of about 200 μm thick. At the early stages of UB diseases, such as dysplasia, first metamorphoses occur in the cell nuclei, which influence the cell optical properties. At dysplasia, for example, the cell nuclei undergo different changes [7], which contribute to the light scattering and absorption properties of the tissue. Thereafter the wave interaction with the epithelial layers at different stages of neoplasm

TABLE 1: Input parameters applied for electro-magnetic theory-based calculations performed on each of the 5 types of bladder epithelial tissue-like models.

Model type	Parameter			
	a, μm	μ_a, cm^{-1}	ρ, nuclei per μm^3	n_{nuc}
I—Normal	5	1	0.00015	$1.42 + 0.000413i$
II—Nuclei size growth	10	1	0.00015	$1.42 + 0.000051i$
III—Chromaticity changes	5	2.5	0.00015	$1.42 + 0.00101i$
IV—Population density changes	5	2	0.0003	$1.42 + 0.000413i$
V—All changes together	10	5	0.0003	$1.42 + 0.000121i$

formation should be taken into a special consideration and will be discussed below.

As modern techniques require a complex approach for solving diagnostic problems, then not only instrumentation has to be determined. Mathematical modelling is also a useful tool for modern diagnostic techniques. The present study describes forward experimental and mathematical (Monte Carlo-based) methods of visualization of the DR light on a surface of 3-layered models of the UB wall.

2. Materials and Methods

2.1. Input Parameters: Light Scattering in Bladder Multilayered Wall

2.1.1. Bladder Parameters and Model Construction. In order to reproduce the optical properties of the UB wall, several three-layered models, mimicking mucosa, submucosa, and muscle layer, were considered. To trace the influence of each intra- or extracellular modifications, five "states" of the UB urothelium, corresponding to main metamorphosis at dysplasia, were imitated (by varying the scatterers' parameters in the first layers of the models): type (I) normal, with normal size and concentration of the cell nuclei; type (II) enlarged nuclei; type (III) absorption growth; type (IV) nuclear population density increase; type (V) all the changes together.

As the precancerous changes arise mostly in the epithelium and the lower layers do not undergo discriminant modifications in their structure, same optical properties for the second and third layers were reproduced in all types of the models. Implementation of such modelling by Monte Carlo simulation method requires the previous knowledge of the optical parameters of each layer and type of the model. Some bladder parameters are presented in the studies of Cheong et al. [8], Star et al. [9], and Splinter et al. [10]; others have to be determined. Below we present several sets of optical parameters for each layer, necessary for mathematical modelling.

First (Top) Layers. The top layer of the UB wall mostly consists of the epithelial cells (about 15 μm in diameter) with rounded nuclei inside, which we consider to be the main scattering centers of the first layer of our models. As the epithelial layer is a tight pack of cells, the surrounding medium for these scattering centers is intracellular medium (cell cytoplasm) with its refractive index n_{cell} lying between 1.35 and 1.38 [11].

In the present work we have used a value of the cell (cell cytoplasm) refractive index $n_{cell} = 1.37$ for electromagnetic wave theory-based calculations as an input parameter and for the Monte Carlo simulations as a refractive index of the first layers (Table 1). Beauvoit et al. [12] assumed a nucleus refractive index relative to the cell cytoplasm to be about 1.04; thus we considered the nucleus refractive index to be equal to $n_{nuc} = 1.42$. As the cells of the transitional epithelium are densely packed, we considered the refractive index of the surrounding medium for the cell (the extracellular matrix) in the first layers to be minimally different from the cellular one and to be lower than the refractive index of the cytoplasm because of the presence of extracellular composition between the cells, so that $n_{med} = 1.365$.

Based on the study of van Staveren et al. [13], in which the value of the absorption coefficient μ_a for mucosal/submucosal layers lies in the range of 0.6–1 (cm^{-1}) for the green wavelength region, we considered the absorption of the first layers to be equal to the maximum value 1 (cm^{-1}), as the absorption in the top epithelial layers is usually higher than in the second submucosal layers. The calculations of the values of the scattering coefficients μ_s were based on the electromagnetic wave theory described below, in Section 2.2.

Second (Intermediate) Layers. The submucosal layer (which is 400–1000 μm thick) has a small amount of cells and consists generally of the intercellular material with protein fibers, forming a connective tissue, whose main constituent is water, forming about 60% [14]. For that reason, we have taken a value of $n_{exf} = 1.36$ [6] for the extracellular fluid as the refractive index for the intermediate submucosa-like layers. The absorption coefficient and anisotropy factor of the second layers were chosen as minimum values given in [13] for 500–550 nm wavelengths, 0.6 (cm^{-1}), and 0.87, respectively. The results obtained by Qu et al. [15] for the bronchial tissues show that the scattering coefficient of the submucosal layer is about 40 cm^{-1} less than of the one of mucosal layer, which we took into account for the determination of the scattering parameter of the second layer.

Third (Bottom) Layers. The muscle layer of the UB mostly consists of smooth muscle fibres, connective tissue, and nerves and is about 2 mm thick. The refractive index value for this layers muscle layers $n_3 = 1.37$ was taken from [16], and the other optical parameters were based on data from the colon muscle tissues [17], similar by its structure to

the bladder muscle tissue: 193 cm^{-1}, 1.53 cm^{-1}, and 0.941 for the scattering, absorption, and anisotropy coefficients, respectively.

The thicknesses of each layer in each simulation model were fixed to 200 μm for the first, 700 μm for the second, and 2.1 mm for the third layers.

2.1.2. Electrodynamics: Scattering on a Coated Sphere: Nucleus in a Cell. In order to determine the complete set of the optical parameters for performing the Monte Carlo simulations of the first layers of the models, it is necessary to examine the sizes, density, and refractive indices of the scatterers and their influence on the scattering and absorption coefficients and on anisotropy of light distribution. The nuclear sizes of the bladder transitional epithelium are of about 5 μm for the normal cells (I type of the models) and 10 μm for the enlarged (II, V types of the models, Table 1), which is larger than the wavelengths of the visible range 490–750 nm. Such nuclear sizes together with their orbicular shape give us a subject to consider the nuclei as large spherical scattering centres inside the cells having different refractive indices. Thus, Mie calculations for "coated spheres" were chosen as a basis for determination of the input parameter values required for Monte Carlo simulations of the light distribution in the first layers of our models.

By means of the scattering and absorption, the laser electromagnetic waves interact with the inner structural elements inside a biological turbid medium. Physically such process is the changes of the electromagnetic fields generated inside the tissue. Generally speaking, the "prediction" of behaviour of the electromagnetic waves in the tissue is hampered to the solution of the Maxwell's equations for the macroscopic electromagnetic field at the interior points in matter [18].

We consider an electromagnetic wave to be incident to a "coated" sphere with an inner radius (a) equal to the mean radius of a nucleus and the outer (b) of a cell. The maximum number of iterations for determining the scattering efficiency for the case of biological scatterers is

$$n_{\max} = x + 4x^{1/3} + 2, \tag{1}$$

where $x = kb$—is a size parameter with the wave vector k and radius of the "coat" b.

In the present study, the imaginary part of the refractive indices was chosen in a way that the final calculated absorption coefficient matched with the value $\mu_a = 1$ presented in the Section 2.1 and with the corresponding absorption changes according to the cases III–V of the neoplasm formation. The results of van Staveren et al. [13] and Wei et al. [17] show that the absorption of diseased bladder and colon tissues exceeds the normal one by a factor of about 1.5 to 3. Consequently, in the III^d type of our models, we increased the absorption coefficient from 1 cm^{-1} (for normal tissue, type I) to 2.5 cm^{-1}.

For the IVth type it was considered that the scatterers in the epithelium have multiplied so that the population density has changed from 1.5×10^8 to 3×10^8 cells per mL and the absorption at the first layer has grown. The average density

(ρ) of scatterers is defined for the first layers of the models from the histological studies.

Taking into account that in case of population density augmentation the nuclei multiply inside the cells, the computations for the type IV consisted of two parts: (1) the scattering coefficients of the normal tissue (type I), calculated for the "coated" spheres (nuclei in cells), were summed up with (2) those ones, computed for the nuclei as separate spherical scatterers without the "coat", which was already taken into account in the first part. The equations for such computation can be found by considering the refractive index of the "coat" to be equal to the surrounding medium. Although our calculations allowed for obtaining the values of the anisotropy factor g, they did not reflect the contribution of all the compounds of the tissue (including small cellular and intracellular components). Thus, for our models average values for the anisotropy parameter of the epithelial tissue [13, 15, 17] were used.

Summary of the input parameters for the Monte Carlo modelling of the laser light interaction with the models, mimicking five states of the bladder epithelium, is presented in the Table 2.

2.2. Monte Carlo Forward Solution. Based on the transport equation, Monte Carlo modelling methods can be used for describing light transport in tissues and to receive photons distributions on the surface of absorbing and scattering multilayered media [19–22]. For the present study an algorithm, allowing for obtaining the matrices of the backscattered light distribution, was developed in order to simulate the light propagation into the multilayered bladder wall for quantitative differentiation of cancerous and normal states.

Behaviour of the photons at the interface boundaries of the layers is quite particular and should be taken into a special consideration. In general, scattering on the boundary surface of a layer is induced by the interface roughness, while the spatial scattering (inside the medium) is created by inhomogeneities inside the medium. After a collision act with the boundary between the layers of the UB tissue, the packet of the photons underwent the reflection in the case when a random variable γ, uniformly distributed in the interval from 0 to 1, was less or equal to the probability of the Fresnel reflection. Otherwise, in our models, the photons continued to spread into the other layer in a direction according to the Snell's law for the angles of refraction, with the deviation caused by the interface irregularities. The deviation angle was calculated as an angle of scattering on the medium scattering element of the current layer. The photons, colliding with the layers' interfaces, deviate from the direction of the Fresnel angle due to the optical properties of a layer [23]. The diameter of the imitated irradiation laser beam was 0.5 mm. The number of initialized photons was 10^7. The final sizes of the statistical matrices of the surface diffuse-reflected photons distributions were 30 × 30 pixels (0.2 × 0.2 cm).

2.3. Experimental Validation. For experimental estimation of dependence of the surface laser light distribution on

TABLE 2: Input parameters for Monte Carlo modelling of light distribution in the bladder wall. The calculations of the parameters marked with *are based on the electromagnetic wave theory.

| Modelling parameters	Layer 1 (transitional epithelium), 200 μm Tissue type					Layers 2 (submucosa), 700 μm	Layers 3 (muscle), 2100 μm
	I	II	III	IV	V		
g	0.91	0.91	0.91	0.91	0.91	0.87	0.941
μ_s, cm^{-1}	190*	262*	187*	272	513	150	193
μ_a, cm^{-1}	1	1	2.5	2*	5*	0.6	1.53
n of the layer	1.37	1.37	1.37	1.37	1.37	1.36	1.37
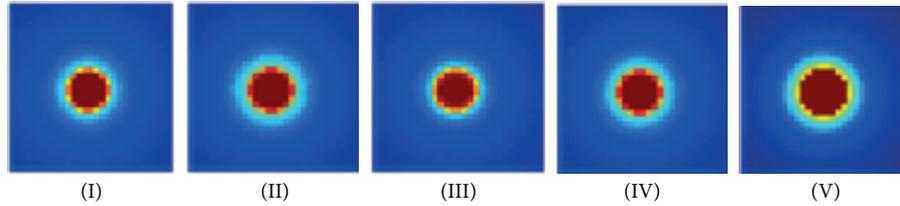
FIGURE 1: Processed matrices of the Monte Carlo simulated surface backscattered laser light: (I) normal, with normal size of cell nuclei, (II) enlarged nuclei, (III) absorption growth, (IV) population density augmentation, and (V) all the changes together. The size of the picture is 30 per 30 pixels.
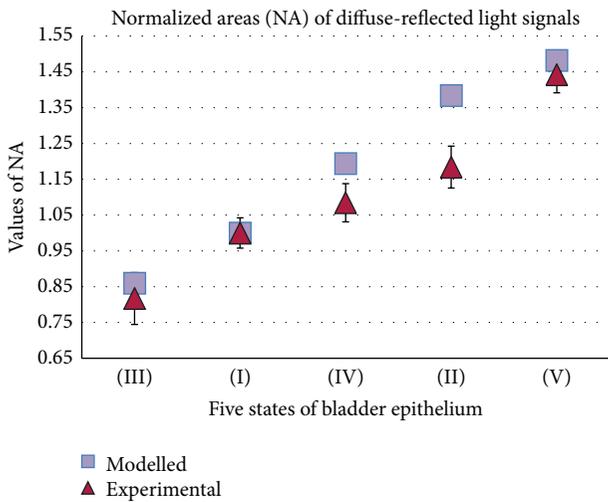
FIGURE 2: Comparison of experimental (average values) and simulation diffuse-reflected light area ratios for 5 states of bladder epithelium: (I) normal, with normal size of cell nuclei, (II) enlarged nuclei, (III) absorption growth, (IV) population density augmentation, and (V) all the changes together.

the microchanges of the tissues, five types of three-layer phantoms simulating the bladder wall were prepared. According to the bladder structure and initial precancerous changes, five phantoms types were chosen to simulate several possible changes in tissue.

The third layers, mimicking the muscular layer of the bladder, were identical for all the phantom types and consisted of 7% of gelatine dissolved in distilled water, 2% of Intralipid, and an absorber (black ink at a concentration of 0.001%). The second layers, simulating tissue submucosa,

were also identical for all the five phantom types and consisted of 7% of gelatine and 1.6% of Intralipid. The phantoms were classified into 5 types according to the composition of their first layers, simulating the transitional epithelium of the urinary bladder. The basis of all the first layers was made of 7% of gelatin, of an absorber (black ink) at 0.0005% concentration, and polystyrene microspheres (Bang Laboratories) of 0.05 μm and 0.53 μm diameters in a concentration of 10^{10} particles per mL each.

The first layer of the first phantom type contained polystyrene particles of 5.09 μm diameter at a concentration of 8×10^6 spheres per mL. In the second type of the phantoms the mean diameter of the scatterers was bigger: to the basis of the first layers the particles of 5.09 and 20.92 μm in a concentration of 4×10^6 particles (of each size) per mL were added. The third phantom type differed from the first and second types by the presence of additional absorber at a concentration of 0.00075%. Thus, the total concentration of the absorber in the first layers of the third type of the phantom was 0.00125%. The fourth type of phantoms differed from the others by a more dense packing of the scattering particles: the concentration of the microspheres of 5.09 μm diameter was 1.6×10^7 spheres per mL. The last (fifth) type of the phantoms consisted of the scatterers with increased average sizes and density and higher absorber concentration: the microspheres of 5.09 and 20.92 μm diameter were added in a concentration 8×10^6 each, and the total absorber concentration was 0.0025%. The thickness of the third layers was 2.1 mm, that of the second was 0.7 mm, and that of the first was 200 μm.

The surface of the phantoms was simultaneously illuminated by six laser beams (allowed for expanding the scanning surface area, for raising the sensitivity of the DR measurements, and for reducing the measurement errors)
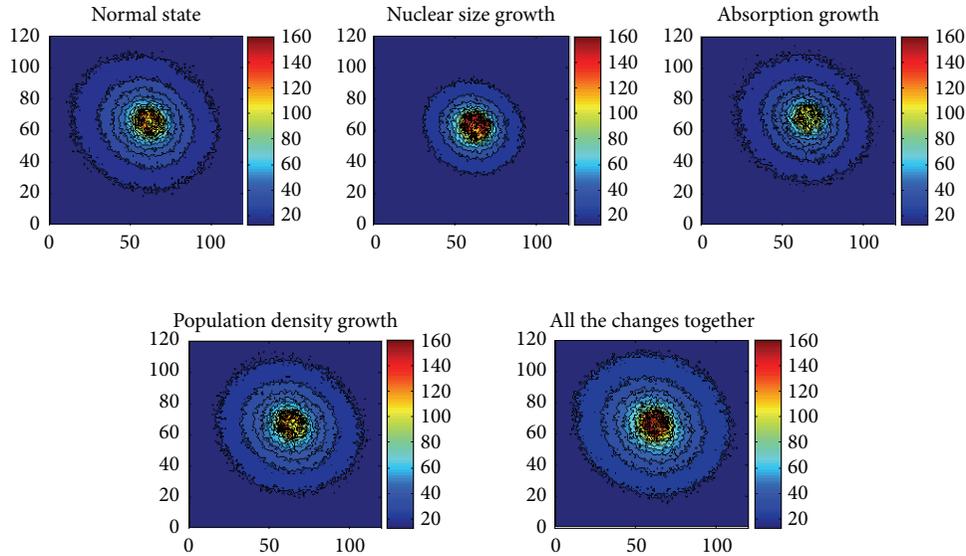
FIGURE 3: Processed matrices of the Monte Carlo simulated surface backscattered laser light at 15 threshold levels.

generated by a copper vapour laser (510.6 nm, Mechatron), an optical probe with 6 fibers of 200 μm, and an optical lens (f = 17 mm) for the light collimation. The lens was located at an equal distance of 4.6 mm to the fiber end and to the surface of the phantoms. The backscattered light signals were acquired from the surfaces of the phantoms by a video camera (Videoskan, 30 ms exposure, 200 amplification). The final diameter of each beam was 0.5 mm. Fifteen images for each phantom type were acquired from further procession and analysis.

3. Results and Discussion

In order to perform the quantitative differentiation between the bladder early-pathological states, the raw signals from both, experimental and mathematical simulations, were normalized between 0 and 1. The areas of the DR images corresponding to the intensity values over the threshold of 0.3 (found by varying the most distinguishing differences between the five models) were calculated and then normalized to the area of back-scattered signal for the normal tissues (type I). Pixel areas below the threshold level were calculated for all the experimental and modelled images. The matrices of the DR light, obtained by the Monte Carlo simulations, are presented in Figure 1 (the threshold level is shown by light blue areas).

Figure 2 presents a comparison of the simulation and experimental data. The results show a positive correlation for all the five bladder tissue states. For some states the normalized values differ from each other due to the differences in the mathematical and experimental models (real bladder tissues and phantoms, resp.). Besides, due to the idealization of mathematical simulations, the normalized modelled area values are higher than the experimental for all the 5 states

of the bladder tissue. This signifies more considerable differences between the bladder states for the case of mathematical modelling in comparison to the experimental detection.

Both, experimental and modelling results showed that the most significant differences in obtained signals between normal and early-pathological states of the UB arise in the case of the absorption growth (models of type III) and all the changes together (models of type V), whereas the contribution of the population density (models of type IV) and of the scatterers' size (models of type II) to the backscattered light is less detectable.

The analysis of the back-scattering distributions on tissue optical properties allowed for revealing that the augmentation of the scattering coefficient increases the size of the surface laser spot, while the absorption coefficient decreases its size. However, in biological tissues, the higher increase in absorption or the diminution of scatterers (like mitochondria) in number or sizes with the neoplasm formation can also lead to decrease of the total backscattered signals. Thereafter, any (up or down) deviations in the surface DR light signal indicate the presence of an abnormality in the tissue and should be analysed according to each particular case.

In order to avoid the interpretation errors in the issues of the presented modelling method (due to the big variety of the scattering and absorption tissue optical parameters: scattering coefficient, anisotropy factor, absorption coefficient, refractive indices, and sizes and shapes of scatterers for which the results of the mathematical modelling can differ), the surface DR light signals should be normalized to a "normal" signal; thus they will depend only on the changes in the scatterers' sizes and density and absorber quantity and will be rather important for the calibration of the measurements.

Another possibility to obtain more holistic view of the influence of the changes in optical parameters on the detected signals is to process the obtained matrices at other intensity

threshold levels (15 levels, Figure 3). By such an analysis it was revealed that at the same size of the epithelial scatterers the intensity of light is higher than at the increased sizes (even at increased absorption) in the areas distant from the center of incidence. This distribution pattern of diffusevely reflected light is caused by reduction of wide-angle scattering due to increase of forward scattering by enlarged "nuclei".

4. Conclusions

The presented study, dedicated to the forward problem analysis for simulating surface backscattering intensity matrices, gave an opportunity to analyse on models the differences, occurring in the tissue on cellular-intercellular level, without the use of any additional markers (like photosensitizers). It was revealed that the complementary characteristics of the distribution of diffusely reflected laser light can be obtained by analyzing the images simultaneously on different intensity threshold levels, which allows detecting differences in both absorption and scattering properties of the tissue.

The flexibility of the method allows changing input parameters in accordance with the tissue type that makes it possible to detect early changes not only in the bladder epithelium but also in other organs by adapting the method to the tissue under consideration. Besides, the proposed analytical method can potentially serve as a base for inverse problem solution for interpretation of the DR signals from bladder tissues.

Conflict of Interests

The authors declare that there is no conflict of interests regarding the publication of this paper

Acknowledgments

References

[1] E. C. C. Cauberg, D. M. de Bruin, D. J. Faber, T. G. van Leeuwen, J. J. M. C. H. de la Rosette, and T. M. de Reijke, "A new generation of optical diagnostics for bladder cancer: technology, diagnostic accuracy, and future applications," *European Urology*, vol. 56, no. 2, pp. 287–297, 2009.

[2] M. Babjuk, "Transurethral Resection of Non-muscle-invasive Bladder Cancer," *European Urology, Supplements*, vol. 8, no. 7, pp. 542–548, 2009.

[3] N. Nese, R. Gupta, M. H. T. Bui, and M. B. Amin, "Carcinoma in situ of the urinary bladder: review of clinicopathologic characteristics with an emphasis on aspects related to molecular diagnostic techniques and prognosis," *Journal of the National Comprehensive Cancer Network*, vol. 7, no. 1, pp. 48–54, 2009.

[4] T. J. Beck, W. Beyer, T. Pongratz et al., "Clinical determination of tissue optical properties in vivo by spatially resolved reflectance measurements," in *Photon Migration and Diffuse-Light Imaging*, vol. 5138 of *Proceedings of SPIE*, pp. 96–105, June 2003.

[5] N. Kalyagina, V. Loschenov, D. Wolf, C. Daul, W. Blondel, and T. Savelieva, "Experimental and Monte Carlo investigation of visible diffuse-reflectance imaging sensitivity to diffusing particle size changes in an optical model of a bladder wall," *Applied Physics B*, vol. 105, no. 3, pp. 631–639, 2011.

[6] L. Perelman and V. Backman, "Spectroscopy of light scattered by epithelial tissues: principles and applications," in *Handbook of Optical Biomedical Diagnostics*, V. Tuchin, Ed., chapter 12, pp. 36–76, Fizmalit, Moscow, Russia, 2007.

[7] V. Backman, M. B. Wallace, L. T. Perelman et al., "Detection of preinvasive cancer cells," *Nature*, vol. 406, no. 6791, pp. 35–36, 2000.

[8] W. F. Cheong, M. Motamedi, and A. J. Welch, "Optical modeling of laser photocoagulation of bladder tissue," *Lasers in Surgery and Medicine*, vol. 7, p. 72, 1987.

[9] W. M. Star, H. P. Marijnissen, H. Jansen, M. Keijzer, and M. J. van Gemert, "Light dosimetry for photodynamic therapy by whole bladder wall irradiation," *Photochemistry and Photobiology*, vol. 46, no. 5, pp. 619–624, 1987.

[10] R. Splinter, W. F. Cheong, M. J. C. Van Gemert, and A. J. Welch, "In vitro optical properties of human and canine brain and urinary bladder tissues at 633 nm," *Lasers in Surgery and Medicine*, vol. 9, no. 1, pp. 37–41, 1989.

[11] A. Dunn, "Modeling of light scattering from inhomogeneous biological cells," in *Optics of Biological Particles*, A. Hoekstra, V. Maltsev, and G. Videen, Eds., pp. 19–29, Springer, Dordrecht, The Netherlands, 2007.

[12] B. Beauvoit, T. Kitai, and B. Chance, "Contribution of the mitochondrial compartment to the optical properties of the rat liver: a theoretical and practical approach," *Biophysical Journal*, vol. 67, no. 6, pp. 2501–2510, 1994.

[13] H. J. van Staveren, J. F. Beek, J. W. H. Ramaekers, M. Keijzer, and W. M. Star, "Integrating sphere effect in whole bladder wall photodynamic therapy. I. 532 nm versus 630 nm optical irradiation," *Physics in Medicine and Biology*, vol. 39, no. 6, pp. 947–959, 1994.

[14] W. A. Luck, "Water in biological systems," *Topics in Current Chemistry*, vol. 64, pp. 113–180, 1976.

[15] J. Qu, C. MacAulay, S. Lam, and B. Palcic, "Optical properties of normal and carcinomatous bronchial tissue," *Applied Optics*, vol. 33, no. 31, pp. 7397–7405, 1994.

[16] P. Muthu, *Study of cross bridge kinetics in hypertrophic ventricular muscle [Ph.D. thesis]*, University of North Texas (Fort Worth), 2009.

[17] H.-J. Wei, D. Xing, J.-J. Lu, H.-M. Gu, G.-Y. Wu, and Y. Jin, "Determination of optical properties of normal and adenomatous human colon tissues in vitro using integrating sphere techniques," *World Journal of Gastroenterology*, vol. 11, no. 16, pp. 2413–2419, 2005.

[18] C. Bohren and D. R. Huffman, *Absorpttion and Scattering of Light by Small Particles*, A Wiley-Interscience Publication, John Wiley & Sons, New York, NY, USA, 1998.

[19] A. Doronin and I. Meglinski, "Online object oriented Monte Carlo computational tool for the needs of biomedical optics," *Biomedical Optics Express*, vol. 2, no. 9, pp. 2461–2469, 2011.

[20] L. Wang, S. L. Jacques, and L. Zheng, "MCML—Monte Carlo modeling of light transport in multi-layered tissues," *Computer Methods and Programs in Biomedicine*, vol. 47, no. 2, pp. 131–146, 1995.

[21] G. M. Palmer and N. Ramanujam, "Monte Carlo-based inverse model for calculating tissue optical properties. Part I: theory

and validation on synthetic phantoms," *Applied Optics*, vol. 45, no. 5, pp. 1062–1071, 2006.

[22] Z. Matuszak, A. Sawow, and M. Wasilewska-Rdwanska, "Fluorescence spectra of some photosensitizers in solution and in tissue-like media. Experiment and Monte Carlo simulation," *Polish Journal of Medical Physics and Engineering*, vol. 10, no. 4, pp. 209–221, 2004.

[23] C. Amra, "From light scattering to the microstructure of thin-film multilayers," *Applied Optics*, vol. 32, no. 28, pp. 5481–5491, 1993.

Research Article

Photoprotective Effect of the Plant *Collaea argentina* against Adverse Effects Induced by Photodynamic Therapy

Leandro Mamone, Daniel Sáenz, Pablo Vallecorsa, Alcira Batlle, Adriana Casas, and Gabriela Di Venosa

Centro de Investigaciones sobre Porfirinas y Porfirias (CIPYP), CONICET, Hospital de Clínicas José de San Martín, Universidad de Buenos Aires, Córdoba 2351 1er subsuelo, Ciudad de Buenos Aires, 1120AAF Buenos Aires, Argentina

Correspondence should be addressed to Gabriela Di Venosa; gabrieladivenosa@yahoo.com.ar

Photodynamic therapy (PDT) is a treatment modality for tumours and other accessible lesions based on the combination of light and a photosensitizer (PS) accumulated in the target tissue. The main disadvantage of PDT is PS retention after treatment during long time periods that conduces to cutaneous damage. It is believed that singlet oxygen is responsible for that skin photosensitization. The aim of this work was to evaluate the photoprotective activity of the methanolic extract of the Argentinian plant *Collaea argentina* against PDT under several treatments and employing different PSs. *C. argentina* exhibited photoprotective activity against aminolevulinic acid- (ALA-) PDT in the LM2 murine adenocarcinoma cell line. The photoprotection was dependant on the extract concentration and the incubation time, being detectable from $40\,\mu g/mL$ onwards and at least after 3 h exposure of the cells. *C. argentina* extract protects these mammalian tumor cells against PDT effects, and it interferes with the oxygen singlet production from PSs during PDT treatment. We propose that it will be a promising agent to protect cells against PDT-induced skin sensitivity.

1. Introduction

Photodynamic therapy (PDT) is a treatment modality for tumors and other accessible lesions. It is based on the combination of light and a photosensitizer (PS), which is a light-sensitive drug selectively accumulated in the target tissue [1].

It is widely accepted that photosensitivity is primarily caused by the production of reactive oxygen species (ROS). The cytotoxic effect of these species, through its reaction with cellular targets such as proteins, lipids, and DNA, is the rationale for the use of PDT in the treatment of cancer. Most clinical work on PDT has been carried out employing Photofrin, Temoporfin, or Verteporfin, that is, porphyrin derivatives.

5-Aminolevulinic acid (ALA) has also been successfully used as a tool for the photodiagnosis [2] and PDT of neoplastic tissue [3]. While ALA itself is neither fluorescent nor a photosensitiser, it can induce the biochemical formation of protoporphyrin IX (PpIX). Two molecules of ALA are converted into porphobilinogen, reaction mediated by porphobilinogen synthase, and 5 other enzymes, 3 cytosolic and 2 mitochondrial, which lead to the formation of PpIX, which is

a very efficient photosensitizer. Photodynamic action of PpIX is mainly induced by the generation of singlet oxygen in a type II photodynamic reaction [4].

ALA and other PSs currently employed in clinical PDT, such as Verteporfin and Temoporfin, produce singlet oxygen during the light exposure and in addition all the PSs are retained in other sites other than the tumor, thus inducing skin photosensitivity [4–7].

Photodynamic activity of certain plant components was first described about one hundred years ago. Bleaching of laundry on a lawn may be the earliest practical application of photodynamic activity. Chlorophyll, the green plant pigment, plays the main role in the production of this photodynamic action and, as well as some of its derivatives, it is used as a photosensitizer in PDT [8]. In addition, the anthraquinone, *Hypericum perforatum* extract, has recently been developed as a novel and natural PS for use in PDT of cancer. An analysis of a number of chemotherapeutic agents and their sources reveals that over 60% of approved drugs are derived from natural compounds [9].

Argentina has an abundant and diverse flora ranging from subarctic to subtropical climates; however, the medicinal properties of these plants have not been fully exploited. In previous work, we have carried out a screening of Argentinian plants in the search of new photosentizers (PSs) [10].

All the methanolic leaf extracts showed photoactivity due to their chlorophyll or their derivatives content [10]. However, the extract of *C. argentina* leaves did not induce photodamage. Since this extract contains chlorophyll and its derivatives, we hypothesised that this lack of photosensitization could be due to the presence of photoprotective compounds. The aim of this work was to evaluate the photoprotective activity of *C. argentina* leaf extract against PDT under several conditions using different PSs.

2. Materials and Methods

2.1. Chemicals. ALA and 3-[4,5-dimethylthiazol-2-yl]-2,5-diphenyltetrazoliumbromide (MTT) were obtained from Sigma-Aldrich (Poole, UK). Verteporfin was obtained from Conifarma, Argentina. Temoporfin was obtained from Biolite Pharma (Ireland, UK). The rest of the chemicals employed were of analytical grade. Chlorin e6 was from Frontier Scientific, USA, and Toluidine blue was from Merck.

2.2. Cell Line and Cell Culture. The cell line LM2 was derived from a spontaneous murine mammary adenocarcinoma of BALB/c mice. It was obtained from Instituto Roffo, Buenos Aires, Argentina [11]. The cells were cultured in RPMI 1640 medium, supplemented with 2 mM L-glutamine, 80 μg/mL gentamycin, and 5% fetal bovine serum and were maintained in a humidified atmosphere of 5% CO_2 at 37°C.

2.3. Plant Material. Collaea argentina Griseb. (BAA 2664) was collected from the Botanical Garden Lucien Hauman of the Agronomy School, University of Buenos Aires, and was identified by Ing. Agr. Juan Manuel Valla. A voucher specimen is kept in the herbarium of the mentioned institution. Plant nomenclature is according to Zuloaga et al. [12].

2.4. Extraction Procedure. Fresh leaves of *C. argentina* (100 to 200 g) were washed with distilled water, dried, and homogenized in absolute methanol. Methanolic extracts of *C. argentina* were filtered and evaporated under reduced pressure using a rotary evaporator and lyophilized afterwards to remove any traces of solvent. The obtained yields were 3% to 5%, and the resulting powders were stored at −20°C.

2.5. PDT Treatment. The cells were exposed to the different PSs (1 mM ALA, 3 mM Verteporfin, or 3 mM Temoporfin) in medium without serum. After 3 h exposure, the cells were irradiated for different time periods employing a light source located below the plate, at a distance of 20 cm. Afterwards, the medium was replaced by medium containing serum and the plates were incubated for 19 hours at 37°C and the MTT assay was performed.

The light source employed was a bank of two fluorescent lamps (Osram L 36W/10). The spectrum of the light is
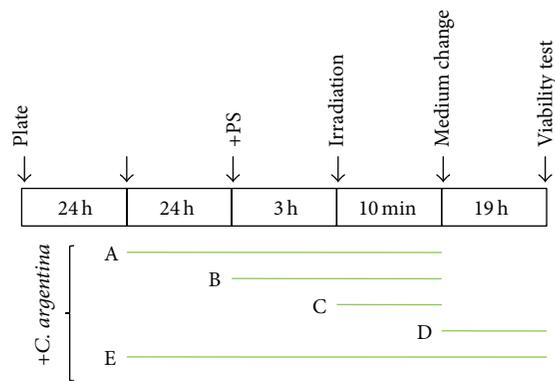
FIGURE 1: Scheme of the different treatments designed to evaluate the photoprotective effect of *C. argentina*.

between 400 and 700 nm with the highest radiant power at 600 nm. Fluence rate was measured with a Yellow Springs Kettering model 65 radiometer (Yellow Springs, OH, USA). We used fluences between 0 and 38 mJ/cm^2, corresponding to 0 to 10 min of irradiation.

2.6. Photoprotection Experiments. To test the possible photoprotective activity of *C. argentina*, the cells were plated at 5×10^4 cells/mL and 24 h afterwards, and they were exposed to different concentrations of *C. argentina*, before, during, and/or after PDT, according to Figure 1. *C. argentina* cytotoxicity (CI_{XX}) was defined as the concentration to kill XX% of cells.

2.7. Singlet Oxygen Production. To detect singlet oxygen ($^1O_2$), the shift of fluorescence of the fluorescent marker "Singlet Oxygen Sensor Green" (Invitrogen, USA) was used. The probe was added to the PSs solutions in PBS and the mixtures were irradiated with a 635 nm Lumiia Laser system (Buenos Aires, Argentina) coupled to a fibre optic at 500 W during different times, ranging from 2 to 10 min. The fluorescent product was quantified at 504 and 525 nm excitation and emission wavelengths, respectively, in a Perkin Elmer LS55 fluorometer (UK). *C. argentina* + PS mixtures kept in dark were employed as controls.

2.8. MTT Viability Assay. Cytotoxicity and phototoxicity were documented by the MTT assay [13], a method based on the activity of mitochondrial dehydrogenases. Following appropriate treatments, MTT (3-[4,5-dimethylthiazol-2-yl]-2,5-diphenyltetrazoliumbromide) solution was added to each well in a concentration of 0.5 mg/mL, and plates were incubated at 37°C for 1 h. The resulting formazan crystals were dissolved by the addition of DMSO and absorbance was read at 560 nm.

2.9. Statistical Treatment. The values in the figures and tables are expressed as means ± standard deviations of the means. A two-tailed Student's *t*-test was used to determine statistical significance between means. *P* values < 0.05 are considered significant.
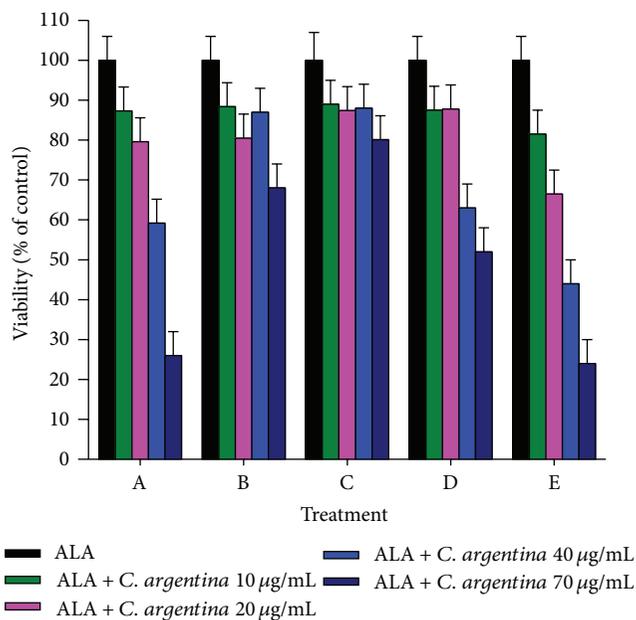
Figure 2: Cytotoxicity *per se* of *C. argentina* extract in LM2 cells. LM2 cells were incubated with *C. argentina* during different time periods according to each treatment described in Section 2. Cell death is referred as percentage of the nontreated control.

Table 1: Photoprotection indexes of *C. argentina* against ALA-PDT in LM2 cells after 10 min of irradiation.

| *C. argentina*	10 μg/mL	20 μg/mL	40 μg/mL	70 μg/mL
Treatment A	0,02	0,10	**0,92**	**0,84**
Treatment B	0,02	0,04	**0,25**	**0,59**
Treatment C	0,02	0,02	0,17	0,21
Treatment D	0,02	0,02	0,06	0,03
Treatment E	0,02	0,06	0,69	0,74

Photoprotective indexes of *C. argentina* were determined as the ratios between % cell viability after Treatment A and % cell viability after *C. argentina* dark exposure, that is, without irradiation.

3. Results

In the first stage, we attempted to assess *C. argentina* dark toxicity under the different treatments (A to D), and it was known that the methanolic extract of *C. argentina* leaf is slightly toxic to LM2 cells under darkness (CI_{50} 56 ± 5 μg/mL) [14].

Figure 2 shows cytotoxic effects of *C. argentina* under darkness (0 min irradiation). During Treatment A, at low concentrations of *C. argentina* (10 and 20 μg/mL), the toxicity *per se* was less than 20%, and at higher concentrations (40 and 70 μg/mL) *C. argentina* toxicity is proportionally increased to 41% and 75%, respectively. In Treatment B, the extract exhibits less cytotoxicity since incubation time was decreased. In Treatment C, *C. argentina* cytotoxicity is negligible since incubation time is only 10 min. Treatment D shows the highest cytotoxicity employing the highest concentrations (40 and 70 μg/mL). Treatment E involves the longest incubation time in the presence of the extract, thus showing even more marked viability decrease. To sum up, cell viability decreases as a function of the incubation time and the concentration of *C. argentina*.

In the second stage, we evaluated the effect of *C. argentina* extract to abrogate ALA-PDT induced phototoxicity in LM2 cells (Figure 3), employing ALA-PDT conditions taken from previous work [15].

C. argentina extract was added 24 h before photodynamic treatment to allow cell incorporation and during ALA-PDT (Treatment A), during ALA-PDT (Treatment B), just during the irradiation (Treatment C), after ALA-PDT (Treatment D), and before, during, and after ALA-PDT (Treatment E).

Figure 3 shows phototoxicity of ALA-PDT in the presence of *C. argentina*, normalized to the nonirradiated control. At low concentrations (10 and 20 μg/mL) of *C. argentina* under Treatment A showed no protection against ALA-PDT, but when *C. argentina* concentration was increased to 70 μg/mL, the percentage of living cells did not change upon irradiation, thus suggesting a protective effect against photosensitization.

When *C. argentina* was added only during ALA-PDT treatment (Treatment B), the photoprotection obtained was lower than that observed for Treatment A. The effect was more marked at high extract concentrations, and they increased the amount of light dose necessary to induce a certain percentage of cell death. That is, ALA-PDT with 10 min of irradiation induced 98% of cell death in absence of *C. argentina*, whereas in the presence of *C. argentina*, 40 μg/mL and 70 μg/mL, the values decreased to 70% and 40%, respectively ($P < 0.05$).

When *C. argentina* was added just during the irradiation (Treatment C), the incubation time with the cells was not enough to allow photoprotection in all the concentration range, showing only a slight protection at the highest concentrations, achieving 83% and 79% of cell death employing 40 μg/mL and 70 μg/mL, respectively, versus 98% of the control ($P < 0.05$).

When the extract was added after ALA-PDT and withdrawn just before MTT viability assay (Treatment D), photoprotection was not observed in all the concentration range of *C. argentina*.

In addition, when the incubation was performed before, during, and after ALA-PDT with *C. argentina* (Treatment E), the photoprotective effect was observed again, at the highest concentrations of *C. argentina*, leading only to 31% and 26% of cell death at 40 μg/mL and 70 μg/mL, respectively, as compared to 98% of the control ($P < 0.05$).

Throughout the experiments, we noticed that the highest concentrations of *C. argentina*, the highest photoprotection indexes, independently on the treatment, employed.

We defined a photoprotection index, which allowed us to compare the protection of each treatment, independently on *C. argentina* cytotoxity (Table 1). Indexes around 1 denote photoprotection, since they suggest no phototoxicity, whereas values around 0 indicate no protection at all. Those indexes let us know the best conditions to continue with our studies. We considered that Treatment A (incubation before and during ALA-PDT) and 40 μg/mL of *C. argentina* would be

(a)

(b)

(c)

(d)

(e)
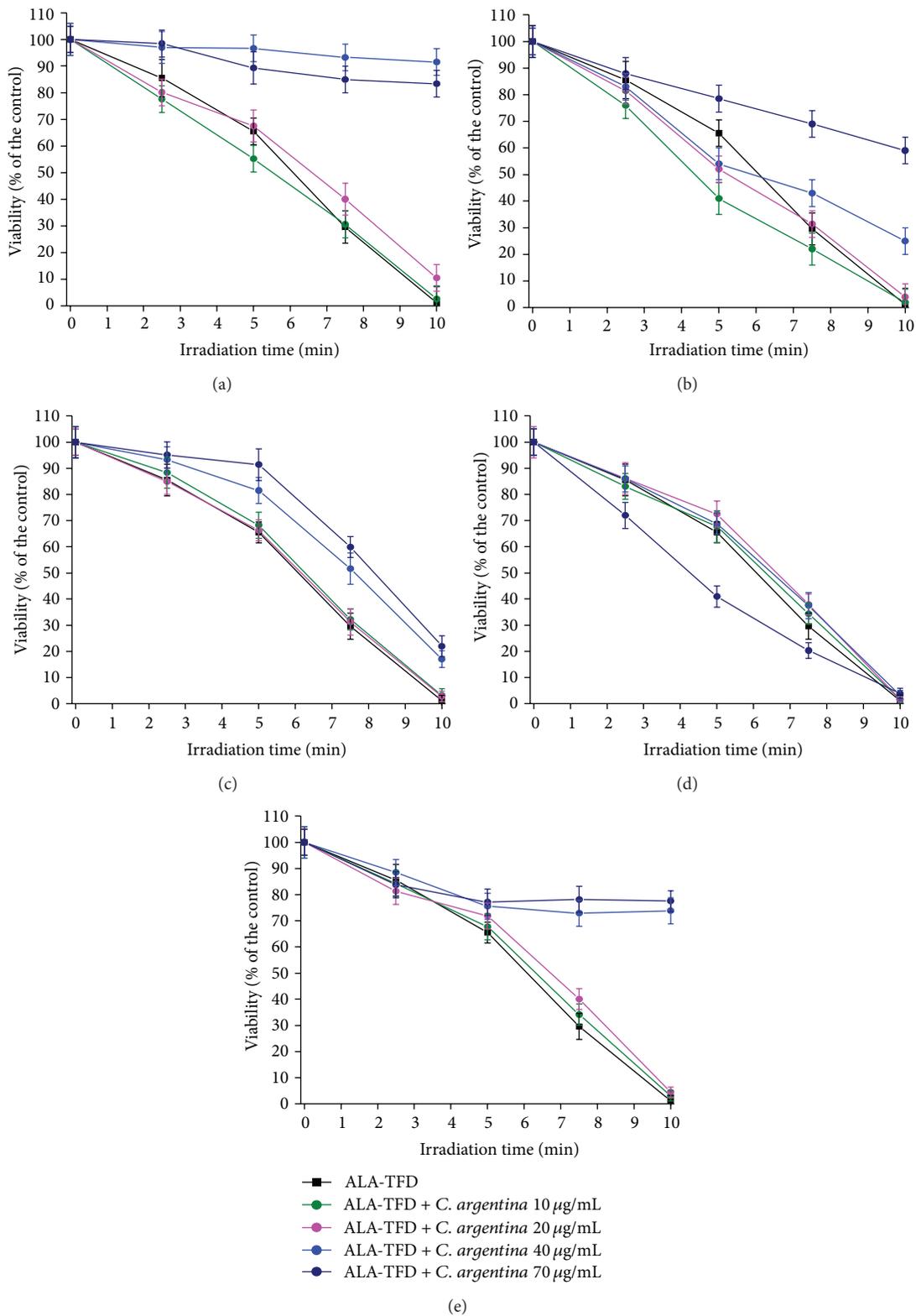
FIGURE 3: Photoprotective assays of *C. argentina* extract against ALA-PDT in LM2 cells. ALA-PDT was performed employing 0.6 mM ALA, 3 h of incubation, and different irradiation times. ((a)–(e)) correspond to the different protocols employed, as explained in Section 2. Cell viability was expressed as percentage of the control without irradiation.

FIGURE 4: ALA-PDT of LM2 cells in the presence of *C. argentina* methanolic extract or tryptophan. Cells were subjected to ALA-PDT with 0.6 mM ALA, 3 h of incubation, and then 10 min of irradiation, in the presence of either 40 μg/mL *C. argentina* or 8 mM tryptophan (treatment A). Viability was expressed as percentage of the control without treatment ($^*P < 0,05$).

TABLE 2: Photoprotection indexes of ALA, Verteporfin, and Temoporfin-PDT in LM2 cells.

Photosensitizer	*C. argentina* concentration			
	10 μg/mL	20 μg/mL	40 μg/mL	70 μg/mL
ALA (PpIX)	0,02	0,10	**0,92**	0,84
Verteporfin	0,09	0,12	**0,79**	0,75
Temoporfin	0,06	0,15	**0,61**	0,81

Photoprotective indexes of *C. argentina* were determined as the ratios between % cell viability after Treatment A and % cell viability after *C. argentina* dark exposure, that is, without irradiation.

can observe that the highest indexes were obtained against ALA-PDT (Table 2).

With the aim to test possible interferences of *C. argentina* with $^1O_2$ production during PDT, we employed Toluidine blue and Chlorin e6 as well-known PSs to induce a high singlet oxygen production (Figure 6). A dramatic decrease of $^1O_2$ production was observed in the presence of *C. argentina*, showing a direct relationship with the scavenging activity of the extract.

4. Discussion

C. argentina protected the murine LM2 adenocarcinoma cell line against PDT damage. The photoprotection was dependant on the extract concentration and the incubation time, being detectable from 40 μg/mL onwards, and at least 3 h of cell exposure. Since *per se* cytotoxicity of the extract interferes with the analysis of the results, it was necessary to determine the best conditions to perform the studies, seeking the highest photoprotection with the lowest cytotoxicity. The best conditions were 40 μg/mL of *C. argentina* methanolic extract and 24 h incubation before PDT and during PDT treatment.

Extract concentrations lower than 40 μg/mL were less toxic but, however, they did not induce photoprotection. The highest concentration employed was 70 μg/mL, and even when the photoprotection was higher, *per se* cytotoxicity of *C. argentina* was extremely high (CI_{75}).

In terms of incubation time, the strongest photoprotective effects were observed at the longest incubation times, and those are 24 and 48 h. However, 48 h incubation resulted in extremely high cytotoxicity. When the extract was added just during the irradiation or after PDT treatment, no protection was observed, thus allowing us to think that the potential photoprotective compound needs longer incubation times to be taken up by the cells. This observation agrees with a previous work of our group [15] where compounds like L-tryptophan, N-acetyl-L-cystein, melatonin, L-methionine, L-cystein, mannitol, and glycine incubated before and during PDT treatment showed the best photoprotective effects. The photoprotection of *C. argentina* was comparable with that of tryptophan, which is a well-known oxygen singlet scavenger [15].

C. argentina protection against Verteporfin and Temoporfin-PDT was also observed at a lesser extent as compared to ALA-PDT. PpIX from ALA and Verteporfin are

the best condition, since we obtained the higher photoprotective effect with the lower extract cytotoxicity.

Tryptophan is a well-known singlet oxygen scavenger and is a photoprotective compound against ALA-PDT [15]. We decided to compare the effect of tryptophan with the one excerpted by *C. argentina* under Treatment A. Figure 4 shows that tryptophan induces slight dark toxicity (CI_{10} for 8 mM Tryptophan), and at that concentration, it abrogated ALA-PDT effect completely. That protection was stronger than the one obtained from *C. argentina*.

With the aim to know if the photoprotective effect was exclusive to ALA-PDT or if it was independent on the PS used, we evaluated the photoprotection of *C. argentina* against PDT with the other two PSs of clinical use, Verteporfin and Temoporfin which produce singlet oxygen as the main ROS [4, 6, 7]. Figure 5 shows the effect of *C. argentina* against PDT under different schemes and extract concentrations. At low concentrations (10 and 20 μg/mL) it was not possible for the extract to excerpt photoprotection against Verteporfin or Temoporfin-PDT.

Employing 40 μg/mL and 70 μg/mL of the extract, a photoprotective effect against PDT with both PSs was observed. The highest photoprotection was excerpted against Verteporfin-PDT, at similar rates as compared to ALA-PDT. Cell death was reduced to 18%, which is significantly higher than 92% observed in the control of Verteporfin-PDT without extract. For Temoporfin-PDT, similar results were obtained, but achieving lower rates of photoprotection.

When we compared the photoprotective indexes of *C. argentina* against ALA, Verteporfin, or Temoporfin-PDT, we

(a)

(b)

Figure 5: Photoprotection assays of *C. argentina* against Verteporfin and Temoporfin-PDT. LM2 cells were incubated 3 h with 3 mM Verteporfin (a) or 3 mM Temoporfin (b), and *C. argentina* was added before and during PDT (Treatment A). Viability was expressed as percentage with respect to the nonirradiated control.

accumulated mainly in mitochondria and plasma membrane. Verteporfin in addition is accumulated in the endoplasmatic reticle. Temoporfin accumulates in Golgi apparatus, endoplasmatic reticle, and at minor levels, in mitochondria [16–18]. The highest photoprotection against ALA and Verteporfin-mediated PDT may be related to their subcellular localization sites.

Not always the antioxidant defenses can cope with the entire PDT damage. It was reported that nasopharyngeal tumor cells that overexpress metallothioneins, which act as free radicals scavengers, were overcome by hypericin-PDT. Hypericin is a PS extract from a plant, which produces O_2^- and $^1O_2$, and upon irradiation induces necrosis in the mentioned cells [19].

Few authors reported photoprotection against PDT. Nitroimidazoles were found to be photoprotectors against PDT using Photofrin, in the emt-6 mammalian murine tumor cell line [20]. *In vivo* studies demonstrated that 1,3 diphenyl-benzofuran and tryptophan were photoprotective compounds in rats treated with PDT using hematoporphyrin as PS [21].

A disadvantage of PDT is the PS retention in sites other than tumor during long time periods after treatment, even weeks, which induces skin photosensitivity. *In vitro* and *in vivo* studies describe that singlet oxygen is responsible for cutaneous photosensitization. It is highly important to find compounds to reduce adverse effects of PDT.

Plants have biochemical systems that attenuate the harmful effects of reactive oxygen species, in particular those generated during the photosynthesis, and xanthophylls and carotenoids account for these antioxidant defenses involved. Other compounds are able to synthesize molecules which respond to biotic and abiotic stress, commonly called secondary metabolites. Some of these compounds have been reported as photoprotectors and/or antioxidants. Beta-carotene and flavonoids usually are in chloroplast membranes to protect the damage caused by $^1O_2$, in a particular way to protect against lipid photoperoxidation. Scavenger effects of lipid plant extracts against $^1O_2$ were detected [22].

Polyphenols synthesized in higher plants, in response to stress, constitute also part of their antioxidant defense system [23]. Curcumin extracted from *Curcuma longa* is able to inhibit the apoptosis generated by oxidant damage of $^1O_2$ during PDT treatment in A431 epidermoid carcinoma cells [24].

UV and psoralen therapy is a kind of photochemotherapy which uses UV radiation instead of visible light as it is used in PDT. The use of plant extracts for UV protection is wildly known. The extract of *Polypodium leucotomos* administrated orally or topically, resulted in photoprotection in Langerhans cells against UV and psoralens employed in vitiligo treatment [25].

Employing qualitative tests to identify organic molecule functional groups, we detected the presence of anthraquinones, saponins, carbohydrates, and tanins in *C. argentina* extract. However, we do not know the exact composition of *C. argentina* and its relationship with its photoprotective properties.
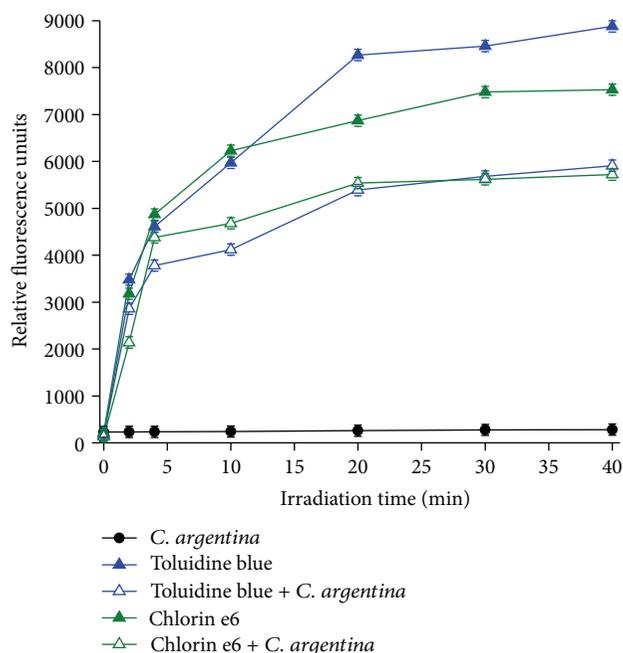
Figure 6: *C. argentina* as scavenger of singlet oxygen produced by Toluidine blue and Chlorin e6-PDT. Singlet oxygen production was quantified using a fluorescent specific probe at different times of PDT employing Toluidine blue and Chlorin e6 as photosensitizers.

To sum up, our results indicate that *C. argentina* extract protects mammalian tumor cells against PDT effects, and it interferes with singlet oxygen production during photodynamic treatment. We propose this will be a promising agent to protect skin from adverse photosensitivity. It is our hope to continue this work with *in vivo* studies and purification of the extract with the aim to isolate the compound responsible for the photoprotection and further studies in normal skin tissue are needed to ascertain that the plant *C. argentina* may be employed in the prevention from side effects caused by PDT. Our findings would be useful in the design of ointments to protect normal skin against the undesirable effects of PDT.

Abbreviations

ALA: 5-Aminolevulinic acid
MTT: 3-[4,5-Dimethylthiazol-2-yl]-2,5-diphenyltetrazoliumbromide
PDT: Photodynamic therapy
PpIX: Protoporphyrin IX
PS: Photosensitizer
PSs: Photosensitizers.

Conflict of Interests

The authors declare that there is no conflict of interests regarding the publication of this paper.

References

[1] T. J. Dougherty, "Photodynamic therapy (PDT) of malignant tumors," *Critical Reviews in Oncology and Hematology*, vol. 2, no. 2, pp. 83–116, 1984.

[2] R. Baumgartner, R. M. Huber, H. Schulz et al., "Inhalation of 5-aminolevulinic acid: a new technique for fluorescence detection of early stage lung cancer," *Journal of Photochemistry and Photobiology B*, vol. 36, no. 2, pp. 169–174, 1996.

[3] J. C. Kennedy, R. H. Pottier, and D. C. Pross, "Photodynamic therapy with endogenous protoporphyrin. IX: basic principles and present clinical experience," *Journal of Photochemistry and Photobiology B*, vol. 6, no. 1-2, pp. 143–148, 1990.

[4] B. Liu, T. J. Farrell, and M. S. Patterson, "A dynamic model for ALA-PDT of skin: simulation of temporal and spatial distributions of ground-state oxygen, photosensitizer and singlet oxygen," *Physics in Medicine and Biology*, vol. 55, no. 19, pp. 5913–5932, 2010.

[5] R. R. Allison, G. H. Downie, R. Cuenca, X.-H. Hu, C. J. H. Childs, and C. H. Sibata, "Photosensitizers in clinical PDT," *Photodiagnosis and Photodynamic Therapy*, vol. 1, no. 1, pp. 27–42, 2004.

[6] B. Hu, N. Zeng, Z. Liu et al., "Two-dimensional singlet oxygen imaging with its near-infrared luminescence during photosensitization," *Journal of Biomedical Optics*, vol. 16, no. 1, Article ID 016003, 2011.

[7] E. B. Gyenge, D. Lüscher, P. Forny et al., "Photodynamic mechanisms induced by a combination of hypericin and a chlorin based-photosensitizer in head and neck squamous cell carcinoma cells," *Photochemistry and Photobiology*, vol. 89, no. 1, pp. 150–162, 2013.

[8] R. Ebermann, G. Alth, M. Kreitner, and A. Kubin, "Natural products derived from plants as potential drugs for the photodynamic destruction of tumor cells," *Journal of Photochemistry and Photobiology B*, vol. 36, no. 2, pp. 95–97, 1996.

[9] G. M. Cragg, D. J. Newman, and K. M. Snader, "Natural products in drug discovery and development," *Journal of Natural Products*, vol. 60, no. 1, pp. 52–60, 1997.

[10] L. Mamone, A. Casas, L. Rodriguez, L. Gándara, A. Batlle, and G. di Venosa, "Estudios *in vitro* de extractos de plantas autóctonas argentinas como potenciales antineoplásicos o fotosensibilizantes en la Terapia Fotodinámica del cáncer," *Medicina Buenos Aires*, vol. 70, pp. 125–126, 2010.

[11] S. E. Werbajh, A. J. Urtreger, L. I. Puricelli, E. S. de Lustig, E. Bal de Kier Joffé, and A. R. Kornblihtt, "Downregulation of fibronectin transcription in highly metastatic adenocarcinoma cells," *The FEBS Letters*, vol. 440, no. 3, pp. 277–281, 1998.

[12] F. O. Zuloaga, O. Morrone, and M. Belgrano, *Catálogo de Plantas Vasculares del Cono Sur*, vol. 1, 2009.

[13] F. Denizot and R. Lang, "Rapid colorimetric assay for cell growth and survival—modifications to the tetrazolium dye procedure giving improved sensitivity and reliability," *Journal of Immunological Methods*, vol. 89, no. 2, pp. 271–277, 1986.

[14] L. Mamone, G. di Venosa, J. J. Valla et al., "Cytotoxic effects of argentinean plant extracts on tumour and normal cell lines," *Cellular and Molecular Biology*, vol. 57, pp. 1487–1499, 2011.

[15] C. Perotti, A. Casas, and A. M. del C. Batlle, "Scavengers protection of cells against ALA-based photodynamic therapy-induced damage," *Lasers in Medical Science*, vol. 17, no. 4, pp. 222–229, 2002.

[16] C. M. N. Yow, J. Y. Chen, N. K. Mak, N. H. Cheung, and A. W. N. Leung, "Cellular uptake, subcellular localization and photodamaging effect of Temoporfin (mTHPC) in nasopharyngeal carcinoma cells: comparison with hematoporphyrin derivative," *Cancer Letters*, vol. 157, no. 2, pp. 123–131, 2000.

[17] L. D. Barnes, E. A. Giuliano, and J. Ota, "Cellular localization of Visudyne as a function of time after local injection in an in vivo model of squamous cell carcinoma: an investigation into tumor cell death," *Veterinary Ophthalmology*, vol. 13, no. 3, pp. 158–165, 2010.

[18] A. D. Tekrony, N. M. Kelly, B. A. Fage, and D. T. Cramb, "Photobleaching kinetics of Verteporfin and Lemuteporfin in cells and optically trapped multilamellar vesicles using two-photon excitation," *Photochemistry and Photobiology*, vol. 87, no. 4, pp. 853–861, 2011.

[19] H.-Y. Du, Y. Li, M. Olivo, G. W.-C. Yip, and B.-H. Bay, "Differential up-regulation of metallothionein isoforms in well-differentiated nasopharyngeal cancer cells in vitro by photoactivated hypericin," *Oncology Reports*, vol. 16, no. 6, pp. 1397–1402, 2006.

[20] R. Santus, C. C. Stobbe, M. S. McPhee, and J. D. Chapman, "Protection against light-activated photofrin II killing of tumor cells by nitroimidazoles," *Radiation Research*, vol. 130, no. 1, pp. 31–37, 1992.

[21] N. D. Hogikyan, R. E. Hayden, and P. W. McLear, "1991Cutaneous photoprotection using a hydroxyl radical scavenger in photodynamic therapy," *American Journal of Otolaryngology*, vol. 12, no. 1, pp. 1–5.

[22] R. Ferrari-Iliou, A. D'Arcy-Lamenta, J.-P. Iliou et al., "In vitro photodynamic lipid peroxidation of total lipophilic extracts from leaves of bean plants," *Biochimica et Biophysica Acta*, vol. 1166, no. 1, pp. 48–54, 1993.

[23] L. G. Korkina, S. Pastore, E. Dellambra, and C. de Luca, "New molecular and cellular targets for chemoprevention and treatment of skin tumors by plant polyphenols: a critical review," *Current Medicinal Chemistry*, vol. 20, no. 7, pp. 852–868, 2013.

[24] W.-H. Chan and H.-J. Wu, "Anti-apoptotic effects of curcumin on photosensitized human epidermal carcinoma A431 cells," *Journal of Cellular Biochemistry*, vol. 92, no. 1, pp. 200–212, 2004.

[25] S. González, M. A. Pathak, J. Cuevas, V. G. Villarrubia, and T. B. Fitzpatrick, "Topical or oral administration with an extract of Polypodium leucotomos prevents acute sunburn and psoralen-induced phototoxic reactions as well as depletion of Langerhans cells in human skin," *Photodermatology Photoimmunology and Photomedicine*, vol. 13, no. 1-2, pp. 50–60, 1997.

Research Article

Safety Study of Photodynamic Therapy Using Talaporfin Sodium in the Pancreas and Surrounding Tissues in the Syrian Golden Hamster

Johannes Wittmann,[1] Matthew T. Huggett,[2] Stephen G. Bown,[1] and Stephen P. Pereira[2]

[1] *National Medical Laser Centre, Division of Surgery and Interventional Science,*
  University College London Medical School, London, UK
[2] *UCL Institute for Liver and Digestive Health, University College London Medical School, London, UK*

Correspondence should be addressed to Stephen P. Pereira; stephen.pereira@ucl.ac.uk

Aim. To assess the safety of photodynamic therapy (PDT) using talaporfin sodium on the pancreas and surrounding organs in normal hamsters. *Methods*. Fluorescence microscopy documented talaporfin levels in liver, duodenum, and pancreas up to 24 hours after photosensitisation. Lesion size in liver 3 days after PDT (50 J, 5 mg/kg, variable drug-light interval (DLI)) was documented to optimise the DLI. Using optimum DLI, pancreas and surrounding organs were treated with laser fibre touching the surface and animals were killed at 3 or 21 days. *Results*. Peak fluorescence was seen in duodenum and pancreas at 15 mins (second lower peak at 2 hours). Liver fluorescence was consistently high (peak 1 hour) until after 4 hours. Optimum DLI was seen at 15 minutes. The pancreas was relatively resistant to direct PDT injury (small lesions at high doses) but surrounding stomach, duodenum, and liver were more susceptible with evidence of adhesions and full thickness damage (localised peritonitis and duodenal perforation at highest doses). *Conclusion*. The safety profile is similar to PDT with longer acting photosensitisers. The pancreas appears safe to treat, but care is required to avoid high light doses to the intestinal tract, particularly the duodenum.

1. Introduction

In the UK approximately 8000 people are diagnosed with pancreatic adenocarcinoma each year [1, 2]. Surgical resection is the only chance of cure and is only possible in a minority of subjects. Even after resection, the median survival is only 10–20 months and only 12–35% of resected patients survive five years or more [3–6]. Palliative chemotherapy can improve both quality of life and survival in advanced disease [7–10], but overall, the long-term prognosis of the disease is poor with a one-year survival rate of 15–39% [11–16]. These dismal results stimulated the search for a minimally invasive treatment capable of local destruction of tumour tissue with low morbidity that might have a place in the treatment of unresectable disease.

Photodynamic therapy (PDT) for pancreatic cancer was first described in 2002 [17]. This showed that image guided,

interstitial PDT using the photosensitiser mTHPC (Foscan) could produce localised tumour necrosis with low morbidity, although the prolonged skin photosensitivity associated with mTHPC limited its acceptability for patients. This stimulated the search for shorter acting photosensitisers, with less potential photosensitivity.

Talaporfin sodium (LS11, Laserphyrin, mono-L-aspartyl chlorin; Light Sciences Corporation, Snoqualmie, WA, USA) is a chlorophyll and L-aspartic acid derived, pure photosensitiser codeveloped by Meiji Seika and Nippon Petrochemicals. The expected 1-2 week cutaneous photosensitivity following talaporfin administration is considerably shorter than that associated with other commonly used agents like porfimer sodium and mTHPC [18, 19]. In 2004, talaporfin was approved in Japan for PDT for early stage non-small-cell lung cancer [20]. The drug is mainly confined to the vasculature during the first hour after intravenous injection

and Phase II clinical trials using talaporfin sodium for palliation of colorectal liver metastases have been completed with minimal toxicity using drug light intervals of 15–60 minutes [18, 21].

Animal studies have established the safety and potential efficacy of PDT for pancreatic cancer using a variety of photosensitisers including mTHPC, dihaematoporphyrin ether (DHE), and 5-ALA [22–24]. However, the effects and safety of talaporfin PDT on the normal pancreas and surrounding abdominal organs have not been studied. This study reports safety data using the normal female Syrian golden hamster.

2. Methods

The study was undertaken on normal mature, female Syrian golden hamsters, 90–120 g in weight. Approval was obtained from the local ethics committee and performed under UK Home Office licenses issued under "The Protection for Animals (Scientific Procedures) Act, 1986". All animals were cared for within university animal facilities and published guidelines on the care and treatment of laboratory animals were followed. All procedures were carried out under general anaesthesia, initiated by an intraperitoneal injection of Hypnorm (fentanyl and fluanisone, Janssen Pharmaceuticals), midazolam 5 mg/mL (Roche Pharmaceuticals), and sterile water in a 1 : 1 : 2 mixture; and maintained by inhalational halothane (ICI Pharmaceuticals, Cheshire, UK) with oxygen supplementation for a maximum duration of two hours. Subcutaneous buprenorphine hydrochloride (Reckitt & Colman Products Ltd., UK) was administered to provide up to 24 hours of postoperative analgesia. No hamster required further doses of analgesia in the postoperative period.

Talaporfin sodium was kindly supplied free of charge (Light Sciences Corporation, Snoqualmie, WA, USA) as a green lyophilised powder in 100 mg vials and reconstituted using sterile normal saline to a suitable concentration for hamster use. For drug administration, a laparotomy was performed under sterile conditions to provide access for direct intracaval injection and light delivery. The animals remained in a darkened environment for a total of 48 hours after photosensitisation and were assessed daily.

2.1. Fluorescence Microscopy.
The pharmacokinetics of talaporfin were studied using fluorescence microscopy. Hamsters were injected with 5 mg/kg and killed at time intervals of 15, 30, 60, 120, and 240 minutes and 24 hours after sensitisation (2 animals at each time point, including 2 unsensitised animals to measure autofluorescence). At postmortem, samples of liver, duodenum, and pancreas were harvested and snapfrozen by immersion in isopentane (2-methylbutane; BDH, UK) prechilled in liquid nitrogen and stored at $-80°C$. For analysis, the tissue blocks were mounted on OCT medium (tissue tek II embedding compound; BDH, UK) and 4, 10 μm thick sections cut from each block using a Cryocut E microtome (Reichert-Jung) and thawed prior to fluorescence microscopy.

Fluorescence was excited by a 1.8 mW helium-neon laser (532.8 nm) coupled to a liquid light guide with the beam directed via a band-pass filter at 540 nm into the dichroic mirror housing for epifluorescence studies (Omega Optical Inc.). Fluorescence was detected between 630 and 690 nm using a combination of band-pass (Omega Optical Inc.) and long-pass (Schott) filters using an Olympus IMT-2 inverted microscope (10x objective magnification) with epifluorescence and phase-contrast attachments.

Fluorescence was quantified using a highly sensitive, cryogenically cooled CCD (charge-coupled device) camera (Wright Instruments, Model 1, resolution 400 × 600 pixels) fitted to the microscope and was processed by an IBM personal computer into a falsely colour-coded image of the tissue sections. Fluorescence was reported in counts per pixel, corrected for autofluorescence (about 30 counts per pixel). Tissue samples were taken from two animals per time point with at least two sections per organ from each animal. Four readings per tissue section were then taken for a minimum of 16 separate fluorescence readings per time point per organ.

2.2. Photodynamic Therapy.
The PDT studies were divided into 2 sections—the first to optimise the drug light interval and the second to study the specific effects on the pancreas and the surrounding organs. In both, the hamsters were sensitised by an intracaval injection of talaporfin at laparotomy and light from a 664 nm laser (IRIS Medical OcuLight 664) delivered using a 400 μm diameter, cleaved optical fibre placed perpendicular to and touching the surface of the targeted organ. There was no shielding of surrounding organs and light scatter with illumination through and beyond the directly targeted organs was observed. The laser power output from the fibre tip was set at 100 mW using a power meter (Model TPM-300, Gentec Electro-Optics Inc., Qc, Canada).

2.3. Drug Light Interval (DLI).
Studies to establish the drug light interval for maximum PDT effect were undertaken on the liver using a talaporfin dose of 5 mg/kg and a light dose of 50 J, the interval between drug administration and light delivery being varied from 5 to 240 minutes (2 animals at each DLI). After light delivery, the laparotomy wound was closed and the animal was killed 3 days later. At postmortem, the dimensions of the near spherical zone of PDT necrosis in the liver were measured in three axes and the volume of necrosis was calculated: $V = 4/3\pi \cdot a \cdot b \cdot c$ (where a, b, and c = perpendicular axes of necrosis in mm). This study showed that the optimum drug light interval was 15 minutes, so this value was used in the subsequent safety studies.

2.4. Safety Study.
The main purpose of the study was to establish the safety of talaporfin PDT for treatment of pancreatic cancer, so this part of the work was to examine the effect of delivering light directly to the pancreas and the immediately adjacent organs that might be at risk. In addition to the work in the pancreas, the organs specifically targeted were the liver, spleen, duodenum, and retroperitoneum (major blood vessels), with most studies being undertaken targeting the pancreas with increasing drug and light doses. The resources available made it unrealistic to treat each target organ under all the conditions under consideration, so only selected values

TABLE 1: Summary of treatment response of individual hamsters in the safety study.

Target organ	Drug dose (mg/kg)	Light dose (J)	Day of cull	Comment
Liver	1	50	3	Macroscopic lesion
	1	50	3	Macroscopic lesion, adhesion to colon
	1	50	21	Small superficial lesion, adhesion to colon
	1	50	21	Small superficial lesion
	5	50	3	Large lesion with adhesion to stomach
	5	50	3	Large lesion with adjacent duodenal injury
Pancreas	1	20	3	Minimal erythema
	1	20	3	No definite effect
	5	20	3	No lesion in pancreas. Adhesions and full thickness gastric lesion
	1	20	21	No lesions
	1	20	21	No lesions
	1	25	21	No lesion in pancreas. Adhesion to liver
	5	20	21	No lesion in pancreas. Scar in stomach
	5	20	21	No lesion in pancreas. Scar in stomach
	5	50	12 (>10% weight loss)	Lesion in pancreas, multiple adhesions, ascites, small bowel perforation
	5	50	13 (>10% weight loss)	Lesion in pancreas, multiple adhesions, small and large bowel perforation
Duodenum	2	15	3	Sealed perforation, adhesions
	2	20	3	Sealed perforation, adhesions
Spleen	1	20	3	Small lesion, minor bowel adhesion
	1	20	3	Small lesion and subcapsular haematoma
Aorta	2	15	3	No lesions seen
	2	15	3	No lesions seen

of the drug and light doses were studied. This approach was felt to be justified as the value of the whole study was essentially to compare the safety of talaporfin PDT with that of PDT in these organs with other photosensitisers, as has been reported in many earlier publications from this and other centres. The actual treatment parameters studied are shown in Table 1.

After treatment and recovery, the hamsters were killed at 2 different time points. The first group was culled at 72 to 96 hours, known to be the best time interval to ascertain the maximum extent of PDT tissue injury (Day 3 group). Hamsters in the second group were allowed to recover for 21 days as a survival study and were then culled to establish whether the healing of PDT-treated areas was satisfactory in terms of structural integrity and function of organs (Day 21 group). Any animal that had lost more than 10% of its pretreatment weight prior to the scheduled day for culling was killed immediately, in accordance with the care of laboratory animals guidelines. The effects of PDT were documented at postmortem. Apart from the liver, the treated organs were too small for accurate quantification of the extent of necrosis, so the results were limited to macroscopic assessment for evidence of necrosis, perforation, leakage of blood, bile or gastrointestinal contents, gastric or duodenal ulceration, and ascites.

The pancreas, free edge of lesser omentum, duodenum, stomach, aorta, vena cava, bile duct, and liver were removed at necropsy if macroscopic lesions were evident, or if these were the targeted tissue sites, regardless of obvious PDT lesions. Tissue was preserved in formalin and processed for wax block sectioning and haematoxylin-eosin staining for histological analysis. One unsensitised animal was treated with 100 J of light at 100 mW targeted at the pancreas to exclude a thermal laser effect. Another received 5 mg/kg talaporfin without light activation to exclude any dark toxicity.

3. Results

3.1. Fluorescence Microscopy. The results are shown in Figure 1. The highest drug concentrations were seen in the liver with the peak at one hour. Intermediate levels were seen in the duodenum and with the lowest values being documented in the pancreas. In the pancreas and duodenum, peak levels were seen after 15 minutes with a second slightly lower peak at 2 hours, after which the concentration fell in all 3 organs.

3.2. Drug Light Interval (DLI). Full thickness liver lobe lesions (3–5 mm thickness) were seen at all DLI measurements up to 4 hours. The lesions were well demarcated and
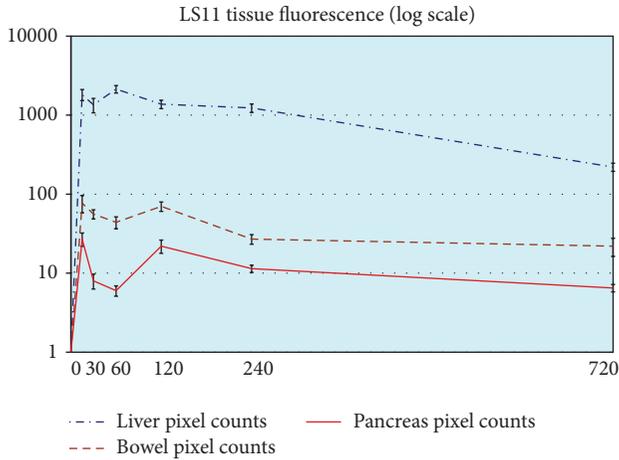
FIGURE 1: Fluorescence (in counts per pixel ± SD as a log scale, corrected for autofluorescence) measured in cryosections of liver, duodenum, and pancreas as a function of the time after administration of 5 mg/kg talaporfin.
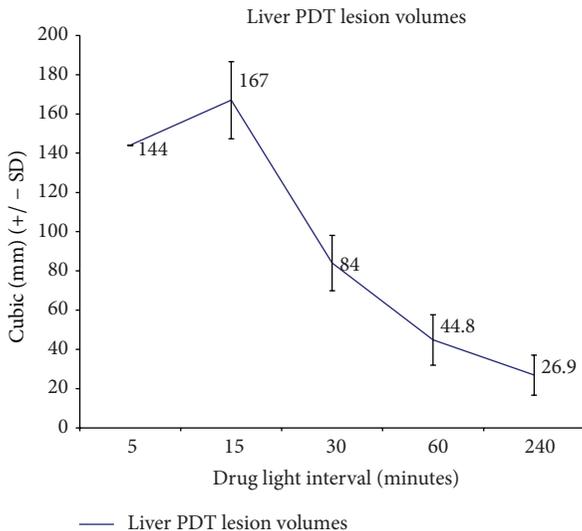

FIGURE 2: Volume of PDT necrosis in liver from hamsters treated with 50 J red light (664 nm) as a function of time after administration of 5 mg/kg talaporfin.

roughly spherical in shape. The volume of necrosis as a function of the DLI is shown in Figure 2. The greatest volume of necrosis was observed with a 15 minute DLI (167 mm^3 ($n = 3$; SD 19.7 mm^3)) and this interval was therefore chosen for the subsequent safety studies. Lesions at longer intervals became progressively smaller.

3.3. Safety Study. All animals in the safety study were treated with a DLI of 15 minutes. The results for individual animals are summarised in Table 1. No lesions were seen in the control animals treated with drug alone or light alone.

3.3.1. General Morbidity. All animals lost some weight initially, up to 5% of baseline body weight, indicating a degree of physical harm as a result of the laparotomy and PDT treatment, compared to the control animals having laparotomy and drug alone or light alone. Recovery, including regaining lost weight, was universal by 21 days post-PDT in all but the two hamsters which received high dose pancreatic PDT who were culled prematurely for severe complications.

3.3.2. Liver. Four animals in the Day 3 group (including 2 from the DLI study) and two in the Day 21 group underwent PDT of the middle or left liver lobes with a 15-minute DLI. Those treated with the highest doses of drug (5 mg/kg) and light (50 J) showed macroscopic PDT lesions with adhesions to adjacent stomach, small bowel, or colon. A section of treated liver is shown in Figure 3(a). Those treated under less severe conditions, including the two hamsters in the Day 21 group, showed similar, but milder effects. There were no fatal complications and no evidence of biliary obstruction or gallbladder injury.

3.3.3. Pancreas. Ten animals underwent PDT with light applied directly to the pancreas and a DLI of 15 minutes. Three were culled on day 3 and 7 on day 21. With a light dose of 20–25 J, no pancreatic lesions were seen with a drug dose up to the maximum of 5 mg/kg. However, some of these animals showed lesions in adjacent organs. Full thickness gastric lesions, but without evidence of perforation, were seen in one animal culled on day 3 and in 2 culled on day 21 (all treated with 5 mg/kg, 20 J). Adhesions were noted in 1 of 3 animals culled on day 3 post-PDT and in 1 of 5 animals in the group culled on day 21. There was no evidence of biliary obstruction at light doses of up to 25 J. Significant pancreatic lesions were seen in 2 animals treated with 50 J and 5 mg/kg. These animals were culled at 12 and 13 days due to more than 10% weight loss. At necropsy there was macroscopic evidence of duodenal perforation, full thickness gastric lesions, and peritonitis with extensive local adhesions to liver, stomach, small bowel, and colon in both. A histological section showing the junction of normal and PDT-treated pancreas is shown in Figure 3(b).

3.3.4. Duodenum. The most severe damage was seen with duodenal treatment. Two animals treated with the low doses of 2 mg/kg and 15–20 J showed full thickness lesions with sealed perforations and adhesions to adjacent liver and colon.

3.3.5. Spleen. Two animals in the Day 3 group had splenic PDT at 1 mg/kg and 20 J. There was localised puckering and scarring at the site of PDT and one animal had histological evidence of a subcapsular haematoma, but with no evidence of clinical distress.

3.3.6. Aorta and IVC. No definite PDT lesions were found macroscopically or on histology in two animals treated with PDT at 2 mg/kg and 15 J, when the laser fibre was used to directly target the exposed vessels.

The severity of scarring and adhesions increased with the severity of the treatment conditions (drug and light doses), as expected. Moderate adhesions were observed between PDT-treated liver and bowel, and PDT-treated pancreas and

(a)

(b)
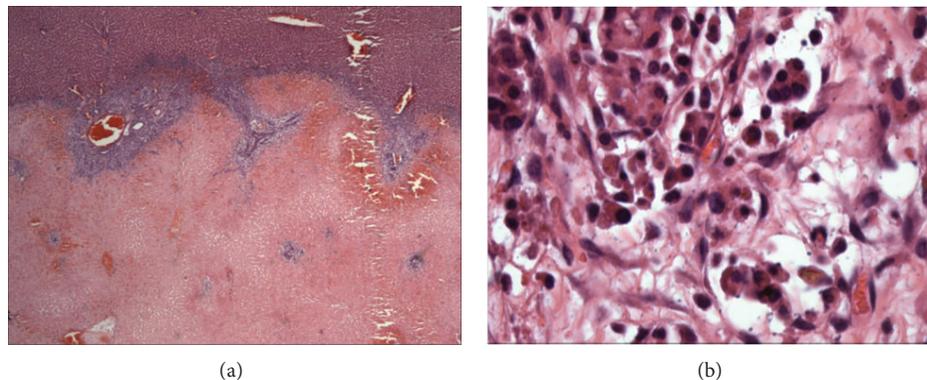
FIGURE 3: (a) Histological section of liver 3 days after treatment with PDT showing the sharp demarcation between PDT necrosis and untreated liver with a few islands of viable tissue in the necrotic area. (b) Histological section of pancreas 12 days after treatment demonstrating the junction of normal pancreas (top left) with PDT necrosis (bottom right).

bowel. In the maximally treated animals, adhesions were more extensive and were seen in multiple areas between the pancreas, liver, and intestinal tract.

4. Discussion

Destroying a cancer of localised and known extent with PDT is relatively straightforward. A key issue is what happens where the cancer meets normal tissue and how the treated area heals. The aim of this study was to establish if talaporfin PDT is safe for the treatment of pancreatic adenocarcinoma. Previous hamster studies have looked at the effect of PDT with mTHPC, with which the optimum drug light interval is up to 4 days for treating cancers of the pancreas [19]. In this work, treating normal pancreas was shown to be safe, but the duodenum was found to be vulnerable under conditions required for cancer therapy [22]. These hamster results were borne out in our clinical study with mTHPC [17]. The present study shows that the most effective DLI for talaporfin is 15 minutes, at which time the drug is predominantly in the vasculature, so different effects might be anticipated. It is of interest to note that the highest concentration of drug in the liver measured by fluorescence was at one hour, whereas the volume of necrosis was nearly 4 times greater at 15 minutes than it was at one hour, suggesting that the drug is more effective if it remains in the vasculature. Nevertheless, our results show that PDT with talaporfin is remarkably similar to that seen with mTHPC. In the liver, quite large areas of necrosis can be produced, but these heal safely and without sequelae.

One of the major attractions of PDT is that there is no significant change in tissue temperature during treatment, so connective tissues like collagen are largely unaffected [25]. This helps to maintain the mechanical integrity of tissue, particularly hollow organs. However, if the conditions used for treating a cancer cause serious damage to the normal tissue in which the cancer arose or adjacent normal tissues, then the treatment may be detrimental. For this reason, it is essential to understand what PDT does to a normal organ before using it to treat a cancer in that organ. In the case of

the pancreas, the risks are that PDT might cause a fistula or lead to duct obstruction with consequent pancreatitis and also that it might seriously injure adjacent tissues like the duodenum. The pancreas, however, seems relatively resistant and lesions can only be produced with high drug (5 mg/kg) and light (50 J) doses. These lesions heal safely, but light scattered from the pancreas under these conditions causes overwhelming damage to adjacent organs. Perforations to the large and small intestine were seen, together with full thickness lesions in the stomach wall, ascites, and multiple adhesions. Preservation of collagen in the gastric wall probably explained why the stomach was less prone to perforation than the thinner-walled duodenum but, fortunately, there was no evidence of biliary tree or vascular injury.

These results help to define how PDT with talaporfin might safely be used for cancers of the pancreas in humans. The red light used in this study (664 nm) produced effects up to 6–8 mm deep in tissue. Due to the smaller scale of the hamster pancreas, it is not unexpected that a significant amount of light directed at the head of the pancreas was scattered to the duodenum. However, in humans, the distances are much greater, so that as long as the light delivery fibre is separated from the duodenum by more than about 1 cm (for example by positioning the fibre tip 1 cm deep into the pancreatic tissue), duodenal damage is unlikely, as shown in the clinical studies with mTHPC.

Previous work has also looked at the effect of PDT with mTHPC on cancers of pancreatic origin transplanted into the hamster pancreas [19]. The present study did not extend to looking at the effects on transplanted cancers, as our aim was to establish safety. Skin photosensitivity was also not assessed in the present study, but other publications have shown that this is a maximum of 1-2 weeks for talaporfin [18].

In patients, talaporfin doses of 2 mg/kg or 40 mg/m^2 have been used safely in Phase I and II studies of solid tumours [18, 21]. The light dose delivered determines the size of the PDT lesion, so that larger tumour masses can be treated using multiple laser fibres or with sequential fibre placement within a treatment window of 15 minutes to 1 hour after injection of photosensitiser. Waiting for longer periods of up to

4 hours, as shown in Figure 2, to allow talaporfin to distribute into the extracellular matrix, did not seem advantageous in this study, as fluorescence data showed no increase in talaporfin tissue levels than earlier time periods and PDT lesions seen in the liver were smaller than at 15 minutes. These results are comparable to those reported for another short acting photosensitiser, verteporfin, in both experimental and clinical studies [26, 27].

It is concluded that the results of the current work, together with other published experimental and clinical data, support the use of talaporfin in Phase 1 studies of PDT for pancreatic cancer in inoperable patients with localised disease, although care must be taken to minimise the exposure of the duodenum to light.

Abbreviations

mTHPC: Meso-tetrahydroxyphenyl chlorin
PDT: Photodynamic therapy
DLI: Drug light interval.

Conflict of Interests

The authors declare that there is no conflict of interests regarding the publication of this paper.

Acknowledgments

References

[1] A. Jemal, A. Thomas, T. Murray, and M. Thun, "Cancer statistics, 2002," *CA-A Cancer Journal for Clinicians*, vol. 52, no. 1, pp. 23–47, 2002.

[2] D. M. Parkin, P. Pisani, and J. Ferlay, "Global cancer statistics," *CA-A Cancer Journal for Clinicians*, vol. 49, no. 1, pp. 33–64, 1999.

[3] T. J. Kinsella, Y. Seo, J. Willis et al., "The impact of resection margin status and postoperative CA19-9 levels on survival and patterns of recurrence after postoperative high-dose radiotherapy with 5-FU—based concurrent chemotherapy for resectable pancreatic cancer," *The American Journal of Clinical Oncology*, vol. 31, no. 5, pp. 446–453, 2008.

[4] G. Eeson, N. Chang, C. E. McGahan et al., "Determination of factors predictive of outcome for patients undergoing a pancreaticoduodenectomy of pancreatic head ductal adenocarcinomas," *HPB*, vol. 14, no. 5, pp. 310–316, 2012.

[5] O. Turrini, F. Paye, P. Bachellier et al., "Pancreatectomy for adenocarcinoma in elderly patients: postoperative outcomes and long term results: a study of the French Surgical Association," *European Journal of Surgical Oncology*, vol. 39, no. 2, pp. 171–178, 2013.

[6] J. He, B. H. Edil, J. L. Cameron et al., "Young patients undergoing resection of pancreatic cancer fare better than their older counterparts," *Journal of Gastrointestinal Surgery*, vol. 17, no. 2, pp. 339–344, 2013.

[7] H. A. Burris III, M. J. Moore, J. Andersen et al., "Improvements in survival and clinical benefit with gemcitabine as first-line therapy for patients with advanced pancreas cancer: a randomized trial," *Journal of Clinical Oncology*, vol. 15, no. 6, pp. 2403–2413, 1997.

[8] T. Conroy, F. Desseigne, M. Ychou et al., "FOLFIRINOX versus gemcitabine for metastatic pancreatic cancer," *New England Journal of Medicine*, vol. 364, no. 19, pp. 1817–1825, 2011.

[9] B. Glimelius, K. Hoffman, P.-O. Sjödén et al., "Chemotherapy improves survival and quality of life in advanced pancreatic and biliary cancer," *Annals of Oncology*, vol. 7, no. 6, pp. 593–600, 1996.

[10] D. D. Von Hoff, T. Ervin, F. P. Arena et al., "Increased survival in pancreatic cancer with nab-paclitaxel plus gemcitabine," *The New England Journal of Medicine*, vol. 369, no. 18, pp. 1691–1703, 2013.

[11] R. H. Hawes, Q. Xiong, I. Waxman, K. J. Chang, D. B. Evans, and J. L. Abbruzzese, "A multispecialty approach to the diagnosis and management of pancreatic cancer," *The American Journal of Gastroenterology*, vol. 95, no. 1, pp. 17–31, 2000.

[12] M. Sant, C. Allemani, M. Santaquilani, A. Knijn, F. Marchesi, and R. Capocaccia, "EUROCARE-4. Survival of cancer patients diagnosed in 1995–1999. Results and commentary," *European Journal of Cancer*, vol. 45, no. 6, pp. 931–991, 2009.

[13] T. Kuroda, T. Kumagi, T. Yokota et al., "Improvement of long-term outcomes in pancreatic cancer and its associated factors within the gemcitabine era: a collaborative retrospective multi-center clinical review of 1, 082 patients," *BMC Gastroenterology*, vol. 13, article 134, 2013.

[14] J. Luo, L. Xiao, C. Wu, Y. Zheng, and N. Zhao, "The incidence and survival rate of population-based pancreatic cancer patients: shanghai cancer registry 2004–2009," *PLoS ONE*, vol. 8, no. 10, Article ID e76052, 2013.

[15] Z. Gong, E. A. Holly, and P. M. Bracci, "Survival in population-based pancreatic cancer patients: San Francisco Bay Area, 1995–1999," *The American Journal of Epidemiology*, vol. 174, no. 12, pp. 1373–1381, 2011.

[16] D. P. Cronin-Fenton, R. Erichsen, F. V. Mortensen, S. Dikinis, M. Nørgaard, and J. Jacobsen, "Pancreatic cancer survival in central and northern Denmark from 1998 through 2009: a population based cohort study," *Clinical Epidemiology*, vol. 3, supplement 1, pp. 19–25, 2011.

[17] S. G. Bown, A. W. R. Hatfield, A. Z. Rogowska et al., "Photodynamic therapy for cancer of the pancreas," *Gut*, vol. 50, no. 4, pp. 549–557, 2002.

[18] R. A. Lustig, T. J. Vogl, D. Fromm et al., "A multicenter phase I safety study of intratumoral photoactivation of talaporfin sodium in patients with refractory solid tumors," *Cancer*, vol. 98, no. 8, pp. 1767–1771, 2003.

[19] P. Mlkvy, H. Messman, A. J. MacRobert et al., "Photodynamic therapy of a transplanted pancreatic cancer model using meta-tetrahydroxyphenylchlorin (mTHPC)," *British Journal of Cancer*, vol. 76, no. 6, pp. 713–718, 1997.

[20] J. Usuda, H. Tsutsui, H. Honda et al., "Photodynamic therapy for lung cancers based on novel photodynamic diagnosis using talaporfin sodium (NPe6) and autofluorescence bronchoscopy," *Lung Cancer*, vol. 58, no. 3, pp. 317–323, 2007.

[21] M. Kujundžić, T. J. Vogl, D. Stimac et al., "A phase II safety and effect on time to tumor progression study of intratumoral light infusion technology using talaporfin sodium in patients with metastatic colorectal cancer," *Journal of Surgical Oncology*, vol. 96, no. 6, pp. 518–524, 2007.

[22] P. Mlkvy, H. Messmann, M. Pauer et al., "Distribution and photodynamic effects of meso-tetrahydroxyphenylclhlorin (mTHPC) in the pancreas and adjacent tissues in the Syrian golden hamster," *British Journal of Cancer*, vol. 73, no. 12, pp. 1473–1479, 1996.

[23] J. Regula, B. Ravi, J. Bedwell, A. J. MacRobert, and S. G. Bown, "Photodynamic therapy using 5-aminolaevulinic acid for experimental pancreatic cance—Prolonged animal survival," *British Journal of Cancer*, vol. 70, no. 2, pp. 248–254, 1994.

[24] T. Schroder, I.-W. Chen, M. Sperling, R. H. Bell Jr., K. Brackett, and S. N. Joffe, "Hematoporphyrin derivative uptake and photodynamic therapy in pancreatic carcinoma," *Journal of Surgical Oncology*, vol. 38, no. 1, pp. 4–9, 1988.

[25] H. Barr, C. J. Tralau, P. B. Boulos, A. J. MacRobert, R. Tilly, and S. G. Bown, "The contrasting mechanisms of colonic collagen damage between photodynamic therapy and thermal injury," *Photochemistry and Photobiology*, vol. 46, no. 5, pp. 795–800, 1987.

[26] L. Ayaru, J. Wittmann, A. J. MacRobert, M. Novelli, S. G. Bown, and S. P. Pereira, "Photodynamic therapy using verteporfin photosensitization in the pancreas and surrounding tissues in the Syrian golden hamster," *Pancreatology*, vol. 7, no. 1, pp. 20–27, 2007.

[27] M. T. Huggett, M. Jermyn, A. Gillams et al., "Phase I/II study of verteporfinphotodynamic therapy in locally advanced pancreatic cancer," *British Journal of Cancer*. In press.

Research Article

Potential Use of C_{60}/2-Hydroxypropyl-β-cyclodextrin Nanoparticles as a New Photosensitizer in the Treatment of Cancer

Abdulmalik Altaf,[1,2] Hibah Aldawsari,[1] Zainy M. Banjar,[1] Daisuke Iohara,[3] Makoto Anraku,[3] Kaneto Uekama,[1,4] and Fumitoshi Hirayama[3]

[1] *Faculty of Pharmacy, King Abdulaziz University, Jeddah 21589, Saudi Arabia*

[2] *Faculty of Medicine, King Abdulaziz University, Jeddah 21589, Saudi Arabia*

[3] *Faculty of Pharmaceutical Sciences, Sojo University, 4-22-1 Ikeda, Kumamoto 860-0082, Japan*

[4] *DDS Research Institute, Sojo University, 4-22-1 Ikeda, Kumamoto 860-0082, Japan*

Correspondence should be addressed to Fumitoshi Hirayama; fhira@ph.sojo-u.ac.jp

The photosensitizing ability of C_{60}/2-hydroxypropyl-β-cyclodextrin (HP-β-CyD) nanoparticles under visible light irradiation was studied by electron spin resonance (ESR) and phototoxicity on cancer cells. In addition, the photoinduced antitumor effect to the tumor-bearing mice was evaluated. C_{60} nanoparticles were prepared by grinding a mixture of HP-β-CyD. The resulting C_{60}/HP-β-CyD nanoparticles were highly-sensitive to visible light and generated higher levels of $^1O_2$ than protoporphyrin IX (PpIX). C_{60}/HP-β-CyD reduced the viability of cancer cells (HeLa cells and A549 cells) in response to irradiation by visible light in a dose-dependent manner. The IC$_{50}$ values of the C_{60}/HP-β-CyD nanoparticles was $10\,\mu$M for HeLa cells and $60\,\mu$M for A549 cells at an irradiation level of $35\,\text{mW/cm}^2$. The photodynamic effect of C_{60}/HP-β-CyD nanoparticles on the *in vivo* growth of mouse sarcoma S-180 cells was evaluated after intratumor injection. The outcome of PDT by C_{60}/HP-β-CyD was directly dependent on the dose of irradiated light. Treatment with C_{60}/HP-β-CyD nanoparticles at a C_{60} dose of 2.0 mg/kg under visible light irradiation at $350\,\text{mW/cm}^2$ ($63\,\text{J/cm}^2$) markedly suppressed tumor growth, whereas that at $30\,\text{J/cm}^2$ was less effective. These findings suggest that C_{60}/HP-β-CyD nanoparticles represent a promising candidate for use in cancer treatment by PDT.

1. Introduction

Photodynamic therapy (PDT), which involves the production of reactive oxygen species (ROS), is a next-generation cancer treatment. In PDT, a photosensitizer is systemically administered, either locally or topically, and tumor sites are then irradiated by visible light to site-selectively generate ROS, leading to cell death and tissue destruction [1–3]. Therefore, PDT is an effective method for destroying diseased tissues without damaging surrounding healthy tissue. The ideal photosensitizer for use in PDT should meet the following requirements: (1) have high quantum yields for generating ROS, (2) have a strong absorbance with a high extinction coefficient in the long-wavelength (600~800 nm) region,

where the maximum penetration of tissue by the penetrating light occurs [4], and (3) have minimal toxicity under conditions of nonlight irradiation. Many of the currently clinically employed photosensitizers are based on porphyrin molecules such as Photofrin, a hematoporphyrin derivative, and 5-aminolevulinic acid (ALA), a precursor of protoporphyrin IX (PpIX). However, these compounds have several disadvantages such as suboptimal tumor selectively and poor light penetration into tumors due to the absorption of the relatively short wavelengths. Therefore, more efficient photosensitizers are currently in various stages of development [5].

Fullerenes are currently of great interest for practical applications that take advantage of their unique electronic

properties and biological activities [6–8]. The fullerene family, especially C_{60}, is generally regarded as an efficient photosensitizer for PDT [9] due to light absorption at relatively long wavelengths and the high quantum yield of photoexcitation reactions [10, 11]. C_{60} molecules generate ROS such as singlet oxygen ($^1O_2$) and superoxide anion radicals ($O_2^{\bullet-}$) under light irradiation [10, 12]. In a previous study, we reported on the preparation of stable C_{60} nanoparticles (mean particle size ca. 90 nm), the surfaces of which were covered by hydrophilic 2-hydroxypropyl-β-cyclodextrin (HP-β-CyD) through physical adsorption and weak hydrophobic interactions [13]. The C_{60}/HP-β-CyD nanoparticles showed cell toxicity due to their ability to generate ROS when irradiated with visible light [14]. However, few studies have focused on the *in vivo* photodynamic activity of C_{60}. In spite of the advantages of PDT over conventional therapies, PDT is not extensively used, compared to the well-established chemo- and radiotherapy due to insufficient understanding of the procedures involved. In particular, the outcome of PDT is influenced by several factors such as the dose of the photosensitizer used, the presence of molecular oxygen, the irradiation time and the interval between drug administration and irradiation, and the correct dose of light. Thus, it is necessary to validate standard protocols for each individual photosensitizer in order to obtain an effective and reliable outcome [15]. In this study, we evaluated the photosensitizing ability of C_{60}/HP-β-CyD nanoparticles under visible light irradiation as a new photosensitizer in PDT. In addition, we examined the *in vivo* photodynamic activity of C_{60}/HP-β-CyD nanoparticles in tumor-bearing mice after visible light irradiation.

2. Materials and Methods

2.1. Materials. C_{60} (nanom purple SUH) was purchased from Frontier Carbon Co. (Tokyo, Japan). 2-Hydroxypropyl-β-CyD (HP-β-CD, degree of substitution (D.S.) of the 2-hydroxypropyl group was 5.6) was a gift from Nihon Shokuhin Kako Co., Ltd. (Tokyo, Japan). Hydrophilic C_{60}/HP-β-CyD nanoparticles were prepared by the coground method reported in previous paper [13]. ALA was purchased from Wako Pure Chemical Industries Ltd. (Tokyo, Japan). PpIX disodium salt was purchased from Sigma-Aldrich Co. LLC. (Tokyo, Japan) and dissolved in 10 mM NaOH or 10% dimethyl sulfoxide (DMSO) for ESR study and cell toxicity study, respectively. 5,5-Dimethyl-1-pyrroline N-oxide (DMPO) was purchased from Labotec Co. Ltd. (Tokyo, Japan). 4-Hydroxy-2,2,6,6,-tetramethylpiperidine (TEMP-OH) was purchased from Wako Pure Chemical Industries Ltd. (Tokyo, Japan). Eagle's minimum essential medium (MEM), Dulbecco's modified Eagle's medium (DMEM), and penicillin-streptomycin were purchased from GIBCO Invitrogen Co. (Tokyo, Japan). Fetal calf serum (FCS) was obtained from Nichirei (Tokyo, Japan). All other materials and solvents were of analytical reagent grade and Milli-Q water was used throughout the study.

2.2. Photosensitizing Ability of C_{60}/HP-β-CyD Nanoparticles under Visible Light Irradiation. The generation of $O_2^{\bullet-}$ and $^1O_2$ from C_{60}/HP-β-CyD nanoparticles and PpIX were measured using an X-band electron spin resonance (ESR) spectrometer (JES-FA100, JEOL Ltd., Tokyo, Japan) under the following conditions: microwave frequency 9.417 GHz, microwave power 4 mW, field modulation 0.1 mT at 100 kHz, and sweep time 30 s. $O_2^{\bullet-}$ was detected using DMPO as a spin-trapping reagent. The DMPO-OH signal was detected on ESR spectra, because the unstable DMPO-OOH adduct was rapidly converted to a DMPO-OH adduct. One hundred microliter aliquots of sample solutions and 80 μL of Milli-Q and 20 μL of DMPO were mixed well under aerobic conditions. $^1O_2$ was also detected by the ESR using TEMP-OH as a spin-trapping reagent. One hundred microliters of a sample solution and 100 μL of TEMP-OH (160 mM) were well mixed under aerobic conditions. The mixed solutions were collected in a flat cell, then exposed to visible light generated by a xenon light source (MAX-303, Asahi spectra Co., Ltd., Tokyo, Japan), and subjected immediately to ESR measurement. Generation efficiency of $O_2^{\bullet-}$ and $^1O_2$ was evaluated by the relative intensity to an external reference of Mn^{2+}.

2.3. Photoinduced Cell Toxicity by C_{60}/HP-β-CyD Nanoparticles. HeLa cells were cultured in MEM containing 100 units/mL penicillin-streptomycin, supplemented with 10% fetal bovine serum at 37°C and 5% of CO_2. A549 cells were cultured in DMEM containing 100 units/mL penicillin-streptomycin, supplemented with 10% fetal bovine serum at 37°C and 5% of CO_2. The cells were seeded in 96-well plates at a density of 2.0×10^4 cells/well for HeLa cells and 1.0×10^4 cells/well in the case of A549 cells. After growing overnight, the cells were incubated with the samples (1 μM~ 150 μM for C_{60} and 1 μM~300 μM for ALA) for 24 h in the dark. The cells were washed with phosphate-buffered saline (PBS) and replaced with fresh culture medium. The treated cells were exposed to light (35 mW/cm^2, 400–700 nm) for 30 min, using a xenon light source. To measure the viability of cells as a ratio (%) compared with cells which were not treated with the samples, a WST-1 (4-[3-(4-iodophenyl)-2-(4-nitrophenyl)-2H-5-tetrazolio]-1,3-benzene disulfonate) assay was carried out 24 h after the photoirradiation, by using a Cell Counting Kit (Dojindo Laboratories, Kumamoto, Japan). WST-1 works by reacting with the mitochondrial succinate-tetrazolium reductase forming the formazan dye. The effect of ROS scavengers on cell viability was studied used HeLa cells. The cells were incubated with C_{60}/HP-β-CyD nanoparticles for 24 h and then washed with PBS and the medium was replaced with fresh medium including 10 mM of L-histidine, 2,5-dimethylfuran (DMF) and 1,4-diazabicyclo [2, 2, 2] octane (DABCO) or 500 unit/mL of superoxide dismutase (SOD). After 1 h incubation, the treated cells were exposed to the light. To measure the viability of cells, WST-1 assay was carried out 24 h after the photoirradiation.

2.4. In Vivo Photodynamic Activity of C_{60}/HP-β-CyD Nanoparticles. The care and maintenance of animals were conducted in accordance with the institutional guidelines of the Institutional Animal Care and Use Committee of Sojo

University. To prepare a mouse tumor model, mouse sarcoma S-180 cells were acclimatized to the *in vivo* conditions by intraperitoneal growth in ddY mice (Kyudo Co. Ltd., Saga, Japan). The cells were implanted by subcutaneous injection in the dorsal skin of 6-week-old ddY mice (2×10^7 cells/mL, 100μL/mouse). When the tumor mass reached a diameter of 7~8 mm, 0.1 mL of C_{60}/HP-β-CyD nanoparticles in 5% glucose solution ($C_{60} = 1$ mM) were injected to the intratumor (2.0 mg/kg of C_{60}, i.e., 0.072 mg of C_{60} per 35 ± 2 g body weight). The tumor tissue was exposed to visible light from a xenon light source at 400~700 nm (100~350 mW/cm^2). Tumor volume (mm^3) was calculated as $(W^2 \times L)/2$ by measuring the length (L) and width (W) of the tumor on the dorsal skin.

3. Results and Discussion

3.1. Photosensitizing Ability of C_{60}/HP-β-CyD Nanoparticles under Visible Light Irradiation. C_{60} is generally regarded to be an effective photosensitizer for PDT [9]; however, its extremely low solubility and poor dispersibility in water have significantly impeded pharmaceutical applications [16, 17]. Although several water soluble fullerene derivatives have been produced and their photodynamic activity evaluated [18, 19], only few studies in which the efficacy of C_{60} was compared with other photosensitizers have appeared. We therefore examined the *in vitro* photosensitizing ability of C_{60}/HP-β-CyD nanoparticles, in comparison with that of PpIX by means of an ESR spin-trapping method. A xenon light source was used to produce homogenous light in the visible light range (Supplementary Figure 1(S) in Supplementary Material available online at http://dx.doi.org/10.1155/2014/570506). Figure 1(a) shows ESR spectra of C_{60}/HP-β-CyD colloidal and PpIX solutions under photoirradiation. These photosensitizers produced three characteristic signals for TEMPO-OH in ESR spectra [20], indicating that $^1O_2$ was generated by the photoirradiation. The relative intensity of the TEMPO-OH to an external reference (Mn^{2+}) in these solutions increased with the photoirradiation time (Figure 1(b)). C_{60}/HP-β-CyD nanoparticles generated higher levels of $^1O_2$ than PpIX at every time period of photoirradiation. As shown in Figure 1(c), the generation of $^1O_2$ from these photosensitizers was almost the same as that produced under low light energy (5 mW/cm^2); however, the C_{60}/HP-β-CyD nanoparticles were highly sensitive to the power of the light and large amounts of $^1O_2$ were generated when a higher energy light source was used. It was estimated that at least 1.5 times larger energy is needed for PpIX to generate the same amount of $^1O_2$ as that produced in the case of a C_{60} colloidal solution. For both C_{60}/HP-β-CyD and PpIX, the generation of $^1O_2$ under visible light irradiation was concentration dependent (Figure 1(d)). The generation of $^1O_2$ at a low concentration (20 μM) was low in both the C_{60} and PpIX systems, whereas C_{60}/HP-β-CyD showed higher generation ability in the higher concentration range compared with that for PpIX. We previously reported that the HP-β-CyD-enhanced generation of $^1O_2$ was due to the partial deposition of C_{60} in the hydrophobic CyD cavity [13], because the

production of $^1O_2$ shows a preference for nonpolar solvents. The low generation of $^1O_2$ at low concentrations may be due to the dissociation of HP-β-CyD from the C_{60} nanoparticles. These collective results indicate that C_{60}/HP-β-CyD has a potent photosensitizing ability when compared with PpIX under visible light irradiation. In addition, C_{60} has capability to generate $O_2^{\bullet-}$ when irradiated with visible light, as shown in Figure 2. A four-line ESR signal corresponding to DMPO-OH was detected in the ESR spectra [21], suggesting that $O_2^{\bullet-}$ is generated in the C_{60}/HP-β-CyD colloidal solution. On the other hand, such a signal was not observed for PpIX. The generation of $O_2^{\bullet-}$ by C_{60}/HP-β-CyD was also light power dependent and dose dependent, similar to that for the generation of $^1O_2$ (Figure 1). C_{60}/HP-β-CyD showed the higher absorption than that of PpIX at the region of 420 nm~540 nm and almost the same absorption spectra at the region of 600~700 nm where the maximum light absorption of C_{60} occurred at 620 nm, while that of PpIX was at 635 nm (Supplementary Figure 1(S)). The quantum yield for $^1O_2$ at this wavelength was reported to be 0.96 for C_{60} in benzene [10], while the corresponding value was 0.56 for PpIX in phosphate buffer, the former value being higher than those for Photofrin and other photosensitizers [22, 23]. In this study, constant light energy was supplied in the wavelength range of 400~700 nm. Therefore, the different ROS generation ability of C_{60} and PpIX is probably due to not only the higher absorption at blue region but also the difference in the intrinsic photoexcitation properties of the photosensitizers. Further, it is known that extensive aggregation of photosensitizers significantly accelerates the decay of the excited triplet state [24], thus reducing the photosensitizing ability. In a previous study, we reported that C_{60} exists in the form of stable small aggregates with a particle size ca. 90 nm in C_{60}/HP-β-CyD colloidal solutions [13]. This might explain the higher photosensitizing ability of colloidal solutions of C_{60}/HP-β-CyD, compared to PpIX solutions.

3.2. Photoinduced Cell Toxicity by C_{60}/HP-β-CyDs Nanoparticles. The photodynamic activity of C_{60}/HP-β-CyD nanoparticles on human cervical cancer HeLa cells and human lung carcinoma A549 cells was evaluated by WST-1 assays. We chose ALA as a control photosensitizer because PpIX is administered clinically in the form of a precursor. ALA is a naturally occurring amino acid that endogenously produced PpIX and the resulting PpIX can generate singlet oxygen leading to cancer cell death. The use of ALA has become a widely acceptable and popular procedure, particularly for the treatment of skin cancer [25]. As shown in Figure 3, C_{60}/HP-β-CyD nanoparticles and ALA reduced the viability of these cells in response to the visible light irradiation and in a dose-dependent manner. The IC$_{50}$ value of ALA for HeLa and A549 cells was 100 μM and 150 μM, respectively. In the case of C_{60}/HP-β-CyD nanoparticles, the cellular survival significantly decreased at lower concentrations of C_{60} as a result of the photoirradiation. The IC$_{50}$ value of the C_{60}/HP-β-CyD nanoparticles was 10 μM for HeLa cells and 60 μM for A549 cells, which were much lower than those of ALA.

(a)

(b)

(c)

(d)
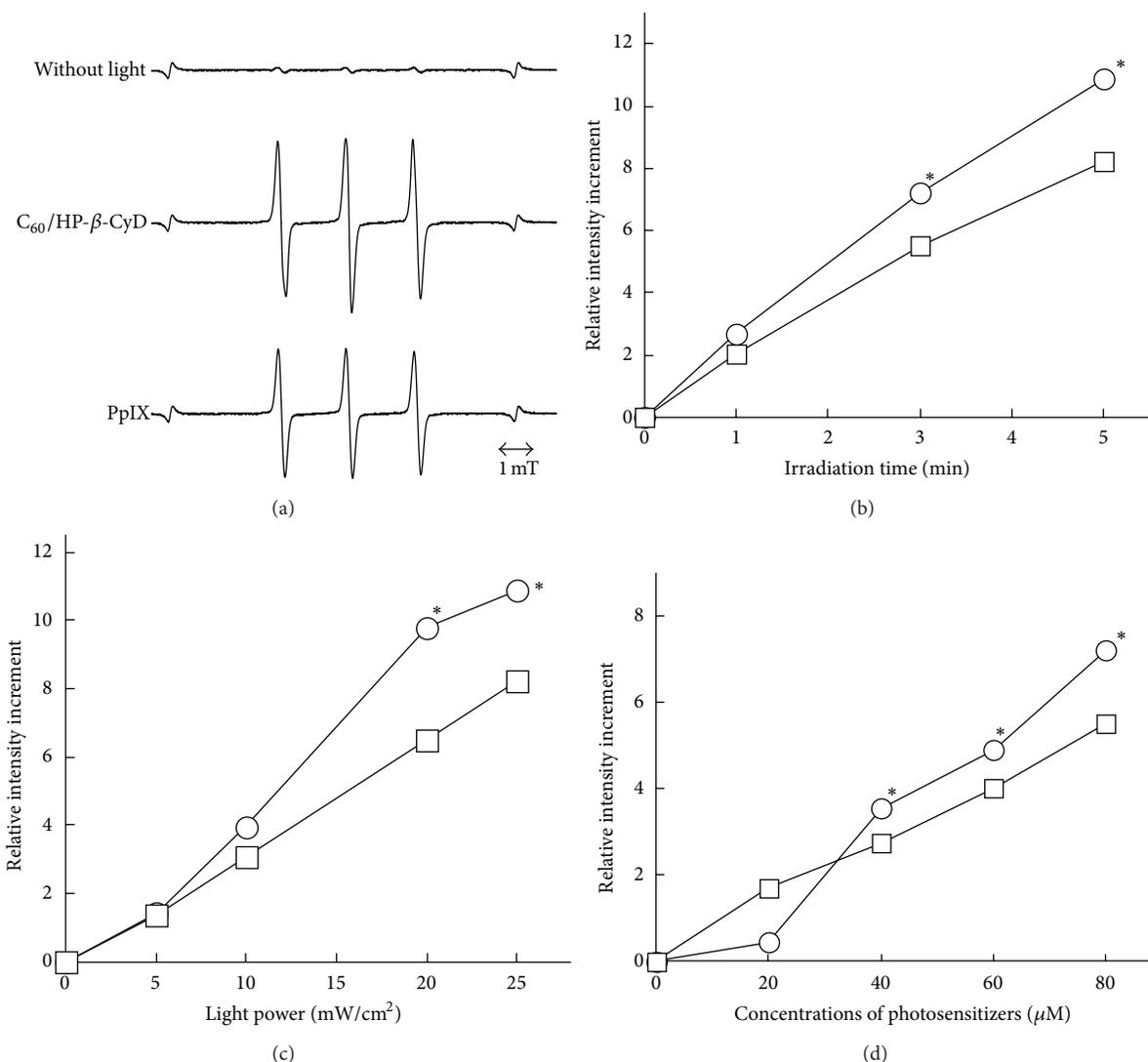
Figure 1: ESR spectra of the TEMPO-OH adduct generated in a C_{60}/HP-β-CyD colloidal solution and a PpIX solution (C_{60} and PpIX = 80 μM, light irradiation at 25 mW/cm^2 for 5 min) (a). Its relative intensity increment after visible light irradiation. (b) Effects of the light power (c) and concentrations of photosensitizers (d) on the generation of $^1O_2$. Empty circle: C_{60}/HP-β-CyD nanoparticles; empty square: PpIX. Each point represents the mean ± S.E. of 3 experiments. $^*P < 0.05$ versus PpIX.

This is probably due to the great ROS generation of C_{60}/HP-β-CyD nanoparticles compared with ALA. When the cell viability test was conducted in the dark, no cell toxicity was observed at these concentrations of photosensitizers. In addition, C_{60}/HP-β-CyD nanoparticles have capability to generate $O_2^{\bullet-}$ when irradiated with visible light as described above. In this study, the extracellular C_{60} was washed away prior to light irradiation; therefore, ROS such as $O_2^{\bullet-}$ and $^1O_2$ might be generated from C_{60} taken up by cells, leading to the cell death. To assess the contribution of $O_2^{\bullet-}$ and $^1O_2$ to the cell death, the effects of $^1O_2$ scavengers, such as L-histidine, 2,5-dimethylfuran (DMF) and 1,4-diazabicyclo [2, 2, 2] octane (DABCO) [20] and $O_2^{\bullet-}$ specific scavenger, superoxide dismutase (SOD), were studied. As shown in Figure 4, cell viability was increased by the addition of these ROS scavengers. These results indicate that both $O_2^{\bullet-}$ and $^1O_2$

contribute to the potent photoinduced cell toxicity of C_{60}/HP-β-CyD nanoparticles. However, we could not discuss which ROS is more effective to the cell death because the scavenging ability and cellular permeability of these scavengers were different from each other. Also, the amounts of C_{60} and ALA (or PpIX produced in the cells), especially C_{60}, taken up in the cells could not be measured accurately due to the UV detection limit. The present results clearly indicate that C_{60}/HP-β-CyD nanoparticles are toxic to cells only when irradiated by visible light, although further study is still needed to precisely evaluate the differences of the photosensitizers, C_{60} and ALA.

3.3. In Vivo Photodynamic Activity of C_{60}/HP-β-CyD Nanoparticles. Since C_{60}/HP-β-CyD nanoparticles demonstrated a potential to succeed as photosensitizer in PDT, a subsequent in vivo study was conducted to determine the standard

(a)

(b)

(c)

(d)
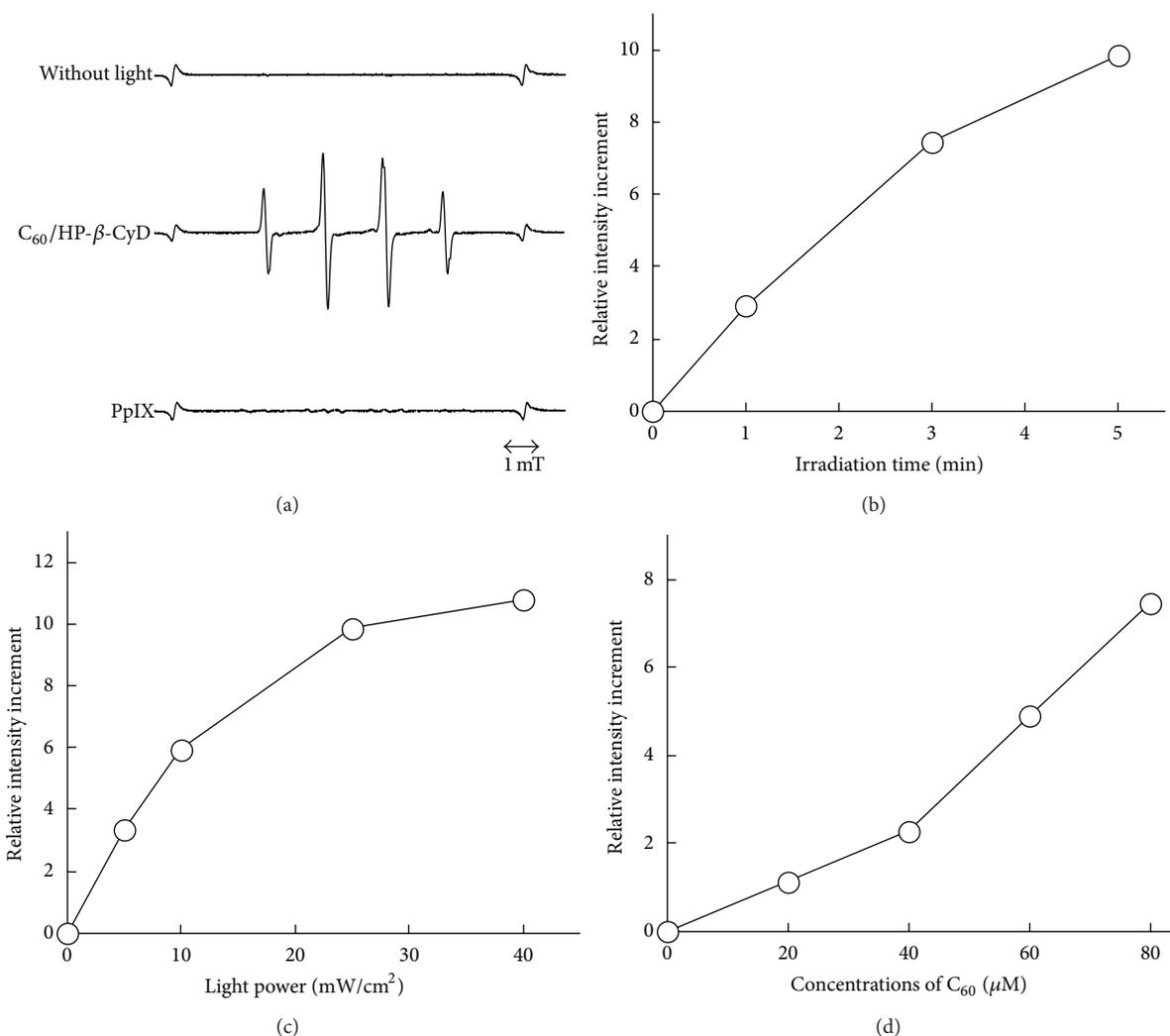
FIGURE 2: ESR spectra of the DMPO-OH adduct generated in the C_{60}/HP-β-CyD colloidal solution ($C_{60} = 40\,\mu M$, light irradiation at 40 mW/cm^2 for 5 min) (a). Its relative intensity increment after visible light irradiation (b). Effects of the light power (c) and concentrations of photosensitizers (d) on the generation of $O_2{}^{\bullet-}$. Each point represents the mean ± S.E. of 3 experiments.

protocols for the effective application of PDT by C_{60}. Figure 5 shows the photodynamic effect of C_{60}/HP-β-CyD nanoparticles on the *in vivo* growth of mouse sarcoma S-180 cells after intratumor injection. The tumor was irradiated for a short time period which was repeated at 30 s intervals. The tumor growth was similar to that observed for a saline injection, when treated with C_{60}/HP-β-CyD nanoparticles at a C_{60} dose of 2.0 mg/kg, followed by visible light irradiation once at 100 mW/cm^2 for 300 s (30 J/cm^2) or 5 times at 200 mW/cm^2 for 60 s (total light does 60 J/cm^2). On the other hand, it was significantly suppressed when the irradiation power was increased, that is, 5 times at 250 mW/cm^2 for 60 s (total light does 75 J/cm^2). However, light irradiation alone at 75 J/cm^2 significantly affected the tumor growth, as shown by the symbol of the empty triangle in Figure 5. In fact, the temperature increased to 50°C from 37°C when a mercury thermometer was directly light-irradiated at 250 W/cm^2 for 60 s and normal skin was burned after being irradiated at

this power. Therefore, it is very important to choose adequate irradiation doses to avoid damage to healthy tissues caused by a temperature increase. Figure 6 shows the photodynamic effects of C_{60}/HP-β-CyD nanoparticles on tumor growth as the result of visible light irradiation 12 times at 350 mW/cm^2 for 15 s (total light dose 63 J/cm^2). As shown in Figures 6(a) and 6(b), tumor growth was significantly suppressed by this treatment at a dose of 2.0 mg/kg C_{60}/HP-β-CyD. The treatment with C_{60}/HP-β-CyD at a dose of 0.4 mg/kg was less effective against tumor growth, when compared with a dose of 2.0 mg/kg. The light irradiation alone had no effect on tumor growth and there was no significant difference compared with the saline injected group, suggesting a minor hyperthermia of the irradiation alone in this condition. The time profile for mice tumor growth treated with C_{60}/HP-β-CyD nanoparticles without light irradiation was similar to that for the saline injection. Thus, C_{60}/HP-β-CyD itself had no detectable cytocidal effect on the tumor tissue in the

(a)

(b)
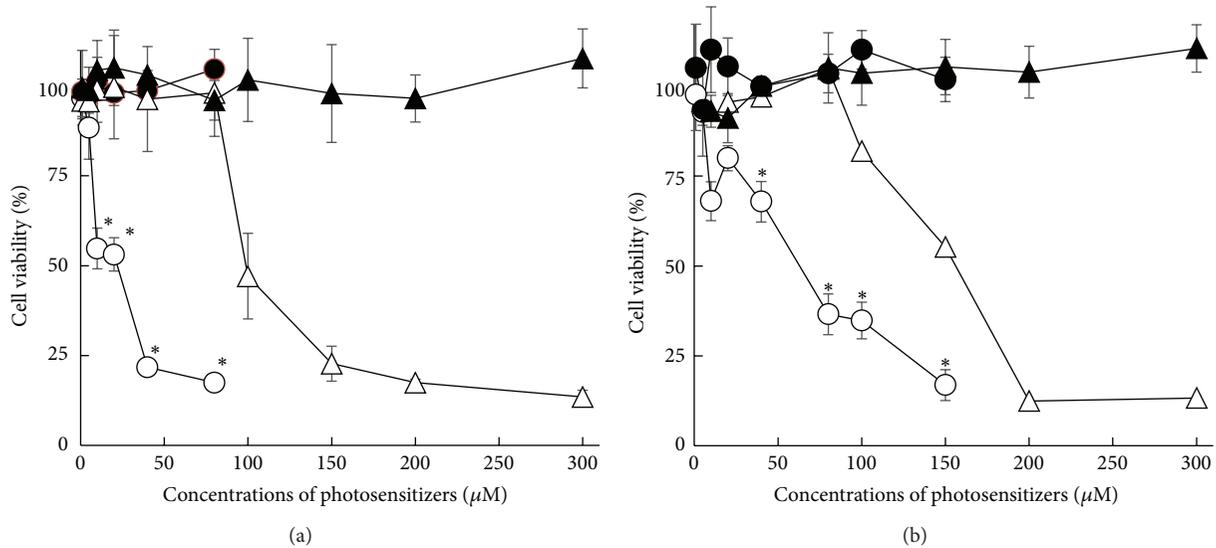
FIGURE 3: Photodynamic activities of C_{60}/HP-β-CyD nanoparticles and ALA for HeLa cells (a) and A549 cells (b) after visible light irradiation at 35 mW/cm^2. Black filled circle: C_{60}/HP-β-CyD in the dark; black filled triangle: ALA in the dark; empty circle: C_{60}/HP-β-CyD with light irradiation; empty triangle: ALA with light irradiation. Each value points the mean $\pm$ S.E. of 3–5 experiments. $^*P < 0.05$ versus ALA with light irradiation.
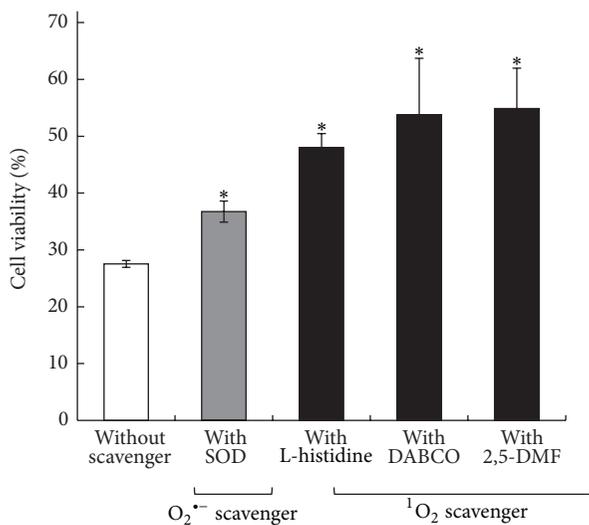

FIGURE 4: Effect of ROS scavengers on photodynamic effect by C_{60}/HP-β-CyD nanoparticles on HeLa cells. Each value represents the mean $\pm$ S.E. of 5 experiments. $^*P < 0.05$ versus without ROS scavenger.

FIGURE 5: Photodynamic effects of C_{60}/HP-β-CyD nanoparticles (C_{60} = 2.0 mg/kg) on tumor growth after intratumor injection to the tumor-bearing mice plus light irradiation. Black filled circle: saline; empty square: C_{60}/HP-β-CyD plus light irradiation (30 J/cm^2); empty circle: C_{60}/HP-β-CyD plus light irradiation (60 J/cm^2); empty lozenge: C_{60}/HP-β-CyD plus light irradiation (75 J/cm^2); empty triangle: saline plus light irradiation (75 J/cm^2). Each point represents the mean $\pm$ S.E. of 3–9 experiments. $^*P < 0.05$ versus saline.

absence of irradiation. At this power, the temperature rise was within 5°C for 15 s and no light-induced skin damage was observed. It is interesting to note that the photodynamic effect was completely different depending on the protocol of light irradiation, even though the light energy supplied to tumor was almost the same (60 J/cm^2 in Figure 5 and 63 J/cm^2 in Figure 6). These results indicate that the PDT effect mainly depends on total light doses. Another parameter that limits tumor cell kill is the availability of oxygen in the

tissue undergoing PDT treatment [26]. Since ROS arises from ground state oxygen, this process consumes oxygen in the tissue environment. The repeated intervals in the treatment at 63 J/cm^2 might allow to oxygen to be regenerated and for a constant oxygen level to be maintained during PDT [27], leading to a sufficient PDT effect. Therefore, efficient PDT using C_{60} can be achieved by the repeated, short periods of high power irradiation. As shown in Figure 6(c),
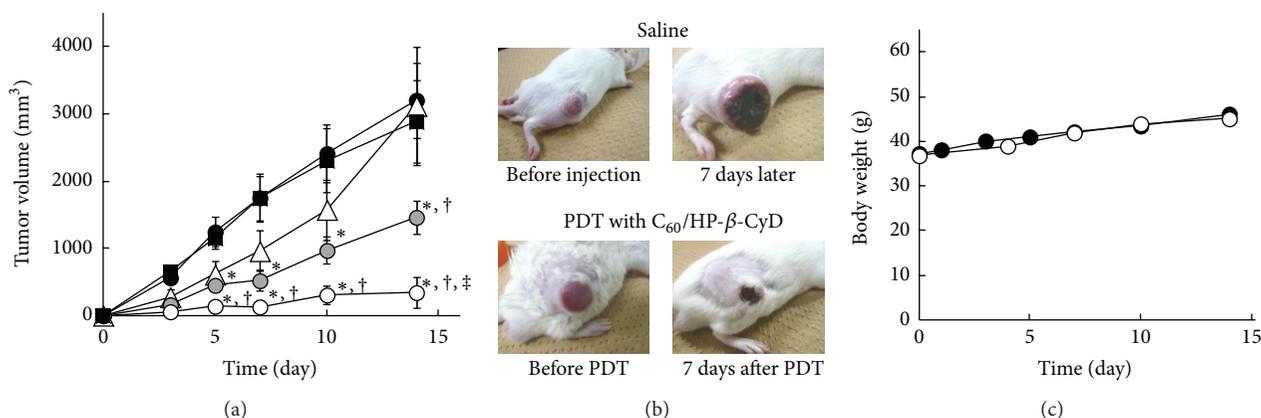
FIGURE 6: Photodynamic effects of C_{60}/HP-β-CyD nanoparticles on tumor growth (a). Appearances of tumor (b) and changes in body weight (c) after intratumor injection to the tumor-bearing mice plus light irradiation. Black filled circle: saline; black filled square: C_{60}/HP-β-CyD; empty triangle: saline plus light irradiation (63 J/cm^2); shadowed circle: C_{60}/HP-β-CyD (0.4 mg/kg) plus light irradiation (63 J/cm^2); empty circle: C_{60}/HP-β-CyD (2.0 mg/kg) plus light irradiation (63 J/cm^2). Each point represents the mean ± S.E. of 6–9 experiments. $^*P < 0.05$ versus saline. $^\dagger P < 0.05$ versus saline plus light irradiation. $^\ddagger P < 0.05$ versus C_{60}/HP-β-CyD (0.4 mg/kg) plus light irradiation (63 J/cm^2).

no significant difference in change of body weight was observed between C_{60}/HP-β-CyD nanoparticles and the saline solution injected mice, suggesting that the C_{60}/HP-β-CyD nanoparticles are relatively nontoxic. The light dose supplied in this experiment was not as high as the clinically used dose of 60~200 J/cm^2 from a laser [15, 28]. Therefore, C_{60}/HP-β-CyD nanoparticles appear to have great potential for use as a new photosensitizer for cancer treatment in PDT.

4. Conclusion

We investigated the potency of C_{60}/HP-β-CyD nanoparticles as a new photosensitizer in the treatment of cancer. C_{60}/HP-β-CyD nanoparticles had substantial photosensitizing ability compared with PpIX for the generation of $^1O_2$ under visible light irradiation. In addition, C_{60}/HP-β-CyD nanoparticles were capable of generating $O_2^{\bullet-}$ under visible light irradiation. The IC$_{50}$ value of the C_{60}/HP-β-CyD nanoparticles under photoirradiation was 10 μM for HeLa cells and 60 μM for A549 cells at an irradiation level of 35 mW/cm^2. Efficient PDT using C_{60}/HP-β-CyD nanoparticles in tumor-bearing mice was achieved by a treatment with C_{60}/HP-β-CyD nanoparticles at a C_{60} dose of 2.0 mg/kg followed by 12 periods of visible light irradiation at 350 mW/cm^2 for 15 s (total light dose 63 J/cm^2). These results demonstrate that C_{60}/HP-β-CyD nanoparticles are promising candidates for cancer treatment by PDT. The accumulation of C_{60} in the tumor and the pharmacokinetics of the process after injection of C_{60}/HP-β-CyD nanoparticles are currently under investigation in our laboratory.

Conflict of Interests

The authors declare that there is no conflict of interests regarding the publication of this paper.

References

[1] A. P. Castano, T. N. Demidova, and M. R. Hamblin, "Mechanisms in photodynamic therapy. Part one: photosensitizers, photochemistry and cellular localization," *Photodiagnosis and Photodynamic Therapy*, vol. 1, no. 4, pp. 279–293, 2004.

[2] A. P. Castano, T. N. Demidova, and M. R. Hamblin, "Mechanisms in photodynamic therapy. Part two: cellular signaling, cell metabolism and modes of cell death," *Photodiagnosis and Photodynamic Therapy*, vol. 2, no. 1, pp. 1–23, 2005.

[3] A. P. Castano, T. N. Demidova, and M. R. Hamblin, "Mechanisms in photodynamic therapy. Part three: photosensitizer pharmacokinetics, biodistribution, tumor localization and modes of tumor destruction," *Photodiagnosis and Photodynamic Therapy*, vol. 2, no. 2, pp. 91–106, 2005.

[4] T. J. Dougherty and S. L. Marcus, "Photodynamic therapy," *European Journal of Cancer A*, vol. 28, no. 10, pp. 1734–1742, 1992.

[5] S. Yano, S. Hirohara, M. Obata et al., "Current states and future views in photodynamic therapy," *Journal of Photochemistry and Photobiology C*, vol. 12, no. 1, pp. 46–67, 2011.

[6] R. Bakry, R. M. Vallant, M. Najam-ul-Haq et al., "Medicinal applications of fullerenes," *International Journal of Nanomedicine*, vol. 2, no. 4, pp. 639–649, 2007.

[7] A. W. Jensen, S. R. Wilson, and D. I. Schuster, "Biological applications of fullerenes," *Bioorganic and Medicinal Chemistry*, vol. 4, no. 6, pp. 767–779, 1996.

[8] R. Partha and J. L. Conyers, "Biomedical applications of functionalized fullerene-based nanomaterials," *International Journal of Nanomedicine*, vol. 4, pp. 261–275, 2009.

[9] M. R. Hamblin, P. Mroz, G. P. Tegos et al., "Photodynamic therapy with fullerenes," in *Fullerene Research Advances*, C. N. Kramer, Ed., chapter 1, pp. 1–31, Nova Science, New York, NY, USA, 2007.

[10] J. W. Arbogast, A. P. Darmanyan, C. S. Foote et al., "Photophysical properties of C_{60}," *Journal of Physical Chemistry*, vol. 95, no. 1, pp. 11–12, 1991.

[11] T. Nagano, K. Arakane, A. Ryu et al., "Comparison of singlet oxygen production efficiency of C_{60} with other photosensitizers, based on 1268 nm emission," *Chemical and Pharmaceutical Bulletin*, vol. 42, no. 11, pp. 2291–2294, 1994.

[12] J. W. Arbogast, C. S. Foote, and M. Kao, "Electron transfer to triplet fullerene C_{60}," *Journal of the American Chemical Society*, vol. 114, no. 6, pp. 2277–2279, 1992.

[13] D. Iohara, F. Hirayama, K. Higashi, K. Yamamoto, and K. Uekama, "Formation of stable hydrophilic C_{60} nanoparticles by 2-hydroxypropyl-β-cyclodextrin," *Molecular Pharmaceutics*, vol. 8, no. 4, pp. 1276–1284, 2011.

[14] D. Iohara, M. Hiratsuka, F. Hirayama et al., "Evaluation of photodynamic activity of C_{60}/2-hydroxypropyl-β-cyclodextrin nanoparticles," *Journal of Pharmaceutical Sciences*, vol. 101, no. 9, pp. 3390–3397, 2012.

[15] M. Triesscheijn, P. Baas, J. H. M. Schellens, and F. A. Stewart, "Photodynamic therapy in oncology," *Oncologist*, vol. 11, no. 9, pp. 1034–1044, 2006.

[16] D. Heymann, "Solubility of fullerenes C_{60} and C_{70} in seven normal alcohols and their deduced solubility in water," *Fullerene Science and Technology*, vol. 4, no. 3, pp. 509–515, 1996.

[17] R. S. Ruoff, D. S. Tse, R. Malhotra, and D. C. Lorents, "Solubility of C_{60} in a variety of solvents," *Journal of Physical Chemistry*, vol. 97, no. 13, pp. 3379–3383, 1993.

[18] A. Ikeda, Y. Doi, M. Hashizume, J.-I. Kikuchi, and T. Konishi, "An extremely effective DNA photocleavage utilizing functionalized liposomes with a fullerene-enriched lipid bilayer," *Journal of the American Chemical Society*, vol. 129, no. 14, pp. 4140–4141, 2007.

[19] H. Tokuyama, S. Yamago, E. Nakamura, T. Shiraki, and Y. Sugiura, "Photoinduced biochemical activity of fullerene carboxylic acid," *Journal of the American Chemical Society*, vol. 115, no. 17, pp. 7918–7919, 1993.

[20] Y. Yamakoshi, N. Umezawa, A. Ryu et al., "Active oxygen species generated from photoexcited fullerene (C_{60}) as potential medicines: $O_2^{\cdot-}$ versus $^1O_2$," *Journal of the American Chemical Society*, vol. 125, no. 42, pp. 12803–12809, 2003.

[21] G. R. Buettner, "Spin Trapping: ESR parameters of spin adducts 1474 1528V," *Free Radical Biology and Medicine*, vol. 3, no. 4, pp. 259–303, 1987.

[22] M. R. Detty, S. L. Gibson, and S. J. Wagner, "Current clinical and preclinical photosensitizers for use in photodynamic therapy," *Journal of Medicinal Chemistry*, vol. 47, no. 16, pp. 3897–3915, 2004.

[23] J. M. Fernandez, M. D. Bilgin, and L. I. Grossweiner, "Singlet oxygen generation by photodynamic agents," *Journal of Photochemistry and Photobiology B*, vol. 37, no. 1-2, pp. 131–140, 1997.

[24] L. Jaesang, Y. Yamakoshi, J. B. Hughes, and K. Jae-Hong, "Mechanism of C photoreactivity in water: fate of triplet state and radical anion and production of reactive oxygen species," *Environmental Science and Technology*, vol. 42, no. 9, pp. 3459–3464, 2008.

[25] B. Krammer and K. Plaetzer, "ALA and its clinical impact, from bench to bedside," *Photochemical and Photobiological Sciences*, vol. 7, no. 3, pp. 283–289, 2008.

[26] T. J. Dougherty, C. J. Gomer, B. W. Henderson et al., "Photodynamic therapy," *Journal of the National Cancer Institute*, vol. 90, no. 12, pp. 889–905, 1998.

[27] J. Zilberstein, A. Bromberg, A. Frantz et al., "Light-dependent oxygen consumption in bacteriochlorophyll-serine-treated melanoma tumors: online determination using a tissue-inserted oxygen microsensor," *Photochemistry and Photobiology*, vol. 65, no. 6, pp. 1012–1019, 1997.

[28] S. Mimura, T. Otani, and S. Okuda, "Photodynamic therapy for superficial esophageal cancer using an excimer dye laser," *Diagnostic and Therapeutic Endoscopy*, vol. 1, no. 2, pp. 99–105, 1994.

Research Article

Fluorescence Diagnostics of Colon Malignant and Premalignant Lesions Using 5-Aminolevulinic Acid

Elena V. Filonenko,[1] Andrey D. Kaprin,[1] Antonina A. Raszhivina,[2] Antonina N. Urlova,[1] and Andrey M. Nechipai[2]

[1] *P. A. Herzen Moscow Cancer Research Institute, 2nd Botkinskiy Proezd 3, Moscow 125284, Russia*
[2] *Department of Endoscopy, Russian Medical Academy for Postgraduate Training, 2nd Botkinskiy Proezd 5, Moscow 125284, Russia*

Correspondence should be addressed to Elena V. Filonenko; derkul23@yandex.ru

Academic Editor: Victor Loschenov

Improvement of colon cancer diagnosis is a very important medical problem. Methods of fluorescence diagnosis (FD) with 5-aminolevulinic acid (5-ALA) have been used in detection of early cancer on the surface of mucosa. The objective of the study was to estimate the effectiveness of FD with 5-ALA in the detection of malignant lesions in the colon. From 2008 to 2010 full examinations have been performed in 78 patients suffering from colon polyps. For the study we used drug Alasens based on 5-ALA. Fluorescence colonoscopy with Alasens was made using the visual assessment of fluorescence images in combination with local fluorescence spectroscopy. The results of FD were compared with those of final histopathological study. The application of the method during colonoscopy allows specifying diagnosis, identifying areas of colon tumors transformation, and also showing a place for targeted biopsy. Sensitivity and specificity of FD with Alasens were 94.9% and 62.5%, respectively. The application of local fluorescence spectroscopy as a step of the combined approach allows increasing the specificity of fluorescence colonoscopy from 62.5% up to 93.7%.

1. Introduction

The accurate and early diagnosis of colon cancer provides the success of surgical and combined modality treatment, allows increasing the rate of good outcomes, extends the life expectancy, and improves the quality of life in cancer patients. Therefore, improvement of colon cancer diagnosis is a very important medical problem.

The colorectal cancer is known to arise from adenomatous polyp; thus early endoscopic diagnosis and treatment of such tumors are an effective method of colon cancer prevention [1]. According to literature data, adenomatous polyps are the origin of malignant tumors in 4–10% of cases, and true colon neoplasms are of a great concern. The main difficulties for diagnosis of early cancer developed from colon adenomas include the lack of specific presentation and pathognomonic features obtained by the instrumental examination and possible missing of colon adenomas, particularly flat and depressed adenomas [2]. Diagnostic possibilities of routine colonoscopy to identify such pathology are limited as there are no reliable visual criteria for neoplastic transformation of adenomas, and verification of endoscopic diagnosis based only on biopsy using forceps is successful only in 30–50% of cases [3].

Advanced endoscopic instruments may therefore decrease the miss rate of adenomas and optimize the potential for colorectal cancer prevention. One of these novel technologies is autofluorescence imaging (AFI), which can capture fluorescence (500–630 nm) emitted from intestinal or other tissues. The Japanese group of authors [4] showed that AFI increased the detection rate and reduced the miss rate of colorectal adenoma, particularly flat and depressed adenomas. However, this advantage of AFI was limited to the less-experienced endoscopists. The review of the available literature on the use of AFI for the diagnosis of colorectal neoplasms [5] also showed that the utility of AFI for "optical

diagnosis" is limited. This may be due to the low resolution of current AFI video-endoscopy systems or to the subjective nature of interpreting color density of the images.

Therefore development of new methods for early diagnosis of colon polyp cancer transformation is necessary. One of such methods is fluorescence diagnosis (FD) with 5-aminolevulinic acid (5-ALA).

Tumor cells are known to accumulate increased levels of photoactive protoporphyrin IX (PpIX) in presence of exogenous 5-ALA. This can be explained by a greater enzymes activity in the initial stages of heme synthesis and by lack of ferrochelatase, an enzyme turning PpIX into photoinactive heme [6]. This form of heme cannot be detected by fluorescence. Ferrochelatase activity is decreased in tumor cells due to limited iron availability and is considered to be the main cause of selective fluorescence of PpIX in tumor by many authors [7, 8].

5-ALA is used both for local and systemic application. Increased fluorescence of 5-ALA-induced PpIX in tumor compared with normal tissue allows identifying the areas of high PpIX accumulation, detecting occult precancer and early cancer foci, and outlining localization of different tumors. Sensitivity and specificity of the method according to different authors are ranging from 43% to 100% and from 51% to 96%, respectively, depending on the tumor localization [9–16].

In the study of Bulgarian group of authors [17] exogenous fluorescence spectroscopy of esophageal and stomach tumors in vivo after oral application of 5-ALA six hours before spectroscopic measurements and video visualization of the patients using excitation at 405 nm was described. For rectal cancer there are also studies with other agents. For example, in the pilot study of German authors hexaminolevulinate-based fluorescence endoscopy was shown to be useful for detection of premalignant lesions. The study included ten patients with known rectal adenoma or cancer.

Thus, we decided to estimate the effectiveness of fluorescence diagnosis with 5-ALA in the detection of malignant lesions in the colon.

2. Materials and Methods

From 2008 to 2010 full examinations have been performed in 78 patients suffering from colon polyps. Twenty-seven (35%) patients were men and 51 (65%) were women. The age of patients was from 52 to 80 years. The mean age was 64.0 ± 8.3 years. The plan of full examination included clinical and biochemical blood analysis, clinical urine analysis, blood tests for syphilis, hepatitis B virus antigen, human immunodeficiency virus, electrocardiography, abdominal ultrasound, colonoscopy with biopsy using forceps, and FD. At the end of the examination, an endoscopic polypectomy was performed. The excised specimens were submitted to histopathological study.

For FD we used the photosensitizer Alasens (Research Institute of Organic Semi-Finished Products and Dyes, Moscow, Russia) given per os in the form of aqueous solution at a dose of 20–30 mg/kg body weight 3 h before fluorescence colonoscopy.

FD included colon examination in fluorescent mode. After endoscopic excision, polyps were reexamined in fluorescent mode and local fluorescence spectroscopy of the polyp's surface was performed in all cases.

For imaging under blue light excitation we used equipment produced by companies "Karl Storz" (Tuttlingen, Germany), "Olympus" (Japan). Video-assisted fluorescent light-emitting diode device UFF-630/675-01 produced by company "BIOSPEK" (Moscow, Russia) was used during the endoscopy. Laser electron-spectrum analyzer for FD (LESA-01) by "BIOSPEK" (Moscow, Russia) with a wavelength of laser source at 632.8 nm and recoding spectrum of fluorescence in the range from 635 up to 800 nm was used to register local fluorescence spectrum.

During local fluorescence spectroscopy 5–65 spectra were recorded in every patient. From 5 to 65 spectra were registered and recorded for each patient during the local fluorescence spectroscopy; 2615 spectra of fluorescence were registered and analyzed. The values of diagnostic parameter (DP) were calculated and recorded in all cases. The values of DP were taken from several parts of the neoplasm under visual detection of fluorescence; after that the average value was calculated for each tumor. The fluorescence intensity of polyp tissues was estimated by DP, which was calculated automatically by a special program as a ratio of the peak area of PpIX (690–720 nm) to the area of the reflected laser light (620–640 nm) and represented indirectly evidence of the Alasens-induced PpIX accumulation in the tissues. Fluorescence spectra of Alasens-induced PpIX in the intact colon mucosa were recorded with the determination of the fluorescent contrast of neoplastic/normal mucosa.

Malignant and premalignant (dysplasia) lesions with no fluorescence were defined as false-negative and benign tumors with fluorescence were defined as false-positive. Malignant and premalignant lesions with fluorescence were defined as positive and benign lesions without fluorescence were defined as negative.

3. Results and Discussion

3.1. Morphologic and Histopathological Findings. According to results of endoscopy 86% of all polyps were located in the lower parts of the left colon (rectum, rectosigmoid part, and sigmoid colon) and 14% were located above this level (descending colon, transverse colon, ascending colon, and caecum). One tumor was removed in 71 patients, two tumors in 5 patients, and 3 tumors in 2 patients. Totally, 87 tumors were diagnosed in 78 patients. According to the final histopathological study hyperplastic polyps were diagnosed in 9 (10.3%) cases, benign adenomas in 39 (44.8%), adenomas with different grades of dysplasia in 23 (26.4%), and malignant adenomas in 16 (18.5%) of the cases (Table 1).

3.2. Fluorescence Diagnosis. In 55 (63.2%) of 87 cases fluorescence of different intensity (from pale pink to bright red) was registered on the surface of the tumors and in 32 (36.8%) cases

TABLE 1: Distribution of tumors depending on the results of visual fluorescence detection (FD) and final histopathological findings.

Histopathological findings	Results of visual FD		Total
	F−	F+	
Benign tumors			
HP	—	9	9
TA	18	2	20
TVA	4	3	7
VA	8	4	12
Total	**30 (62.5%)**	**18 (37.5%)**	**48 (100.0%)**
Adenomas with dysplasia I–III			
TA dII	—	5	5
TA dIII	—	6	6
TVA dI	—	3	3
TVA dII	—	6	6
TVA dIII	—	3	3
Total	—	**23 (100.0%)**	**23 (100.0%)**
Malignant adenomas			
HG AC	1	7	8
MG AC	1	7	8
Total	**2 (12.5%)**	**14 (87.5%)**	**16 (100.0%)**
Total	32 (36.8%)	55 (63.2%)	87 (100.0%)

Note: F−: fluorescence was not detected; F+: fluorescence was registered; HP: hyperplastic polyp; TA: tubular adenoma; TA dII: tubular adenoma with grade II dysplasia; TA dIII: tubular adenoma with grade III dysplasia; TVA: tubular-villous adenoma; TVA dI: tubular-villous adenoma with grade I dysplasia; TVA dII: tubular-villous adenoma with grade II dysplasia; TVA dIII: tubular-villous adenoma with grade III dysplasia; VA: villous adenoma; HG AC: high-grade differentiated adenocarcinoma; MG AC: medium-grade differentiated adenocarcinoma.

had no fluorescence. Fluorescence was registered in 18 (37.5%) of benign tumors, in 23 (100%) of adenomas with dysplasia, and in 14 (87.5%) of malignant adenomas. In 18 benign lesions with false-positive fluorescence 9 had inflammation origin and 12 were characterized by high proliferative activity. We suggested that 100% fluorescence in adenomas with dysplasia compared with benign tumors could be explained by high proliferative activity due to precancer process leading to malignant transformation [18].

The sensitivity of visual detection of fluorescence was 94.9% and the specificity 62.5%.

The results of visual fluorescence detection in comparison with the results of routine histopathological investigation are shown in Table 1.

The spectra were registered in all areas of visual fluorescence. The values of DP were compared with the results of the routine morphological investigation. Distribution of tumors depending on the diagnostic parameter and the results of the final morphological investigation are presented in Table 2.

The level of Alasens-induced PpIX fluorescence on the surface of intact colon mucosa accounted for 0.20 to 0.86 arbitrary units (a.u.) (average, 0.56 ± 0.25 a.u.).

The DP ranged from 0.02 to 1.27 a.u. in 93.7% of benign tumors (average, 0.72 ± 0.43 a.u.). The average value of tumor/normal mucosa fluorescence contrast was 1.32 ± 0.79 a.u. in the group of benign tumors. In three cases (6.3%) the DP was 16.20, 17.80, and 26.84 a.u.; these values were defined as false-positive. All false-positive values were in patients with hyperplastic polyps.

TABLE 2: Distribution of tumors depending on the diagnostic parameter (DP) and final histopathological findings.

Histopathological findings	Value of DP (a.u.)					Total
	0-1	1-2	2-3	3-4	>4	
HP		6			3	9
TA	7	13				20
TVA	3	4				7
VA	6	6				12
TA dII			5			5
TA dIII		1	5			6
TVA dI	1	2				3
TVA dII			6			6
TVA dIII		1	2			3
HG AC		1	—	2	5	8
MG AC			1	2	5	8
Total	17	34	19	4	13	87

Note: HP: hyperplastic polyp; TA: tubular adenoma; TA dII: tubular adenoma with grade II dysplasia; TA dIII: tubular adenoma with grade III dysplasia; TVA: tubular-villous adenoma; TVA dI: tubular-villous adenoma with grade I dysplasia; TVA dII: tubular-villous adenoma with II dysplasia; TVA dIII: tubular-villous adenoma with grade III dysplasia; VA: villous adenoma; HG AC: high-grade differentiated adenocarcinoma; MG AC: medium-grade differentiated adenocarcinoma.

In the group of tumors with different degrees of dysplasia, DP values ranged from 0.76 to 2.73 (average, 1.83 ± 0.70 a.u.). The average value of fluorescence contrast tumor/normal in this group was 3.33 ± 1.26 a.u.

In a group of patients with malignant colon adenomas the DP ranged from 3.1 to 20.8 (average, 7.32 ± 6.70 a.u.) in 87.5% of cases. The average value of fluorescence contrast in this group was 13.32 ± 12.17 a.u. In two cases (12.5%) the DP was 1.49 and 2.70 a.u.; these values were defined as false-negative.

For a threshold level set at 3 a.u., the sensitivity of the method of the local fluorescence spectroscopy was 84.6% and the specificity 93.7%.

Thus, the study showed that sensitivity and specificity of fluorescence diagnosis with visual evaluation of fluorescence with Alasens were 94.9% and 62.5%, respectively. For example, Messmann et al. showed sensitivity and specificity to be 43% and 73% [18]. Complementation of this method by local fluorescence spectroscopy allows increasing the specificity up to 93.7%. The values of DP for normal mucosa were 0.56 ± 0.25, pre-cancer (dysplastic tissue)—1.83 ± 0.7, and cancer—7.32 ± 6.7. These differences were significant (Mann-Whitney U-test) between normal mucosa and cancer ($P = .018$) and normal mucosa and precancer (I–III grades of dysplasia) ($P = .043$). Thus, combined method of fluorescence diagnosis is a highly informative method for detecting malignant transformation in colon adenomas. Visual fluorescence diagnosis allows detecting fluorescence area on surface of colon polyps that is indicative for increased proliferation or transformation in benign lesions; these areas are difficult to be found for routine colonoscopy without using fluorescence diagnosis. According to results of study colon lesions with fluorescence should be excised with further histopathological verification.

4. Conclusions

FD with 5-ALA is an effective method of colon cancer detection. The application of the method during colonoscopy allows specifying diagnosis, identifying areas of colon tumors transformation, and also showing a place for targeted biopsy. The local fluorescence spectroscopy as a highly informative diagnostic method increased specificity of fluorescence colonoscopy with 5-ALA from 62.5% to 93.7%.

Conflict of Interests

The authors declare that there is no conflict of interests regarding the publication of this paper.

References

[1] P. Mlkvy, J. Majek, L. Jurgos, P. Makovnik, and S. Durdik, "Endoscopic treatment of praecancerous colorectal lesions and early colorectal cancer," *Bratislavské Lekárske Listy*, vol. 111, no. 1, pp. 50–53, 2010.

[2] S. Tsuda, B. Veress, E. Tóth, and F.-T. Fork, "Flat and depressed colorectal tumours in a southern Swedish population: a prospective chromoendoscopic and histopathological study," *Gut*, vol. 51, no. 4, pp. 550–555, 2002.

[3] V. V. Veselov, *Endoscopic treatment of patients with large and giant colon adenomas [Doctoral dissertation]*, State Science Center of Coloproctology, Moscow, Russia, 1997.

[4] K. Moriichi, M. Fujiya, R. Sato et al., "Back-to-back comparison of auto-fluorescence imaging (AFI) versus high resolution white light colonoscopy for adenoma detection," *BMC Gastroenterology*, vol. 12, article 75, 2012.

[5] Y. Takeuchi, N. Uedo, M. Hanafusa et al., "Endoscopic diagnosis of colorectal neoplasms using autofluorescence imaging," *Intestinal Research*, vol. 10, no. 2, pp. 142–151, 2012.

[6] V. Manivasager, K. K. L. Yee, P. W. S. Heng, K. C. Soo, and M. Olivo, "A study comparing endogenous protoporphyrin IX induced by 5-ALA and ALA-methyl ester with exogenous PpIX and PpIX dimethyl ester in photodynamic diagnosis of human nasopharyngeal carcinoma xenografts," *International Journal of Oncology*, vol. 29, no. 4, pp. 997–1002, 2006.

[7] M. Triesscheijn, P. Baas, J. H. M. Schellens, and F. A. Stewart, "Photodynamic therapy in oncology," *The Oncologist*, vol. 11, no. 9, pp. 1034–1044, 2006.

[8] D. L. Campbell, E. F. Gudgin-Dickson, P. G. Forkert, R. H. Pottler, and J. C. Kennedy, "Detection of early stages of carcinogenesis in adenomas of murine lung by 5-aminolevulinic acid-induced protoporphyrin IX fluorescence," *Photochemistry and Photobiology*, vol. 64, no. 4, pp. 676–682, 1996.

[9] W. J. Piotrowski, J. Marczak, A. Nawrocka, A. Antczak, and P. Górski, "Inhalations of 5-ALA in photodynamic diagnosis of bronchial cancer," *Monaldi Archives for Chest Disease*, vol. 61, no. 2, pp. 86–93, 2004.

[10] H. Stepp and R. Waldelich, "Fluorescence diagnosis and photodynamic therapy in urology," *Aktuelle Urologie*, vol. 38, no. 6, pp. 455–464, 2007.

[11] R. Baumgartner, R. M. Huber, H. Schulz et al., "Inhalation of 5-aminolevulinic acid: a new technique for fluorescence detection of early stage lung cancer," *Journal of Photochemistry and Photobiology B*, vol. 36, no. 2, pp. 169–174, 1996.

[12] H. Hautmann, J. P. Pichler, H. Stepp, R. Baumgartner, F. Gamarra, and R. M. Huber, "In-vivo kinetics of inhaled 5-aminolevulinic acid-induced protoporphyrin IX fluorescence in bronchial tissue," *Respiratory Research*, vol. 8, no. 1, article 33, pp. 33–39, 2007.

[13] S. G. Piccirillo, S. Dietz, B. Madhu et al., "Fluorescence-guided surgical sampling of glioblastoma identifies phenotypically distinct tumour-initiating cell populations in the tumour mass and margin," *British Journal of Cancer*, vol. 107, no. 3, pp. 462–468, 2012.

[14] E. V. Filonenko, V. V. Sokolov, V. I. Chissov, E. A. Lukyanets, and G. N. Vorozhtsov, "Photodynamic therapy of early esophageal cancer," *Photodiagnosis and Photodynamic Therapy*, vol. 5, no. 3, pp. 187–190, 2008.

[15] E. V. Filonenko, *Fluorescence diagnosis and photodynamic therapy in oncology [Doctoral dissertation]*, P. A. Herzen Moscow Cancer Institute, Moscow, Russia, 2006.

[16] H. Stepp, R. Sroka, and R. Baumgartner, "Fluorescence endoscopy of gastrointestinal diseases: basic principles, techniques, and clinical experience," *Endoscopy*, vol. 30, no. 4, pp. 379–386, 1998.

[17] E. Borisova, B. Vladimirov, and L. Avramov, "5-ALA mediated fluorescence detection of gastrointestinal tumors," *Advances in Optical Technologies*, vol. 2008, Article ID 862081, 7 pages, 2008.

[18] H. Messmann, E. Endlicher, G. Freunek, P. Rümmele, J. Schölmerich, and R. Knüchel, "Fluorescence endoscopy for the detection of low and high grade dysplasia in ulcerative colitis using systemic or local 5-aminolaevulinic acid sensitisation," *Gut*, vol. 52, no. 7, pp. 1003–1007, 2003.